



Light-Harvesting Antennae Using The Host-Guest Chemistry Of Mesoporous Organosilica

Student Name: Ben Jarman

Supervisor: Dr. Fabio Cucinotta

Doctor of Philosophy

School of Natural and Environmental Sciences

July 2018

Abstract

This thesis presents preliminary work into the synthesis of light-harvesting antennae using mesoporous silica (m-SiO₂). By forcing spatial constraint on components, nature can achieve unparalleled efficiencies when compared to artificial photosynthetic devices. Here, using supramolecular host-guest chemistry, systems are presented where the high chemical, thermal and mechanical stability of mesoporous silica has been combined with the excellent photophysical properties of BODIPY dyes and platinum(II) complexes. In contrast to other work in the literature, amphiphilic dyes have been used as a template for the silica, eliminating the need for removal of the micelles while retaining the mesoporous structure of the framework. Much of this thesis will be the exploration of this process. Next, zinc bis-quinolinolate complexes were incorporated into the silica framework. This will result in a bichromophoric system where the BODIPY dyes absorb light and transfer the excitation energy to the zinc complex, or vice versa, for use in such fields as photocatalysis and OLEDs. As this is preliminary work, these two processes have not been combined but lay the foundation for future experiments.

*To Mrs. Hooley, Mr. Tweddle, Mr. Rogozinski and Dr. Hodrien,
who instilled a lifetime passion in a wayward teenager*

Acknowledgements

Of course, I would first like to thank my supervisor, Fabio, who took me, a disorganised overconfident undergraduate, and helped to make me into a slightly less disorganised (the last year notwithstanding...) and humble(-ish) researcher. I will always be thankful, not only for his expertise and guidance, but his compassion and limitless patience. I'm sure he's blushing reading this so I'll stop the compliments there.

There are a number of factors that have contributed to this work being possible not least the funding from the EPSRC and general support from the School of Natural and Environmental Sciences. There are also a number of summer students, MChem students and collaborators without whom this thesis would be far thinner. I'd like to thank Jonathan Martinelli for synthesising **JM1**, Calvin Caplan for making the COK-12 samples and Matthew Bell for his tireless work on the aqueous synthesis of BODIPY. Much thanks to Emmanuele "I love hugs" La Mazza and Fausto Puntoriero for running the fs-TAS experiments. I'd also like to thank Valery Kozhevnikov and his group for synthesising the Pt(II) complexes and Richard Hunter for the silica synthesised using them. Finally, thank you to Andrew Bage and Sophie Berry for their work on the zinc complex-based PMOMs.

I have had the opportunity to work around some wonderful and genuinely inspiring people who, while offering much needed advice on chemistry, were always happy to have a good old moan with me. Firstly, I would like to thank my colleague, Marina. My PhD would not have been anywhere near as exciting, interesting or argumentative if you were not around. You may be Fabio's favourite for now but he'll come around again; you never forget your first...PhD student that is. Thanks to the many students of the Photonics at Newcastle group past and present: Fiona, Gareth, Chris, Nils, Nathan, Stu and Jamie for helping to further contextualise my research beyond my field as well as being generally wonderful people. The same applies to the members of the Molecular Photonics Laboratory: Pau, Dima, Yvonne, Josh and Owen and all members of the Johnston Lab for making me feel so welcome.

I'd like to thank my family for their support in this endeavour and for always pushing me to try to be better. My parents especially deserve credit, as they taught me from a very young age think for myself and to pay attention to detail (... oh and the financial support).

Last but by no means least, I would like to thank Rosie without whom this thesis would probably never have been finished. She worked under very difficult circumstances to get me through this final year (not least getting me to write) with very little reward for herself. We made it though, you and I. Who'd have thought?

Contents

Chapter 1. Mesoporous Silica – A Scaffold for Light-Harvesting Applications	1
1.1 Introduction – Global Energy Consumption	1
1.2 Photosynthesis – Natural and Artificial	4
1.3 Antennae in Porous Materials	10
1.4 Mesoporous Silica	14
1.5 Dipyrrromethene Complexes	20
1.6 Aims	23
References	25
Chapter 2. Analytical Techniques: Theory and Applications	29
2.1 Introduction	29
2.2 Optical Spectroscopy	29
2.2.1 Steady-State UV/Visible Absorption Spectroscopy	30
2.2.2 Steady-State Photoluminescence Spectroscopy	31
2.2.3 Emission Lifetime Studies	32
2.2.4 Transient Absorption Spectroscopy	34
2.3 Structural Analysis	35
2.3.1 Powder X-Ray Diffraction	35
2.3.2 Small Angle X-Ray Scattering	36
2.3.3 Transmission Electron Microscopy	38
References	40
Chapter 3. Mesoporous Silica Templated with Dye-Doped Micelles	43
3.1 Introduction	43
3.2 COK-12	44
3.2.1 Structural Analysis	48
3.2.2 Spectroscopic Analysis	49
3.3 MCM-41	52
3.3.1 Structural Analysis	54
3.3.2 Spectroscopic Analysis	56

3.4	Conclusion	58
3.5	Experimental	62
References		65
 Chapter 4. BODIPY-Doped Micelle and Silica Formation Dynamics		69
4.1	Introduction	69
4.2	The Base Test	70
4.3.1	Step-by-Step Investigation – Step 1) Micelle Formation	72
4.3.2	Step 2) Addition of NaOH	74
4.3.3	Step 3) Addition of TEOS	76
4.3.4	Step 4) Post-Synthetic Drying	77
4.4	Inverse Relationship Between % BPJ2 and Amount of BS	79
4.5	Conclusion	81
4.6	Experimental	81
References		83
 Chapter 5. Emission Tuning with Pt(II) Complexes in m-SiO₂ via Aggregation		85
5.1	Introduction	85
5.2.1	Micelle Formation and Morphology Changes	90
5.2.2	¹ H NMR Co-Solvent Studies	94
5.3	Platinum(II) Complexes in Silica	98
5.3.1	Structural and Morphological Analysis	100
5.3.2	Spectroscopic Analysis	101
5.4	Conclusion	105
5.5	Experimental	105
References		108
 Chapter 6. Synthesis and Optical Properties of a New Organometallosilica		111
6.1	Introduction	111
6.1.1	Zinc(II) Complexes	112
6.1.2	Quinolate Ligands	113
6.2	Synthesis and Photophysics of Zn(Br₂-q)₂ and Zn(Si₂-q)₂	114

6.3	Zn(Si₂-q)₂-PMOM	118
6.3.1	Structural Analysis	118
6.3.2	Spectroscopic Analysis	120
6.3.3	Rhodamine B-Zn(Si _x -q) ₂ Antenna	121
6.4	Conclusion	126
6.5	Experimental	127
References		129
Chapter 7. Summary		133
Appendix		142
Publications		152

Chapter 1. Mesoporous Silica – A Scaffold for Light-Harvesting Applications

1.1 Introduction – Global Energy Consumption

In the modern world, cheap and widely-available energy is a top priority. Fuelling this demand is no small endeavour with around 95% coming from fossil fuels.¹ These ancient carbon-rich resources are also used as a chemical feedstock in a wide variety of products including plastics, clothing, medicine and cosmetics.^{2,3} They are in fact so intrinsic that major economies are built around their use as evidenced by the almost complete collapse of the Russian rouble when oil prices fell to less than \$50 per barrel in late 2014.^{4,5} A similar event is possible once coal production is deemed no longer economically viable with China being simultaneously its largest producer and consumer.²

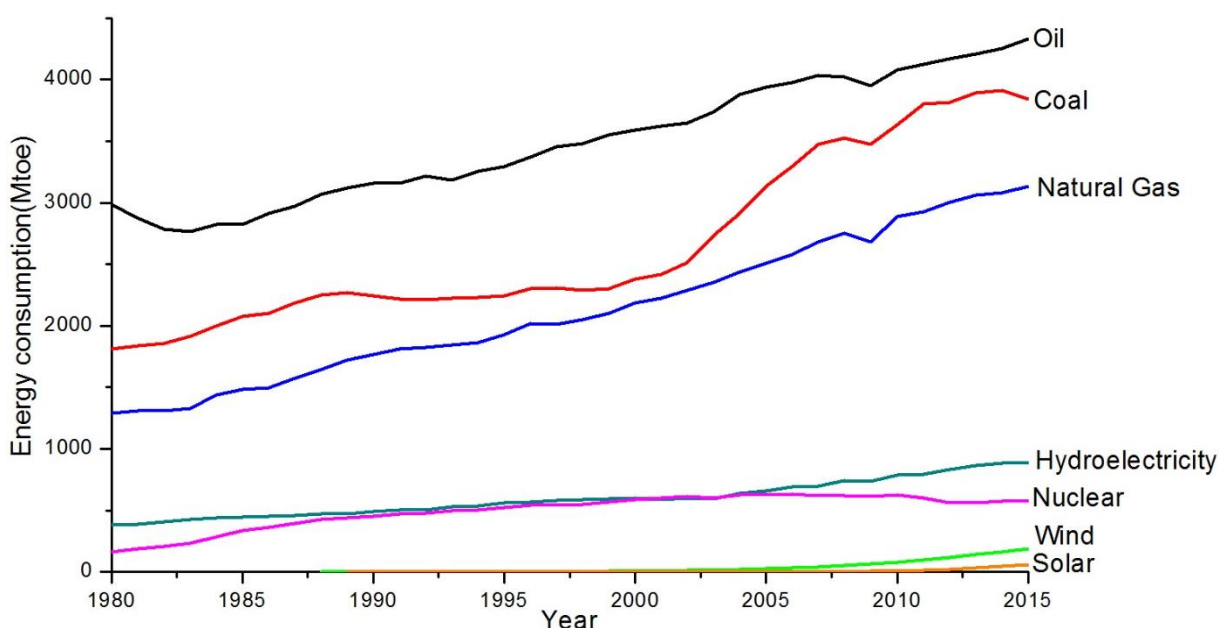


Figure 1: A plot adapted from BP Statistical Review of World Energy June 2014 showing the global consumption of energy derived from different sources since 1980 (toe – tonne of oil equivalent).⁵

Figure 1 is a plot of data gathered by British Petroleum (BP) showing the global consumption of energy from different resources since 1980. In all cases shown, there has been a steady increase in consumption over the last 35 years (excluding nuclear). It is clear that a vast proportion of the world's energy is derived from fossil fuels, most predominantly crude oil. In contrast, most renewable sources, solar energy in particular, have seen almost no increase at all. Despite this, it is a well-known fact that fossil fuels are a finite resource and

will run out. There have been several viable alternative methods developed over the last century that could help to extend this deadline, whether by increasing fossil fuel stockpiles (e.g. shale gas) or utilising completely different paths (e.g. nuclear power).⁵

The former was proposed as one source of “unconventional” natural gas in the early 20th century but the technology used to extract it was deemed too expensive to make it economically viable. However, as is the way with such things, necessity and global politics drove governments to invest more in shale gas resulting in the bustling infrastructure seen today. This method is not without controversy though, with environmental factors like pollution of nearby water tables and continued CO₂ production making shale gas far from ideal.⁶ The latter alternative, in the form of nuclear fission, was hailed as a cheap and clean source of energy with many plants having been built around the world.⁷ However, this has been counteracted by incidents such as the Chernobyl disaster (1986) and the Fukushima Daiichi meltdown (2011), not to mention the threat of nuclear weapons, which have chipped away at public opinion. This social stigma has led to lower investment resulting in a marked decrease in nuclear power consumption as evidenced on Figure 1.⁵

These economic arguments alone, environmental effects notwithstanding,⁸ should be enough to convince even the most fervent of climate change sceptics that a move away from fossil fuels is needed. It seems sensible therefore, while resources are readily available, to try and develop alternative methods of energy production. These include the well-known examples such as wind, geothermal and hydroelectric sources all of which are seeing increased usage, particularly in the 21st century. It can be argued that a combination of all viable methods is the best approach in the replacement of fossil fuels lending equal merit to all avenues of research. However these methods only represent ways of creating electricity and thus do not address the issue of chemical feedstock.⁹

Another alternative to fossil fuels that can act towards electricity generation and feedstock issues is to use the power of the ever abundant source that has been investigated, revered and worshipped throughout human history; the Sun. At 1.2×10^5 terawatts, it delivers more energy to the Earth than any other power source, far outweighing the current demand.¹⁰ It does however supply this power intermittently, depending on time of day and weather conditions, and in a diffuse manner at high latitudes, where countries such as the UK are situated, so collecting this energy is difficult and therein lies the challenge for modern photochemists.

Figure 2 shows a schematic of a silicon-based solar panel which represents the most commercially viable way so far to achieve solar energy conversion directly into electricity. Monocrystalline-based devices have been shown to have an efficiency of around 18%, with higher values demonstrated in the literature and polycrystalline versions being of comparable efficiency and commercial value. Put simply, when illuminated with sunlight they absorb at energy equal to the electronic band gap of the semiconductor (for Si, $E_g = 1.11$ eV) and generate an electron(e^-)-hole(h^+) pair known as an exciton. Holes and electrons then migrate through the material to their respective electrodes forming a potential difference equal to that of the band gap and so a current is generated.¹⁰

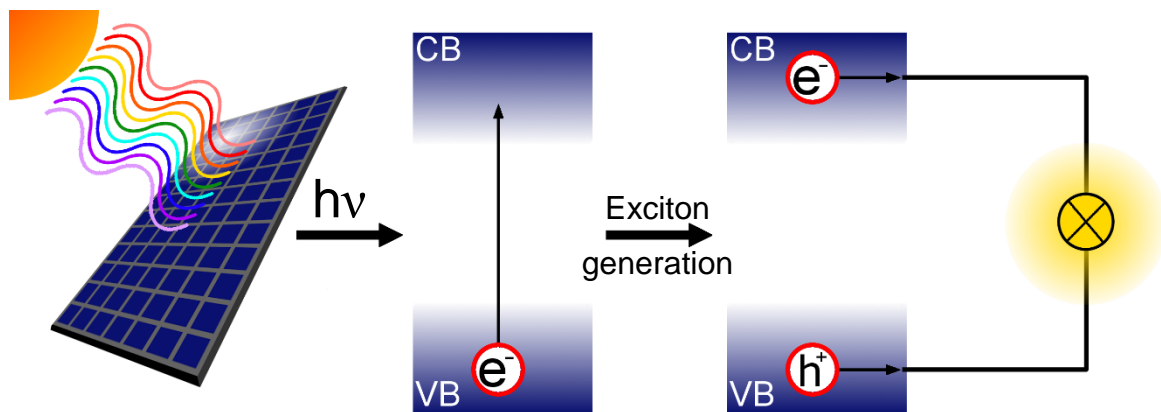


Figure 2: Schematic of electricity generation in a monocrystalline silicon solar cell. CB - conduction band, VB - valence band, e^- - electron, h^+ - hole.¹¹

There are notable advantages to using systems such as these. Mainly, while processing costs are high, silicon is the second most abundant element in the Earth's crust making it a readily available material with a long working lifetime (approximately 30 years). However, this technology does have its drawbacks due to silicon being an indirect band gap semiconductor. Without delving in specifics, this means that any electron in the valence band must absorb energy from a photon as well as momentum from lattice vibrations (phonons) in order to access the conduction band. Excitation therefore relies on the coincident interaction of three components as opposed to two (photons and electrons) as is seen in direct band gap semiconductors (e.g gallium arsenide, GaAs). This results in a relatively low probability of absorption which means that silicon crystals must be thicker (typically 200 μm) and therefore use more material in order to efficiently generate electricity. Also, while silicon can be seen as a panchromatic absorber, in that it absorbs energy from much of the solar spectrum from ultra-violet all the way up to the infra-red, a significant proportion from high-energy photons is lost as heat to allow for excitation.¹⁰

Another major disadvantage with commercial single junction solar cells in particular is that their maximum theoretical efficiency under normal solar illumination (AM1.5G) is 33.7%. This is known as the Shockley-Queisser limit and arises from a variety of reasons including recombination and black body radiation of the silicon. Also, while they do absorb much of the ultraviolet and visible range, silicon-based solar panels are transparent to low-energy infra-red, microwaves and radio photons, which take up around 19% of the solar spectrum.¹² Add to this the fact that no chemicals are made in this process meaning these systems do not contribute to feedstocks.

These disadvantages lead to the conclusion that alternative methods of solar energy conversion that can generate chemical fuels need to be developed. In this case, light is absorbed generating a state with high chemical potential energy. This state subsequently uses this energy to form products instead of a current. Such systems can then be used to either provide in the areas silicon-based technologies fail to or replace them altogether.

1.2 Photosynthesis – Natural and artificial

As with most scientific advances, nature had developed photocatalytic methods of energy production long before humans even existed in the form of photosynthesis. Figure 3 shows a schematic of a light harvesting system typical within biological systems.¹³ This shows a simplistic view of the specialised components found in the cell membranes of purple bacteria

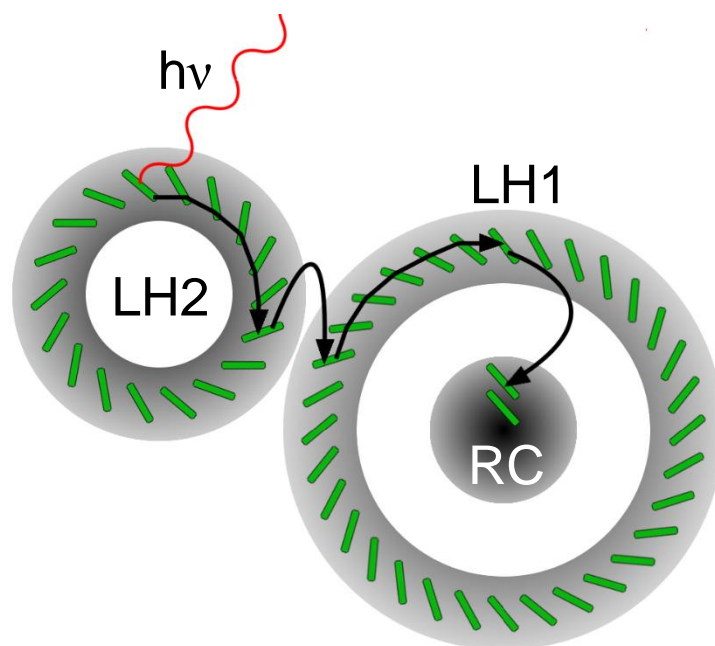


Figure 3: A diagram showing how light harvested by chlorophyll units that are arranged into the LH1 and LH2 ring. They then transfer absorbed energy to a reaction centre in natural photosynthetic systems.¹³

Rhodospseudomonas acidophila called light harvesting (LH) units. Higher plant life has been shown to use the same overall mechanism, albeit with a more complicated system held in chloroplasts.¹⁴⁻¹⁶ Both bacteria and plants possess specialised LH units arranged in such a way as to funnel energy from diffuse sunlight into a concentrated area where it can be used for chemistry. In this example, photons are absorbed by chromophoric units (green rods) in the relatively smaller ring of LH2 and the energy is transferred around the ring and eventually to

the larger LH1 unit. The energy is then transferred around the ring and to the reaction centre (RC) within LH1. Here, the energy is used to prompt the synthesis of molecules such as glucose from CO₂, producing O₂ as a by-product. In doing so, nature has found a way to simultaneously fix carbon from the atmosphere and form a chemical feedstock.¹³

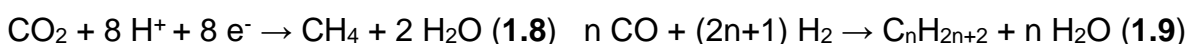
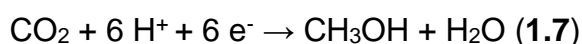
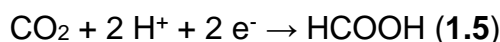
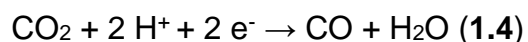
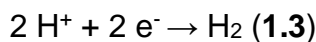
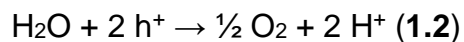
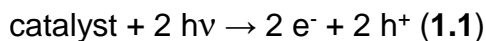


Figure 4: Generation of electron-hole pairs (1.1, assuming 100% yield of exciton generation per photon absorbed) and the half reactions for water splitting (1.2-1.3), CO₂ reduction (1.2, 1.4-1.8) and straight chain alkane formation from syngas (1.9).¹⁹

When mimicking photosynthesis artificially, a number of considerations must be made. First is the type of output, in that while sugars are useful fuels for living organisms, man-made infrastructure is better suited to simpler molecules. Because of this, artificial photosynthesis usually centres on redox reactions with H₂O to form H₂ or reduction of CO₂ into small carbon-based products. Both of these reactions were first demonstrated by Honda *et al.* in the 1970's.^{17, 18} The former was first achieved by submersing TiO₂ and platinum black electrodes in an acidic electrolyte. The TiO₂ electrode was then illuminated with UV light of energy corresponding to the band gap, which formed the initial exciton pair (1.1). It was found that O₂ and H₂ were evolved on the TiO₂ and platinum electrode respectively (see equations (1.2) and (1.3)). The latter was achieved by bubbling CO₂ through stirred suspensions of a variety of semiconductors (e.g. TiO₂, SiC, CdS) while under UV illumination. Gas chromatography was used to show that a wide range of products were formed including carbon monoxide(1.4), formic acid(1.5), formaldehyde(1.6), methanol(1.7) and methane(1.8), all of which can be used as fuels and/or chemical feedstocks.¹⁹ From both of these reactions, CO and H₂ can be taken and mixed to form syngas, which is already used to form higher carbon chains via the Fischer-Tropsch process(1.9).²⁰ These pioneering experiments showed that it is possible to use light to make fuels using relatively simple setups.

The semiconductors mentioned above, however, only absorb in the UV region so there has been much research into accessing more of the solar spectrum by using molecular units that

can absorb and emit across visible region. Commonly, molecular units are used in conjunction with semiconductors. One notable example of this would be dye-sensitised solar cells (DSSCs) whereby an organic dye is anchored directly on a semiconductor surface. Here, the dye absorbs a visible light photon generating an exciton. Either the hole or electron is then transferred to the semiconductor (depending on type) which is connected in a circuit and thus generates a current.¹¹ Another example of this would be luminescent solar concentrators (LSCs) in which highly luminescent molecules are bound in or upon a transparent substrate, such as glass or polycarbonate. When the dyes absorb and emit a photon from diffuse sources, the light is held within the substrate by internal reflection. This substrate acts as a waveguide, directing the light to the thin edges where photovoltaic materials are located. These then generate current as demonstrated in Figure 2.²¹ While neither of these systems have beaten silicon solar cells in terms of overall efficiency, the molecular units exhibit relatively higher absorption of light allowing them to be used even under highly diffuse lighting conditions such as inside buildings. They show that a movement towards molecular based systems may hold the key to higher efficiency of solar energy conversion in the future.

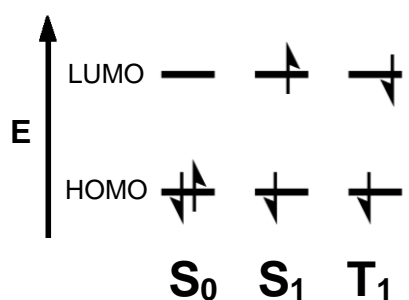


Figure 5: An electronic energy level diagram showing the electronic structure of the singlet ground state (S_0), first excited singlet state (S_1) and the first excited triplet state (T_1) of an organic molecule.²²

As this thesis will focus primarily on these kinds of photoactive units, a brief introduction into molecular photophysics will be given here. Figure 5 shows the electronic energy level diagrams for the valence electrons in the three most common states seen in molecular photophysics. In the absence of external stimuli, most organic molecules reside in the singlet ground state (S_0) where two electrons are spin-paired in the highest occupied molecular orbital (HOMO). Once excited with light, an electron transitions to the lowest

unoccupied molecular orbital (LUMO). The spin of the electron is conserved during this process making this state the first excited singlet state (S_1). Another state that features frequently in this field is the first excited triplet state (T_1) in which the spin of one electron flips resulting in a spin parallel system. In accordance with Hund's first rule, the T_1 state is typically lower in energy than the S_1 state.²² These excited states can be seen as analogues of the excitons seen in bulk semiconductors (see above) where the hole resides in the HOMO and the electron resides in the LUMO.

While it is useful to visualise the electronic configuration of a molecule in different states, it is far more beneficial to consider the energy of the molecule as a whole when thinking

about light induced processes. Figure 6 shows a Jablonski diagram which is commonly employed to represent the basic photophysics of organic molecules. Changes in energy level that result from or in a photon are represented by straight lines and those involving vibrational energy changes are represented by wavy lines. Using this we can outline the transitions between the electronic states (black lines) shown in Figure 5 while also adding more detail.²²

At absolute zero, only the electronic states would be seen in this diagram. However, at elevated temperatures, the molecule is allowed to vibrate which causes all electronic states to shift up in energy. Like electronic states, vibrational energy is also quantised resulting in discrete levels (grey lines) denoted by v_n ($n = 1-4$). In the absence of external stimuli, most organic molecules reside in the S_0 state as well as the vibrational ground state (v_0). Upon absorption of a photon (i) of energy equal to the energy gap between S_0 and S_1 , the molecule moves from the former to the latter. Higher energy photons can also be absorbed to access the higher vibrational modes of the S_1 state.²² Absorption of photons by molecular units is quantified by using the Beer-Lambert law, which gives the molar absorption coefficient (ϵ) given in $M^{-1}.cm^{-1}$. In organic molecules, absorption of a photon that results in an $S_0 \rightarrow S_1$ transition is typically between 10,000 and 100,000 $M^{-1}.cm^{-1}$.²³ Such high values of ϵ are typical for allowed transitions such as these. This concept will be expanded in Chapter 2 of this thesis. After initial excitation, the molecule will relax vibrationally down to the S_1, v_0 state, giving out any excess energy as heat (ii) in accordance with Kasha's rule.^{22, 24}

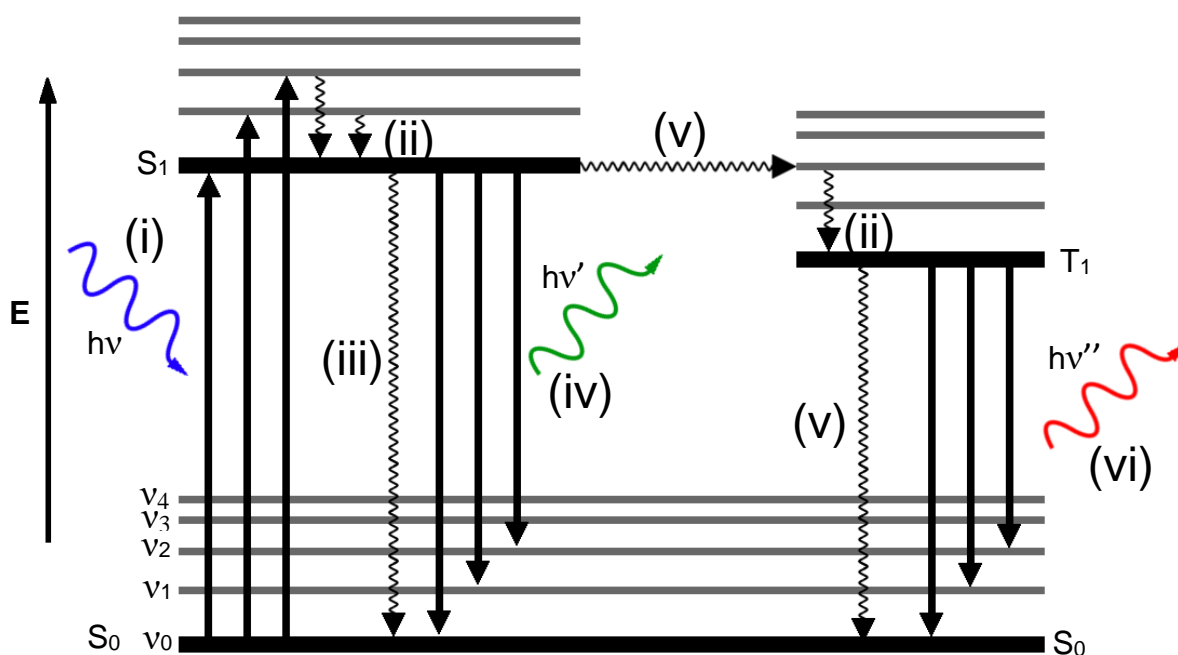


Figure 6: A molecular energy level (Jablonski) diagram showing the different light-induced transitions between electronic (black) and vibrational (grey) energy levels in an organic molecule. (i) Absorption, (ii) thermal relaxation, (iii) internal conversion, (iv) fluorescence, (v) intersystem crossing and (vi) phosphorescence.²²

From here, there are three paths that can be taken, the first being internal conversion (IC, iii), whereby the molecule relaxes non-radiatively from S_1 to S_0 also giving this energy out as heat similar to (ii). The second path is fluorescence (iv) where, in the process of relaxation, the molecule emits a photon, which is of lower energy than the one that was initially absorbed. The difference in the absorption and emission wavelength is called the Stokes shift which, due to it being principally caused by the vibrational relaxation in a molecule, can give insight into the rigidity of a system. Fluorescence is spin-allowed in that the electron spin is not changed during relaxation making it a relatively probable and fast process, typically within timescales of picoseconds (ps) and nanoseconds (ns). The alternative pathway from the S_1 state is intersystem crossing (ISC) where the spin of the excited electron is flipped causing the molecule to enter the T_1 state (v). While this is a spin-forbidden process, ISC can be promoted if the S_1 and T_1 possess degenerate vibrational states and if heavy atoms are present in the system. This is the only efficient way to populate the T_1 state as direct excitation from S_0 to T_1 in organic molecules and simple metal complexes is incredibly weak with ϵ values in

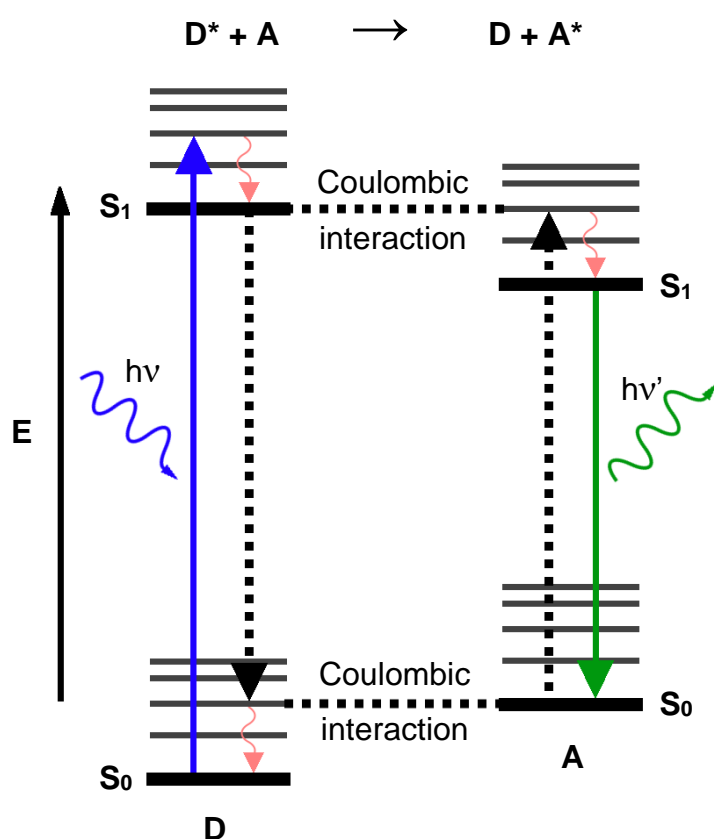


Figure 7: A Jablonski diagram outlining the process of Förster Resonance Energy Transfer (FRET).²⁹

the order of $1-100 \text{ M}^{-1} \cdot \text{cm}^{-1}$ ²⁵ (although there are certain examples of exceptionally high ϵ values for this transition in the literature²⁶). After further thermal relaxation (vi), the T_1 state can decay to S_0 in two ways: non-radiative ISC (vii) or phosphorescence (viii). Due to it being spin-forbidden, phosphorescence is a slow process typically having lifetimes from microseconds (μs) up to seconds or even minutes and hours. As T_1 is usually lower in energy than S_1 , the phosphorescence tends to be red-shifted with respect to fluorescence.^{22, 27}

By manipulating these energy levels, it is possible to access wavelengths across the UV, visible and near infra-red region of the solar spectrum using molecular units. Indeed, natural

photosynthetic systems use a range of dyes to optimise the intake of sunlight.²⁸ In this case however, the absorbed energy must be funnelled to the reaction centre before it can perform any useful reactions as seen in the case of LH units (Figure 3). This is achieved using a phenomenon known as Förster Resonance Energy Transfer (FRET), shown in Figure 7.²⁹ In this mechanism, a donor chromophore (D) absorbs light, moving it from the singlet ground state (S_0) to the first excited singlet state (S_1). If isolated, this molecule would lose some vibrational energy then fluoresce, emitting a photon. In the case of FRET however, the donor is close in space to an acceptor molecule (A), typically from 1-10 nm, but not too close as to facilitate orbital overlap (<1 nm). In this specific region, the transition dipoles of the molecules can couple through coulombic interactions. This results in the concerted relaxation of the donor and excitation of the acceptor, resulting in the latter being in the S_1 state.³⁰

It should be noted here that FRET is a non-radiative process in that the donor does not emit a photon which is then reabsorbed by the acceptor, although this can take place under different conditions. FRET is also very sensitive to D–A proximity, with the efficiency of energy transfer being inversely proportional to distance between the dye units raised to the sixth power. This property allows it to be a useful tool in probing supramolecular processes such as protein folding. FRET will be expanded upon later in this thesis when specific examples arise.³⁰ In the case of orbital overlap, electrons can be exchanged between donor and acceptor units in a different mechanism known as Dexter energy transfer³¹ and will not feature heavily in this thesis.

Once the energy is transferred, the acceptor will then utilise the energy for instance by fluorescing as shown in Figure 7. Alternatively, the energy could be used to form a state with high chemical potential. This can then be used for chemical reactions in order to make fuels. It is this process that takes place in natural LH systems whereby the exciton is generated on the LH2 then transferred to LH1 and eventually to two electronically coupled metalloporphyrins in the RC known as the “special pair”. From here, charge-separation occurs whereby the electron is transferred to other units while the hole stays on the special pair. The electron is then used to reduce quinones and eventually for the formation of sugars.²⁸

These types of systems that absorb over a range of wavelengths and funnel the energy to a final unit are known as light-harvesting antennae and many artificial systems exist in the literature. This is achieved by using what is called an energy cascade whereby several units of differing spectroscopic properties are coupled together. In order to make this energy cascade happen efficiently, units must be held in close proximity to allow exchange processes to take

place, mostly in the form of FRET although other phenomena can occur (e.g. Dexter energy transfer, excimer/exciple formation, charge transfer etc.).^{32, 33}

Certainly, one of the most demonstrable examples comes in the form of dendrimers, so called because of their branched structure. In these systems, a central primary unit (C) is synthesised in such a way that secondary units (B) can be covalently attached in several positions. From here, a third set of groups (A) are attached as shown in Figure 8a). The different units are chosen specifically for their main transition energy gap in order to result in a cascade. The exciton is therefore transferred from the high energy A unit to the intermediary B unit and finally to the low energy C unit as shown in Figure 8b). Due to the close proximity enforced by the architecture, energy transfer from A and B is favoured as opposed to competing processes such as fluorescence and thermal deactivation. This type of system allows sensitisation of a single unit, for instance a photocatalytic centre, without limiting excitation to the parts of the solar spectrum where that unit absorbs.^{32, 33}

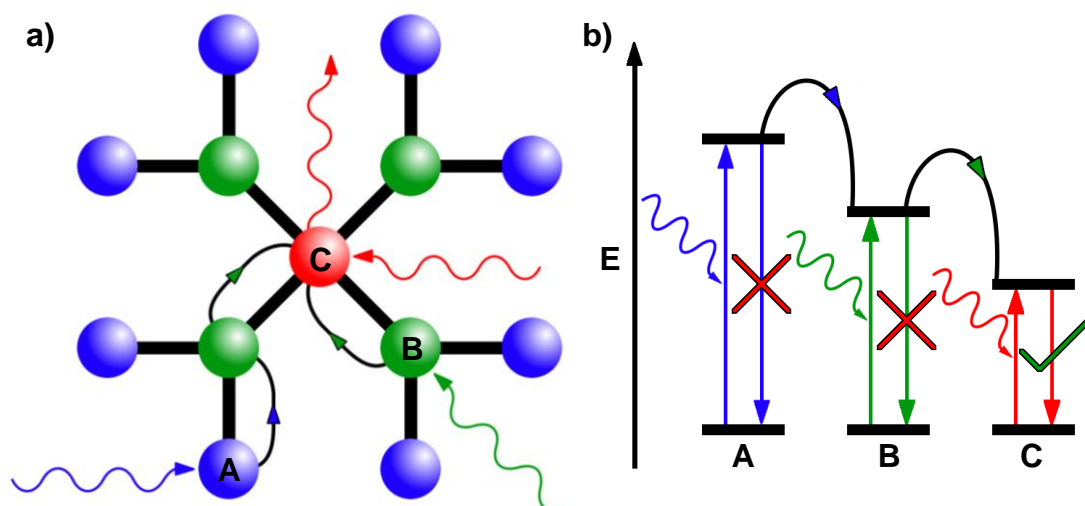


Figure 8: A schematic showing how photon energy is transferred through space in a dendrimeric antenna and the corresponding energy level diagram.^{32, 33}

1.3 Antennae in Porous Materials

One other aspect of biological photosynthesis that improves efficiency is the fact that chromophoric units are enclosed in a protein membrane. The effects of this are threefold. Firstly, the scaffold provides primary mechanical and chemical protection to the delicate chromophores and reaction centres. One of the most common deactivation mechanisms takes place under high intensity lighting conditions such as at midday. Here, excess absorbed energy can lead to recombination of the charge-separated state formed in the reaction centre

resulting in triplet chlorophyll units. These can then react with molecular oxygen (which is a triplet in its ground state) to form singlet oxygen which can be lethal to these systems and thus to the organism as a whole. The protein manifold can prevent access to delicate components by any reactive oxygen species, such as peroxides and radicals, that are formed without.²⁸

Secondly, as was touched upon earlier, the scaffold holds all of the units at specific positions in space. This is particularly important for intermolecular distances that allow FRET to take place efficiently facilitating energy transport from peripheral chlorophyll units to the reaction centre. This is particularly impressive when one considers that the individual molecules in the special pair are the same type of metalloporphyrin as the chlorophyll units seen in the LH rings. What distinguishes them is the protein environment around them which in the case of the special pair forces them to be very close in space, which encourages electron transfer as opposed to FRET resulting in the charge-separated state needed for photosynthesis to take place.²⁸

Lastly, the protein membrane wraps itself around the different components of the systems forming a rigid network that dampens atomic movement. This means that molecules cannot vibrate as much as they would in solution and so less energy is lost to vibrational relaxation. It also helps to lower the reorganisation energy (λ) of any reactions that take place. This refers to the change in bond lengths and angles as a result of chemical change and can be broken down into two components: nuclear (λ_N) and solvent (λ_S). λ_N refers to the movement of atoms in the specific reactants in the RC as they change into products. While atomic movements are relatively small in this regard, resulting in a small λ_N , the effect on their inner and outer coordination spheres is far reaching, particularly if the reaction takes place in solution phase. Here, intermolecular distances and angles are changed more subtly but over a much wider range resulting in a large λ_S value thus a dramatic increase in λ as a whole. This is particularly prominent in aqueous systems which feature a large hydrogen-bonded network coordinated around the reaction centre.³⁴ With this in mind, one can see why reaction centres and chromophoric units in natural systems are contained within large proteins through coordination with amino acid residues.¹⁴⁻¹⁶ In doing so, this rigid backbone moves very little as a result of reaction when compared to solvent coordination spheres so reorganisation energies are decreased. This in turn leads to lower activation enthalpies making reactions take place with much lower input energy thus increasing the efficiency of the entire system.³⁴

Porous inorganic materials offer an avenue towards mimicking this spatial constraint artificially. These systems can possess pores of varying sizes and can be categorised as

microporous ($< 20 \text{ \AA}$) or mesoporous ($20\text{-}500 \text{ \AA}$). Like proteins, they can accommodate molecular units within them either covalently or through intermolecular interactions. This is the principle behind host-guest chemistry. It can be visualised by thinking of these materials as hotels whereby rooms, representing pores, are built in such a way as to be arranged in a regular arrangement with inorganic material as walls. This “hotel” forms the host portion of these systems. Molecules can occupy space within the pores in the same way guests occupy rooms in a hotel.

Introduction of guests into host materials comes in two forms: physisorption and chemisorption. In physisorption, guests are diffused into adsorption sites on the host from a gas or solution where they held via Van der Waals interactions. Due to the relative weakness of these forces, this process is usually reversible, much like tourists visiting a different country as temporary guests in the above hotel metaphor. Chemisorption on the other hand involves reacting guests with the surface of the host in such a way as to result in formal covalent bonds. This process is therefore irreversible as the energy needed to break the linker would likely result in decomposition of the guest. This would be like a traveller emigrating and settling down. In reality, interaction between hosts and guests have varying degrees of strength whether physi- or chemisorbed. As such, there are certain cases which lie in the overlap of these definitions such as instances where hydrogen bonds are involved.³⁵

Inorganic host materials come in a variety of compositions and morphologies and can be seen with applications across research and industry. They can feature layers between which guests can intercalate such as with clays³⁶ or have pores of various shapes such as triangles, circles and hexagons designed to suit specific guests as in the case of metal-organic frameworks (MOFs).³⁷ Both these and other host-guest systems have been found to be useful for many uses including, but not limited to, catalysis, chromatography and pollutant removal.

One class of porous materials that dominates this field are zeolites. Zeolites are aluminosilicates that exhibit three-dimensional order resulting in unidirectional parallel pores running the length of the crystal. At certain points, aluminium replaces silicon in the tetrahedral network causing these materials to have an overall negative charge. Due to this, water molecules and metal cations, usually Na^+ , are loosely bound in the pores and can be substituted readily by cationic or polar guests.³⁸ A simple example comes when protons (H^+) replace the cations resulting in a solid state acid catalyst used in a variety of applications.³⁹

The most notable examples of these materials being used as light-harvesting antennae that utilise an energy cascade in a zeolite crystal come from Calzaferri et al. First published in 1998, this system featured the red emitting dye oxonine (Ox^+) and the green dye pyronine (Py^+) which were loaded into the channels of a zeolite L crystal. This was achieved via sequential ion exchange between the Ox^+/Py^+ units and Na^+ ions left over from the zeolite synthesis. Fluorescence microscopy images show that upon excitation of Py^+ , green fluorescence could be seen at the edges of the crystal and red light was emitted from the centre. This proved that both dyes were located where intended and more importantly that energy was transferred via FRET from donor Py^+ units to acceptor Ox^+ units.⁴⁰

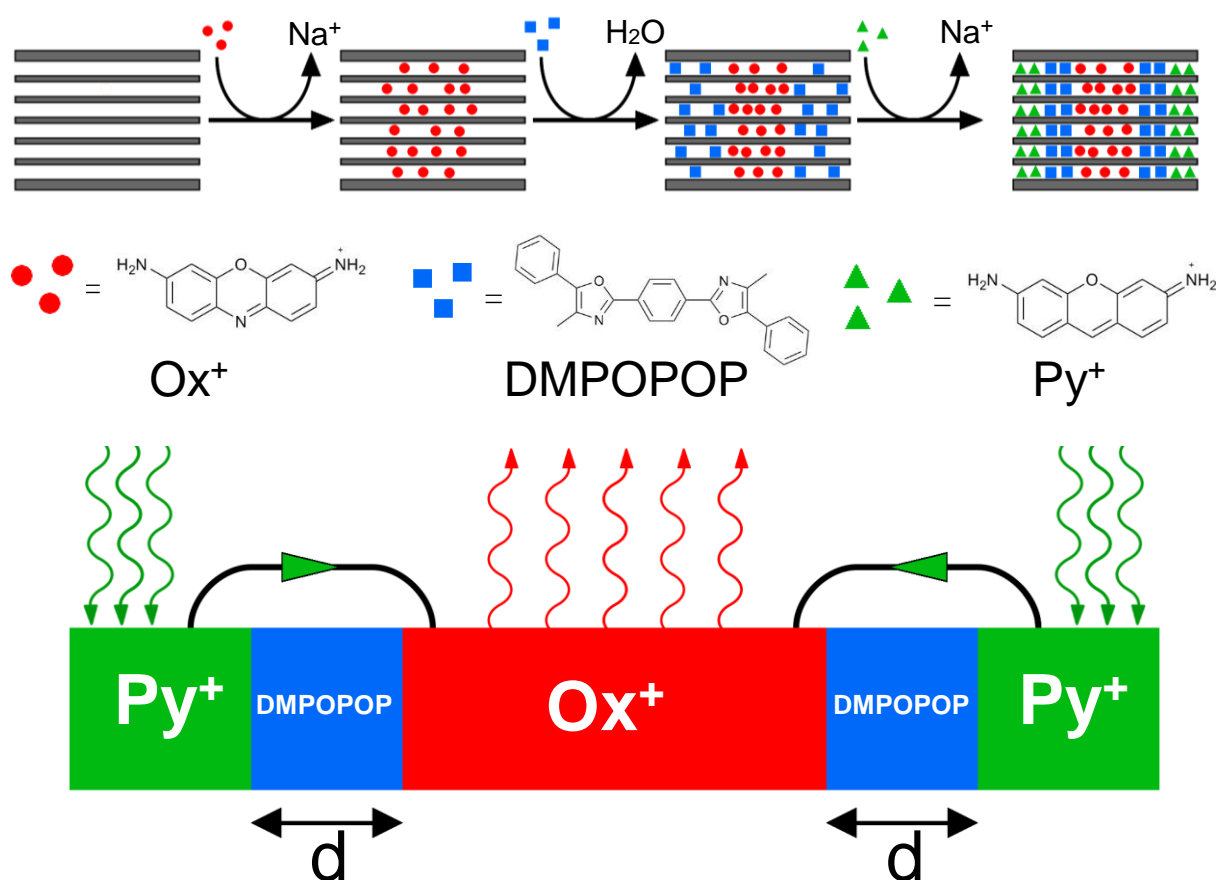


Figure 9: A schematic showing of the synthesis and FRET processes of an example of a light-harvesting zeolite crystal made by Calzaferri et al.^{40,41}

This was expanded further when the blue absorber 1,4-bis(5-phenyl-4-methyloxazol-2-yl) benzene (DMPOPOP) was used as a spacer molecule between Ox^+ and Py^+ as shown in Figure 9. As DMPOPOP is neutral, ion exchange cannot be used to load the zeolite. Instead, the crystal was placed under vacuum to remove any latent water left over from the zeolite synthesis allowing the DMPOPOP to be loaded as a gas. The thickness of this layer could be changed by varying the amount of DMPOPOP used during the gas phase insertion. With this

in mind, this system can be used to elegantly study the dependence of FRET efficiency and intermolecular distance. It was found that as the DMPOPOP layer thickness was decreased, energy transfer efficiency significantly increased, in accordance with Förster theory outlined earlier. Also, as this system is trichromophoric in nature, when illuminated with white light, high energy light is absorbed by the DMPOPOP and Py^+ units and funnelled to the Ox^+ portion resulting in a large amount of red fluorescence.⁴¹

1.4 Mesoporous Silica

Zeolites, while versatile materials, do not come without flaws. Due to their molecular templates, their pores, while highly monodisperse, are very small at around 4-7 Å in diameter. This means that only small molecules and ions are truly able to be inserted into the pores. Also, due to the methods by which guests are introduced into the framework, their relative positions within the channels are diffusion controlled. This means one cannot guarantee a uniform distribution of guests and ensure that desired processes take place efficiently or at all.⁴²

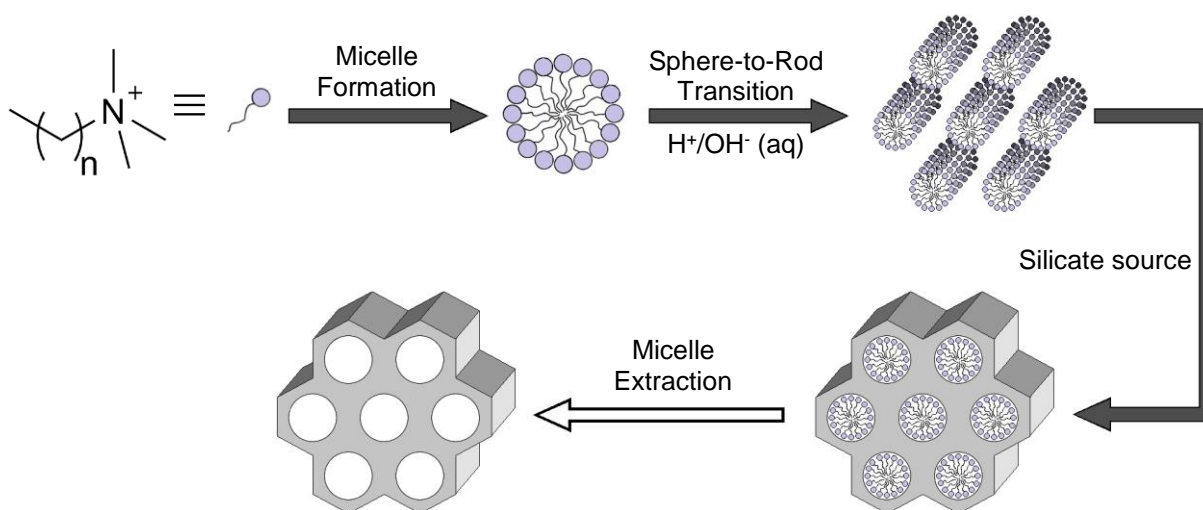


Figure 10: A scheme showing the steps involved in synthesis of mesoporous silica around micelles.

To be able to accommodate a larger range of guests, one can move to the mesoporous regime with materials such as silica gel which is often used in product purification. This can possess pores of up to 150 Å but is mostly amorphous exhibiting a very large pore size distribution as it is synthesised without a template.⁴³ To introduce order into porous silica systems, Kresge *et al.* at Mobil Oil formed silica using micelles as a template using the synthesis outlined in Figure 10. Here, an amphiphilic molecule known as a surfactant is dissolved in water. In such a polar medium, the surfactant molecules aggregate and self-

assemble into spherical micelles in which the hydrophobic portion of the surfactants point towards the centre of the micelle and the hydrophilic portion is pointing outwards. Under certain conditions a morphology change is induced in the micelles known as a “sphere-to-rod transition” causing the micelles to change from spherical to cylindrical. In this form, the micelles arrange into a hexagonal array to which a silicate precursor is added. Upon heating and/or pH change, the silicate precursors hydrolyse and condense around the micelles, forming a robust SiO₂ network with pores in ordered hexagonal arrangement. It is common practice to remove the micelles whether via Soxhlet extraction or calcination to make way for guests to be inserted into the pores. The subject of micelles will be explored in further detail in Chapter 5 of this thesis.⁴⁴

The first case of mesoporous silica (m-SiO₂) developed by Kresge *et al.* was dubbed hexagonal Mobil Composition of Matter (MCM-41). A trimethylammonium surfactant is used to make the micelles as shown in Figure 10, with the standard synthesis taking place at pH = 12 and elevated temperatures. They used tetraethylorthosilicate (TEOS) as a silicate precursor and hexadecyltrimethylammonium bromide (CTAB) where n = 15, resulting in pore diameters of around 40 Å.⁴⁴ One feature that makes these materials particularly desirable is that the pore sizes can be varied by changing the length of surfactant. For instance using tetradecyltrimethylammonium bromide (TTAB) would result in smaller pores. Another option is to use additives that cause the micelles to swell such as 1,3,5-trimethylbenzene (TMB) which resulted in pore diameters of around 100 Å albeit with much larger polydispersity than unaltered samples.⁴⁵

By using a block co-polymeric surfactant like polyethylene-polypropylene (PEO-PPO), the resulting silica would have significantly larger pores than if one used CTAB. This was demonstrated by Zhao *et al.* in 1998 when they introduced hexagonal Santa Barbara Amorphous silica (SBA-15). The somewhat misleading name refers to a series of ordered m-SiO₂ materials made using a variety of PEO-PPO-based surfactants, strong acid catalysts (pH < 1) and tetraalkylorthosilicate precursors under hydrothermal conditions (in H₂O, T > 398 K, p > 1 bar). The culmination of these experiments were samples that possessed pore diameters upwards of 300 Å that did not exhibit the same loss in order as seen in the TMB-altered MCM-41 mentioned above.⁴⁶

Another useful advantage of these materials is that they can be functionalised easily and in a variety of ways. Here, a short introduction will be given into silica material synthesis and the most common strategies for functionalisation. The formation of silica as well as other metal/metalloid (B, Al, Ti etc.) ceramics (oxides, nitrides, carbides etc.) is governed by the sol-gel process.⁴⁷ First observed in the 1840s by J. J. Ebelmen,⁴⁸ it has been widely researched and applied in material design. As it happens, sol-gel reactions involving tetraalkylorthosilicate precursors have been some of the most detailed in the literature. The process essentially denotes two reactions shown in Figure 11.



Figure 11: The reactions that take place in the sol-gel process: hydrolysis (1.10) and condensation (1.11a & b).⁴⁷

Initially, there is the hydrolysis step (1.10) which involves a substitution of an -OR group with an -OH group. As with many hydrolysis reactions, a H^+ or OH^- ion is needed as a catalyst and, in the case of silicon centres, this reaction is facile particularly below $\text{pH} = 7$. Next is the condensation step which forms an oxo bridge between two silicon centres. This can result from reaction between two silanol groups (1.11a) or a silanol and an unhydrolysed precursor (1.11b). It is easy to see how from here the reaction can repeat and polymerise resulting in an extended SiO_2 network.⁴⁷

While alkoxy silicate precursors certainly dominate in the literature, other starting materials do exist. Most notably for this thesis is sodium silicate solution, also known as water glass, which is used in a variety of way in industry for instance as an adhesive or in the treatment of cement. It is made from 10% NaOH and 27% SiO_2 in water and exists as solubilised oligomeric species with the formula $\text{Na}_x\text{SiO}_x(\text{OH})_{4-x}$. In the context of the sol-gel process, reaction (1.10) has been taken to its extreme resulting in a fully pre-hydrolysed silicate source⁴⁷. This particular precursor condenses very quickly meaning reactions can be undertaken even under very mild conditions ($\text{pH} = 6.5$, $T = 298\text{K}$).⁴⁹

When it comes to functionalising silica, there are three procedures to be aware of; each with their own advantages and disadvantages. The first of these is a post-synthetic method known as ‘grafting’. As shown in Figure 12(a), silanol groups are formed on the surface of the silica walls due to incomplete polycondensation of the silicate precursor during the sol-gel synthesis. These can be further reacted with a desired group (R, Figure 12) that has been functionalised with a trialkoxysilane to yield organic groups that point into the pores. The disadvantage with this method is that it is difficult to achieve truly ubiquitous incorporation of the functional group, particularly if the group is large and/or the pores are small. This is due to the silanol groups on the pore entrances being kinetically more likely to react with any incoming organosilane. Once the first few groups are bound near the pore entrance, it is even less likely for any precursors to diffuse into the pores leading to a cyclical process of outer surface functionalisation. This eventually results in the pore being completely blocked up so no further grafting can take place.⁴³

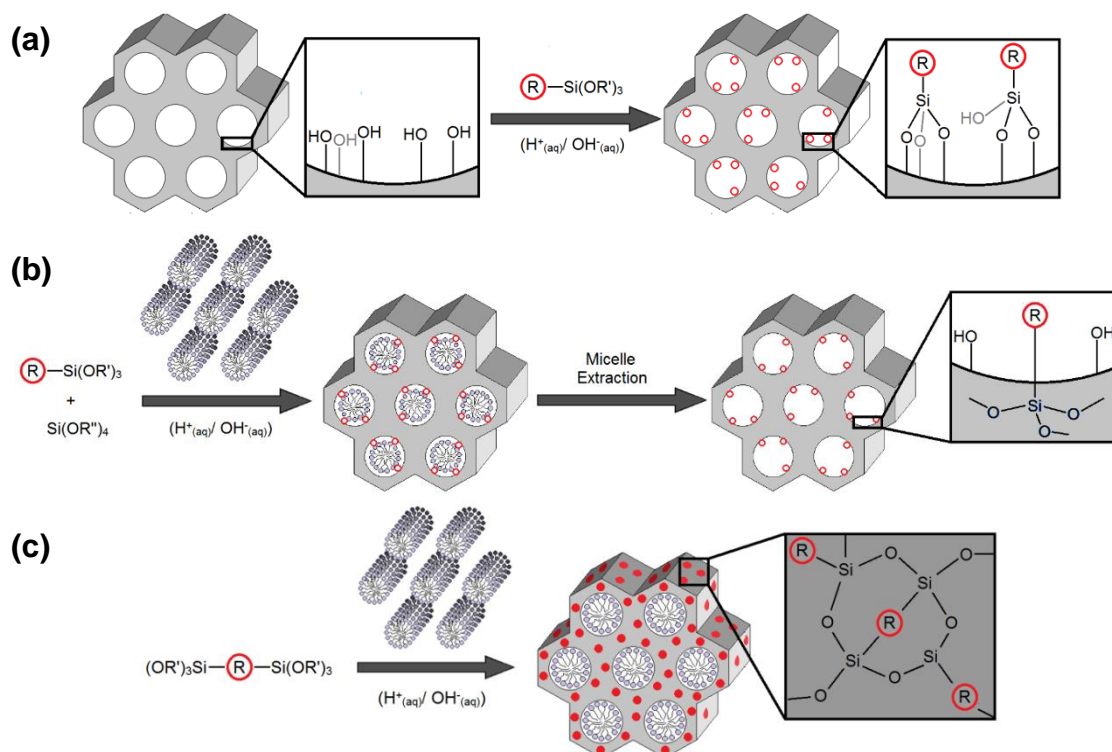


Figure 12: Schemes showing the different ways to functionalise mesoporous silica; (a) grafting, (b) co-condensation and (c) periodic mesoporous organosilica (PMO).⁴³

The second is known as co-condensation and is shown in Figure 12(b). This method involves inserting the organosilane into the reaction at the same time as the standard silicate precursor prior to the formation of the $m\text{-SiO}_2$. It undergoes the polycondensation with normal silicate precursors resulting in R-groups sticking into the pores and out from the

surface. This is due to the fact that, as the precursors hydrolyse during the sol-gel process, they form a highly polar medium which will push out the relatively apolar organic R-group. This method results in a much more homogeneous distribution of functional groups throughout the silica network and a much lower loss of porosity when compared to the grafting procedure.⁵⁰ The disadvantage with this method however is that higher loadings of the organosilane in the reaction cause the final silica product to be less ordered; sometimes resulting in it being totally amorphous. This is because the R-group can perturb the micellar template causing it to change morphology, particularly if this group is relatively polar.⁵¹ Practically, this means that the loading of the organosilane is kept low (<15%) with higher values reported although to limited degrees of success.⁴⁴

The third and arguably best method for homogeneous distribution of organic groups in the silica framework is by synthesising what is called ‘periodic mesoporous organosilica’ (PMO). First developed in 1999 by various research teams, they feature organic groups ubiquitously bonded as part of the structure of the silica walls. These teams demonstrated this primarily with simple organic groups including ethylene ($[-\text{CH}_2-\text{CH}_2-]$), vinylene ($[-\text{CH}_2=\text{CH}_2-]$) and phenylene ($[-\text{C}_6\text{H}_4-]$)⁵¹ with several more complex PMOs synthesised in the years following⁵². This is achieved by co-condensing a bridged organosilane precursor as shown in Figure 12(c). The walls of such materials have been shown to be remarkably crystal-like with organic groups lining up translationally within the walls. Note that the walls are not truly crystalline because the organic groups can exhibit a small amount of modulation with respect to one another and the silica portion exhibits no translational symmetry whatsoever.⁵³ The major disadvantage with this method is that most of the silicate precursors are not commercially available and so must be synthesised especially.

These methods have now been expanded to a variety of functional groups with many applications.⁵⁴ They are often used in tandem as demonstrated in various papers by Inagaki *et al.* who use a combination of functionalisation techniques to generate an array of light-harvesting systems. First, as shown in Figure 13(a), a tetraphenylpyrene (TPPy) group was used as a four-way bridge in a PMO. This was used in conjunction with the host-guest properties of these materials whereby Rhodamine-6G (R-6G) was loaded into the pores. Partial energy transfer can then take place from the blue-emitting TPPy to the yellow-emitting R-6G. Depending on the amount of R-6G used, the apparent colour emitted by this material can be tuned with certain ratios emitting white light. This type of material could find use in lighting devices such as light-emitting diodes (LEDs).⁵⁵

Figure 13(b) shows a different system that uses a PMO that has been post-synthetically grafted. A relatively simple biphenylene bridge was used in the PMO while bipyridine groups were grafted on. A rhenium carbonyl centre was then complexed by the bipyridine ligand. The biphenylene groups act as sensitisers, absorbing light and transferring the energy to the rhenium complex. From there, the complex uses that energy to facilitate the reduction of CO₂ into CO.⁵⁶

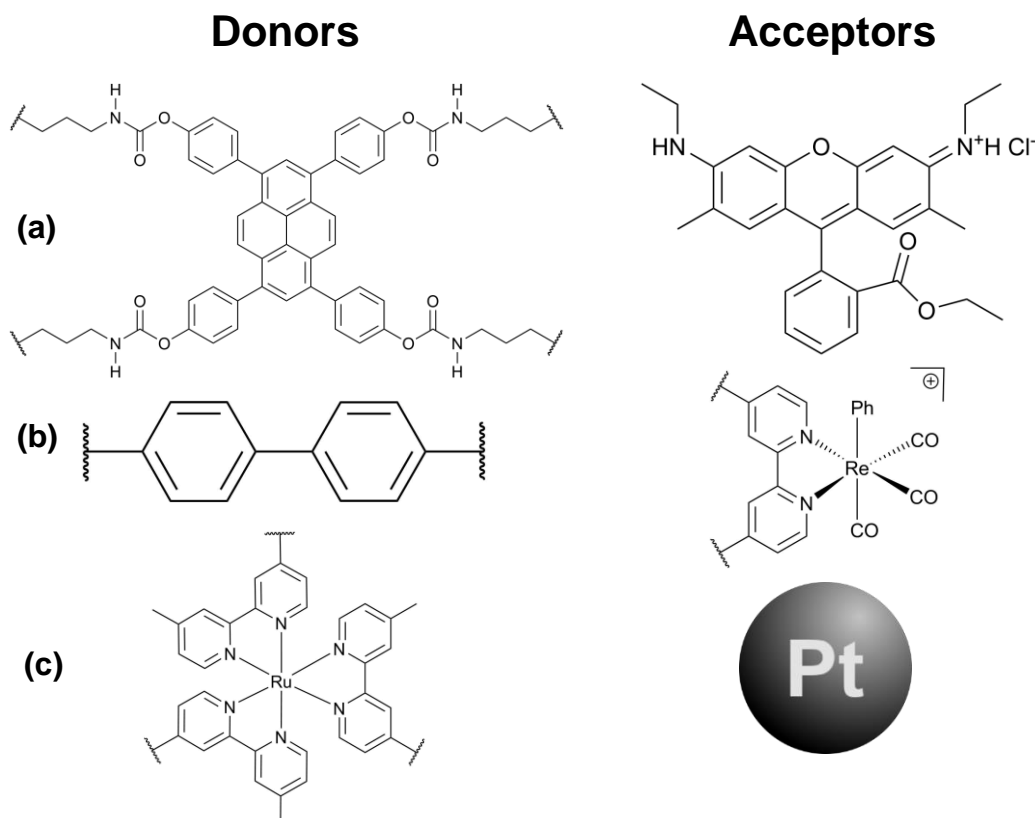


Figure 13: Examples of how mesoporous silica functionalisation methods have been used in tandem for light-harvesting applications.⁵⁵⁻⁵⁷

Lastly is arguably the most complex PMO bridge to date which comes in the form of a ruthenium tris-bipyridine (Ru(bpy)₃) complex as shown in Figure 13(c). The first example demonstrated using a metal complex as a bridge which was coupled with platinum nanoparticle (Pt-NP) guests in the pores. Like in example (b), the Ru(bpy)₃ sensitises the Pt-NP so that it can form H₂ from water.⁵⁷ These last two examples particularly show the potential for m-SiO₂ to be used as an artificial photosynthetic system using not just host-guest chemistry but functionality within the network itself.

1.5 Dipyrrromethene Complexes

While there will be a variety of molecules and complexes used throughout the course of this thesis, one class of materials will certainly stand out as being the most frequently utilised: dipyrrromethene (a.k.a. dipyrroin) complexes. The synthesis of a general dipyrrromethene is shown in Figure 14, where an acid-catalysed condensation between an aldehyde and pyrrole is used to form the initial dipyrrromethane intermediate. Excess pyrrole and tailored synthesis conditions should be used to prevent formation of the porphyrin. From here, the dipyrrromethane is oxidised using agents such as 2,3-dichloro-5,6-dicyanobenzoquinone (DDQ) or p-chloranil to form the dipyrrromethene ligand. This can then be deprotonated using a variety of bases forming an anionic bidentate ligand capable of complexing a wide range of elements, making it incredibly versatile.⁵⁸

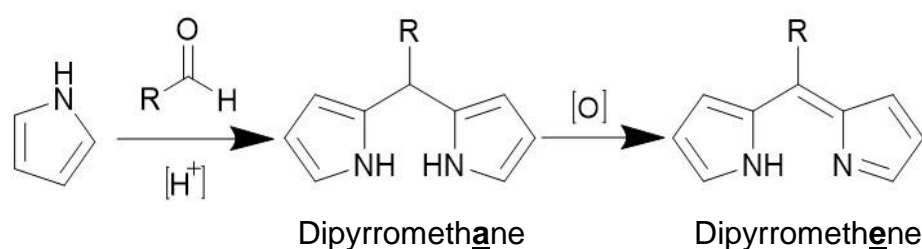


Figure 14: The most common synthesis of the dipyrrromethene core.⁵⁷

When discussing dipyrrromethene complexes, it is impossible to avoid the boron-complexed derivative known as BODIPY (**B**oron **DIPY**rromethene). First synthesised in 1968 by Treibs and Kreuzer,⁵⁹ BODIPY dyes have been used in a wide variety of applications like laser dyes and fluorescent biosensors. This class of molecules has proven to be popular due to their excellent photophysical properties, namely sharp absorption and emission profiles, high fluorescence quantum yields and small Stokes shift. They are usually made by deprotonation of a dipyrrromethene with a mild base (e.g. triethylamine) followed swiftly by a condensation with boron trifluoride diethyl etherate ($BF_3 \cdot OEt_2$) resulting in fumes of hydrogen fluoride (HF) as a by-product.

Another attractive feature of BODIPYs is that their chemical structure can be modified trivially through a combination of careful choice of starting materials and post-synthetic alterations. Indeed, despite arguably inferior photophysical properties, substituted derivatives are usually preferred in practice as opposed to the unsubstituted core; the reasons for which are twofold. Firstly, the bare BODIPY is highly unstable under normal atmospheric conditions and decomposes almost immediately upon exposure to oxygen. In fact, it took over

40 years since their initial synthesis for this BODIPY to be isolated.⁶⁰ Secondly, through substitution, functional groups can be added that allow their useful properties to be tapped. For instance, anchoring groups like carboxylic or phosphonic acids can be added to attach them to inorganic surfaces in DSSCs. Another example would be a BODIPY functionalised with an amino acid chain to allow easy access to biological substrates for biosensors.⁶¹

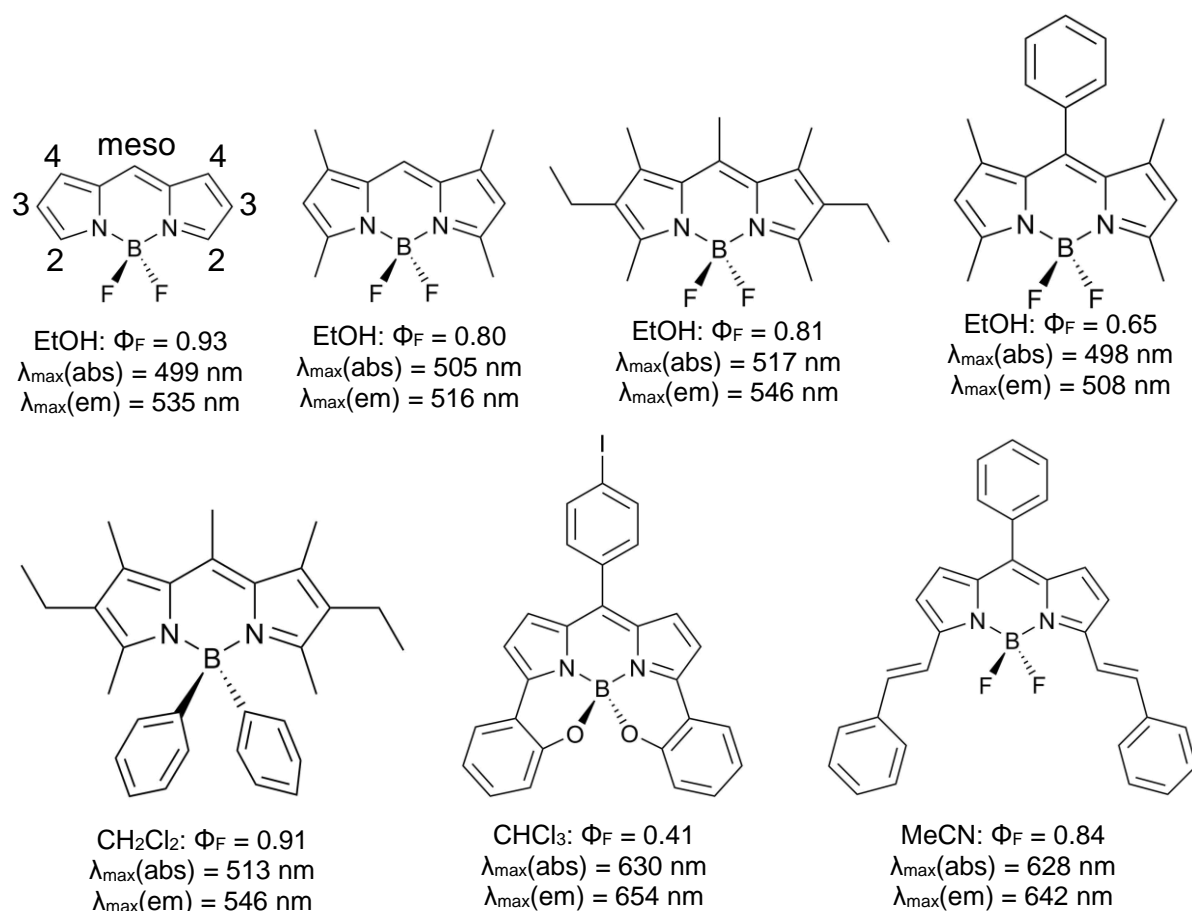


Figure 15: The structure of the BODIPY core and the effect of substitution on the photophysical properties.^{60,61}

Figure 15 shows a small library of BODIPY dyes developed over the last half century. First shown is the unsubstituted core with different functionalisation positions labelled. Most frequently, the α - (2) and β - (3 and 4) positions can be changed by choosing particular pyrrole starting materials (Figure 14). The electron donating properties of these groups cause a change in the absorption and emission profiles but generally also decrease the fluorescence quantum yield.⁶¹

Functionalisation on the meso-position is achieved by careful choice of the aldehyde (Figure 14). Often a phenyl group is added in the meso-position which can freely rotate

meaning it is electronically decoupled from the fluorophore. This is a particularly efficient thermal deactivation pathway resulting in low fluorescence quantum yields if the pyrrole units are unsubstituted. This can be combatted by having methyl groups on the 4-position limiting rotation of the phenyl group thus pushing up quantum yield as shown in Figure 15.⁶¹ It is also possible to substitute the fluoride groups on the boron centre with carbon or oxygen donors. This can be done with simple methyl or methoxy groups to more complex aromatic groups or polyethylene glycol chains to name but a few.⁶¹

More recent work into these dye molecules has concentrated on extending the conjugated system of the fluorophore pushing absorption and emission bands into the red and near-IR region. When looking at this from the context of the technologies mentioned above, it is easy to see why this is a useful avenue of research. Firstly, standard green dyes can be used in conjunction with these red-shifted analogues in special tandem-DSSCs in order to capture more of the solar spectrum. In biosensing technologies, red light is absorbed by tissue much less than green and blue light allowing for deeper tissue penetration. This also gives it the added advantage of being much less damaging to tissues making it much more useful in diagnostic and therapeutic procedures.⁶¹

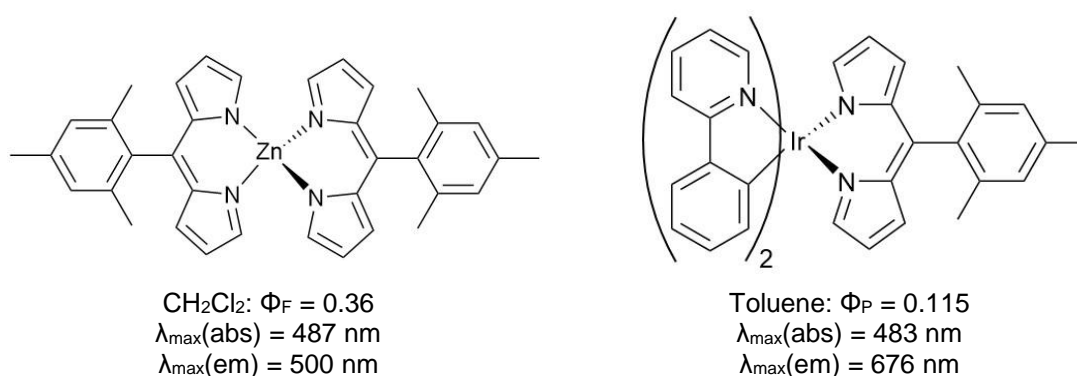


Figure 16: Dipyrromethene complexes made with zinc and iridium highlighting the versatility of this ligand due to its variable bite angle.⁶²

The applications of the dipyrromethene ligand extends beyond complexation of boron and it can chelate around a wide variety of elements both metallic and non-metallic. Figure 16 shows two examples featuring a zinc dipyrromethene complex (Zn-dipy) and an iridium complex (Ir-dipy). Both of these have vastly different properties to standard BODIPYs. Firstly the Zn-dipy features two perpendicular dipyrromethene ligands on either side of the metal centre. Due to zinc having a full d-shell, it is essentially optically inert and so does not induce much change in the photophysics of the ligands directly. Instead, by holding the

ligands in such close proximity to one another, it can induce a particular transition called ligand-to-ligand charge transfer (LLCT), where an electron is formally transferred from one ligand to another. Many other first row transition metals (e.g. Fe, Cu and Ni) also adopt this tetrahedral geometry with the added feature that they have unfilled d-shells allowing other processes to take place such as metal-to-ligand charge transfer (MLCT).⁶²

In the case of the Ir-dipy, the triplet manifold (see Figure 6) is now accessible due to increased spin-orbit coupling induced by the presence of the heavy iridium atom. This effect results in room temperature phosphorescence (note Φ_P in Figure 16), meaning that the emission is shifted towards the red region of the visible spectrum and the lifetime is increased to around 12 μs .⁶³ These examples, along with BODIPY, show only a portion of the vast range of elements that can be complexed by dipyrromethene further highlighting the versatility of these ligands.⁶²

1.6 Aims

As mentioned earlier, the micellar template is typically removed from the mesoporous scaffold post-synthesis. While this does allow the diffusion of guests into the pores, it also presents two distinct disadvantages. Firstly, from an economic point of view, the templating process would be an expensive endeavour at large scale as it requires a large amount of material which is ultimately discarded. Added to this is the substantial cost spent on their removal which either involves a large amount of solvent (Soxhlet extraction) or high heat (calcination). This is analogous to the issue presented by protecting group chemistry in industrial-scale organic synthesis. Secondly, the introduction of the molecules into the pores via diffusion results in a non-uniform distribution of guests within the system with them preferentially staying near the pore entrances.

With this and the concept of energy transfer between specially designed hosts and guests in mind, this thesis will present the preliminary work into a novel method of synthesising m-SiO₂-based light-harvesting antennae. Figure 17 shows the overall schematic of this work which can be broken down into two parts. Firstly, surfactants will be synthesised with BODIPY moieties in such a way as to be structurally similar to ones used in m-SiO₂ synthesis i.e. CTAB and Pluronic (see Chapter 3). Results will be shown for both MCM-41 and COK-12 systems to see how differing syntheses and size regimes change the photophysical properties of the dyes within the scaffold. Due to the dynamic nature of micelles, this should mean that dye units are distributed evenly throughout the template and subsequently the silica

(see Chapter 4). To belabour a tired metaphor further, this is like forcing guest tourists into positions where their rooms would be, then building the hotel around them.

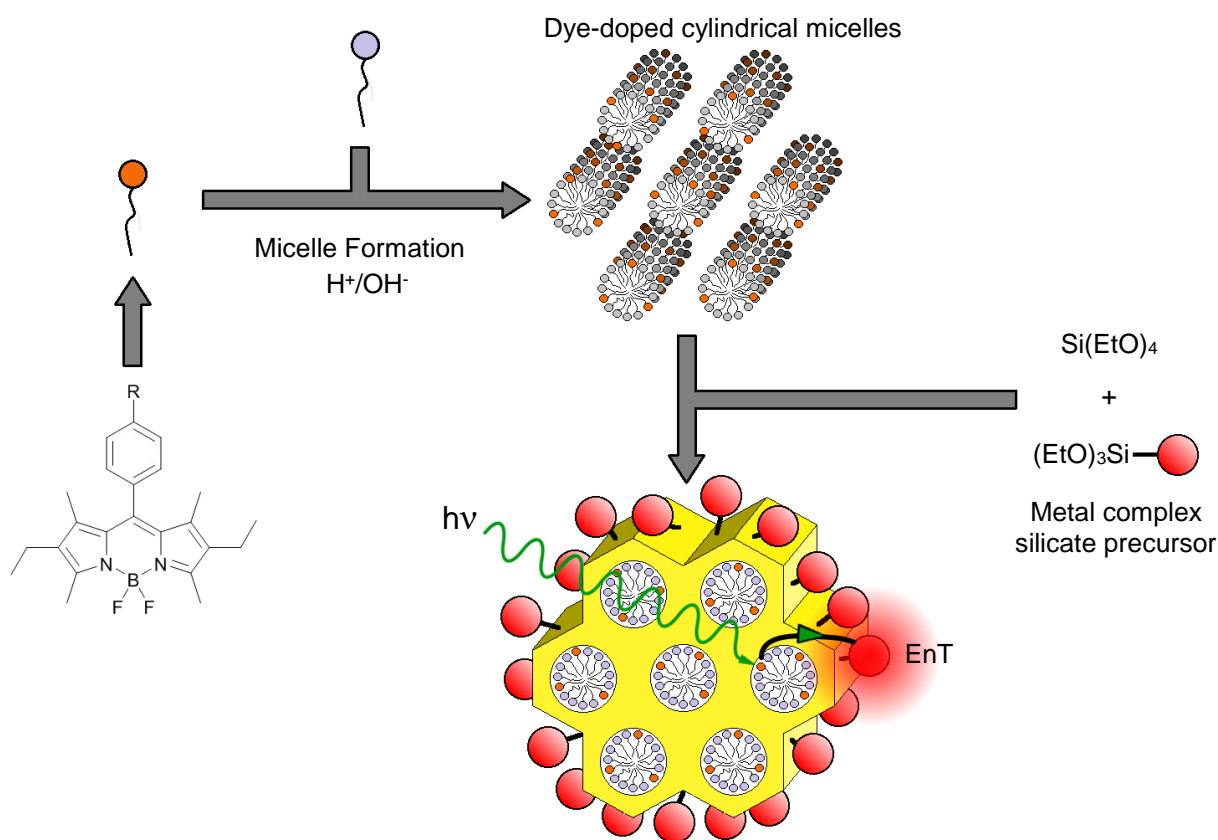


Figure 17: The outline for the synthesis of a light-harvesting antenna using mesoporous organometallosilica built around a dye-doped micelle template.

The second step of this synthesis will involve the incorporation of metal complexes into the silica walls by both grafting and co-condensation. Due to the pores being filled with dye-doped micelles, grafting will most likely take place on the surface as shown in Figure 17. These two steps will be combined with the aim of allowing sensitisation of the metal complexes via FRET from the dyes in the micellar template, or viceversa. A variety of metal complexes will be showcased in order to see how having different photophysical and geometrical properties affect energy transfer processes.

In conclusion, the aim is to synthesise an economically-viable light-harvesting mesoporous organosilica. In doing so, the versatility of molecular systems will be combined with the organisation of nanomaterials exhibited by natural photosynthetic systems which simultaneously arrange their vital units very specifically as well as protect them from harmful degradation processes.

References

1. J. Chow, R. J. Kopp and P. R. Portney, *Science*, 2003, **302**, 1528-1531.
2. R. Heinberg and D. Fridley, *Nature*, 2010, **468**, 367-369.
3. O. C. Eneh, *J. Appl. Sci.*, 2011, **11**, 2084-2091.
4. BBC News, <http://www.bbc.co.uk/news/business-29643612>, (accessed May 2015).
5. BP Statistical Review of World Energy June 2016, <http://www.bp.com/en/global/corporate/about-bp/energy-economics/statistical-review-of-world-energy/review-by-energy-type.html> (accessed May 2017).
6. P. Hardy, in *Fracking*, ed. R. E. Hester and R. M. Harrison, Royal Society of Chemistry, Cambridge, UK, 1st edn, 2015, ch. 1, pp. 1-3.
7. C. Hohenemser, R. Kasperson and R. Kates, *Science*, 1977, **196**, 25-34.
8. I. Medhaug, M. B. Stolpe, E. M. Fischer and R. Knutti, *Nature*, 2017, **545**, 41-47.
9. A. García-Olivares, J. Ballabrera-Poy, E. García-Ladona and A. Turiel, *Energy Policy*, 2012, **41**, 561-574.
10. A. Goetzberger, J. Knobloch and B. Voss, in *Crystalline Silicon Solar Cells*, ed. B. G. Teubner, Wiley, Chichester, UK, 1st edn, 1998, ch. 3, pp 9-33.
11. M. Graetzel, R. A. Janssen, D. B. Mitzi and E. H. Sargent, *Nature*, 2012, **488**, 304-312.
12. W. Shockley and H. J. Queisser, *J. Appl. Phys.*, 1961, **32**, 510-519.
13. V. Balzani, A. Credi and M. Venturi, *ChemSusChem*, 2008, **1**, 26-58.
14. J. Deisenhofer, O. Epp, K. Miki, R. Huber and H. Michel, *Nature*, 1985, **318**, 618-624.
15. W. Kuhlbrandt, N. W. Da and F. Yoshinori, *Nature*, 1994, **367**, 614-621.
16. E. Formaggio, G. Cinque, and R. Bassi, *J. Mol. Biol.*, 2001, **314**, 1157-1166.
17. T. Inoue, A. Fujishima, S. Konishi and K. Honda, *Nature*, 1979, **277**, 637-638.
18. A. Fujishima and K. Honda, *Nature*, 1972, **238**, 37-38.
19. S. Xie, Q. Zhang, G. Liu and Y. Wang, *Chem. Commun.*, 2016, **52**, 35-59.
20. M. E. Dry, *Catal. Today*, 2002, **71**, 227-241.
21. J. L. Banal, B. Zhang, D. J. Jones, K. P. Ghiggino and W. W. Wong, *Acc. Chem. Res.*, 2017, **50**, 49-57.
22. J. Michl, M. Montalti, A. Credi, L. Prodi and M. T. Gandolfi, in *Handbook of Photochemistry*, CRC Press, Boca Raton, USA, 3rd edn., 2006, ch. 1, pp 19-21.
23. A. D. McNaught and A. Wilkinson, in *Compendium of Chemical Technology (the "Gold Book")*, Blackwell Scientific Publications, Oxford, UK, 2nd edn., 1997, online corrected version: <https://goldbook.iupac.org/html/R/R05230.html>, (accessed July 2017).
24. M. Kasha, *Discuss. Faraday Soc.*, 1950, **9**, 14-19.
25. G. Y. Zheng, D. P. Rillema, J. Depriest and C. Woods, *Inorg. Chem.*, 1998, **37**, 3588-3592.
26. Y. Sasaki, S. Amemori, H. Kouno, N. Yanai and N. Kimizuka, *J. Mater. Chem. C*, 2017, **5**, 5063-5067.
27. M. Baroncini, G. Bergamini and P. Ceroni, *Chem. Commun.*, 2017, **53**, 2081-2093.
28. I. McConnell, G. Li and G. W. Brudvig, *Chem. Biol.*, 2010, **17**, 434-447.
29. T. Förster, *Discuss. Faraday Soc.*, 1959, **27**, 7-17.
30. J. Michl, M. Montalti, A. Credi, L. Prodi and M. T. Gandolfi, in *Handbook of Photochemistry*, CRC Press, Boca Raton, USA, 3rd edn, 2006, ch. 1, pp 41-42.
31. D. L. Dexter, *J. Chem. Phys.*, 1953, **21**, 836-850.

32. V. Balzani, S. Campagna, G. Denti, A. Juris, S. Serroni and M. Venturi, *Acc Chem Res*, 1998, **31**, 26-34.
33. E. Marchi, M. Baroncini, G. Bergamini, J. Van Heyst, F. Vogtle and P. Ceroni, *J. Am. Chem. Soc.*, 2012, **134**, 15277-15280.
34. R. A. Marcus, *Annu. Rev. Phys. Chem.*, 1964, **15**, 155-196.
35. IUPAC, old.iupac.org/reports/2001/colloid_2001/manual_of_s_and_t/node16.html, (accessed November 2017)
36. C. V. Kumar, A. Chaudhari and G. L. Rosenthal, *J. Am. Chem. Soc.*, 1994, **116**, 403-404.
37. M. O'Keeffe, M. A. Peskov, S. J. Ramsden and O. M. Yaghi, *Acc. Chem. Res.*, 2008, **41**, 1782-1789.
38. T. Maesen, in *Introduction to Zeolite Science and Practice*, ed. J. Čejka, H. van Bekkum, A. Corma and F. Schüth, Elsevier, Amsterdam, The Netherlands, 3rd edn, 2007, ch. 1.
39. R. Zhao, Z. Zhao, S. Li and W. Zhang, *J. Phys. Chem. Lett.*, 2017, **8**, 2323-2327.
40. N. Gfeller, S. Megelski and G. Calzaferri, *J. Phys. Chem. B*, 1998, **102**, 2433-2436.
41. G. Calzaferri, S. Huber, H. Maas and C. Minkowski, *Angew. Chem. Int. Ed. Engl.*, 2003, **42**, 3732-3758.
42. K. Möller and T. Bein, *Chem. Soc. Rev.*, 2013, **42**, 3689-3702..
43. F. Hoffmann and M. Fröba, *Chem. Soc. Rev.*, 2011, **40**, 608-620.
44. C. Kresge, M. Leonowicz, W. Roth, J. Vartuli and J. Beck, *Nature*, 1992, **359**, 710-712.
45. J. S. Beck, J. C. Vartuli, W. J. Roth, M. E. Leonowicz, C. T. Kresge, K. D. Schmitt, C. T.-W. Chu, D. H. Olson, E. W. Sheppard, S. B. McCullen, J. B. Higgins and J. L. Schlenker, *J. Am. Chem. Soc.*, 1992, **114**, 10834-10843.
46. (a) D. Zhao, J. Feng, Q. Huo, N. Melosh, G. H. Fredrickson, B. F. Chmelka and G. D. Stucky, *Science*, 1998, **279**, 548-552. (b) D. Zhao, Q. Huo, J. Feng, B. F. Chmelka and G. D. Stucky, *J. Am. Chem. Soc.*, 1998, **120**, 6024-6034.
47. C. J. Brinker and G. W. Scherer in *Sol-Gel Science: The Physics and Chemistry of Sol-Gel Processing*, Academic Press, London, UK, 1st edn, 1990, ch. 3 pp. 99-113.
48. J. J. Ebelmen, *Ann.*, 1846, **57**, 331.
49. (a) J. Jammaer, A. Aerts, J. D'Haen, J. W. Seo and J. A. Martens, *J. Mater. Chem.*, 2009, **19**, 8290-8293 (b) J. Jammaer, T. S. van Erp, A. Aerts, C. E. Kirschhock and J. A. Martens, *J. Am. Chem. Soc.*, 2011, **133**, 13737-13745.
50. F. Cagnol, D. Grosso and C. Sanchez, *Chem. Commun.*, 2004, 1742-1743
51. L. Nicole, C. Boissière, D. Grosso, P. Hesemann, J. Moreau and C. Sanchez, *Chem. Commun.*, 2312-2313.
52. (a) B. J. Melde, B. T. Holland, C. F. Blanford and A. Stein, *Chem. Mater.*, 1999, **11**, 3302-3308. (b) T. Asefa, M. J. MacLachlan, N. Coombs and G. A. Ozin, *Nature*, 1999, **402**, 867-871. (c) S. Inagaki, S. Guan, Y. Fukushima, T. Ohsuna and O. Terasaki, 1999, **121**, 9611-9614.
53. M. Cornelius, F. Hoffman and M. Fröba, *Chem. Mater.*, 2005, **17**, 6674-6678.
54. P. van der Voort, D. Esquivel, E. de Canck, F. Goethals, I. van Dreissche and F. J. Romero-Salguero, *Chem. Soc. Rev.*, 2013, **42**, 3913-3955.
55. N. Mizoshita, Y. Goto, Y. Maegawa, T. Tani and S. Inagaki, *Chem. Mater.*, 2010, **22**, 2548-2554.
56. H. Takeda, M. Ohashi, T. Tani, O. Ishitani and S. Inagaki, *Inorg. Chem.*, 2010, **49**, 4554-4559.
57. H. Takeda, M. Ohashi, Y. Goto, T. Ohsuna, T. Tani and S. Inagaki, *Adv. Funct. Mater.*, 2016, **26**, 5068-5077.

58. L. Yu, K. Muthukumar, I. V. Sazanovich, C. Kirmaier, E. Hindin, J. R. Diers, P. D. Boyle, D. F. Bocian, D. Holten, J. S. Lindsey, *Inorg. Chem.*, 2003, **42**, 6629-6647.
59. A. Treibs, F. H. Kreuzer, *Justus Liebigs Ann. Chem.*, 1968, **718**, 208-23.
60. I. J. Arroyo, R. Hu, G. Merino, B. Z. Tang, E. Pena-Cabrera, *J. Org. Chem.*, 2009, **74**, 5719-5722.
61. A. Loudet, K. Burgess, *Chem. Rev.*, 2007, **107**, 4891-4932
62. S. A. Baudron, *Dalton T.*, 2013, **42**, 7498-7509.
63. (a) K. Hanson, A. Tamayo, V. V. Diev, M. T. Whited, P. I. Djurovich, M. E. Thompson, *Inorg. Chem.*, 2010, **49**, 6077-6084. (b) D. Ramlot, M. Rebarz, L. Volker, M. Ovaere, D. Beljonne, W. Dehaen, L. Van Meervelt, C. Moucheron, A. Kirsch-De Mesmaeker, *Eur. J. Inorg. Chem.*, 2013, 2031-2040.

Chapter 2. Analytical Techniques: Theory and Application

2.1 Introduction

This thesis features a variety of techniques used for the characterisation of dye-loaded mesoporous silica (m-SiO₂) which in this chapter will be described in detail. Steady-state and time-resolved absorption and photoluminescence spectroscopy were employed to study dyes both in solution and as part of m-SiO₂ host-guest systems. Powder X-ray diffraction (XRD) and small angle X-ray scattering, used for structural analysis, will be outlined as well as a brief introduction into electron microscopy.

2.2 Optical Spectroscopy

Photochemistry is fundamentally governed by the transition of electrons from an occupied to an unoccupied molecular orbital, induced by illumination by ultra-violet (UV), visible and near infra-red (NIR) light. The energy difference (ΔE , in J) between these two molecular orbitals corresponds to the frequency (ν , in cycles per second, Hz) of the photon absorbed via Equation 2.1:

$$\Delta E = h\nu \quad (2.1)$$

where h is Planck's constant, 6.626×10^{-34} J.s. By convention, it is more common however to relate ΔE to the physical length of a cycle of a photon, i.e. the wavelength (λ , in m) using Equation 2.2:

$$\nu = \frac{c}{\lambda} \quad (2.2)$$

where c is the speed of light in a vacuum. 3.00×10^8 m.s⁻¹, to make Equation 2.3:

$$\Delta E = \frac{hc}{\lambda} \quad (2.3)$$

Using this equation, it is possible to ascertain that a photon with wavelength of 200 nm for instance will have an energy of 9.94×10^{-19} J (approx. 600 kJ.mol⁻¹) which would be absorbed by an electron in a bonding σ -orbital causing it to transition up to an unoccupied anti-bonding σ^* -orbital¹. This most commonly induces a photochemical reaction² and so is not typically used as a diagnostic tool. Moving towards lower energy into the UV-Visible-NIR region (250 – 800 nm), transitions from p, n and π to π^* are commonplace with a higher degree of conjugation resulting in a lower energy transition as a general rule. As the energies of these

transitions are affected greatly by the molecular vibration, the bands in these spectra tend to be broad when compared to other spectroscopic techniques such as IR or NMR with exceptions found in the photophysics of highly rigid molecules or lanthanide complexes.^{1,3}

2.2.1 Steady-State UV/Visible Absorption Spectroscopy

The amount of light absorbed by a species at wavelength, λ , is quantified using the dimensionless variable known as absorbance, $A(\lambda)$. Underpinning this is the Beer-Lambert law (Equation 2.4):

$$A = \log\left(\frac{I_0}{I}\right) = \varepsilon \cdot c \cdot l \quad (2.4)$$

where I and I_0 are the intensities of light before and after passing through the sample, ε is the molar absorption coefficient in $M^{-1}\cdot\text{cm}^{-1}$, c is the concentration of the sample in M and l is the path length in cm . Typically, these experiments are performed using a double beam spectrometer where monochromatic light is sent down two paths using a beam splitter. One beam probes the absorptive properties of a reference cell, commonly containing the solvent in which the analyte is dissolved with the second beam being sent through the analyte solution.¹ By comparing the two, this eliminates signals from the solvent as well as from stabilising chemicals such as butylated hydroxy toluene (BHT) which absorbs around 280 nm.⁴ For this thesis, the baseline-corrected UV/Vis absorption spectra were performed using a Shimadzu UV-1800 spectrophotometer with 1 cm quartz cuvettes.¹

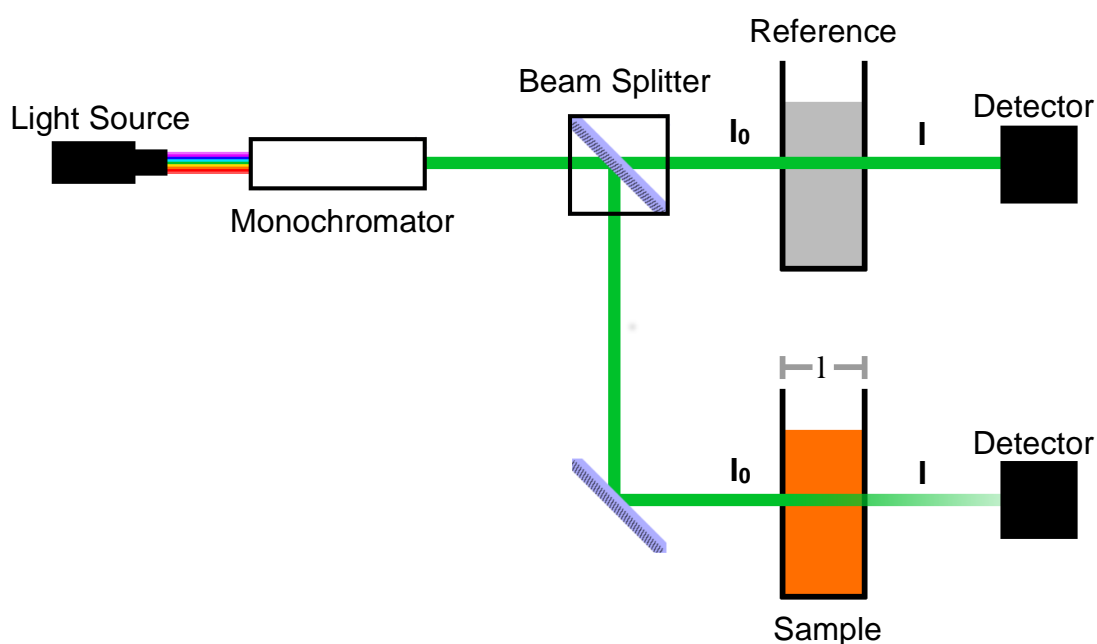


Figure 1: A schematic for UV/Vis absorption spectroscopy.

2.2.2 Steady-State Photoluminescence Spectroscopy

Upon absorption of light, a dye can undergo a variety of processes with the most common in this field being luminescence. Figure 2 shows a schematic of a typical photoluminescence spectrometer where light from a Xenon arc lamp is sent through a monochromator to select a wavelength at which the molecule absorbs. This light is then sent through a slit with a variable width to allow control over the bandwidth of the excitation light influencing the amount of fluorescence as well as the resolution of the spectra. Upon excitation, the sample will emit at a variety of wavelengths in all directions with light being collected at 90° to the excitation beam to minimise scattering phenomena. Again, the emitted light is then sent through a slit and a monochromator to control the wavelength and intensity of light hitting the detector.⁵

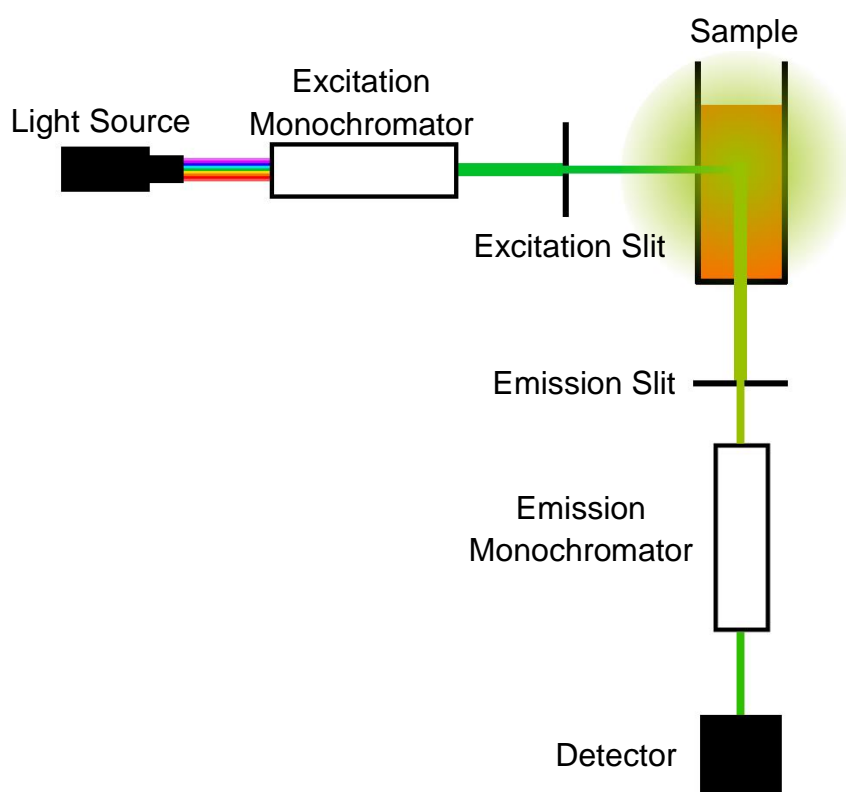


Figure 2: A schematic of a photoluminescence spectrometer.

Using this technique, it is possible to acquire two types of steady-state photoluminescence spectra. Commonly performed first is the emission spectrum whereby the excitation wavelength is kept fixed at a wavelength where the molecule absorbs, typically taken from the largest peak in the absorption spectrum. The emission monochromator is then varied to probe the intensity of light over a range of wavelengths. Secondly, an excitation spectrum is performed whereby the emission wavelength is now fixed and the excitation wavelength is

varied. Using this setup, the emission intensity is probed as the sample is exposed to a range of wavelengths.⁵ In this thesis, these spectra were performed using an Edinburgh FLS980 photoluminescence spectrometer with a 450 W Xenon arc lamp, Czerny Turner monochromators (1.8 nm.mm⁻¹ dispersion; 1800 grooves.mm⁻¹), time-correlated single photon counting (TCSPC) module and a Hamamatsu photomultiplier tube (in fan assisted TE cooled housing, -20°C operating temperature).

A number of artefacts can present on excitation and emission spectra with the most common being caused by scattering of the excitation beam, even when a collection angle on 90° is used. This presents as a large band at the excitation wavelength caused by elastic scattering as well as a smaller band at slightly higher wavelength resulting from inelastic (Raman) scattering which is solvent dependent. For instance the Raman band exhibited by H₂O is seen at an energy 3600-3800 cm⁻¹ lower than the excitation band. Other artefacts include harmonic peaks whereby low intensity peaks at integer multiples of the excitation wavelength are observed throughout the spectrum. For example, if an excitation wavelength of 250 nm is used, the second and third harmonics may be observed at 500 and 750 nm respectively.⁵

The efficiency of photoluminescence by a molecule is quantified through quantum yield (Φ) which is given by the ratio of the number of photons emitted to photons absorbed. Practically, it is acquired using Equation 2.5

$$\Phi_S = \Phi_R \cdot \frac{A_R(\lambda_R)}{A_S(\lambda_S)} \cdot \frac{I_R(\lambda_R)}{I_S(\lambda_S)} \cdot \frac{n_S^2}{n_R^2} \cdot \frac{D_S}{D_R} \quad (2.5)$$

where A and I are the absorbance and excitation light intensity at the excitation wavelength, λ , respectively, n is the refractive index of the solvent and D is the integrated intensity of luminescence. The subscripts R and S denote variables relating to the reference dye and the analyte respectively. For quantum yield experiments in this thesis, dilute solutions of dyes were used so that at excitation wavelength their A values were kept lower than 0.1. Spectra were taken using identical excitation wavelengths in order to simplify Equation 2.5 by cancelling the $I_R(\lambda_R)/I_S(\lambda_S)$ term. All quantum yield experiments performed using fluorescein in aqueous NaOH (0.1 M) as a reference which has a quantum yield of 0.87.^{5,6}

2.2.3 Emission Lifetime Studies

While steady-state spectroscopy can be useful for probing the photophysics of a material, it can give only limited information into the underlying luminescent processes, leading to the

need for time-resolved techniques. The most common of these for organic molecules is the measurement of excited state lifetimes through time-correlated single photo counting (TC-SPC). As shown in Figure 3, a laser pulse is sent towards the sample concurrently with a signal that starts a timer. The sample then emits with light again sent at 90° from the excitation beam. This is then sent through a filter and/or a monochromator towards a detector. Detection of the emitted light sends a stop signal to the timer thus measuring the time taken for the excited state of the dye to relax radiatively. For this technique to be effective, the sample must only emit one photon at a time which is typically achieved by using a low intensity excitation source.⁵

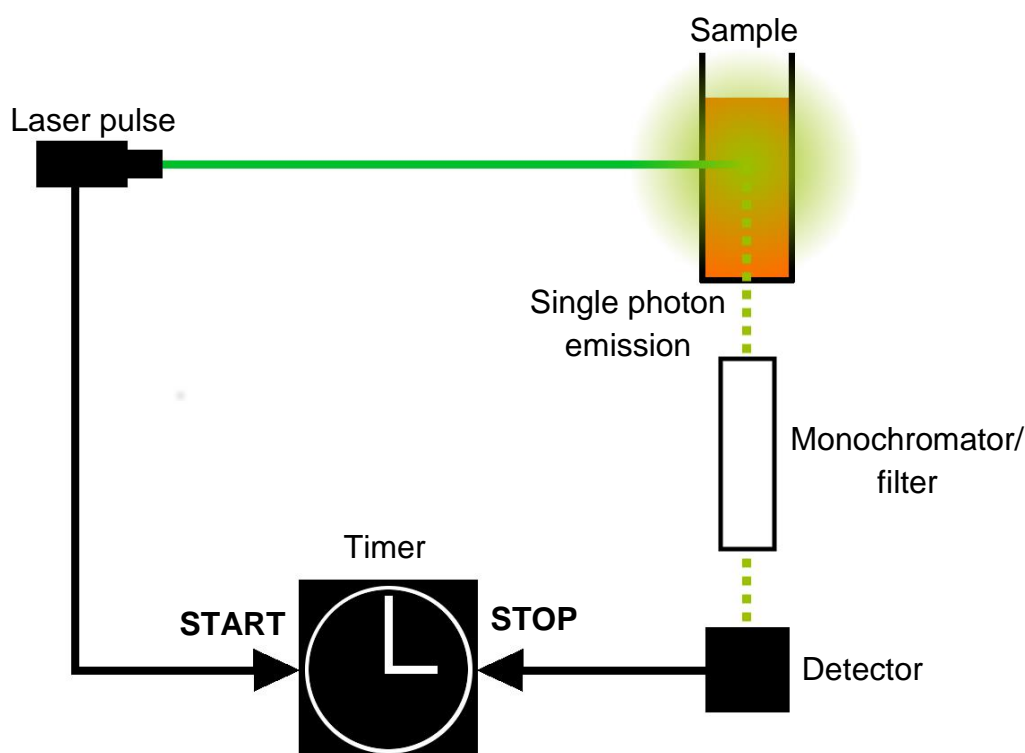


Figure 3: A schematic of a TCSPC setup

As the excited state decays statistically, each emitted photon will take a different amount of time to reach the detector, similar to the process of atomic radioactive decay. As such, this technique is repeated to construct a histogram plot showing the statistical distribution of times after excitation that an emitted photon takes before being detected. Typically, for a low concentration monochromophoric system, the excited state is most likely to decay within a few nanoseconds of the laser pulse with probability decreasing exponentially as time goes on. The resulting decay profile is fitted with F980 software to acquire an exponential function⁷. Through this, the excited state lifetime of the analyte is determined with accuracy of the plot decided by minimising the χ^2 value. These measurements were performed using the

Edinburgh FLS980 mentioned above with EPL-375 (370.8 nm; 61.1 ps pulse width) and EPL-475 (471.8 nm; 61.1 ps pulse width) diode lasers.

2.2.4 Transient Absorption Spectroscopy

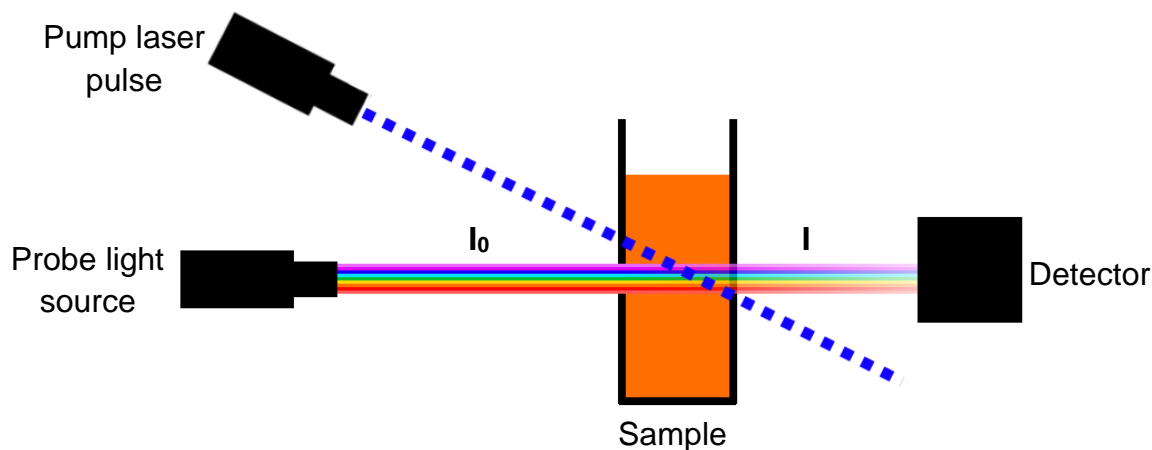


Figure 4: A simple schematic showing how a transient absorption spectrum is obtained from a sample.

If more information is required about the temporal behaviour of certain systems, transient absorption spectroscopy (TAS) may be used. Unlike the other spectroscopic techniques mentioned in this chapter, TAS is a pump-probe technique whereby an initial laser pulse is used to generate the excited state of the analyte. This is followed in quick succession by a standard absorption spectrum using a different light source (typically a Xe arc lamp) being performed whereby the intensity of incoming light is compared with that of the outgoing light. This is repeated with different time intervals between pump and probe pulses resulting in a series of absorption spectra showing how the absorbance of the excited state of the analyte evolves over time. In this thesis, TAS was performed using a Spectra-Physics MAI-TAI setup with a Ti:Sapphire pump laser source and a white light probe pulse was obtained using a continuum generated on a sapphire plate with a spectral range of 450-800 nm. Using this setup, the temporal resolution is approximately 200 fs.⁷

TAS results are typically shown as difference spectra with a diagram for how these are constructed shown in Figure 5. The steady-state absorption spectrum is subtracted from all others in the series hence the ΔA label on the y-axis. Through this, analysis of the spectra becomes the characterisation of positive and negative bands caused by absorption by the excited state and depopulation of the ground state (as a result of excitation) respectively. Negative bands can also arise due to stimulated emission of an excited state which can be

avoided by subtracting an emission spectrum of the sample performed at the same time delay from the transient absorption spectrum.⁷

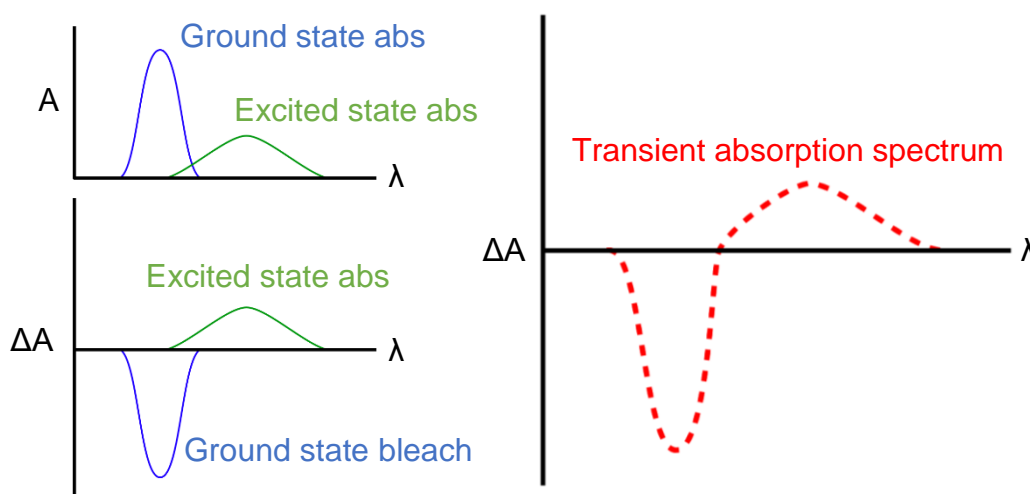


Figure 5: (top left) The absorbance bands of the ground and excited states of a molecule, (bottom left) The difference absorbance spectra of these states and (right) the resulting transient absorption spectrum of a dye molecule.

2.3 Structural Analysis

The standard m-SiO₂ used in this thesis presents pores that exhibit uniform diameter and regular arrangement. By comparing modified silica with standard samples, it is possible to infer direct structural information about the silica as well as indirect analysis of the micellar template. This is because disruption of the mesophase by an additive will detrimentally affect the order of the pores. The analyses presented here include indirect techniques that involve the use of X-rays with electron microscopy being a more direct approach.

2.3.1 Powder X-Ray Diffraction

X-ray diffraction (XRD) is a powerful tool offering a chance for unequivocal proof of a molecules structure. Upon elastic scattering of a plane wave of X-rays (all photons are travelling parallel to one another), spherical waves move outwards from the sample. These waves interfere both con- and destructively resulting in high intensities of X-rays being observed in specific directions. These are known as reflections. Through computer software, it is possible to deconvolute these reflections to determine the absolute positions of atoms in space. This analysis can only be performed if the sample is a perfect single crystal however, as the translational symmetry in the arrangement of the atoms allows the formation of so-

called Bragg reflection planes. The spacing, d , between these planes can be determined using Equation 2.6:

$$n\lambda = 2d \cdot \sin\theta \quad (2.6)$$

where n is an integer value relating to the number of Bragg planes passed through before reflection takes place (e.g. the inset in Figure 6 shows a reflection where $n = 1$); λ is the wavelength of the X-rays and θ is the angle of incidence/scattering from the Bragg plane.⁸

Not all samples, m-SiO₂ included, can be crystallised however, meaning another technique must be used. Powder XRD works under the same principle as regular XRD but now the sample constitutes a large number of very small crystals in an isotropic arrangement. This results in a diffraction pattern presenting not as bright spots but peaks at specific scattering angles. Figure 6 shows a typical powder XRD setup where X-rays are generated and sent towards the surface of a flattened sample at a variable angle with 2θ values typically ranging from 10-100° (although smaller values are possible using specialised holders). The scattered X-rays are then collected by a detector which is again at a variable angle with the resultant X-ray intensity being plotted against 2θ .⁸ Powder X-ray diffractograms in this thesis were obtained with an ARL XTRA48 diffractometer using Cu K α radiation ($\lambda = 1.54062 \text{ \AA}$).

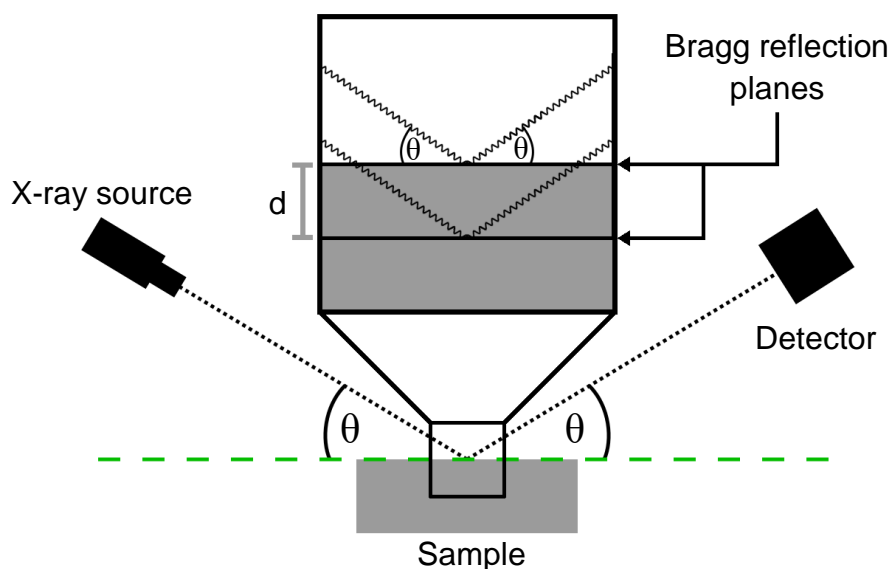


Figure 6: A schematic showing how a powder X-ray diffractogram is acquired. (inset) The reflection of X-rays by Bragg planes within a material.

2.3.2 Small Angle X-Ray Scattering

The pores in m-SiO₂ are generally much larger than the crystal dimensions of the typical inorganic powders analysed by powder XRD; MCM-41 for instance typically exhibits d-spacings of around 4-5 nm. Because of the inverse relationship between scattering angle and

d-spacing, if one were to use systems with larger pores, for instance COK-12, standard powder X-ray diffractometers becomes ineffective as it has a lower operational limit of around 1° . Small angle X-ray scattering (SAXS) is a technique that overcomes this by sending the X-ray beam perpendicularly to the sample (see Figure 7). A far-field scattering pattern is then observed by the detector which is then integrated resulting in a plot of X-ray intensity, $I(q)$, against reciprocal space, q (in nm^{-1}) which is defined by Equations 2.7:

$$q = \frac{4\pi \sin\theta}{\lambda} = \frac{4\pi}{d} \quad (2.7)$$

where θ is the scattering angle, λ is the wavelength and d is the spacing between Bragg reflection planes. The operational range can be varied by changing the distance between the sample holder and the detector, for example a distance of 650 mm will result in a q -range of $0.6\text{-}6.2 \text{ nm}^{-1}$.⁹

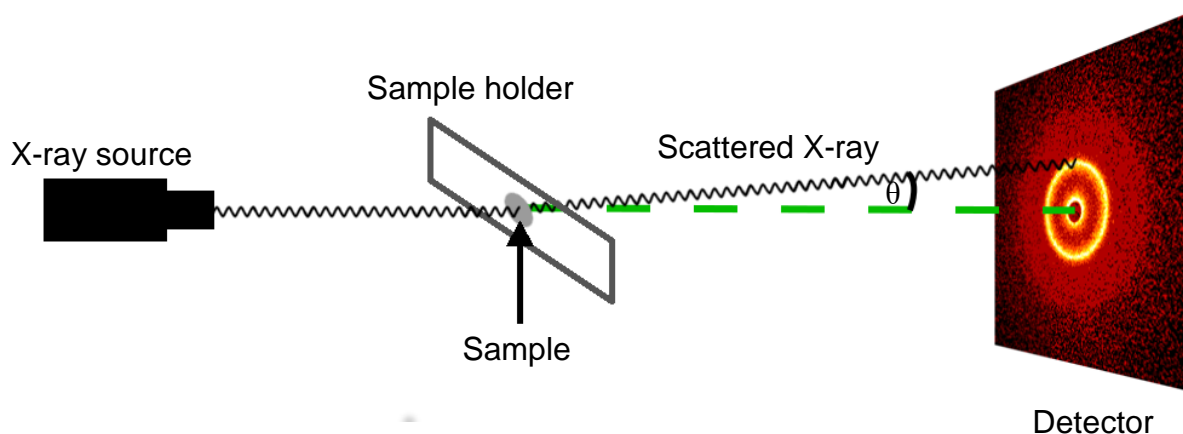


Figure 7: A schematic of the small angle X-ray scattering of a sample.

SAXS patterns acquired in this thesis were obtained with a Bruker Nanostar SAXS machine with cross-coupled Gobel mirrors and pin-hole collimation again using $\text{Cu K}\alpha$ radiation ($\lambda = 1.54062 \text{ \AA}$). Powder samples are introduced into the cuvette using an aluminium foil wrapping. While SAXS machines tend to be much larger and more expensive than standard table-top powder X-ray diffractometer, they offer a number of advantages such as a higher resolution and lower scattering angle detection limit. Also, as materials analysed in this way tend to have much larger d-spacings than the wavelength used, small variations in atomic position have a negligible effect on the final scattering pattern. As a result, it is possible to acquire information not only on powder samples but suspensions such as colloids and liquid crystals as well making this technique far more versatile.⁹

2.3.3 Transmission Electron Microscopy

For a more direct observation of the structure of silica, microscopy can be used. Standard confocal microscopy using light does not offer a high enough magnification for analysis of nanomaterials. However, electrons have a sufficiently low de Broglie wavelength to make this type of imaging possible. While specialised equipment must be used, an electron beam behaves similarly to light with electromagnetic lenses used instead of glass or quartz ones optically speaking. These lenses work by passing a current through a wire coil inducing a magnetic field which is exerted in the electrons causing them to change direction. By varying this magnetic field, the beam can be manipulated in exactly the same way as light.¹⁰

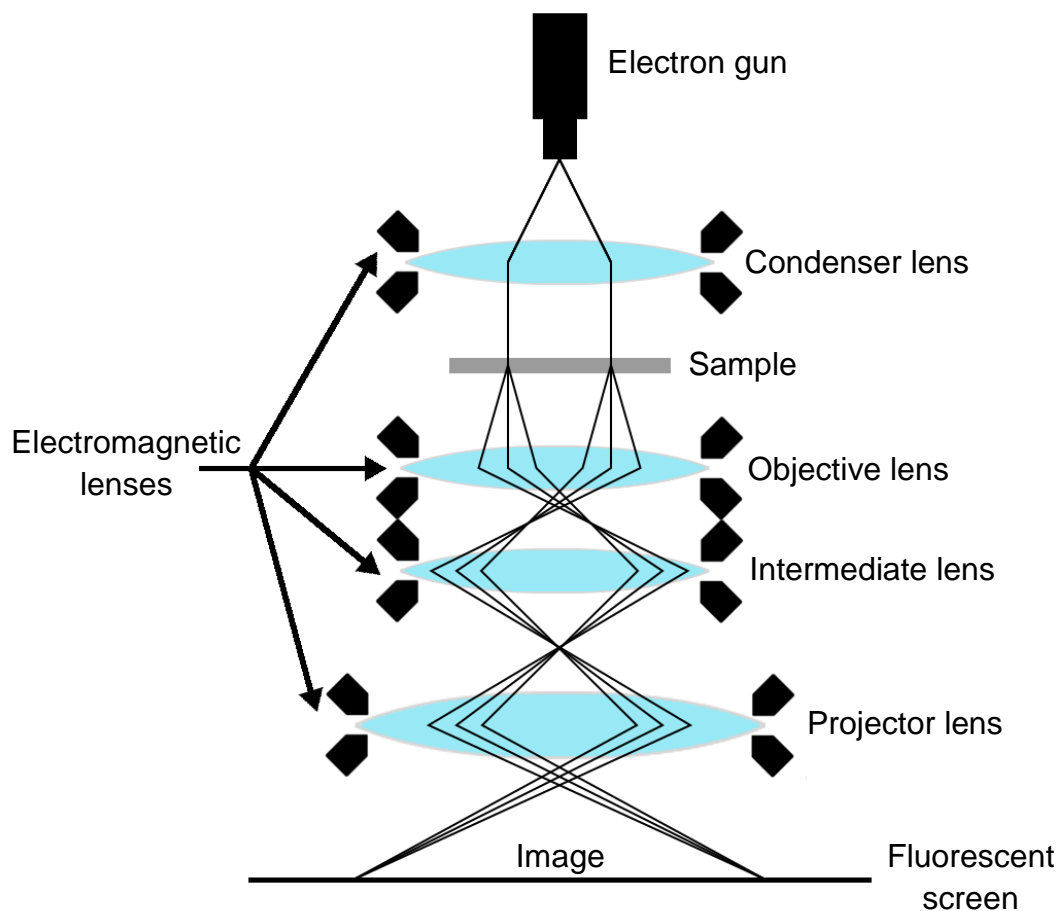


Figure 8: A schematic of transmission electron microscopy.

Figure 8 shows a typical transmission electron microscopy (TEM) setup whereby an electron beam is generated and initially collimated using a condenser lens. The widened beam is then sent through the sample which is typically either very flat or in a dilute suspension causing the electrons to be diffracted and scattered. These electrons are then collected with another series of lenses and projected onto a fluorescent screen showing an image of the

sample. In the structural analysis of m-SiO₂ both electron microscopy and X-ray diffraction techniques are highly useful but are not perfect as isolated experiments. Powder XRD and SAXS give useful data quantifying the porosity of any silica made making comparisons between samples much more distinct. However, samples that have shown featureless diffractograms (suggesting a lack of pore crystallinity) have been shown by TEM to exhibit highly ordered regions (amongst amorphous regions also). TEM however only offers qualitative analysis of samples and as such the two techniques would ideally be used in tandem.¹¹

References

1. D. H. Williams and I. Fleming, in *Spectroscopic Methods in Organic Chemistry*, McGraw-Hill, New York City, New York, USA, 5th edn., 1995, ch. 1, pp. 1-11.
2. N. Turro, V. Ramamurthy and J. C. Scaiano, in *Principles of Molecular Photochemistry: An Introduction*, University Science Books, Sausalito, California, USA, 1st edn., 2009, ch. 1, pp. 14-25.
3. L. Armelo, S. Quici, F. Barigelletti, G. Accorsi, G. Bottaro, M. Cavazzini and E. Tondello, *Coord. Chem. Rev.*, 2010, **254**, 487-505.
4. Sigma Aldrich, <https://www.sigmaaldrich.com/chemistry/solvents/learning-center/stabilizer-systems.html>, (accessed July 2018).
5. J. R. Lakowicz, in *Principles of Fluorescence Spectroscopy*, Springer, Berlin/Heidelberg, Germany, 3rd edition, 2006, ch. 2, pp. 27-54.
6. S. Fery-Forgues and D. Lavabre, *J. Chem. Educ.* 1999, **76**, 1260-1264.
7. M. Montali, A. Credi, L. Prodi and M. T. Gandolfi, in *Handbook of Photochemistry*, Taylor and Francis, Abingdon, UK, 2005, 3rd edn., ch. 10, pp. 561-577.
8. A. Cervellino, R. Frison, N. Masciocchi and A. Guagliari, in *X-ray and Neutron Techniques for Nanomaterials Characterisation*, ed. C. S. S. R. Kumar, Springer, Berlin/Heidelberg, Germany, 1st edn., 2016, ch. 10, pp. 548-555.
9. H. Leopold, in *Small Angle X-ray Scattering*, ed. O. Glatter and O. Kratky, Academic Press, Cambridge, Massachusetts, USA, 1st edn., 1982, ch. 3.III., pp. 105-110.
10. S. Wischnitzer, in *Introduction to Electron Microscopy*, Pergamon Press, New York City, New York, USA, 1st edn., 1962, ch. 3, pp. 4-25.
11. P. J. Goodhew and F. J. Humphreys, in *Electron Microscopy and Analysis*, Taylor and Francis, Abingdon, UK, 2nd edn., 1988, ch. 2, pp. 27-38.

Chapter 3. Mesoporous Silica Templated with Dye-Doped Micelles

3.1 Introduction

To begin the investigation into mesoporous silica in its use as a light-harvesting antenna, the insertion of dye units into the pores will be tested thus focussing on the first step of the synthesis outlined in Chapter 1, Figure 17. This approach has been developed with the aim of making use of the dynamic nature of the micellar template in order to achieve uniform distribution of dyes within the silica pores.^{1,2} While the effect of micelle formation dynamics^{3,4} on BODIPY dyes will be explored in Chapter 4, initial findings into the materials made from this synthesis are presented here. The BODIPYs used in this chapter have been functionalised at the meso-position in order to mimic the surfactants used in the m-SiO₂ syntheses. As shown in Figure 1, these dyes will be dissolved in tandem with the surfactants in order to allow their insertion into the micellar template before the silica is formed around it.⁵

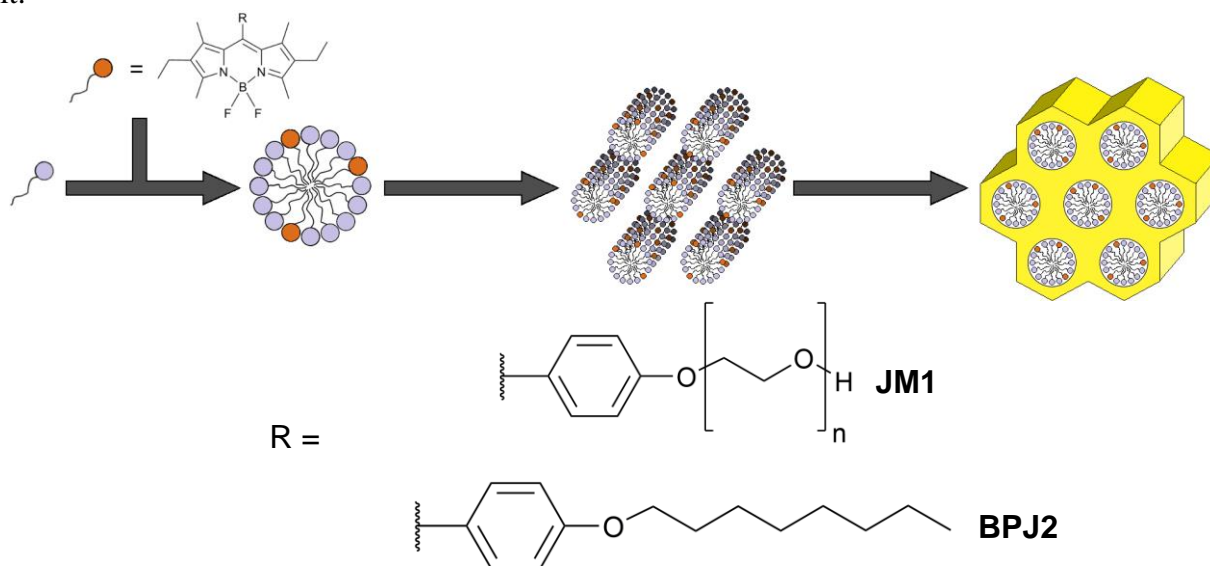


Figure 1: A scheme showing the synthesis of m-SiO₂ where the micelles are doped with BODIPY dyes functionalised with surfactant moieties at the meso-position.

The aim of this chapter is to present two examples of m-SiO₂ that have been synthesised using BODIPY-doped micellar templates. The first will involve a polyethylene glycol functionalised dye for use in COK-12.⁶ The other will be using a shorter alkyl chain to match surfactants used in MCM-41.⁷ Their structural properties will be analysed to see how the dyes have affected the morphology of the silica via disruption of the micellar template. Their

spectroscopic properties will also be analysed to see if the change in environment and proximity to other dyes has changed their photophysical properties. Both silica syntheses were performed at a variety of dye loadings, measured as a molar percentage of the respective surfactants used in the original syntheses.

3.2 COK-12

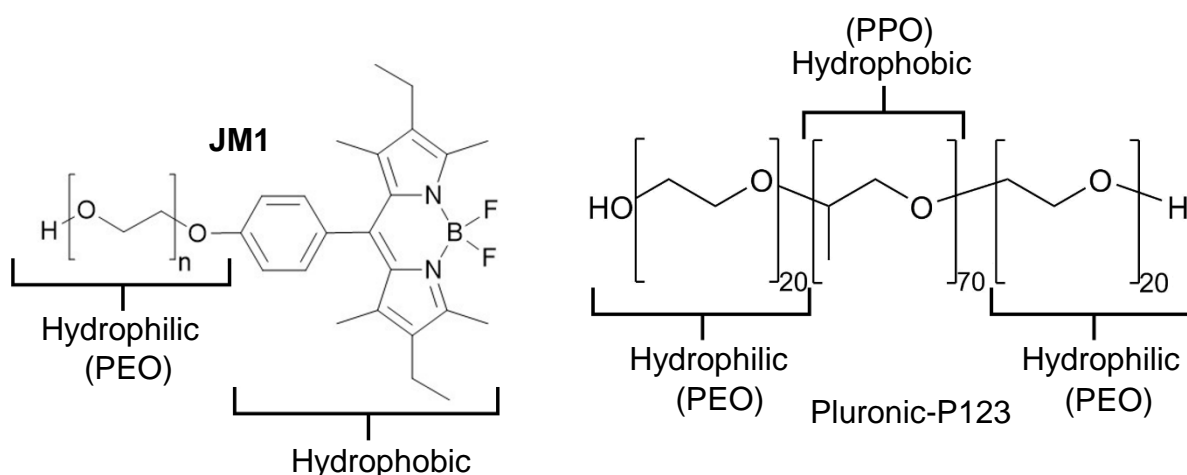


Figure 2: The structures of **JM1** (left) and Pluronic-P123 (right) with their hydrophilic and hydrophobic regions highlighted. On average, $n = 47$ PEG units.

Initially, SBA-15 was proposed as a possible mesoporous silica candidate as it is a well-established material finding a wide variety of uses in the literature.⁸ As mentioned in Chapter 1, it is formed using a polyethylene glycol-polypropylene glycol block co-polymer (PEO-PPO) as a surfactant for the micellar template and in this case, Pluronic-P123, which is shown in Figure 2. It is made up of two blocks of PEO (20 monomer units apiece) interrupted by a PPO block of 70 monomer units. When in a micelle, the PPO portions fold up forming the hydrophobic region, allowing the PEO blocks to point out towards the solvent (see Ch. 5 Fig 1).⁹ As solvation of the surfactant is the first step of m -SiO₂ synthesis, a dye will be added concurrently with the Pluronic-P123. For these reactions, the dye **JM1**, which was synthesised by Dr. Jonathan Martinelli at Delft University (The Netherlands), was chosen and is shown in Figure 2. It consists of a BODIPY dye functionalised with a PEO chain in the meso-position. The PEO chain is water soluble, mimicking the hydrophilic region of the Pluronic-P123, with the BODIPY portion sitting in the hydrophobic core.⁵

Upon solvation of **JM1** in the acidic solution needed for SBA-15 (2M HCl, pH = -0.3), the colour visibly changed from orange with green tints to a deep red within minutes. This is due to dissociation of the -BF₂ unit via protonation of the nitrogen atoms in the dipyrromethene as a result of the extremely low pH.^{10, 11} As such, the standard SBA-15 synthesis was deemed unsuitable and so a new synthesis that does not require the template to be exposed to high levels of acidity was needed.

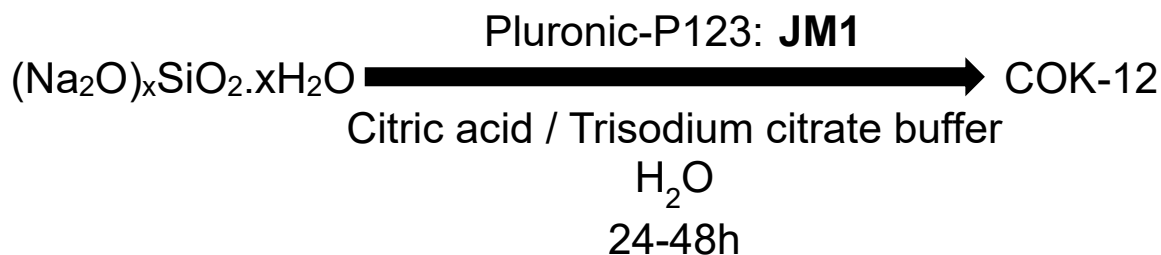


Figure 3: The synthesis of COK-12.

After a search in the literature, a suitable candidate was found in the form of COK-12; the synthesis of which is shown in Figure 3.⁶ This relatively recent form on m-SiO₂ still uses Pluronic-P123 as a surfactant so is suitable for use with **JM1**. Where it differs from the standard SBA-15 synthesis is in the source of H⁺ which in this case is a citric acid/trisodium citrate buffer, holding the solution at pH = 6.5. However, as the reaction mixture is now close to neutral, hydrolysis of a tetraalkylorthosilicate precursor would be slow and as such a new SiO₂ source is needed. The alternative adopted in the COK-12 synthesis is sodium silicate solution (also known as water glass) which exists as an oligomeric species with a general formula (Na₂O)_x.SiO₂.xH₂O (here, x = 2),¹² essentially acting as fully pre-hydrolysed silicate source.¹³ Using this precursor means that only a small amount of acid is needed to initiate polymerisation allowing formation of m-SiO₂ in relatively mild conditions. Also, as the Pluronic-P123 and **JM1** are dissolved in the citrate solution prior to the addition of the sodium silicate, the buffer provides added protection to the dye from the potentially harmful effects of the highly basic precursor solution. An added advantage of sodium silicate solution is that it is far cheaper than tetraalkylorthosilicate-based precursors¹⁴ and reacts under milder conditions making this particular form of m-SiO₂ more economically viable for industrial use.

Figure 4 shows the steady-state absorbance and fluorescence spectra of **JM1** taken in DCM which exhibit the typical band structure for a BODIPY chromophore. Each band has been assigned an electronic transition which are further clarified in the Jablonski diagram in

Figure 5. The maximum absorbance is observed at 522 nm which corresponds to a singlet $\pi \rightarrow \pi^*$ ($S_0, v_0 \rightarrow S_1, v_0$) transition in the extended conjugated system on the BODIPY core. As with other dyes of this class, **JM1** exhibits a high degree of light absorption with a molar absorption coefficient value above $100,000 \text{ M}^{-1} \cdot \text{cm}^{-1}$. This absorption band is also slightly vibronically coupled giving rise to a shoulder at around 490 nm. This corresponds to the transition from the lowest vibrational state of S_0 to the 1st excited vibrational state of S_1 ($S_0, v_0 \rightarrow S_1, v_1$).¹⁵

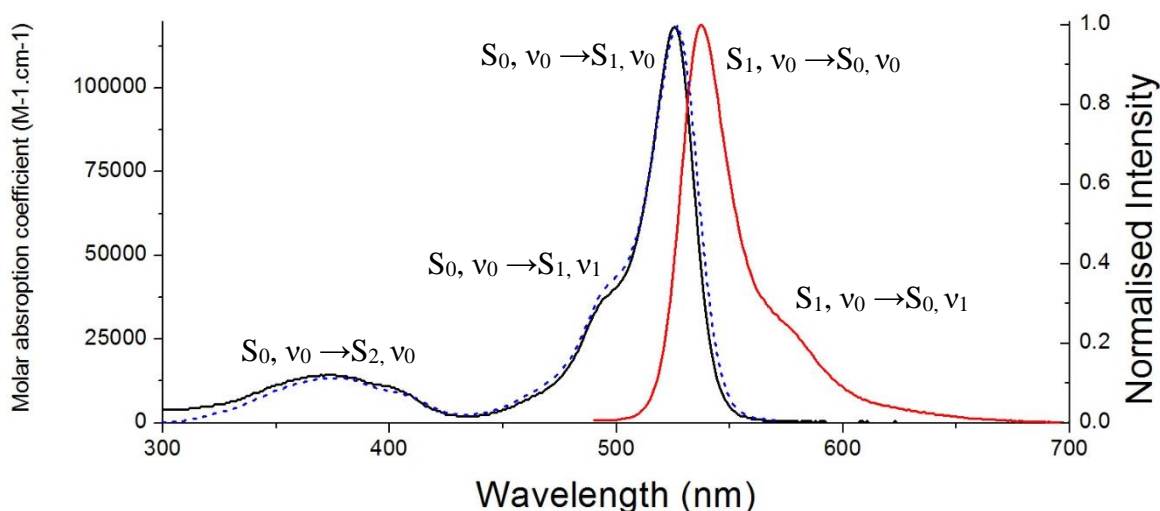


Figure 4: The absorbance (solid black), emission (solid red, $\lambda(\text{exc}) = 480 \text{ nm}$) and excitation (dashed blue, $\lambda(\text{em}) = 580 \text{ nm}$) spectra of **JM1** (10^{-6} M in DCM) with relevant transitions labelled.

These molecules are also highly fluorescent with **JM1** exhibiting an emission band at 537 nm corresponding to the transition from the S_1 to the S_0 state with a quantum yield of 0.44 (in EtOH, reference: fluorescein in 0.1 M NaOH, $\Phi_F = 0.87$). This band is also vibronically coupled showing a shoulder at around 590 nm. Both the main absorption and emission bands are very narrow, typical of organic systems like the BODIPY fluorophore which are rigid; also evidenced by the low Stokes shift of 433 cm^{-1} . Also as with other dyes of

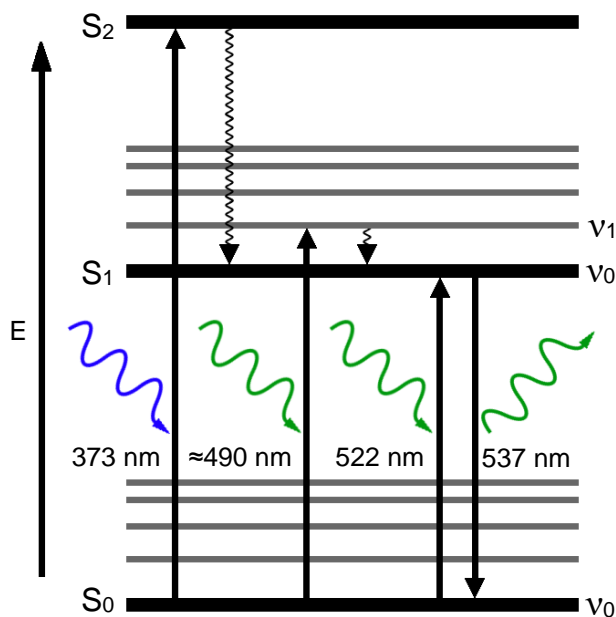


Figure 5: The Jablonski diagram of **JM1** showing the relevant transitions and their respective wavelengths. Only pertinent energy levels are labelled and the vibrational levels of the S_2 are omitted for clarity.

this type, **JM1** deactivates via fluorescence ($S_1 \rightarrow S_0$) an excited state lifetime of 6.05 ns recorded using the TCSPC method using a laser excitation source at $\lambda(\text{exc}) = 471.8 \text{ nm}$.¹⁵

Various COK-12 samples were synthesised where 1, 5, 7.5, 10, 20 and 50 mol% of the Pluronic-P123 was replaced by **JM1**. This was done in order to keep the overall surfactant concentration constant across all samples so that the morphology of the micellar phase would always be in the rod-like regime. The Pluronic-P123 and **JM1** were dissolved at the same time in the citric acid/citrate buffer and stirred for 24 h at room temperature to allow time for the dye to be uniformly incorporated into the micellar structure. After this, diluted sodium silicate solution was added dropwise to the micelle solution, which within minutes turned turbid as the silica began to form. After another 24 h at room temperature, the resulting solid was filtered and dried in an oven resulting in COK-12 with mixtures of Pluronic-P123 and **JM1** in the pores (**JM1/Pluronic P123@COK-12**).⁶

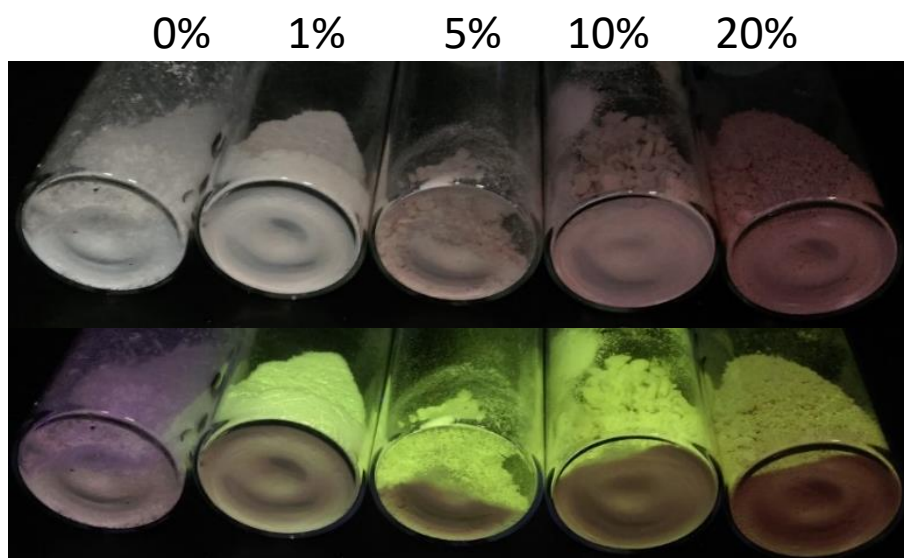


Figure 6: Photographs of a selection of **JM1/Pluronic-P123@COK-12** samples at various dye-loadings under ambient (top) and UV (bottom) light.

Photographs of these samples are shown in Figure 6 under ambient and UV light. It is clear to see under ambient light that as the dye-loading increases the pink hue in the samples becomes more prominent which was as expected. However, a different trend is observed when the samples are illuminated under 366 nm UV light. Here, the 1% sample exhibits the brightest fluorescence by eye with subsequent samples getting gradually dimmer. At this stage, this was originally attributed to aggregation and the inner filter effects which cause a lowering of the observed fluorescence intensity. Interestingly, literature studies of BODIPY dyes loaded into nano- and mesoporous silica found that hydrogen bonding between silanol

groups (formed from incomplete condensation of the silicate precursor) and the pyrrolic nitrogen atoms on the dipyrromethene ligand caused deactivation of the fluorescence and a dramatic drop in fluorescence quantum yield. This however does not seem to be the case here presumably because the Pluronic-P123 micelles shield the fluorophore from any interaction with the silica walls.¹¹

3.2.1 Structural Analysis

As mentioned above, the dye-loaded COK-12 samples were analysed to investigate their structural and spectroscopic properties. Shown below is the experiments to see how dye-loading affects the structure of COK-12. Due to the large pore size seen in SBA-types materials, small angle X-ray scattering (SAXS) measurements were performed by Dr. Helen Riggs at Durham University.

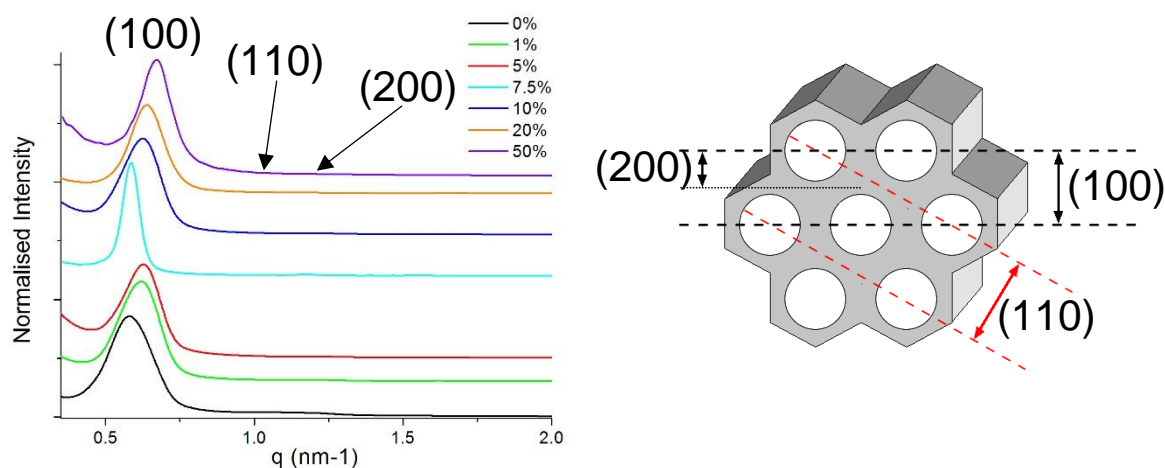


Figure 7: (left) The SAXS profiles of the **JM1**/Pluronic P-123@COK-12 samples and (right) a diagram showing the crystallographic diffraction planes in hexagonal *m*-SiO₂.¹⁶

Figure 7 (See Appendix, Table A1 for peak analysis) shows the SAXS profiles¹⁷ of a selection of dye-loaded COK-12 samples with the main peak at a q value around 0.6 nm⁻¹ corresponding to reflections from the (100) crystallographic plane. This reflection corresponds to the pore diameter plus the wall thickness of the silica. The reflections of the (110) and (200) planes are present as indicated in Figure 7a) but are very small. All signals could be enhanced by removing the micelles from the pores but would somewhat defeat the point of these experiments. Reflections at these relative q -values are distinctive of hexagonal *m*-SiO₂.¹⁶ It is possible to see from these SAXS profiles that the hexagonal structure is maintained even up to a loading of 50%. This is further supported by TEM images which show porosity and order are retained in all **JM1**/Pluronic P123@COK-12 samples (Figure 8).

There is however a small shift in the q -value of the (100) reflection as dye-loading increases. This corresponds to pore shrinkage as at 0%, the $d_{(100)}$ spacing is equal to 11.0 nm whereas at 50% dye-loading this has decreased to 9.40 nm. This has been attributed to the radius of the micellar rods decreasing as relatively large Pluronic-P123 molecules are being replaced with the smaller **JM1** units.⁶

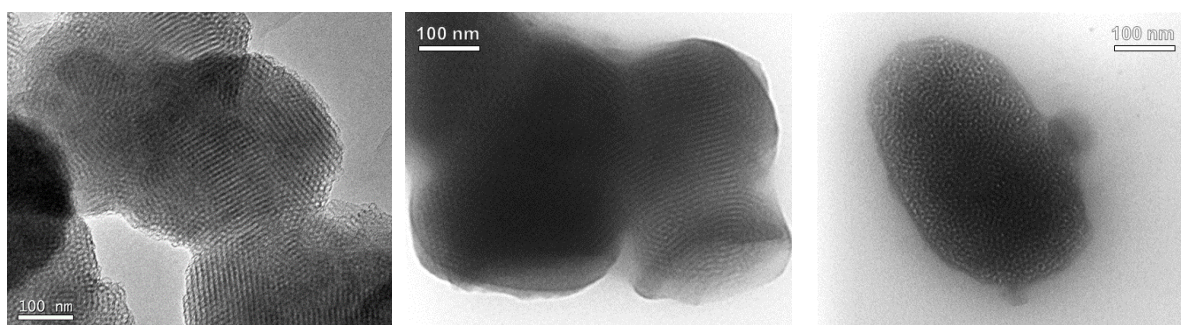


Figure 8: TEM images of 1% (left), 10% (middle) and 50% (right) **JM1**/Pluronic-P123@m-SiO₂ samples.

3.2.2 Spectroscopic Analysis

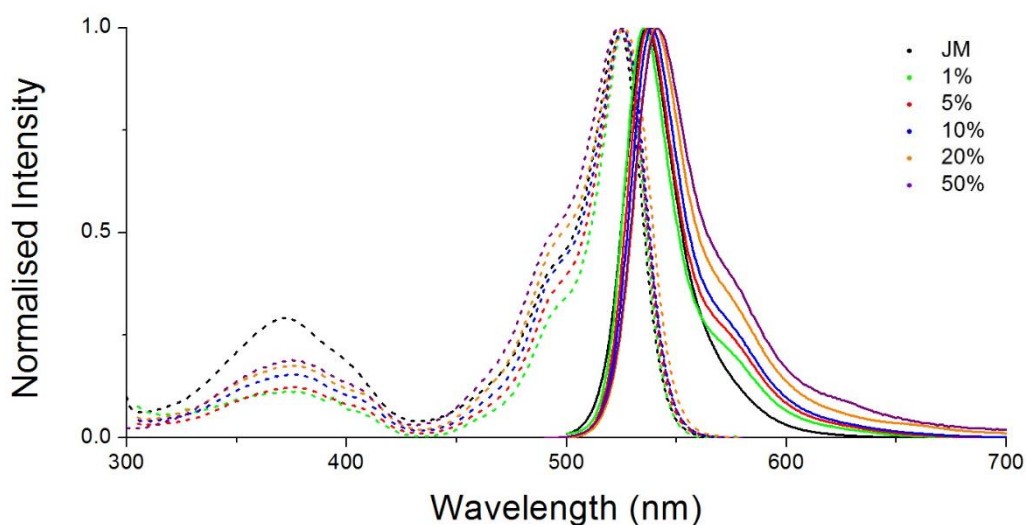


Figure 9: The normalised excitation (dotted lines, $\lambda(\text{em}) = 580$ nm) and emission (solid lines, $\lambda(\text{exc}) = 480$ nm) spectra of **JM1**/Pluronic-P123@COK-12 at a series of dye-loadings taken as 0.3 mg.mL⁻¹ suspensions in cyclohexane.

Optical spectroscopy was used to probe the photophysical properties of **JM1**. Firstly, steady-state photoluminescence emission and excitation spectroscopy were used to show if and how the dye behaves differently in silica when compared to in solution with the spectra shown in Figure 9. To counteract the scattering phenomena exhibited by silica suspensions,

the **JM1**/Pluronic P123@COK-12 samples were suspensions in cyclohexane with a concentration of 0.3 g.mL^{-1} . These were compared to the free **JM1** in EtOH.⁵

Changes observed in the photoluminescence spectra are subtle with the main excitation peak observed at 522 nm. The vibronic component of the emission band become more pronounced as the dye is encapsulated due to increased rigidity provided by the silica.^{18, 19} There is a slight but notable red-shift observed in the emission maxima alongside decreasing values in fluorescence quantum yield seen as a result of increased dye-loading. This is accompanied by a widening of the bands seen in both types of spectra. With this evidence, and the structural analysis, one can say that the synthesis of m-SiO₂ with dye loaded micellar templates has been achieved with the order of the pores. This does not mean that these materials are light-harvesting antennae however with no energetic communication proven between dye units in the pores. To that end, fluorescence lifetime studies were undertaken in order to see how the emission decay was affected by inserting **JM1** into the pores.⁵

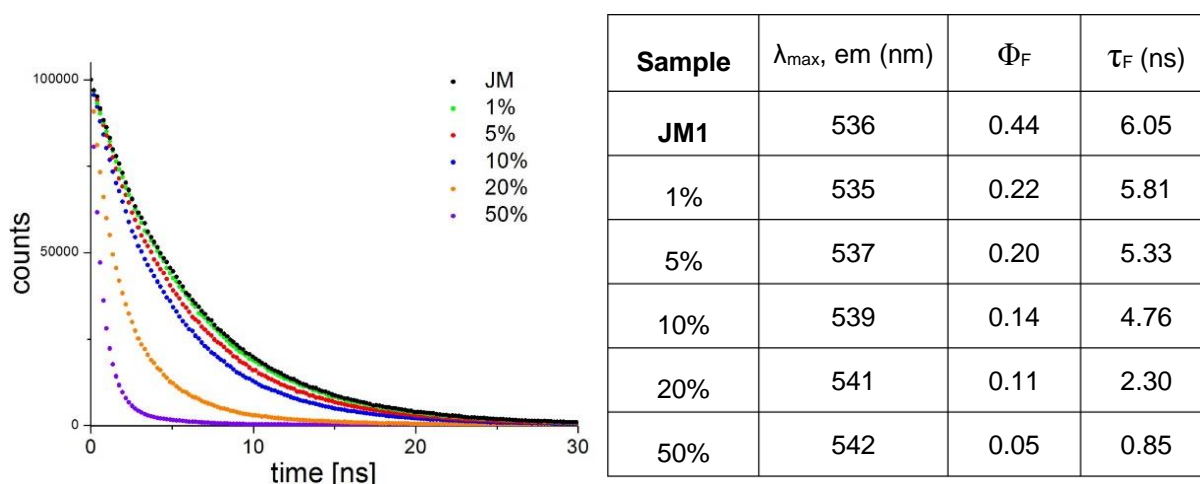


Figure 10: (left) The fluorescence decay traces of **JM1** in solution as well as the various **JM1**/PluronicP-123@COK-12 samples. **Table 1:** (right) Peak emission wavelengths, quantum yields and weighted averaged lifetimes acquired from exponential fitting of the traces in Figure 10.

Shown in Figure 10 are the fluorescence decay traces for a selection of the **JM1**/Pluronic-P123@COK-12 samples yielding averaged fluorescence lifetimes given in Table 1 (see Appendix, Table A2 for multiexponential fittings). From this data, it is clear to see that there is a successive lowering of fluorescence lifetime as dye-loading increases resulting in the decreasing trend in fluorescence quantum yield. By referring to work by Vu et al,²⁰ who investigated the photophysical properties of PMMA films loaded with BODIPY, holding these dyes in solid matrices opens up various excited state deactivation pathways through chromophore aggregation, namely H- and J- aggregates. Figure 11 shows a diagram of how

these types of aggregates form and how this relates to some of their photophysical properties and as they are typically made up of several dye units, a single isolated **JM1** molecule will henceforth be referred to as the monomer.²⁰

Planar organic dyes like BODIPY are prone to π -stacking and thus aggregate with their planes parallel to one another. The relative displacement of these planes (known as the slip angle, see Figure 11) between the dye units determines the nature of the aggregate. At an angle of 54.7° , the monomers in the aggregate have degenerate excited states and fluoresce as normal. As this angle changes from this point, the excited states split into two levels of differing energies. Depending on the type of aggregate, only one of these excited states is accessible where the monomer transition dipoles point in the same direction. When these dipoles are opposing, electronic transition to this excited state is not allowed.²⁰

At a slip angle lower than 54.7° and ideally with monomers orientated end-to-end, a J-aggregate is formed, named after discoverer E. E. Jelley.²¹ Here, only transition from the ground-state to the lower energy excited state is allowed meaning these aggregates exhibit a red-shift in absorption and emission when compared to the monomer. They also exhibit increased and sharpened spectral bands and small Stokes shifts. In the case of H-aggregation, the co-planar displacement needs to be higher than 54.7° where the ideal orientation is where the monomers are stacked directly on top of one another.²² In such systems, the upper excited state is accessible leading to a high-energy transition therefore a hypsochromic spectral shift. These aggregates are typified by a high degree of vibronic coupling and very low fluorescence quantum yields due to their tendency to decay non-radiatively.^{20, 23}

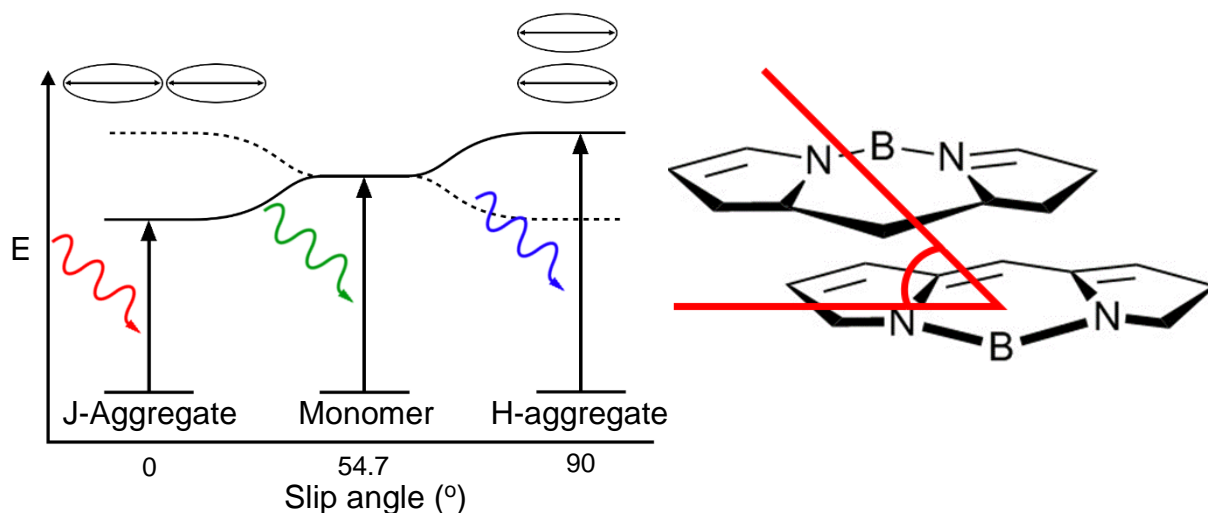


Figure 11: (left) A diagram of how the slip angle between to chromophores determines the type of aggregate formed with solid lines denoting accessible energy levels. (right) A diagram showing the slip angle between two stacked BODIPY cores.²³

Since a red-shift is observed with successive increases in dye-loading, it should not be ruled out that J-type aggregates are formed in the silica. As these are now of lower energy than the isolated dye, FRET²⁴ can take place from monomer to these aggregates. This therefore depopulates the excited state of **JM1** thus lowering the quantum yield. Other quenching phenomena could involve a solvatochromic^{25, 26} effect caused by the insertion of **JM1** into the micelles as well as non-fluorescent excitation energy traps. These effects are concentration dependent and become more prominent as dye-loading increases as evidenced by the decreasing fluorescence quantum yield. It is worth noting however that the **JM1**/Pluronic-P123@COK-12 samples are significantly fluorescent in the green region even at high dye-loadings when compared to films of pure **JM1** which exhibit broad red-shifted emission of low intensity and average lifetime of 220 ps (see Appendix, Figure A2).²⁰

3.3 MCM-41

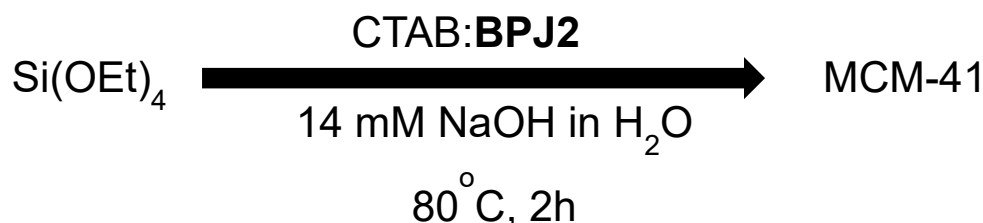


Figure 12: The synthesis of MCM-41.

In order to explore other types of m-SiO₂, an adapted synthesis of MCM-41 was devised. This type of mesoporous silica is synthesised by using hexadecylammonium bromide (CTAB) to form the micellar template as shown in Figure 12.⁷ Sodium hydroxide is used to catalyse the hydrolysis and polycondensation steps with tetraethylorthosilicate (Si(OEt)₄, TEOS) being the silicate source. When comparing this to the COK-12 synthesis, MCM-41 formation occurs under harsh conditions needed whereby a pH of around 12 (14 mM NaOH) and elevated temperatures are required to hydrolyse and polymerise TEOS. However, while these conditions can cause degradation of **BPJ2**, the silica formed as part of the reaction provides adequate protection from hydroxide (see Ch. 4, Figure 3). The resulting precipitate from these reactions is then filtered and dried in an oven overnight giving the MCM-41 mesoporous silica. Once again, a BODIPY dye, **BPJ2** (shown in Figure 13), has been designed to match the surfactant used to form the micellar template i.e. CTAB. This time however the relative polarity of the BODIPY is reversed when compared to **JM1**. Here, an octyloxyphenyl group has been substituted on the meso-position mimicking the hydrophobic hexadecyl chain in

CTAB. The hydrophilic portion of **BPJ2** is in the BF₂ unit which is relatively more polar due to its zwitterionic nature when compared to the alkyl chain. To aid insertion, the BODIPY has also been designed to have approximately the same length as CTAB to reduce the possibility of disruption of the micellar structure.⁵

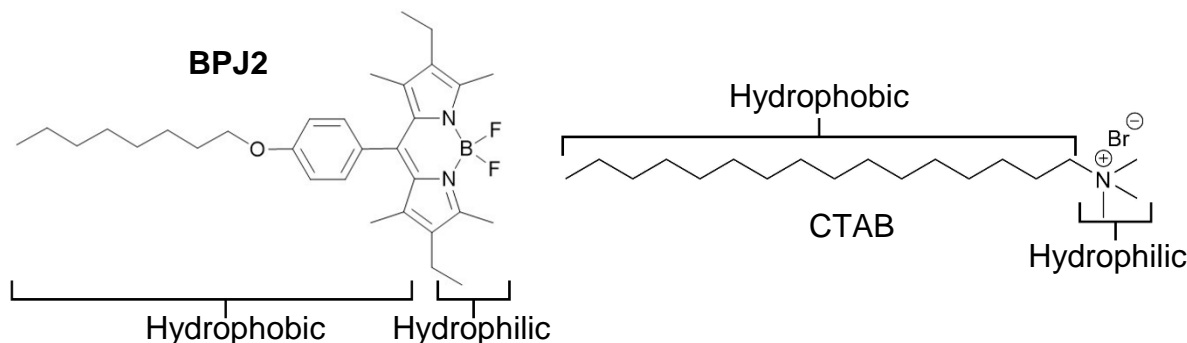


Figure 13: The structures of **BPJ2** (left) and Pluronic-P123 (right) with their hydrophilic and hydrophobic regions highlighted.

Due to the presence of the same fluorophore, **BPJ2** exhibits very similar photophysical (spectra shown in Figure 14) properties to **JM1** with a vibronically coupled S₀→S₁ transition at 520 nm and an S₀→S₂ peak seen at lower wavelengths in the absorbance spectrum. **BPJ2** has a molar absorption coefficient slightly lower than **JM1** but it is still above 100,000 M⁻¹.cm⁻¹ as is typical for BODIPY dyes.

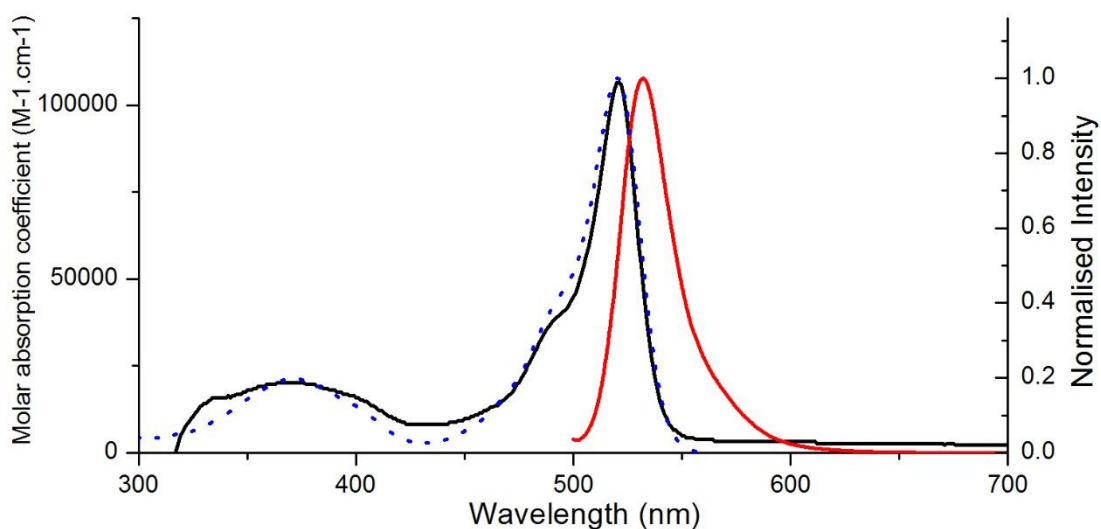


Figure 14: The absorbance (solid black), emission (solid red, $\lambda(\text{exc}) = 490$ nm) and excitation (hashed blue, $\lambda(\text{em}) = 575$ nm) spectra of **BPJ2** in MeCN.

The emission spectrum shows a peak at 532 nm relating to the S₁→S₀ transition leading to a Stokes shift of 433 cm⁻¹ with a lower degree of vibronic coupling seen in the emission when compared to **JM1**. **BPJ2** was also found to be highly fluorescent with a Φ_F of 0.48 and

fluorescence lifetime of 3.4 ns.¹⁵ One disadvantage of using this dye however is the fact that it is insoluble in water. In order to add **BPJ2** to the reaction therefore it was dissolved in a minimum amount of acetonitrile (typically 1% v/v) which was then in turn added dropwise to the CTAB solution which was then stirred at room temperature for 2 h to allow the micelles to form.³ Studies shown in Chapter 5 do suggest that the use of a significant amount of co-solvent (> 5-10% v/v) in the addition of dyes can have a detrimental effect on the micellar structure. To this end, the use of MeCN, shown to be particularly destructive to the template, has been kept to a minimum.⁵

As with the COK-12 samples, a series of **BPJ2/CTAB@MCM-41** was synthesised with different dye loadings at 1, 5, 7.5, 10, 20 and 50 mol% of CTAB used in the unmodified silica synthesis. The pictures of these samples are shown in Figure 15 under both ambient and UV light. While an in-depth spectroscopic analysis will be shown later in this chapter, it is worth noting that there is a clear blue-shift visible by eye in the low dye-loading samples. This is particularly prominent from the 1% **BPJ2/CTAB@MCM-41** sample which exhibits near-white light emission. At higher dye-loadings, the typical green/yellow BODIPY emission seems to be restored.^{5, 15}

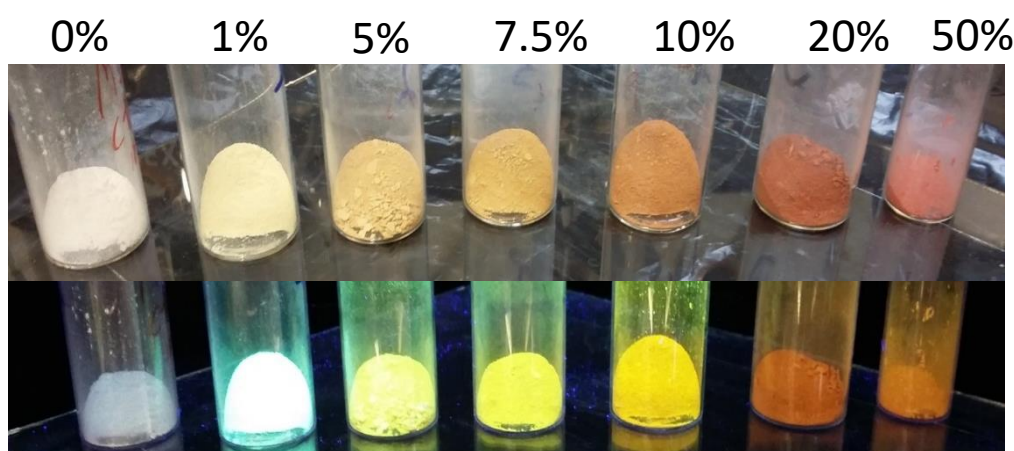


Figure 15: Photographs of **BPJ2/CTAB@MCM-1** at various dye-loadings under ambient (top) and UV (bottom) light.

3.3.1 Structural Analysis

MCM-41 has a typical pore diameter of 3-4 nm and as such can be analysed using powder X-Ray Diffraction (XRD). The diffraction patterns of all **BPJ2/CTAB@MCM-41** in the series is shown in Figure 16 (SAXS patterns shown in Appendix, Figure A3). The 0% sample is the standard diffractogram exhibiting the distinctive (100), (110) and (200) peaks of hexagonal m-SiO₂ but with different 2 θ values when compared to the COK-12 samples, relating to the smaller pore size. Initially, the findings from only samples with dye-loading 0-

10% were published. Here, at 1% loading, the diffraction pattern is very similar to normal MCM-41 with all diagnostic peaks clearly visible. These peaks do however shift to lower 2θ values which is caused by a slight increase in the pore diameter as we replace relatively small trimethylammonium units with large BODIPY moieties in the micellar template. The TEM image of this sample is provided in Figure 16 showing typical spherical particles of MCM-41 with small regular pores.²⁷

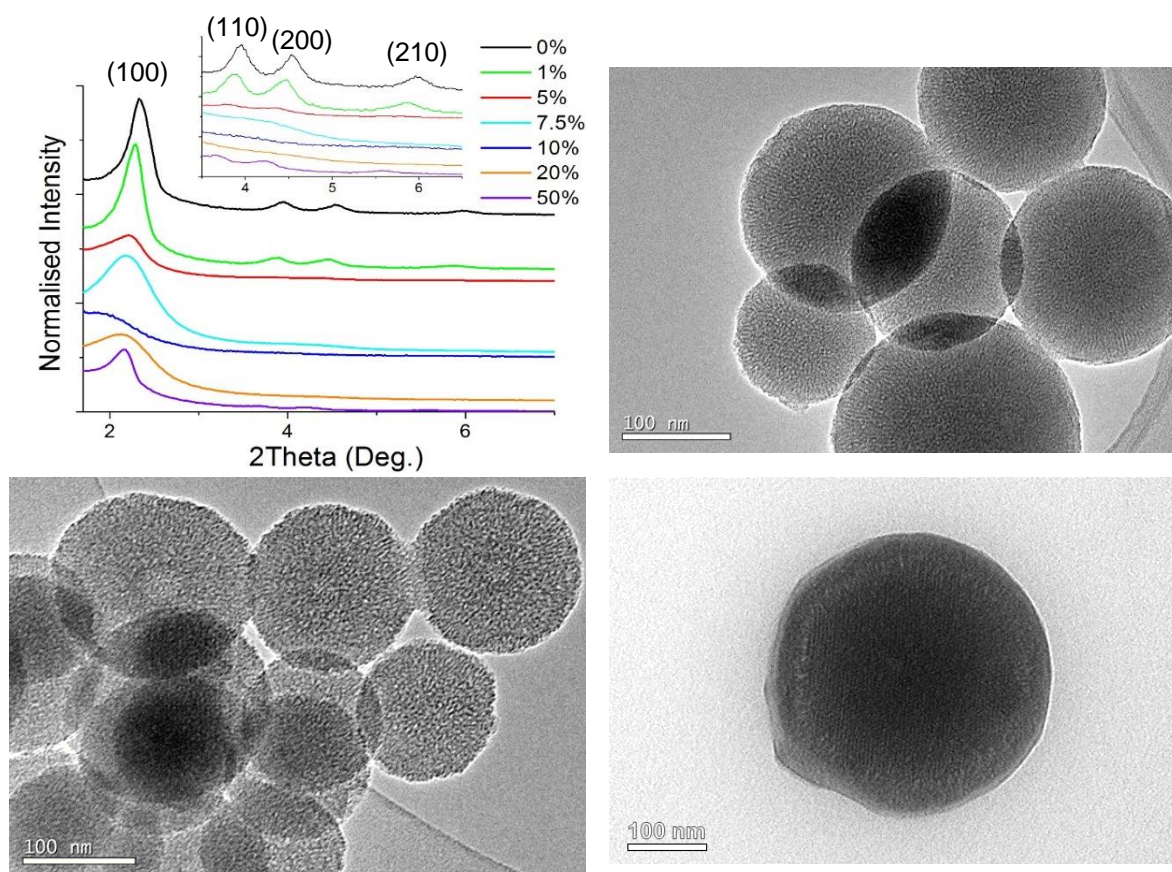


Figure 16: (Top left) The powder X-Ray diffraction patterns of the library of **BPJ2**/CTAB@MCM-41 samples and the TEM images of the 1% (top right) 1%., 10% (bottom left) 10% and 50% (bottom right) 50% samples.

As one moves to higher proportions of **BPJ2** up to 10% the peaks become gradually broader and lower in intensity to the point where the higher reflections (110), (200) and (210) disappear completely. This is caused by the pores becoming larger and more polydisperse. It was originally thought therefore that the introduction of **BPJ2** into the micellar template was disrupting the mesophase structure to the point where the synthesis was resulting in almost completely amorphous m-SiO₂. This finding is supported by the TEM image of the 10% sample which exhibits irregular porosity.¹⁸ However this trend on decreasing crystallinity was shown to reverse once dye-loadings of higher than 10% were explored. As shown in the

powder XRD, the (100) peak begins shifting to higher 2θ values again and becomes narrower. In the diffractogram of the 50% sample, even the higher (110) and (200) reflections are visible indicating the restoration of the hexagonal rod-like micellar phase. This can be seen in the TEM image of the 50% sample shown in Figure 16 which shows channels running along this particle that are so even as to be exemplary.^{5, 27}

Up until this point, these silica syntheses were performed under the assumption that the dye-doped micelles would take the same amount of time to form as standard CTAB micelles i.e. 2 hours. However, upon further analysis of the micelle formation dynamics (results shown in Chapter 4), the **BPJ2** molecules take much longer to find their equilibrated distribution throughout the template. As it was, the formation of the mesophase has been shown to take longer than 24 h. As such, this trend could at least partially be put down to experimental error where a prolonged stirring time could result in a more established hexagonal array prior to the addition of the TEOS which will present as a higher crystallinity in the final silica sample. Another explanation could be down to the use of acetonitrile as a co-solvent. As shown in Chapter 5, acetonitrile can have a highly disruptive effect on the micellar structure. It is therefore possible that in certain experiments, particularly the 10% sample, a large amount of acetonitrile was used to dissolve the **BPJ2** prior to its addition to the CTAB solution.

3.3.2 Spectroscopic Analysis

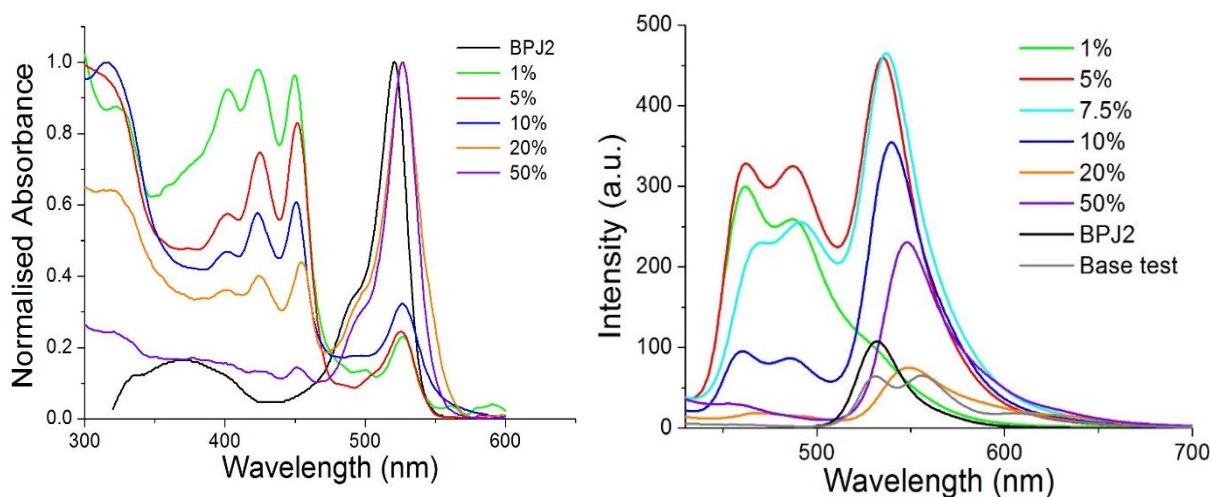


Figure 17: The normalised absorbance (left, as $0.3 \text{ mg}\cdot\text{mL}^{-1}$ suspensions in cyclohexane) and emission (right, $\lambda(\text{exc}) = 400 \text{ nm}$, as $1 \text{ g}\cdot\text{mL}^{-1}$ suspensions in H_2O) of **BPJ2/CTAB@MCM-41** at a series of dye-loading.

Steady state optical spectroscopy was used for the initial analysis for the **BPJ2/CTAB@MCM-41** samples with $0.3 \text{ mg}\cdot\text{mL}^{-1}$ suspensions in cyclohexane used for the absorbance spectra in order to minimise the scattering from the silica (shown in Figure 17).

The typical **BPJ2** absorbance is visible around 520 nm in all samples. Small variations in the absorbance maximum can be seen but these changes are not significant. What is significant is the new set of peaks from 400-450 nm corresponding to a blue-shifted (with respect to **BPJ2**) highly vibronically coupled species which forms at some point during the silica synthesis. The energy difference between these peaks corresponds to the vibrational frequency of aromatic C-C and C-N stretches commonly seen in the electronic transitions localised on rigid organic chromophores.³⁰

Chapter 4 is dedicated to this new species, dubbed the “blue species” (**BS**), i.e. when and how it forms as well as some preliminary findings whereas here will be a discussion of the properties of **BS** and **BPJ2** in MCM-41. To confirm the presence of **BS**, fluorescence emission spectroscopy was performed on 1 mg.mL⁻¹ suspensions in water resulting in the spectra seen in Figure 17. Once again a series of vibronically coupled bands are seen blue-shifted when compared to **BPJ2** emission. This new species is particularly prominent in the 1% sample, where the emission almost entirely originates from **BS**, giving rise to the blue-white colour seen in under 366 nm UV light in Figure 14.

As to what **BS** actually is 2 hypotheses can be put forward. Based on the work by Fernandez *et al.* on self-assembling BODIPY-based surfactants²³ one candidate comes in the form of BODIPY H-aggregates with transitions that fall in the region of the new bands seen in the spectra in Figure 17. These systems often exhibit a high degree of vibronic coupling and large Stokes shifts and are typically seen in the solid state or high concentration solutions. Deactivation of the excited state of these aggregates however typically takes place non-radiatively resulting in very low fluorescence quantum yields which is not seen here. This could be down to the fact that these aggregates are encased in mesoporous silica which provides a rigid framework, hampering molecular vibration and allowing radiative decay. Of course, formation of a new chemical species should not be ruled out. While the specific chemical nature of **BS** is not of concern here, it certainly exhibits some interesting behaviour. Firstly as dye-loading increases, the **BS/BPJ2** absorbance and emission ratio decreases to the point where little to no **BS** is seen in the 50% sample. If the H-aggregate hypothesis is to be supported, **BPJ2** monomers must be more homogeneously distributed in the micellar template at higher dye-loading, leading to the conclusion that concentration is not the only variable determining the degree of aggregation. In the case of a chemical reaction, **BPJ2** would be a reagent that becomes more in excess as dye-loading increases, using up another reactant as **BS**

is formed. Further investigations into the nature and formation of **BS** will be presented in Chapter 4.

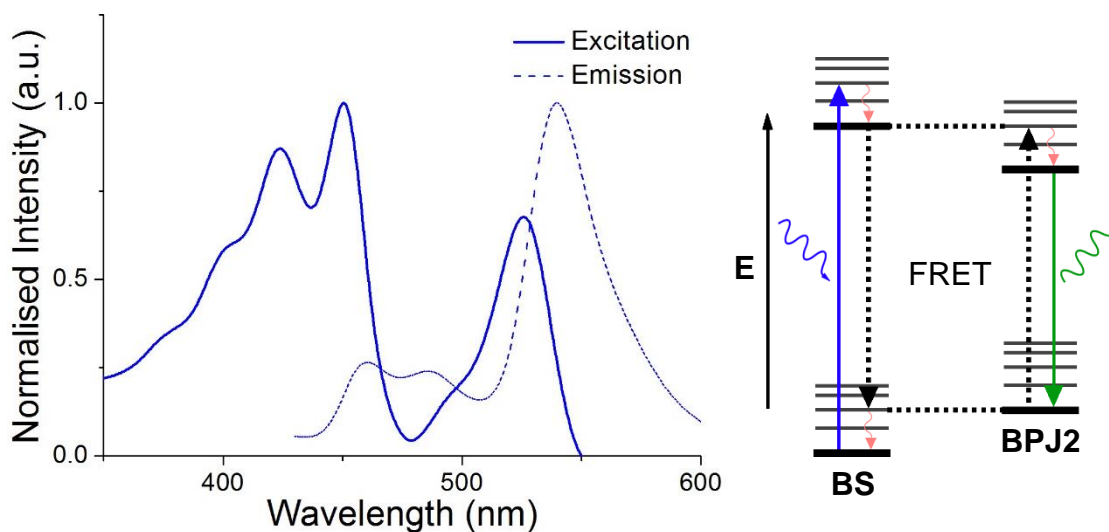


Figure 18: (left) The fluorescence excitation ($\lambda(\text{em}) = 570 \text{ nm}$) and emission ($\lambda(\text{exc}) = 400 \text{ nm}$) of **BPJ2/CTAB@MCM-41** at 10% dye-loading. (right) A Jablonski diagram of FRET from **BS** to **BPJ2**.

All of this aside for now however, one very interesting thing is of note. In forming **BS** during the course of the synthesis of **BPJ2/CTAB@MCM-41** (for simplicity this nomenclature will still be used.), a bichromophoric system has been found despite only one chromophore used in the synthesis. It is possible therefore that FRET could be taking place between the two species present in the silica. Figure 18 shows the steady-state fluorescence excitation and emission spectra of the 10% **BPJ2/CTAB@MCM-41** sample. Looking at the emission spectrum first, the sample is excited at a wavelength absorbed by **BS** (400 nm) resulting in the dashed spectrum. While relatively small bands corresponding to the emission of **BS** (462 and 487 nm) are observed, the spectrum is dominated by the emission of **BPJ2** (540 nm). By probing this emission band at 570 nm, the resulting solid-lined excitation spectrum is generated. While the excitation band corresponding to **BPJ2** (520 nm) is observed, the emission at 570 nm is also generated from light absorbed by **BS**, as evidenced by the presence of the high energy excitation band between 350-470 nm. These experiments mean that upon excitation of **BS**, there is partial energy transfer to **BPJ2** which then emits. In fact, the excitation spectra of all **BPJ2/CTAB@MCM-41** samples exhibit evidence of this FRET behaviour to some degree (see Appendix, Figure A4). Lifetime measurements of the silica samples were recorded using TCSPC measurements with the results shown in Table 2. Decay traces were run corresponding to the emission wavelengths of both **BS** and **BPJ2** (450 and 540 nm respectively). While these results show that the lifetime of **BS**, which in this case would be the donor, is significantly shorter than that of **BPJ2**, no energy transfer processes

could be confirmed using this analysis. As such, a much more sensitive measurement was required.

Sample/dye loading (%)	Decay traces (ns)	
	(a) 450 nm	(b) 540 nm
BPJ2	-	4.7
1	2.0	4.9
5	1.5	4.6
10	1.5	5.2
20	1.3	5.4
50	1.2	5.1

Table 2: Excited state lifetimes of **BPJ2** into MCM-41 at selected dye-loadings, recorded from 0.3 mg.mL⁻¹ suspensions in cyclohexane, using laser excitation sources with wavelengths (a) 371.8 nm and (b) 471.8 nm.

To that end, femtosecond transient absorption spectroscopy (fs-TAS) was performed by Prof. Fausto Puntoriero and Emmanuele La Mazza at the University of Messina (Italy). For reference the spectra for pure **BPJ2** in ethanol is shown in Figure 19. Immediately upon excitation, an intense bleaching is observed around 530 nm ascribed to the depopulation of the S₀ of **BPJ2**. This bleach is recovered over 4.7 ns (comparable to the lifetime acquired by TCSPC) with no change in wavelength or band shape.³¹ Figure 19 also features the fs-TAS profiles of a selection of the **BPJ2/CTAB@MCM-41** samples (1, 5 10 and 50% dye-loading). These experiments were recorded using 400 nm probe pulse minimising direct excitation of any **BPJ2** in the silica samples. Looking at the 1% sample, noted for its high proportion of **BS**, there is a clear difference in the TAS when comparing to **BPJ2** in solution. The tail-end of the ground-state bleach of **BS** is seen in the range measured below 475 nm. Most notably however is the large broad positive band seen with a peak value of around 600 nm. This peak is absent in the **BPJ2** TAS and as such has been assigned to the excited state absorption of **BS**. This band recovers biphasically, with a short (80 ps) and long (1 ns) component. This takes place in tandem with the recovery of the ground state bleach of **BS** at 475 nm. At 2.9 ns, a small bleach at 520 nm is also observed, which is unlikely to result from direct excitation of **BPJ2** using this setup (120 fs laser pulse at 400 nm) as **BS** dominates the absorptive behaviour of this sample.

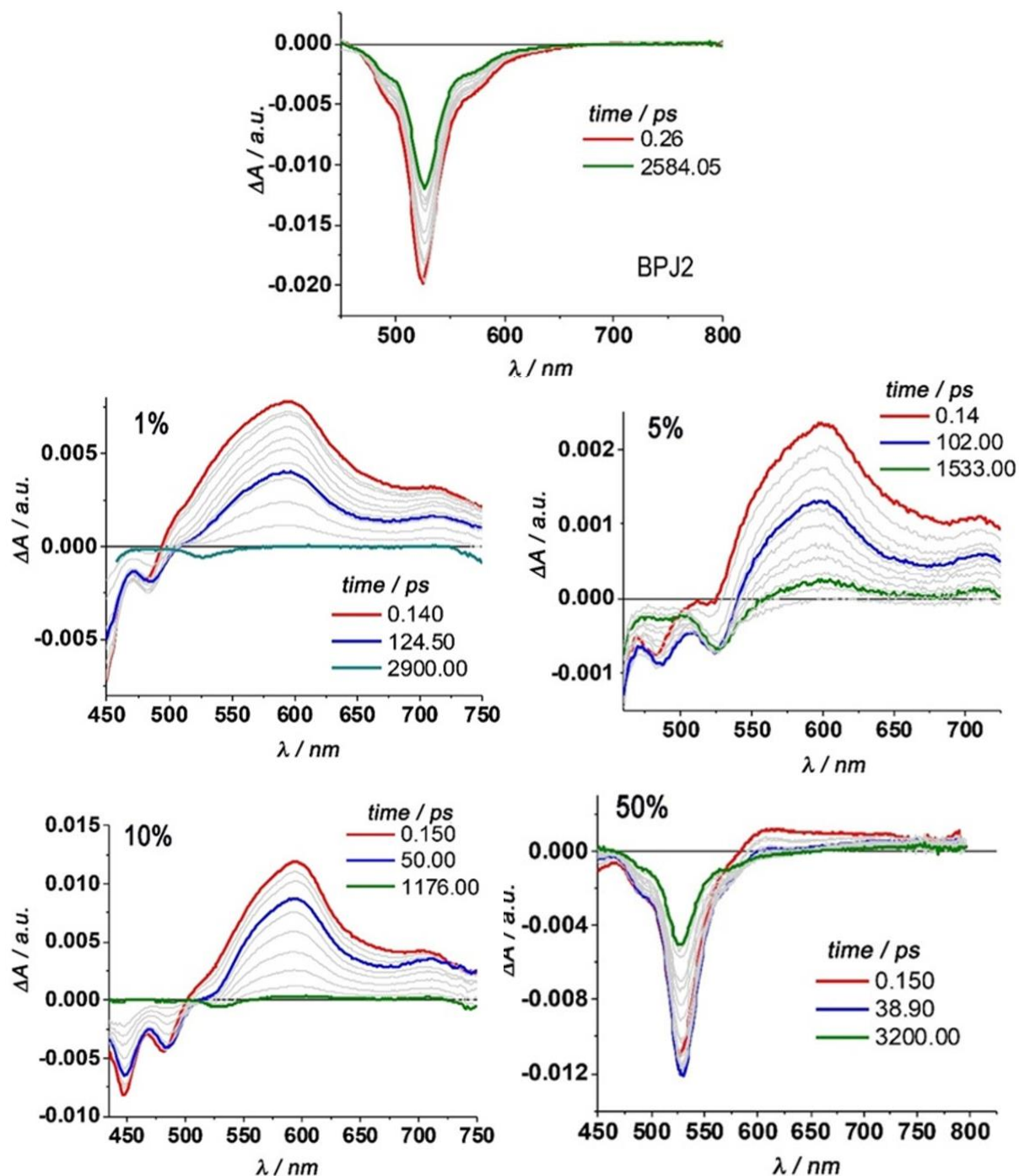


Figure 19: The transient absorption spectra (TAS) of BPJ2 in ethanol (top) and four representative **BPJ2/CTAB@MCM-41** samples (labelled) recorded in $0.3 \text{ mg}\cdot\text{mL}^{-1}$ water suspensions ($\lambda(\text{exc}) = 400 \text{ nm}$, 120 fs probe pulse).

The TAS for the 5% **BPJ2/CTAB@MCM-41** sample exhibits similar behaviour albeit with differing relative heights of peaks as the proportion of **BS** in the template decreases as dye-loading increases (see Figure 19). Initially, below 500 nm bleaching is seen due to the depopulation of the S_0 of **BS**. Over the first 100 ps, this bleaching decreases concomitantly

with a transient bleach at around 530 nm caused by excitation of **BPJ2**. The **BS** ground-state bleach then completely recovers by 1.2 ns after excitation alongside the corresponding excited state absorption band above 500 nm followed by complete recovery of the ground state of **BPJ2** after 4.5 ns.

As **BPJ2** was added to the synthesis during the initial micelle formation stage, it is reasonable to assume that the dyes within the template are statistically distributed resulting in the distances between **BS** and **BPJ2** units being random. As such, it is certainly possible for a certain number of **BS** and **BPJ2** pairs to be within FRET range of each other (1-10 nm). Within 100 ps of the initial probe pulse, the excited state of **BS** is depleted via energy transfer to **BPJ2** resulting in depopulation of its respective ground state hence the bleach seen at 530 nm. As an indicative example, in the 1% sample, this energy transfer has a time constant of 80 ps. Using Förster theory,²⁴ it is possible to acquire an average donor-acceptor distance between **BS** and **BPJ2** of 20 Å. As well as these FRET pairs, it is possible to deduce from the TAS analysis that isolated **BS** and **BPJ2** units are also present in the template resulting in the longer kinetic traces relating to the fluorescence of **BS** and **BPJ2** with decay lifetimes of 1.2 and 4.5 ns respectively (in agreement with TCSPC measurements discussed above).

This behaviour continues in the samples as dye-loading increases although the relative spectral contributions differ as the proportion of **BS** decreases to the point where the TAS profiles of the 50% sample are almost entirely dominated by processes associated with **BPJ2** as seen in the steady-state spectra in Figure 17. The time constant of energy transfer does change however, showing a marked decrease as dye-loading increases. Within 40 ps of excitation of the 50% sample, the bleaching at 530 nm increases relating to FRET from **BS** to **BPJ2**. In this sample, there is the highest proportion of **BPJ2** in the template, meaning that statistically any **BS** units will form the most closely associated FRET pairs with **BPJ2** units in this series of samples. This means that energy transfer from the former to the latter will be highly efficient hence this sample having a FRET time constant of less than 20 ps. From this, it can be deduced that the average donor-acceptor difference in the 50% sample is less than 15 Å.

3.4 Conclusion

Presented in this chapter are two light-harvesting antennae materials formed by exploiting the templating process and host-guest chemistry of mesoporous silica. This has been achieved by using BODIPY dyes (**JM1** and **BPJ2**) specially functionalised to allow insertion into the micelles around which the m-SiO₂ forms. Functionalised with a poly(ethylene glycol) chain,

JM1 could be inserted as part of the Pluronic-P123 micelles in order to form luminescent COK-12. SAXS experiments showed that the regular porous structure of this material was maintained even up to a dye-loading of 50%. The fluorescence quantum yield of **JM1** decreases as dye-loading increased and the excited decay trace convolutes into a multiexponential. This effect has been attributed to self-quenching via the formation of aggregates as a result of increased dye-loading (as evidenced by the broadening of spectral bands), exciton traps and also via additional vibrational relaxation within the solid matrix,.

By employing a short alkyl chain, **BPJ2** was inserted into the CTAB micelles used in the formation of MCM-41. The regularity of the pores is more sensitive to changes in dye-loading when compared to COK-12 but may be remedied by allowing a longer time for the micellar template to form. A new blue-shifted species formed from either H-aggregation or in-situ chemical reaction of **BPJ2**. Energy transfer from this new species **BS** to **BPJ2** was exhibited by this system shown using steady-state fluorescence spectroscopy. Fs-TAS showed that FRET takes place in a time scale of 20-80 ps with the rate increasing with dye-loading. Both of these materials show promise in using the self-assembly of m-SiO₂ templates in the formation of light-harvesting antennae.

3.5 Experimental

Synthesis of COK-12 with a 100% Pluronic-P123 micellar template:

Pluronic-P123 (1.02 g, 0.174 mmol), citric acid monohydrate (953 mg, 4.96 mmol) and trisodium citrate dihydrate (803 mg, 3.11 mmol) were dissolved in H₂O (27 mL) and stirred for 1.5 h during which the mixture turned clear. Sodium silicate solution (1.8 mL, 21.97 mmol) was diluted with H₂O (7.5 mL) and added dropwise to the reaction mixture which within 10 min of stirring turned cloudy. This was then left undisturbed at room temperature for 24 h causing a white precipitate to form which was filtered under vacuum. The filtrate was then washed with water until foaming ceased. The solid was then dried in an oven overnight resulting in a white powder.

Synthesis of COK-12 with **JM1**-doped Pluronic-P123 micelles (**JM1**/Pluronic-P123@COK-12):

Citric acid monohydrate (953 mg, 4.96 mmol) and trisodium citrate dihydrate (803 mg, 3.11 mmol) were dissolved in H₂O (27 mL). Pluronic-P123 and **JM1** were then added in the following molar ratios to result in the desired dye-loadings: 99:1 (Pluronic-P123: 0.169 mmol, **JM1**: 1.71 μmol), 95:5 (Pluronic-P123: 0.162 mmol, **JM1**: 8.54 μmol), 92.5:7.5 (Pluronic-P123: 0.158 mmol, **JM1**: 13.01 μmol), 90:10 (Pluronic-P123: 0.154 mmol, **JM1**: 17.08 μmol), 80:20 (Pluronic-P123: 0.137 mmol, **JM1**: 34.17 μmol), 50:50 (Pluronic-P123: 0.086 mmol, **JM1**: 0.086 mmol). This mixture was stirred for 3 h during which the mixture turned

clear and pink. Sodium silicate solution (1.8 mL, 21.97 mmol) was diluted with H₂O (7.5 mL) and added dropwise to the reaction mixture which within 10 min of stirring turned cloudy and pink. This was then left undisturbed at room temperature for 24 h causing a pink precipitate to form which was filtered under vacuum. The filtrate was then washed with water until foaming ceased. The solid was then dried in an oven overnight resulting in a pink powder.

Synthesis of N,N'-difluoroboryl-2,8-diethyl-1,3,7,9-tetramethyl-5-(4-octyloxyphenyl)-dipyrrin (**BPJ2**):

Octyloxybenzaldehyde (240 μ L, 1.1 mmol) was dissolved in dry DCM (20 mL). 2-Ethyl-1,3-dimethylpyrrole (270 μ L, 2.2 mmol) was then added and the mixture was stirred for 30 min. TFA (15 μ L, 0.2 mmol) was then added under N₂ atmosphere and the resulting red mixture was stirred overnight. Consumption of the aldehyde was confirmed by TLC (silica, eluent: DCM). DDQ (233 mg, 1.0 mmol) was then added and the dark red mixture was stirred for 3.5 hours. Dry NEt₃ (1.1 mL, 7.0 mmol) was added followed by immediate dropwise addition of BF₃.OEt₂ (1.15 mL, 7.6 mmol) causing the mixture to change colour to yellow and dark green respectively. It was stirred overnight under N₂ atmosphere. It was then washed with H₂O (3 x 10 mL), dried over Na₂SO₄ and rotary evaporated which resulted in a viscous purple oil with green tints. The crude product was then purified by column chromatography on silica gel (eluent: petrol/DCM – v/v 1/1): R_f = 0.42. Evaporation of the eluent resulted in an orange-red solid with green tints with a 36.2% yield (181 mg, 0.40 mmol). ¹H NMR (300 MHz, CDCl₃): δ = 7.07 (d, *J* = 9 Hz, 2H, CH_{Ar}), 6.91 (d, *J* = 9 Hz, 2H, CH_{Ar}), 3.93 (t, *J* = 6 Hz, 2H, OCH₂), 2.45 (s, 6H, pyrrole-CH₃), 2.22 (q, *J* = 7 Hz, 4H, pyrrole-CH₂-CH₃), 1.80-1.64 (m, 2H, OCH₂-CH₂), 1.47-1.37 (m, OCH₂CH₂-CH₂), 1.33-1.18 (m, 8H, -CH₂-), 1.26 (s, 6H, pyrrole-CH₃), 0.90 (t, *J* = 7.5 Hz, 6H, pyrrole-CH₂-CH₃), 0.82 (t, *J* = 6 Hz, 3H, -CH₃). ¹³C NMR (300 MHz, CDCl₃): δ = 159.6 (C_{Ar}), 153.4 (C_{Ar}), 140.5 (C_{Ar}), 138.5 (C_{Ar}), 132.6 (C_{Ar}), 131.2 (C_{Ar}), 129.8 (C_{Ar}), 129.4 (C_{Ar}), 127.6 (C_{Ar}), 68.2 (O-CH₂-), 31.9 (-CH₂-), 29.5 (-CH₂-), 29.3 (-CH₂-), 26.1 (-CH₂-), 22.7 (-CH₂-), 17.3 (-CH₂-), 17.1 (-CH₃), 14.7 (pyrrole-CH₂-CH₃), 14.2 (pyrrole-CH₂), 12.5 (pyrrole-CH₃), 9.4 (pyrrole-CH₃).

Synthesis of MCM-41 mesoporous silica with a 100% CTAB micellar template:

Cetyltrimethylammonium bromide (350 mg, 1 mmol) was dissolved in H₂O (180 mL) using an ultrasound bath. Sodium hydroxide (2 M, 1.3 mL, 2.6 mmol) was then added causing the cloudy mixture to turn clear. This was heated to 80 °C and tetraethylorthosilicate (1.8 mL, 8.2 mmol) was added. The mixture was then stirred under reflux at 80 °C for 2 h after which it was filtered under vacuum. The filtrate was washed with H₂O until neutral and dried in an oven overnight. This resulted in a powdery white solid.

Synthesis of MCM-41 with **BPJ2**-doped CTAB micelles (**BPJ2**/CTAB@MCM-41):

Cetyltrimethylammonium bromide and **BPJ2** were mixed in the following molar ratios to result in the desired dye loadings: 99:1 (CTAB: 0.949 mmol, **BPJ2**: 9.6 μ mol), 95:5 (CTAB: 0.911 mmol, **BPJ2**: 48 μ mol), 92.5:7.5 (CTAB: 0.887 mmol, **BPJ2**: 72 μ mol), 90:10 (CTAB: 0.863 mmol, **BPJ2**: 96 μ mol), 80:20 (CTAB: 0.767 mmol, **BPJ2**: 0.192 mmol), 50:50 (CTAB: 0.167 mmol, **BPJ2**: 0.167 mmol). Generally, CTAB was dissolved in H₂O (180 ml) with the help of an ultrasonic bath. In parallel, **BPJ2** was dissolved in a minimum amount of MeCN (typically around 1 mL) and added dropwise to the CTAB resulting in a turbid

orange/pink mixture. Sodium hydroxide (2 M, 1.3 mL, 2.6 mmol) was then added and the mixture was heated to 80 °C at which point tetraethylorthosilicate (1.8 mL, 8.2 mmol) was added. The mixture was then heated at 80 °C under reflux for 2 h. The resulting pink precipitate was filtered and washed with H₂O. The filtrate was then dried in an oven overnight resulting in powders of varying colours: pale yellow (99:1), pink (95:5, 92.5:7.5, 90:10, 80:20) and red (50:50).

References

1. Y. Moroi, in *Micelles: Theoretical and Applied Aspects*, Plenum Press, New York City, New York, USA, 1992, 1st edn., ch. 1, pp 1-5.
2. I. W. Hamley, in *Introduction to Soft Matter: Synthetic and Biological Self-Assembling Materials*, Wiley, Hoboken, New Jersey, USA, 2007, 2nd edn., ch. 4, pp 180-211.
3. J. N. Israelachvili, D. J. Mitchell and B. W. Ninham, *J. Chem. Soc. Farad. T. 2*, 1975, **72**, 1525-1568.
4. S. May and A. Ben-Shaul, *J. Phys. Chem. B*, 2001, **105**, 630-640.
5. F. Cucinotta, B. P. Jarman, C. Caplan, S. J. Cooper, H. J. Riggs, J. Martinelli, K. Djanashvili, E. La Mazza and F. Puntoriero, *ChemPhotoChem*, 2018, **2**, 196-206.
6. (a) J. Jammaer, A. Aerts, J. D'Haen, J. W. Seo and J. A. Martens, *J. Mater. Chem.*, 2009, **19**, 8290-8293 (b) J. Jammaer, T. S. van Erp, A. Aerts, C. E. Kirschhock and J. A. Martens, *J. Am. Chem. Soc.*, 2011, **133**, 13737-13745.
7. (a) C. Kresge, M. Leonowicz, W. Roth, J. Vartuli and J. Beck, *Nature*, 1992, **359**, 710-712. (b) J. S. Beck, J. C. Vartuli, W. J. Roth, M. E. Leonowicz, C. T. Kresge, K. D. Schmitt, C. T.-W. Chu, D. H. Olson, E. W. Sheppard, S. B. McCullen, J. B. Higgins and J. L. Schlenker, *J. Am. Chem. Soc.*, 1992, **114**, 10834-10843.
8. (a) D. Zhao, J. Feng, Q. Huo, N. Melosh, G. H. Fredrickson, B. F. Chmelka and G. D. Stucky, *Science*, 1998, **279**, 548-552. (b) D. Zhao, Q. Huo, J. Feng, B. F. Chmelka and G. D. Stucky, *J. Am. Chem. Soc.*, 1998, **120**, 6024-6034.
9. P. Riachy, M.-J. Stebe, B. Lebeau, A. Pasc, L. Vidal and J-L Blin, *Micropor. Mesopor. Mat.*, 2016, **221**, 228-237.
10. L. Yang, R. Simionescu, A. Lough and H. Yan, *Dyes Pigments*, 2011, **91**, 264-267.
11. E. V. Romyantsev, S. N. Alyoshin and Y. S. Marfin, *Inorg. Chim. Acta*, 2013, **408**, 181-185.
12. Sigma-Aldrich,
https://www.sigmaaldrich.com/catalog/product/sigald/338443?lang=en®ion=GB&gclid=CjwKCAjwp7baBRBIEiwAPtjwxGPGh0tVr4I9B4XvYJmBFUS-WnoQkD6gDQXtHyK09i72kPBIHbYiCRoC-30QAvD_BwE, (accessed Jul 2018).
13. C. J. Brinker and G. W. Scherer in *Sol-Gel Science: The Physics and Chemistry of Sol-Gel Processing*, Academic Press, London, UK, 1st edn, 1990, ch. 3 pp. 99-113.
14. Sigma-Aldrich,
https://www.sigmaaldrich.com/catalog/product/aldrich/131903?lang=en®ion=GB&gclid=CjwKCAjwp7baBRBIEiwAPtjwxCH2FpnwBhyynt0LoM0Q4Hx0KMvOiXWvF12RF58UQtyjZBqHH5DFrBoCWW4QAvD_BwE, (accessed Jul 2018).
15. A. Loudet, K. Burgess, *Chem. Rev.*, 2007, **107**, 4891-4932.
16. D. Rath, S. Rana and K. M. Parida, *RSC Adv.*, 2014, **4**, 57111-57124.
17. F. Michaux, N. Baccile, M. Imperor-Clerc, L. Malfatti, N. Folliet, C. Gervais, S. Manet, F. Meneau, J. S. Pedersen and F. Babonneau, *Langmuir*, 2012, **28**, 17477-17493.
18. N. Gfeller, S. Megelski and G. Calzaferri, *J. Phys. Chem. B*, 1998, **102**, 2433-2436.
19. G. Calzaferri, S. Huber, H. Maas and C. Minkowski, *Angew. Chem. Int. Ed. Engl.*, 2003, **42**, 3732-3758.
20. T. T. Vu, M. Dvorko, E. Y. Schmidt, J.-F. Audibert, P. Retailleau, B. A. Trofimov, R. B. Pansu, G. Clavier and R. Méallet-Renault, *J. Phys. Chem. C*, 2013, **117**, 5373-5385.
21. E. E. Jelley, *Nature*, 1937, **139**, 631-632.
22. F. Fennel, J. Gershberg, M. Stolte and F. Wuertner, *Phys. Chem. Chem. Phys.*, 2018, **20**, 7612-7620.

23. N. K. Allampally, A. Florian, M. J. Mayoral, C. Rest, V. Stepanenko and G. Fernandez, *Chem. Eur. J.*, 2014, **20**, 10669-10678.
24. T. Förster, *Discuss. Faraday Soc.*, 1959, **27**, 7-17.
25. Y. S. Marfin, O. S. Vodyanova, D. A. Merkushev, S. D. Usoltsev, V. O. Kurzin, E. V. Rumatsev, *J. Fluoresc.*, 2016, **26**, 1975-1985.
26. L. Bolzonello, A. Polo, A. Volpato, E. Meneghin, M. Cordaro, M. Trapani, M. Fontino, A. Pedone, M. A. Casticiano and E. Collini, *J. Phys. Chem. Lett.*, 2018, **9**, 1079-1085.
27. M. Kruk, M. Jaroniec, J. M. Kim and R. Ryoo, *Langmuir*, 1999, **15**, 5279-5284.
28. B. P. Jarman and F. Cucinotta, *Faraday Discuss.*, 2015, **185**, 471-479.
29. M. Lepore, S. Grilli and P. L. Indovina, *P. Soc. Photo.-Opt. Ins.*, 2000, **4161**, 180-189.
30. M. Montali, A. Credi, L. Prodi and M. T. Gandolfi, in *Handbook of Photochemistry*, Taylor and Francis, Abingdon, UK, 2005, 3rd edn., ch. 1, pp. 34-37.
31. Z. Lou, Y. Hou, K. Chen, J. Zhao, S. Ji, F. Zhong, Y. Dede and B. Dick, *J. Phys. Chem. C*, 2018, **122**, 185-193.

Chapter 4. BODIPY-Doped Micelle and Silica Formation Dynamics

4.1 Introduction

Work in the previous chapter showed the initial findings into the doping cylindrical micelles with the boron-dipyrromethene (BODIPY) dyes and synthesising mesoporous silica (m-SiO₂) around them. In using cetyltrimethylammonium-based templates and doping them with **BPJ2** (see Figure 1), a new blue species (**BS**) is formed which exhibits blue-shifted absorptive and emissive transitions. This new chromophore shows a high degree of vibronic coupling and undergoes FRET to any **BPJ2** in the silica, making this type of material a promising candidate for panchromatic light-harvesting antennae based on an energy cascade. **BS** was hypothesised to be the result of either H-aggregates brought on by π -stacking of at least 2 **BPJ2** molecules or a chemical reaction that could have taken place either prior to silica formation or actually *in silico* post-synthetically.¹

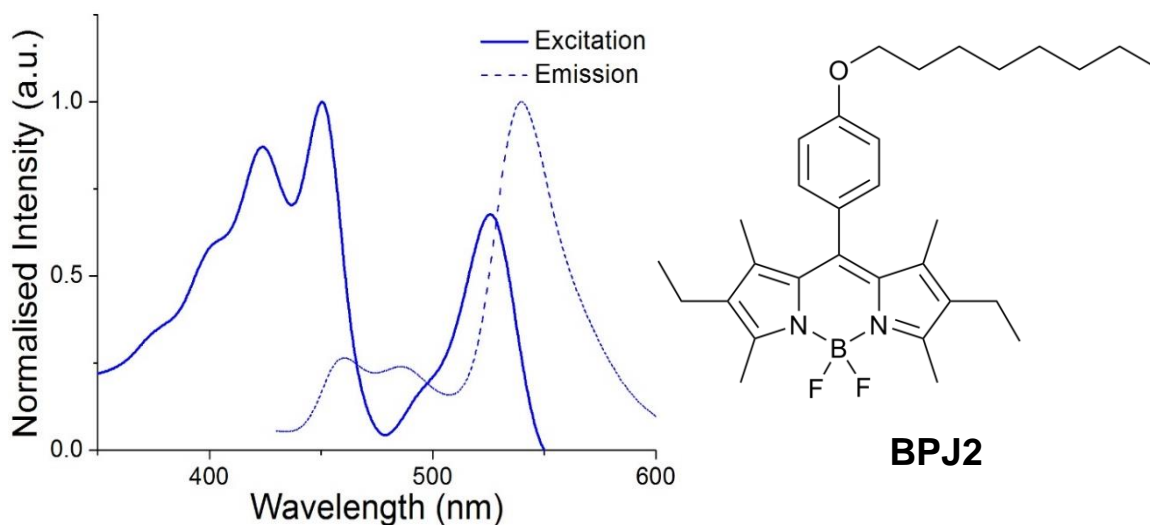


Figure 1: (left) The photoluminescence excitation and emission spectra of 10% **BPJ2**/CTAB@MCM-41 showing bands associated with both **BPJ2** (right) and a new species formed as a result of the silica synthesis dubbed **BS**.

This chapter will be dedicated to finding the synthetic step at which **BS** is formed in order to be able to tune its proportions within an antenna. As it is unknown which stage of the silica synthesis causes this, every step will be investigated (See figure 2). While BODIPY dyes have been well-known for their chemical stability, the conditions of MCM-41 synthesis, being at elevated temperature and high pH,² could cause **BPJ2** to degrade resulting in a new species.

Alternatively, self-assembly of dyes including BODIPYs has been shown to commonly induce H-aggregation resulting in a hypsochromic shift of photoluminescence bands.³⁻⁵ Also time-resolved small angle X-ray scattering (SAXS) studies performed by Babonneau *et al.* found that additives to the reaction mixture during silica formation can have unexpected effects on the morphology of the micellar template.⁶ This would cause a change in the environment around **BPJ2** molecules resulting in altered photophysical properties. The post-synthetic work-up, i.e. the drying of silica samples in an oven will be probed also.

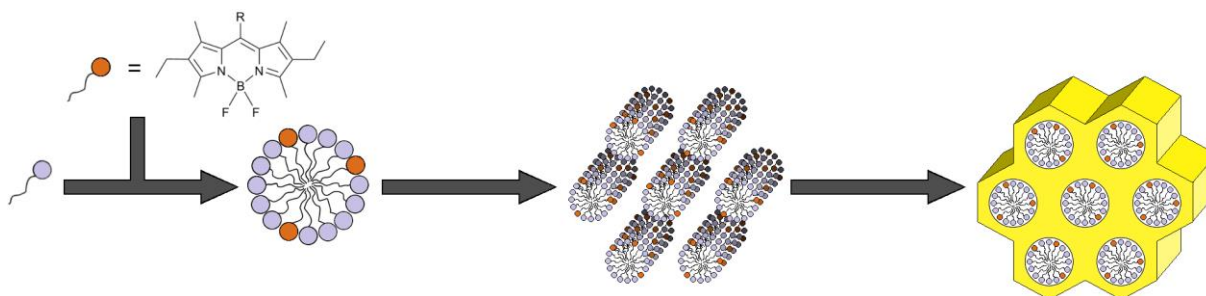


Figure 2: A scheme showing the synthesis of m-SiO₂ where the micelles are doped with BODIPY dyes.

Due to their chemical stability, photophysical properties and ease of synthesis, BODIPY dyes are commonly used as fluorescent probes for various biotechnological applications. Here, they are typically anchored to proteins, DNA and other such structures which can induce subtle effects on their fluorescent properties from which information about their immediate environment can be deduced.^{7, 8} The same principle will be applied in this chapter whereby steady-state photoluminescence spectroscopy will be used with **BPJ2** conveniently acting as a fluorescent probe to monitor the formation dynamics of both the micellar template and the silica scaffold. Through these studies the possible nature of **BS**, as well as the mechanism of its formation, will be investigated

4.2 The Base Test

As MCM-41 synthesis takes place at a pH of 12.17 and temperature of 80 °C, the first thought as to the formation of **BS** was that it had formed by degradation of **BPJ2** as a result of these harsh reaction conditions. To probe the stability of **BPJ2** under such conditions, the base test was devised in which the dye is exposed to the full force of the heating and pH without the micelles and silica for protection. **BPJ2** was dissolved in a minimum amount of acetonitrile (MeCN) before being added to water at the concentration used the synthesis of 1% **BPJ2**/CTAB@MCM-41. The pH was then raised to 12.17 using NaOH and the mixture

was heated at 80 °C for 2 h. As shown in Figure 3, new bands appeared as a result of this treatment around 560 and 610 nm.¹

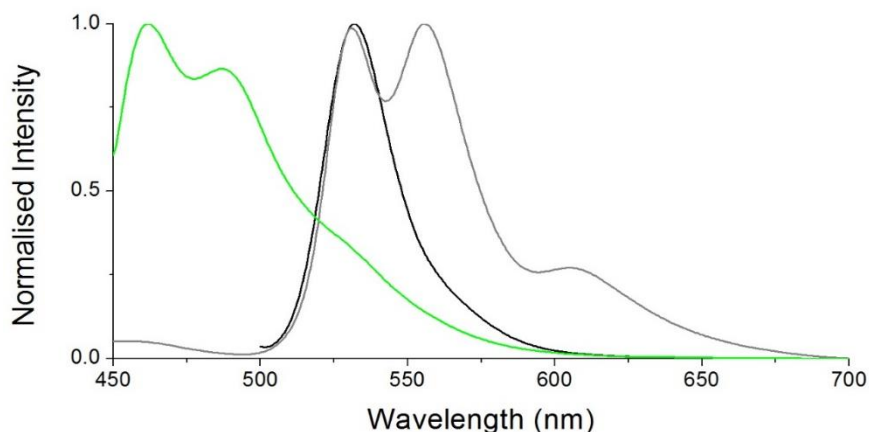


Figure 3: Emission spectrum of pure **BPJ2** in MeCN (black, $\lambda(\text{exc}) = 490 \text{ nm}$), 1% **BPJ2/CTAB@MCM-41** (green, $\lambda(\text{exc}) = 430 \text{ nm}$) and the base test (grey, $\lambda(\text{exc}) = 360 \text{ nm}$).

As BODIPYs (and dipyrromethene complexes in general) attract a large amount of interest from the academic community, there has been extensive investigation into their stability under a wide variety of conditions including acidic and basic environments.⁹ Figure 4 shows the curly arrow mechanism by which BODIPY degrades in the presence of hydroxide ions. Here, hydroxide attacks the boron centre eventually resulting in dissociation of the $-\text{BF}_2$ unit altogether leaving the anionic dipyrromethene behind which now emits light of differing energy compared to the original BODIPY resulting in a new peak in the emission spectrum.¹⁰ As this new peak is not present in any spectra obtained from silica samples, it can be said that, while **BPJ2** is unstable under these reaction conditions, the micellar template and/or initially-formed silica gel provides adequate protection as to prevent significant degradation. However, these peaks do not match those of **BS** meaning dye degradation in the initial portion of the synthesis is not the cause of the formation of this new species.

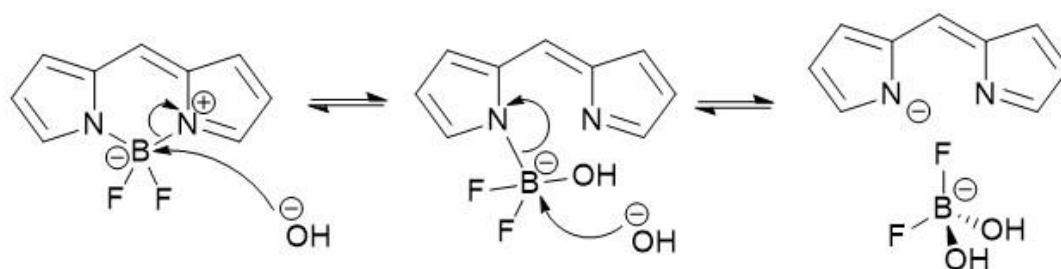


Figure 4: The curly-arrow mechanism for the degradation of BODIPY by hydroxide ions.¹⁰

4.3.1 Step-by-Step Investigation – Step 1) Micelle Formation

After a look into the overall synthetic conditions yielded no insight into that **BS** is, the next step was to investigate the individual steps in detail. This was done using photoluminescence emission spectroscopy periodically i.e. every 15 min for the first 2 h after reagent addition then every 30 min thereafter for 8h which was then finalised by a spectrum taken at 24 h. This test was designed to see how the emission evolved over time and how the effect of reagents effect both **BPJ2** photophysics and micelle structure. Firstly, **BPJ2** dissolved in a minimum amount of MeCN was added to a stirring solution of CTAB at 1% dye-loading and under ambient conditions. This was done as soon as possible as to mimic the practice used in the standard synthesis.

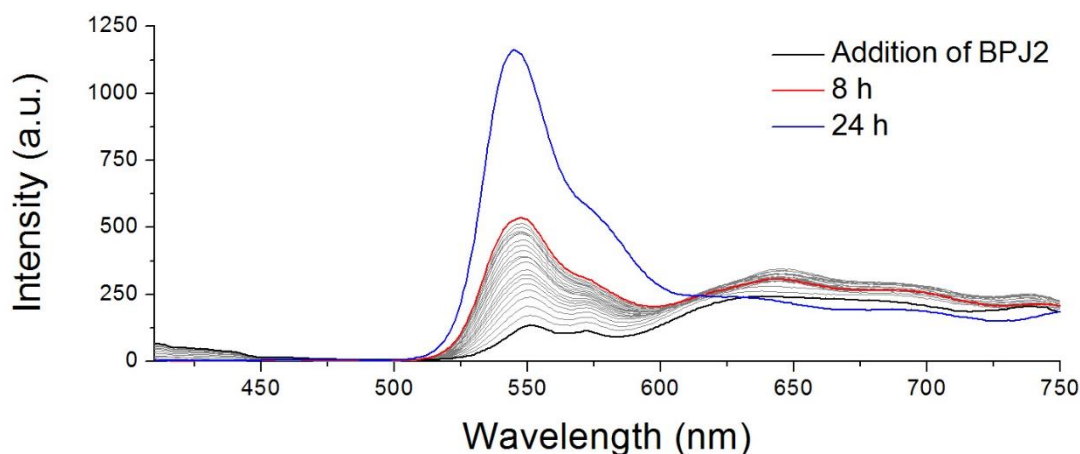


Figure 5: The first series of emission spectra of **BPJ2**-loaded CTAB micelles at 1% dye loading ($\lambda(\text{exc}) = 400 \text{ nm}$).

Figure 5 shows this first series of spectra with spectra taken at significant times coloured and labelled. The major feature of this trace is that the band at 550 nm increases in intensity significantly over the course of 24 h, changing from a small shoulder to the dominant part of the spectrum. This band corresponds to the fluorescence of **BPJ2** (radiative $S_1 \rightarrow S_0$ transition¹¹) with this increase in intensity over time being visible even by eye. This behaviour has been attributed to the dynamic nature of micelles in that an equilibrium is established between surfactant molecules bound to the micelle and moving free in solution with units exchanging between the two states all the time.^{12, 13} Initially, when **BPJ2** is added to the micellar solution it inserts as aggregates due to the dye having low solubility in water. As discussed in the previous chapter, in this form fluorescence of **BPJ2** monomers is quenched due to non-radiative pathways becoming available like self-quenching and thermal relaxation.¹ It is possible however that a dye can dissociate from the aggregate, and by

extension the micelle proper, into the surrounding solution just as a CTAB molecule can as seen in Figure 6.

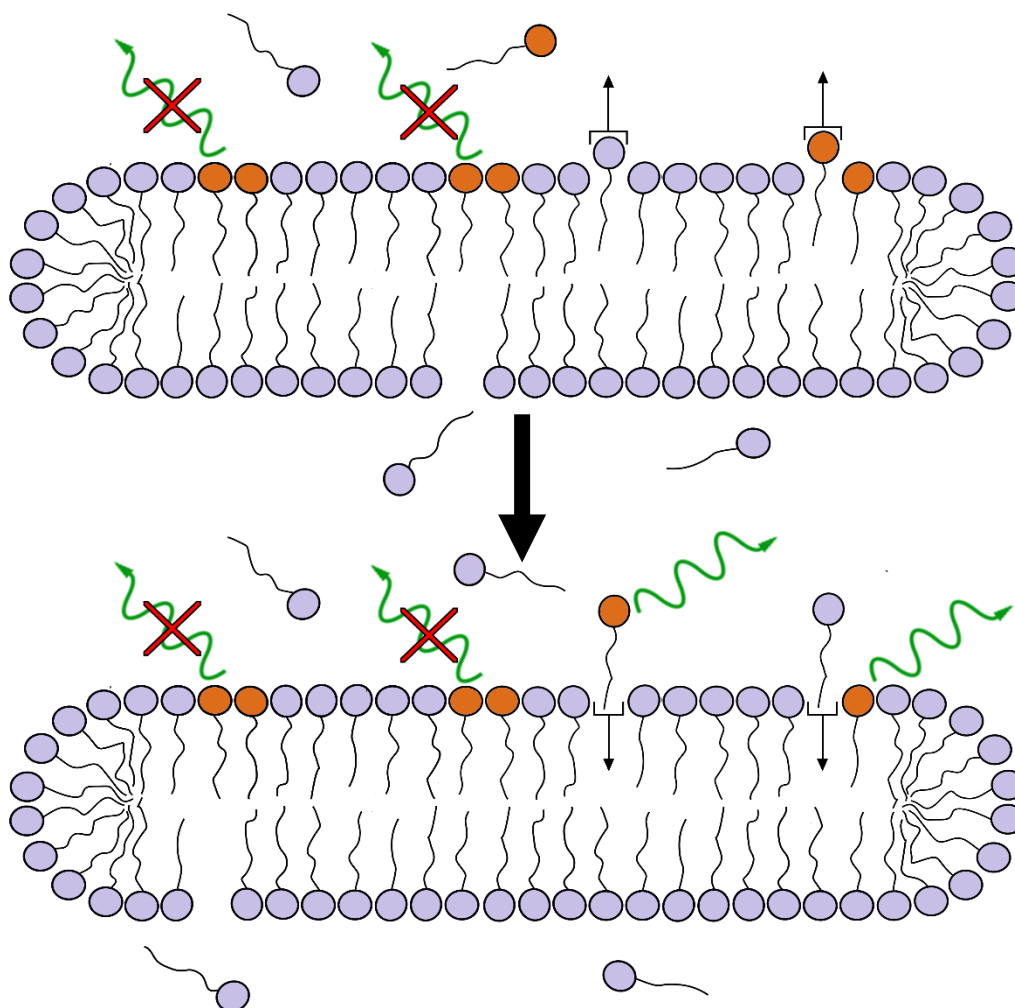


Figure 6: The schematic showing dissociation and distribution of **BPJ2** units within cylindrical micelles

This process is made available by the small amount of MeCN present in the solution. The free **BPJ2** can then re-insert somewhere else in the micelle (or into a different one altogether) where it is statistically unlikely to be within close proximity to another dye molecule. As this unit is now not part of an aggregate it is free to undergo radiative decay. This behaviour is similar to the dynamic behaviour exhibited by microemulsions of decane in weakly charged pentaethylene glycol dodecyl ether-based micelles observed by Schurtenberger *et al.* They found that as the overall charge of the micelle decreases, surfactant molecules were held more weakly by the micelle allowing easier exchange of free and bound monomers.¹²

Due to the relative insolubility of **BPJ2** in the surrounding medium, this process is relatively slow; indeed, stabilisation of pure CTAB micelles takes a matter of minutes with 2

h allowed in the typical MCM-41 synthesis to be sure of a stable mesophase.⁶ The increase in intensity shows a linear relationship with time exhibiting this trend up to 24 h after initial addition of **BPJ2**. This certainly means that uniform distribution of the dyes in the micellar template cannot be achieved even after a full day of stirring. It may also lend credence to the fact that experimental error in the stirring time may affect how established the micellar structure is, especially at higher dye-loadings, which can result in more- or less-ordered silica (see Ch. 3 Figure 16).

There are also some other features in this series of spectra that can give insight into the micelle formation process. Firstly, there are some bands of very low intensity below 450 nm which decrease over time and eventually disappear altogether within the first 2 hours. A spectrum taken before the addition of **BPJ2** (not shown) shows that these bands are present when only CTAB is present in solution. They have been attributed therefore to the scattering of the excitation light by CTAB flocculates. As time goes by, these break up and the CTAB molecules dissolve and form micelles and therefore no longer scatter the excitation light.¹⁵ Secondly, there are some broad bands observed from 600 to at least 750 nm that remain at constant intensity throughout the experiment. These have been attributed to J-aggregates (see section 3.2.2) formed through intermicellar interaction.^{16,17} Seeing as no bands can be seen where **BS** emits, the conclusion is that it does not form as during the initial micellar phase and so the next steps of the synthesis were also investigated.

4.3.2 Step 2) Addition of NaOH

The next step was to investigate how the addition of the base used to catalyse the polycondensation of the silicate precursor affects the photophysics as well as the structure of the dye-loaded micelles. With this in mind, the **BPJ2**/CTAB solution used in the previous section was raised to a pH of 12.17 through addition of NaOH. Shown in Figure 7 is the series of spectra taken for this experiment using the same system of timing as the previous experiment.

The peak ascribed to **BPJ2** emission remains largely unchanged throughout the time period where, over the first 8 h, the intensity gradually decreases slightly. Due to the nature of these micelles, there would be a small but statistically significant number of dye molecules not bound in a micelles and as such moving freely in solution. Upon addition of NaOH, these dyes will undergo base-induced degradation as shown in Figure 4.¹⁰ However, after 24 h, the intensity of this peak has once again risen. As was established in the last experiment, the uniform distribution of the dyes throughout the micelle is not achieved at least in the first 24

h. As such, it is possible that this distribution is still taking place well into the second day of stirring so once all dyes free in solution have been degraded, the intensity continues to rise as normal. Also, as shown in Figure 3, exposure of **BPJ2** to NaOH caused degradation of the chromophore presenting in the spectrum as new emission bands which are not present in Figure 7. This means that the micelles are providing adequate protection from the basic environment in these timescales. This is why micelles have found use as nanocarriers for drug-delivery, protecting sensitive and hydrophobic molecules from being metabolised in the body.

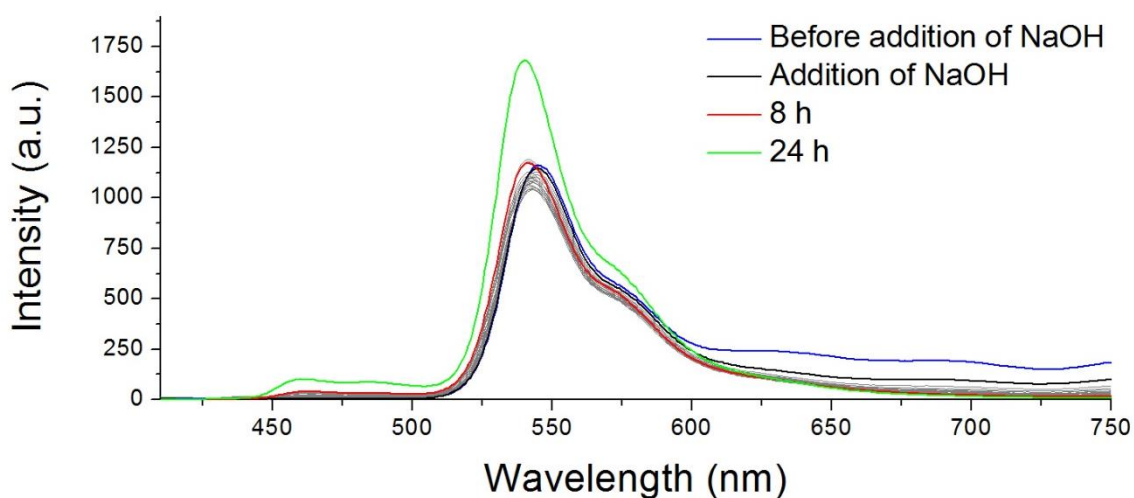


Figure 7: The second series of emission spectra of **BPJ2**-loaded CTAB micelles at 1% dye loading at pH = 12.17 ($\lambda(\text{exc}) = 400 \text{ nm}$).

Once again, there are other features in this series that warrant explanation. Firstly, the effect of NaOH on the low-energy intermicellar bands is noticeable immediately with a rapid decrease in these bands observed. This is most likely due to intercalation of Na^+ and OH^- ions into the gaps between the micelles in the hexagonal array similar to results seen by Yang *et al.* who used ultramicroelectrode voltammetry to investigate intermicellar interactions in aqueous NaCl solutions.¹⁹ Through insertion of ions into the interstitial space in the hexagonal array, these interactions are disrupted thus disallowing J-aggregation manifesting in the spectra as the low-energy bands losing intensity. The second feature is the growth of small vibronically-coupled bands between 450-500 nm corresponding to **BS**. However, the intensity of the bands is minimal, particularly when compared to the intensity of the emission from **BPJ2** monomers. While this bands may be caused by **BS**, they do not dominate the spectrum as seen in the spectrum of 1% **BPJ2**/CTAB@MCM-41 and as such more insight was needed.

4.3.3 Step 3) Addition of TEOS

The last step in this investigation is the addition of the silicate source, TEOS. The initial formation of the silica gel is very fast in the standard synthesis due to the elevated temperature. Even in this experiment, performed at room temperature, the effect of the addition of TEOS on the spectrum is pronounced.

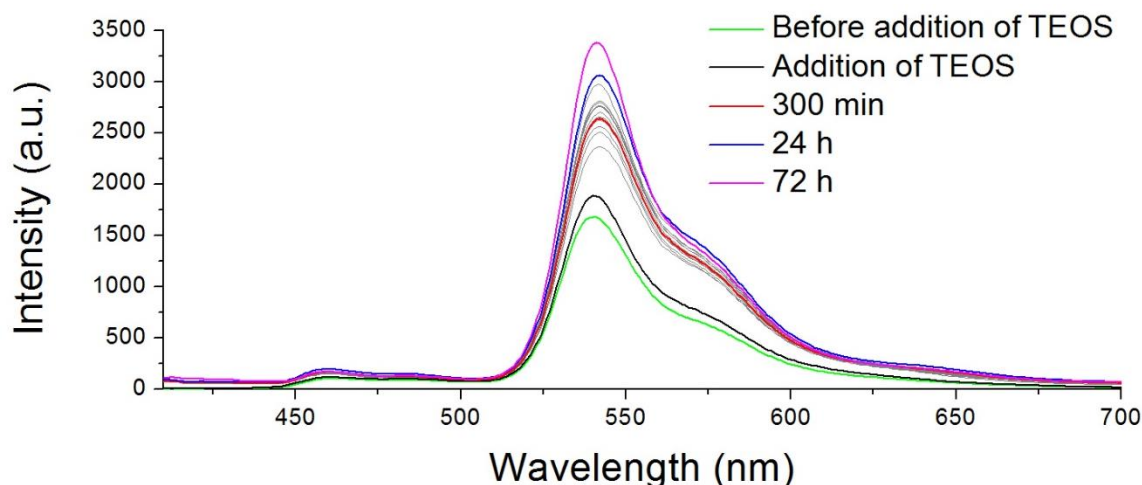


Figure 8: The third series of emission spectra of **BPJ2**-loaded CTAB micelles at 1% dye loading at pH = 12.17 after addition of TEOS ($\lambda(\text{exc}) = 400 \text{ nm}$).

As shown in Figure 8, across the entire spectrum the intensity increases with no change in the relative heights of any peaks. It is also visible by eye that a gel is formed almost immediately after addition. It is this gel that causes the enhancement in the emission intensity via a well-documented mechanism relating fluorescence quantum yield to the viscosity of the sample.²⁰⁻²² In the formation of the gel, the medium around the micelles, and by extension the dye, becomes relatively much more rigid. Due to this, any vibrational motion is dampened meaning thermal deactivation processes become less pronounced leading to an increase in emission intensity across the spectrum.

After the initial enhancement, the emission profile stays broadly stable for up to 72 h. Minor fluctuation in the peak intensity are to be expected once a colloidal sample such as this has formed. The high energy bands are present and enhanced by the formation of the gel but still do not exhibit the relative intensity seen in the fluorescence spectra of 1% **BPJ2**/CTAB@MCM-41. While these experiments give useful insights into how **BPJ2** behaves in the micellar template, they do not explain how **BS** comes to dominate the emission spectra of the silica samples, thus the post synthetic work-up is the next step to investigate.

4.3.4 Step 4) Post-Synthetic Drying

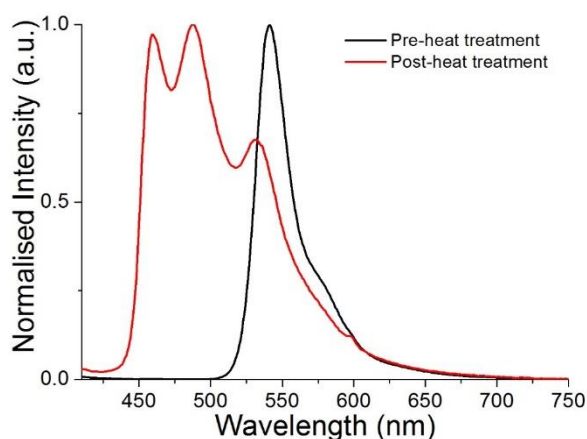


Figure 9: The fluorescence emission spectra ($\lambda(\text{exc}) = 400 \text{ nm}$) of 1% **BPJ2/CTAB@MCM-41** after drying in a vacuum desiccator (black) and after being heated (red).

Once the 2 h reflux is finished, the resulting precipitate is filtered, washed with water and dried in an oven at 85 °C overnight. It is this final drying step which was the last part of the synthesis that was to be probed. In order to achieve this, a sample of 1% **BPJ2/CTAB@MCM-41** was dried in a vacuum desiccator to ensure no heat was supplied to the silica during the drying process. An emission spectrum of a suspension made from this sample was then

taken. The dried sample was then heated in an oven at 85 °C for 16 h after which another emission spectrum was taken. Figure 9 shows the two spectra taken from this experiment and it is clear to see that it was this step that causes the formation of **BS**. The spectrum from the sample dried in the desiccator shows the standard slightly vibronically-coupled emission band around 550 nm expected from a BODIPY dye. After heating, this peak has decreased in intensity giving way to two larger high-energy peaks exhibiting a high degree of vibronic coupling that are distinctive of **BS**. In order to gain more insight into how this in silico conversion from **BPJ2** to **BS** takes place, another long term experiment was devised.

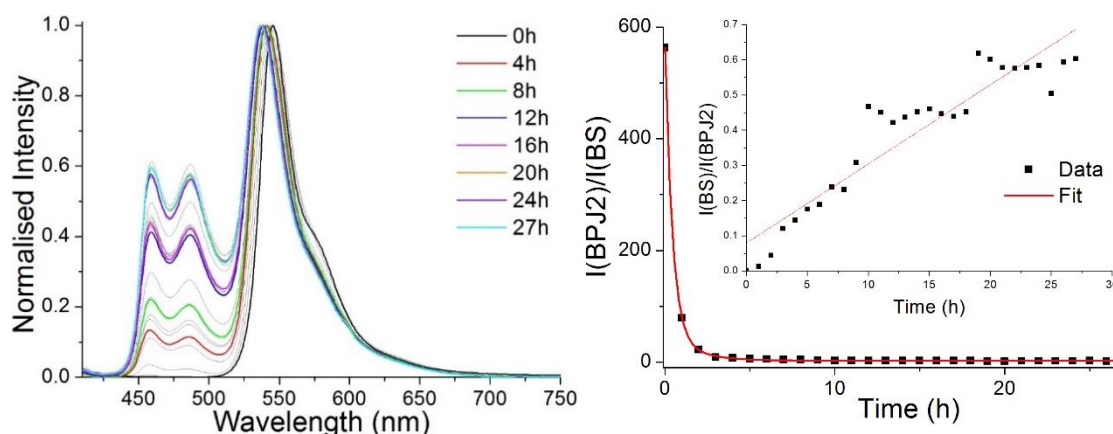


Figure 10: (left) The series of emission spectra ($\lambda(\text{exc}) = 400 \text{ nm}$) taken from the 1% **BPJ2/CTAB@MCM-41** samples removed periodically from the oven. (right) The plot and kinetic fitting of the **BPJ2/BS** intensity ratio against time. (inset) The plot of $I(\text{BS})/I(\text{BPJ2})$ ($1/\{I(\text{BPJ2})/I(\text{BS})\}$) against time.

Using desiccated silica, small samples of 1% **BPJ2**/CTAB@MCM-41 were placed in the oven and heated at 85 °C. Every hour for 27 h, a sample was removed from the oven from which a 1 g.mL⁻¹ suspension was made in order to produce a kinetic trace of the conversion. From these suspensions, emission spectra were taken resulting in the series shown in Figure 10. From this it is clear to see the rising of the intensity of the bands attributed to **BS** over time. In order to measure the kinetics of this process, the ratio between the max intensities corresponding to the **BPJ2** and **BS** bands were calculated. These ratios were then plotted against time resulting on the plot also seen in Figure 10. When fitted, this ratio exhibits biexponential decay resulting in two time constants of 25.8 and 99.9 min. Plotting $1/\{I(\mathbf{BPJ2})/I(\mathbf{BS})\}$ (i.e. $I(\mathbf{BS})/I(\mathbf{BPJ2})$) against time (Figure 10, inset) results in a linear relationship, suggesting the formation of **BS** is a second order process.²³

From here, these results can be interpreted differently depending on which **BS** formation hypothesis is followed. In the H-aggregation case, the elevated temperature allows **BPJ2** units to undergo small vibrations and rotations so that nearby monomers can orientate themselves relative to each other in order to facilitate the slip angle required in the formation of H-aggregates.⁴ From the inset in Figure 10, the formation of **BS** is found to be a second order process. As aggregation behaviour depends on two molecules coming together the rate equation (4.1) for the formation of an H-aggregate is given by:

$$rate = k[\mathbf{BPJ2}]^2 \quad (4.1)$$

where k is the rate constant of the aggregation.

In the case of an in-silico reaction, it is possible that an impurity was introduced at some point during the synthesis. At room temperature, this impurity remains unreacted in the samples. However, raising the temperature could take **BPJ2** and whatever other reagent above the activation energy needed for the conversion to **BS**. This means that the rate determining step here is likely to involve one molecule of **BPJ2** and another of an impurity (I) resulting in this alternative rate equation (4.2):

$$rate = k[\mathbf{BPJ2}][I] \quad (4.2)$$

Recent EDX studies undertaken by members of this research group found that the NaOH used throughout the course of these studies contained up to 20% magnesium silicate (MgSiO₄) which has been shown to directly affect the formation of certain silica samples made with gold nanoparticles (See Appendix Figures A11 and A12). This is particularly interesting as the first instance of **BS** formation is seen in Figure 7 upon addition of the NaOH.

Alternatively, silanol groups on the inside of the m-SiO₂ have been shown to form hydrogen bonds with BODIPY cores in previous studies by other groups.¹⁰ Through these it is possible that the acidic nature of these silanol groups could have caused degradation of **BPJ2** forming **BS**.

4.4 Inverse Relationship Between %BPJ2 and Amount of BS

From Figure 17 and 19 in Chapter 3, it is clear to see the inversely proportional relationship between dye-loading and the relative amount of **BS** in the silica. From some of the findings in this chapter, it is possible to expand on the hypotheses given as to what **BS** is i.e. either H-aggregation or the product of a formal chemical reaction that takes place at some point during the synthesis. While it is now known that raising the silica samples to elevated temperatures caused the formation of **BS**, there are different ways to interpret this finding depending on the initial hypotheses about the nature of **BS**. As such, both avenues will be presented here as further experimentation would be needed for confirmation.

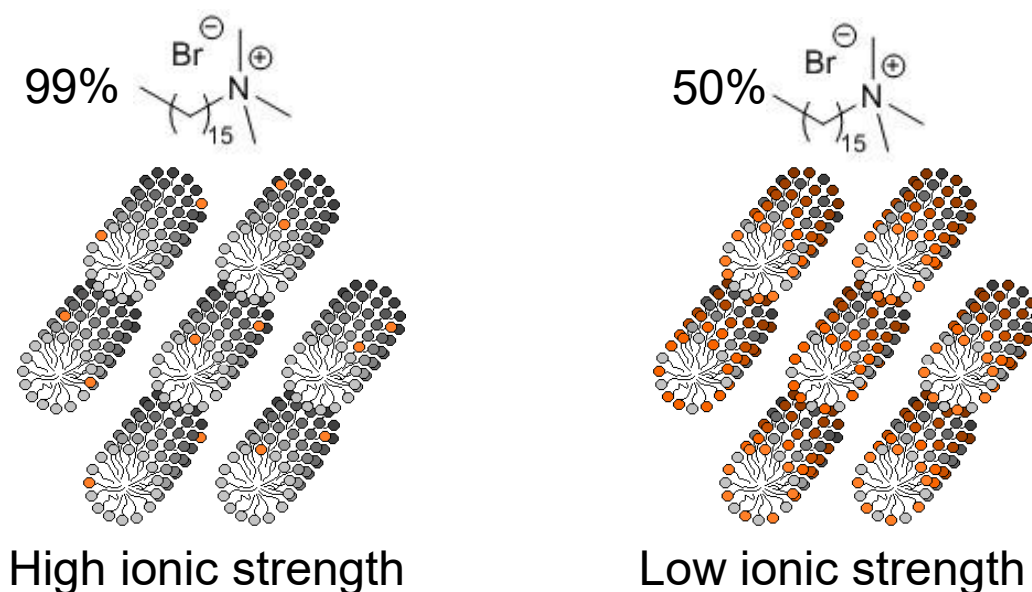


Figure 11: A qualitative comparison of the internal ionic strength in different **BPJ2**-doped CTAB micelles encapsulated within m-SiO₂.

H-aggregation: This hypothesis hinges on the idea that the strength of the interaction between two **BPJ2** monomers in an aggregate is dependent on the polarity of the surrounding medium. At low dye-loading, e.g. 1%, the template within the m-SiO₂ is primarily made up of CTA⁺ units surrounded by bromide ions. As such, the environment in which the **BPJ2** molecules sit in the pores is of relatively high ionic strength. So, at elevated temperatures when the positions of surfactants are allowed to shift slightly, the **BPJ2** units move through

this highly polar medium until they meet another **BPJ2** molecule. Here, as the monomers are relatively hydrophobic they hold together tightly. This means that H-aggregates are formed easily in the 1% **BPJ2**/CTAB@MCM-41 sample. This can be seen Figure 7 where upon addition of NaOH, bands possibly attributed to **BS** are observed rising in intensity over time. This is due to the sudden increase in the ionic strength of the surrounding medium causing the formation of H-aggregates.

At 50% dye-loading, the micelles are much more uniform and will have a much lower internal ionic strength relative to the lower dye loadings. As such, when the dyes become mobile due to elevated temperature, while it is statistically more likely that they will meet another monomer, the interaction between them will be much lower than in samples at lower dye loadings. This means H-aggregates are much less likely to form and if they do, they can easily dissociate resulting in only monomeric emission being observed (see Figure 3). Assuming the 1% and 50% are the extreme cases of the sample series, the other samples would exhibit this behaviour to an extent that leads to the inverse relationship between dye loading and proportion of **BS** exhibited by these materials.

In silico reaction: Alternatively, the explanation for this inverse relationship using the chemical reaction theory is based on the presence of impurities with which **BPJ2** units can react. We can see from the spectra of these materials that the amount of **BPJ2**, which is added in crystalline form (see Appendix, Figure A10), in the micelles does not affect the amount of **BS** formed. Here, it is thought that the amount of impurity in the silica samples is constant and is the limiting reagent in a reaction with **BPJ2**. As the concentration of the impurity stays constant throughout the samples, at 1% dye loadings the majority of the **BPJ2** is converted into **BS**. At higher dye-loadings, the reaction becomes pseudo-first order with **BPJ2** being present in excess of the impurity so only a certain amount of the **BPJ2** degrades as the impurity is used up after which the **BPJ2** will remain unchanged resulting in the inverse relationship observed between dye loading and amount of **BS** formed.

As mentioned above, there are a number of candidates for that this impurity could be. NaOH is used in the same proportions in all samples, as it is used to catalyse the polycondensation of the silica. As such the amount of MgSiO_4 is constant throughout the samples. It cannot be ruled out also that the TEOS used, again in the same proportions for every reaction, could contain a reactive impurity. Also, as silanol groups are formed through incomplete condensation of TEOS, their number throughout the silica samples will be broadly constant in all samples. As such a reaction between these and **BPJ2** could result in the formation of **BS** and exhibit this inverse relationship.

4.5 Conclusion

While the extraction and ultimate identification of **BS** was unsuccessful, the studies presented in this chapter have given insight into the various processes involved in forming m-SiO₂ with dye loaded micellar templates. Long-term photoluminescence emission studies used to monitor micelle formation showed that in order to guarantee uniform distribution the **BPJ2**/CTAB solution needs to be stirred for at least 24 h. Further to this, the addition of NaOH and TEOS does possibly induce the formation of a small amount of **BS** but does not account for the proportions seen in the previous chapter. In the end, it was found that **BS** formed during the drying step in the oven via either in silico dye mobility or chemical reaction induced by the elevated temperatures experienced during this step.

Using this, a hypothesis involving the relative polarity of the dye loaded micelles was used to explain the inverse trend observed between dye loading and **BS** proportion under the assumption that is formed from H-aggregation of **BPJ2**. Alternatively, an impurity may have been introduced in the synthesis but only reacted with **BPJ2** upon a rise in temperature allowing the reactants to get above the activation barrier. It is thought that due to the fact that the proportion of **BS** decreases as dye loading increases, this impurity must be introduced with a reagent that is at constant concentration throughout the samples, so either NaOH, TEOS or silanol groups formed as a result of partial polycondensation of the silica. Further exploration of these processes as well as the time dependence on **BS** formation shown in Figure 10 could give more information that will allow greater control over the proportions of the different chromophores present in these systems. Through this, a finer degree of control can be used to tune the photophysical properties of BODIPY-doped m-SiO₂ antennae.

4.6 Experimental

Reaction of **BPJ2** with hot NaOH solution (the “base test”):

Cetyltrimethylammonium bromide (364 mg, 0.949 mmol) was dissolved in H₂O (100 mL) with the help of an ultrasonic bath. In parallel, **BPJ2** (4.88 mg, 9.6 μmol) was dissolved in a minimal amount of MeCN and transferred to the CTAB solution resulting in a turbid pink mixture. Sodium hydroxide (2 M, 1.3 mL, 2.6 mmol) was added and the mixture was heated at 80 °C under reflux for 2 h. Once cooled, an aliquot was removed for spectroscopic analysis.

Long term fluorescence studies of 1% **BPJ2**/CTAB@MCM-41:

Cetyltrimethylammonium bromide (40 mg, 0.405 mmol) was dissolved in H₂O (20 mL) with the help of an ultrasonic bath. Taken from a stock solution in MeCN, **BPJ2** (9.6 mM, 111 μL, 1.07 μmol) was added to the CTAB solution. Every 15 min for the first 2 h after reagent addition then every 30 min thereafter for 8h, 2 mL aliquots of this mixture were transferred to

a cuvette to run a fluorescence emission spectrum. The aliquots were then transferred back to the reaction flask once spectrum was finished. 24 h after the initial addition of **BPJ2**, sodium hydroxide (2 M, 144 μ L, 0.288 mmol) was added with fluorescence spectra taken in the same way as the first step. 24 h after the addition of NaOH, tetraethylorthosilicate (189 mg, 200 μ L, 0.911 mmol) was added and again fluorescence spectra were taken in the same way as above.

Synthesis of 1% **BPJ2/CTAB@MCM-41**:

Cetyltrimethylammonium bromide (364 mg, 0.949 mmol) was dissolved in H₂O (100 mL) with the help of an ultrasonic bath. Taken from a stock solution in MeCN, **BPJ2** (9.6 mM, 1 mL, 9.6 μ mol) was added to the CTAB solution. Sodium hydroxide (2 M, 1.3 mL, 2.6 mmol) was then added and the reaction mixture was heated to 80 °C. Tetraethyl-orthosilicate (1.7 g, 1.8 mL, 8.2 mmol) was then added and the mixture was heated at 80 °C under reflux for 2 h before being filtered and washed with H₂O. The filtrate was then dried in a vacuum desiccator resulting in a pink solid that fluoresced brightly under UV.

Measuring the kinetics of the in-silico conversion from **BPJ2** to **BS**:

Samples of **BPJ2/CTAB@MCM-41** (3 mg) were heated in an oven at 85 °C with a sample being removed every hour for 27 h. Once cooled, each sample was suspended in H₂O (3 mL) in preparation for fluorescence emission spectroscopy.

References

1. F. Cucinotta, B. P. Jarman, C. Caplan, S. J. Cooper, H. J. Riggs, J. Martinelli, K. Djanashvili, E. La Mazza and F. Puntoriero, *ChemPhotoChem*, 2018, **2**, 196-206.
2. C. Kresge, M. Leonowicz, W. Roth, J. Vartuli and J. Beck, *Nature*, 1992, **359**, 710-712.
3. N. K. Allampally, A. Florian, M. J. Mayoral, C. Rest, V. Stepanenko and G. Fernandez, *Chem. Eur. J.*, 2014, **20**, 10669-10678.
4. T. T. Vu, M. Dvorko, E. Y. Schmidt, J.-F. Audibert, P. Retailleau, B. A. Trofimov, R. B. Pansu, G. Clavier and R. Méallet-Renault, *J. Phys. Chem. C*, 2013, **117**, 5373-5385.
5. A. T. Haedler, K. Kreger, A. Isaac, B. Wittmann, M. Kivala, N. Hammer, J. Köhler, H.-W. Schmidt and R. Hidner, *Nature*, 2015, **523**, 196-200.
6. F. Michaux, N. Baccile, M. Imperor-Clerc, L. Malfatti, N. Folliet, C. Gervais, S. Manet, F. Meneau, J. S. Pedersen and F. Babonneau, *Langmuir*, 2012, **28**, 17477-17493.
7. L. Li, J. Han, B. Nguyen and K. Burgess, *J. Org. Chem.*, 2008, **73**, 1963-1970.
8. G. Fan, L. Yang and Z. Chen, *Front. Chem. Sci. Eng.*, 2014, **8**, 405-417.
9. L. Yang, R. Simionescu, A. Lough and H. Yan, *Dyes Pigments*, 2011, **91**, 264-267.
10. E. V. Rumyantsev, S. N. Alyoshin and Y. S. Marfin, *Inorg. Chim. Acta*, 2013, **408**, 181-185.
11. A. Loudet, K. Burgess, *Chem. Rev.*, 2007, **107**, 4891-4932
12. Y. Moroi, in *Micelles: Theoretical and Applied Aspects*, Plenum Press, New York City, New York, USA, 1992, 1st edn., ch. 1, pp 1-5.
13. I. W. Hamley, in *Introduction to Soft Matter: Synthetic and Biological Self-Assembling Materials*, Wiley, Hoboken, New Jersey, USA, 2007, 2nd edn., ch. 4, pp 180-211.
14. A. Evilevitch, V. Lobaskin, U. Olsson, P. Linse and P Schurtenberger, *Langmuir*, 2001, **17**, 1043-1053.
15. J. R. Lakowicz, in *Principles of Fluorescence Spectroscopy*, Springer, Berlin/Heidelberg, Germany, 3rd edition, 2006, ch. 2, pp. 27-54.
16. S. Choi, J. Bouffard and Y. Kim, *Chem. Sci.*, 2014, **5**, 751-755.
17. A. P. Doherty, P. A. Christensen and K. Scott, *Chem. Commun.*, 1996, 1531-1532.
18. E. Gravel, J. Ogier, T. Arnauld, N. Mackiewicz, F. Ducongé and E. Doris, *Chem. Eur. J.*, 2012, **18**, 400-408.
19. Z. Yang, Y. Lu, J. Zhao, Q. Gong, X. Yin and Z. Yang, *J. Phys. Chem. B*, 2004, **108**, 7523-7527.
20. S. Sharfy and K. A. Muszkat, *J. Am. Chem Soc.*, 1971, **93**, 4119-4125.
21. J. Rice, D. B. McDonald, L-K Ng, and N. C. Yang, *J. Chem. Phys.*, 1980, **73**, 4144-4146.
22. A. Vyšniauskas, M. Qurashi, N. Gallop, M. Balaz, H. L. Anderson and M. K. Kuimova, *Chem. Sci.*, 2015, **6**, 5773-5778.
23. Note: Here, I(**BS**) and I(**BPJ2**) are both variables that change throughout the reaction and photoluminescence intensity does not scale linearly with concentration so the intensity ratio used in the Figure 10(inset) acts as an approximation to the 1/[A] component of a second order rate law i.e. $1/[A] = 1/[A]_0 + kt$.

Chapter 5. Emission Tuning with Pt(II) Complexes in m-SiO₂ via Aggregation

5.1 Introduction

So far, this thesis has only been concerned with the loading of m-SiO₂ with BODIPY dyes in order to fabricate light harvesting antennae. Their ease of synthesis and distinctive photophysical properties made them ideal test compounds for these experiments.¹ However, mesoporous silica has been used for a number of applications including drug transport² and magnetic nanoparticles³ that rely on introduction of guests via diffusion through the pores and as such are susceptible to non-homogenous distribution thereof.⁴ So to widen the scope of the research presented in Chapters 3 and 4, different kinds of guests should be tested.

Another application common in photochemistry is the construction of organic light-emitting devices (OLEDs). Traditional LEDs, typically made using semiconductors, exhibit electroluminescence, phenomenon analogous to the photoluminescence seen throughout this thesis but in which a current or strong external electric field acts as the stimulus instead of light absorption.⁵ Here, an electron-hole pair (exciton) is generated when a current is passed through the material which then decays radiatively. OLEDs work in the same way but instead of the exciton being formed in the conduction and valence bands of an inorganic semiconductor, electrons and holes recombine in an organic semiconductive material forming excited singlet and triplet states which can then decay in the same way. The use of molecular units allows this technology to be manufactured on a very small scale hence their use in high resolution displays on mobile phones and television screens amongst others. In this case a single pixel will typically house three dyes capable of red, green and blue light emission corresponding to the light receptors in the human eye. Different variations in the intensity of these three dyes can result in any colour in the visible spectrum as well as white light.⁶

The first instance of an OLED in the literature was in 1987 when Tang and van Slyke presented the electroluminescent properties of a tris-aluminium quinolate (Al(q)₃) complex shown in Figure 1.⁷ While ground-breaking at the time, the molecule is fluorescent thus only emitting from the first excited singlet state (S₁) meaning that any triplet state decayed non-radiatively. This is particularly problematic as when the excitons are generated, they form as both singlets and triplets in a 1:3 ratio. This means that if a fluorescent OLED with no way of harvesting the triplet states is used, the efficiency of the system is capped at 25%. For this

reason, modern OLED research mostly centres around phosphorescent dyes instead. This way any excited triplet state (T_1) states formed decay radiatively and any S_1 states undergo intersystem crossing to T_1 meaning energy supplied by the electrical current is used much more efficiently (see Figure 1).^{8,9}

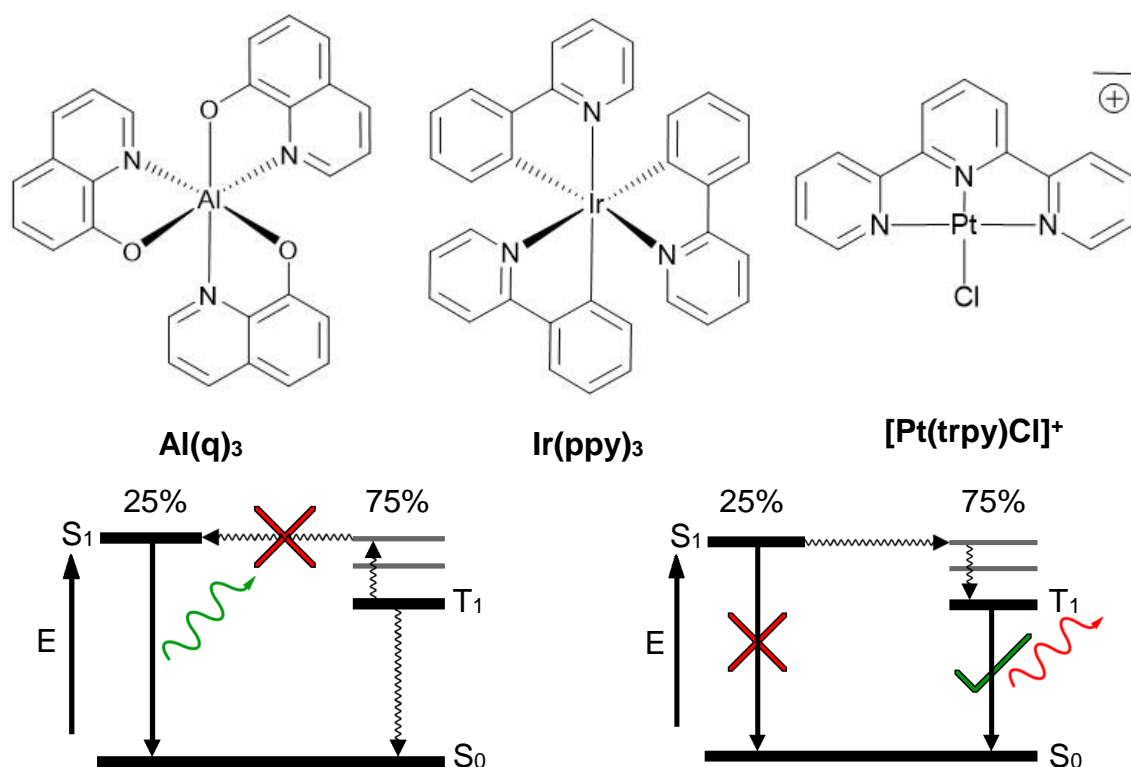


Figure 1: (top) The structures of OLED molecules commonly found in the literature. (bottom left) The Jablonski diagram showing the emission from a fluorescent OLED such as $Al(q)_3$.⁷ (bottom right) The Jablonski diagram for a phosphorescent OLED such as $Ir(ppy)_3$ ⁸ or $[Pt(trpy)Cl]^+$.⁹

Platinum(II) (as well as Ir(III)) complexes most commonly made with strong field bidentate aromatic ligands such as bipyridine (bipy) and 2-phenylpyridine (ppy) have attracted the most attention in the literature for this field.^{8,9} They have proven to be efficient triplet emitters due to the emissive ligand-centred (LC, $\pi \rightarrow \pi^*$) and charge transfer (CT) states lying much lower in energy than the metal-centred (MC, $d \rightarrow d$) state which decays non-radiatively.¹⁰ Much like BODIPY, as organic aromatic ligands are being used, it is possible to tune their photophysical properties through structural modification. While Ir(III) complexes adopt an octahedral geometry, Pt(II) compounds tend to be square planar which, while not necessarily detrimental, does mean that certain considerations need to be made.

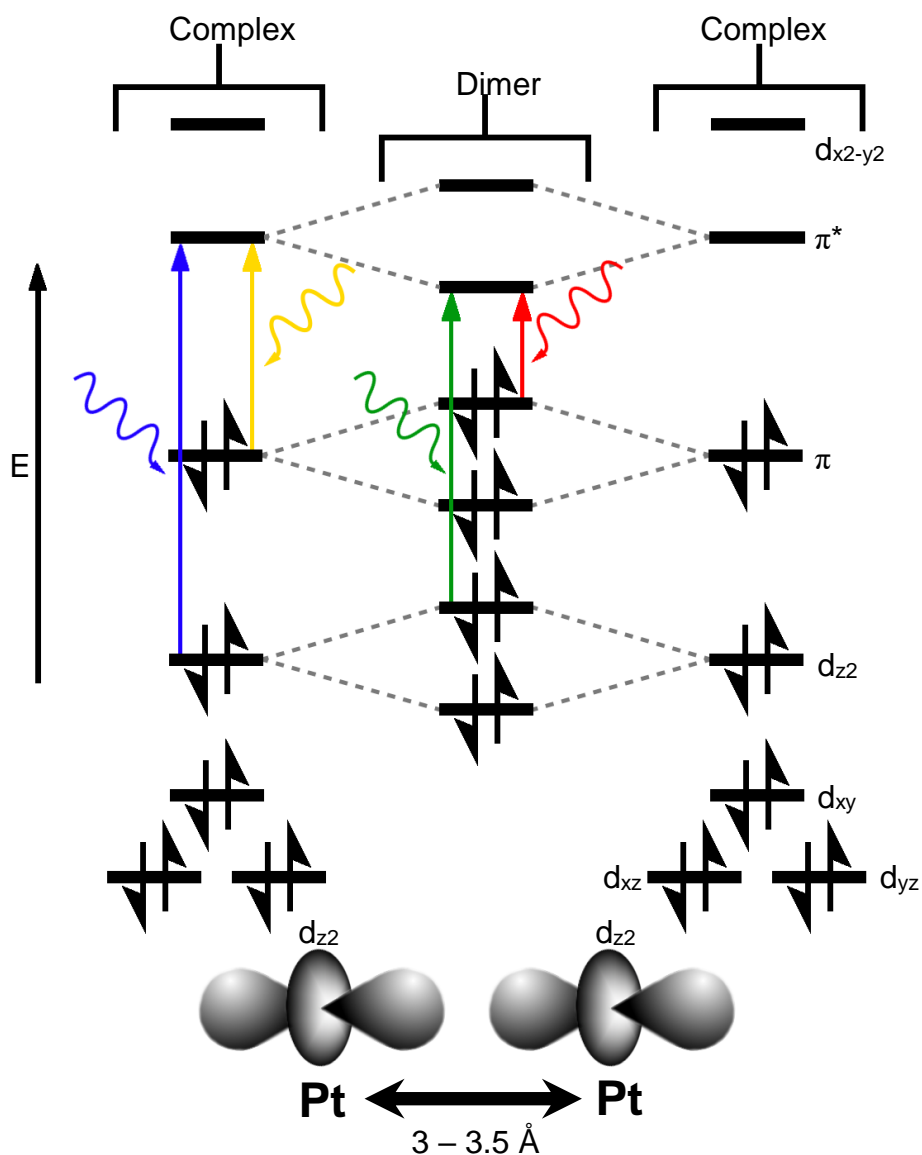


Figure 2: The electronic energy level diagram of two square planar Pt(II) complexes coming together to form a dimer resulting in a red shift of the absorption and emission. Note colours of arrows do not necessarily correspond to specific wavelengths of light but rather are used to highlight the red-shift induced upon aggregation.¹¹

Firstly, due to the planarity of these complexes, it is possible for them to stack upon one another forming aggregates. Pt(II) complexes like $[\text{Pt}(\text{trpy})\text{Cl}]^+$ (see Figure 1) tend to absorb in the UV/blue region in dilute solutions, represented by the yellow (LC) and blue (MLCT) transitional arrows in Figure 2 and emit in the green region (not shown). Upon deposition in a film however, the complexes stack causing an increase in the energy of the highest occupied d and π orbitals on the Pt centre and ligands respectively. This, along with a concerted decrease in the energy of the LUMO results in a red-shift in the absorption (Figure 2, red (LC) and green arrows (MLCT)). This also takes place with the emission profile with a new band

arising around 700 nm. This is due to a metallophilic interaction between the Pt(II) centres through overlap of d_{z^2} orbitals that is perpendicular to the plane of the ligands.¹¹

Of course, this means that the formation of such aggregates causes the depopulation of the green emissive state. However, this allows greater access to the visible spectrum for either light-harvesting or OLED displays with only one input dye. For the former, this would take place in the same way as **BS** and **BPJ2** as presented in Chapter 3 whereby **BS** forms as a result of **BPJ2** presence during the silica synthesis after which it can absorb blue light and pass on the exciton to **BPJ2** via FRET¹². For OLEDs, these complexes could be used as the green and red portions of pixels simply by using solid matrices of differing concentrations. This use of one input dye would be economically advantageous if this research were to be performed on an industrial scale.

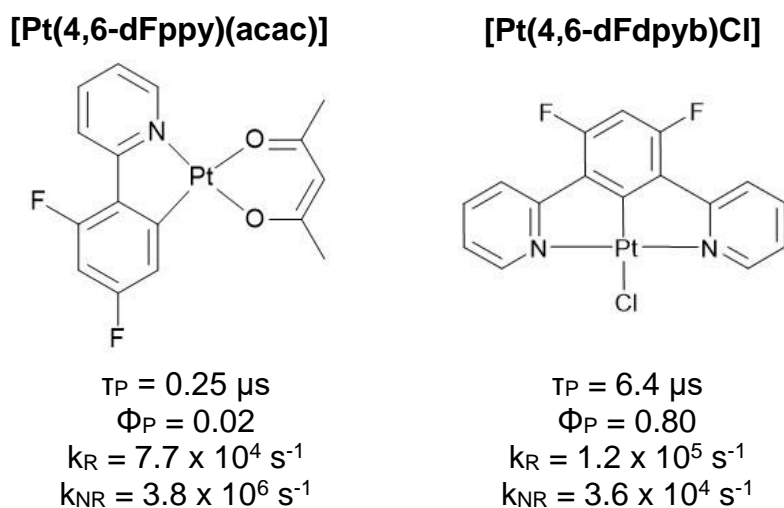


Figure 3: The structures and photophysical properties of two Pt(II) complexes in DCM as presented by Yersin *et al.*¹³

The second consideration with the square planar Pt(II) complexes is in regards to structural modification by substitution of ligands. For instance, if the classic bidentate bpy or ppy ligands are used, it is possible to complex the metal centre with two of these ligands. As the use of one chelating ligand increases the rigidity of the complex through the formation of the metallacycle, addition of another cyclometalating ligand would seem like a sensible step to increase the quantum efficiency of the molecule. However, as shown by Yersin *et al.*, a distortion is induced in the plane causing it to move towards a tetrahedral geometry in their Pt(4,6-dFppy)(acac) molecules. This distortion, induced by steric interactions between the two ligands, introduces another vibration degree of freedom into the complex through which non-radiative decay can occur rendering this kind of molecule largely non-emissive in solution (see Figure 3).¹³

The use of tridentate ligands, similar to that in Figure 1, has become popular now as these types of ligands lock the complex into the square planar geometry providing a highly rigid backbone reducing non-radiative decay. As a result, complexes synthesised with these ligands tend to be highly emissive (Figure 3)¹³. This is not to say that the auxiliary ligand does not play a role either, however seeing as in this study these are all chloro-groups, this effect will not be discussed. When used in Pt(II) complexes for OLED design, these ligands are usually derivatives of 2,6-diphenyl pyridine (C[^]N[^]C), 6-phenyl bipyridine (C[^]N[^]N), 1,3-dipyridyl benzene (N[^]C[^]N). Synthesised by the group of Dr Valery Kozhevnikov at Northumbria University and shown in Figure 4, the complexes **VNK-40-C12**, **TGV-19**, **NCN-60** and **N-129** take the forms of the latter two ligands.

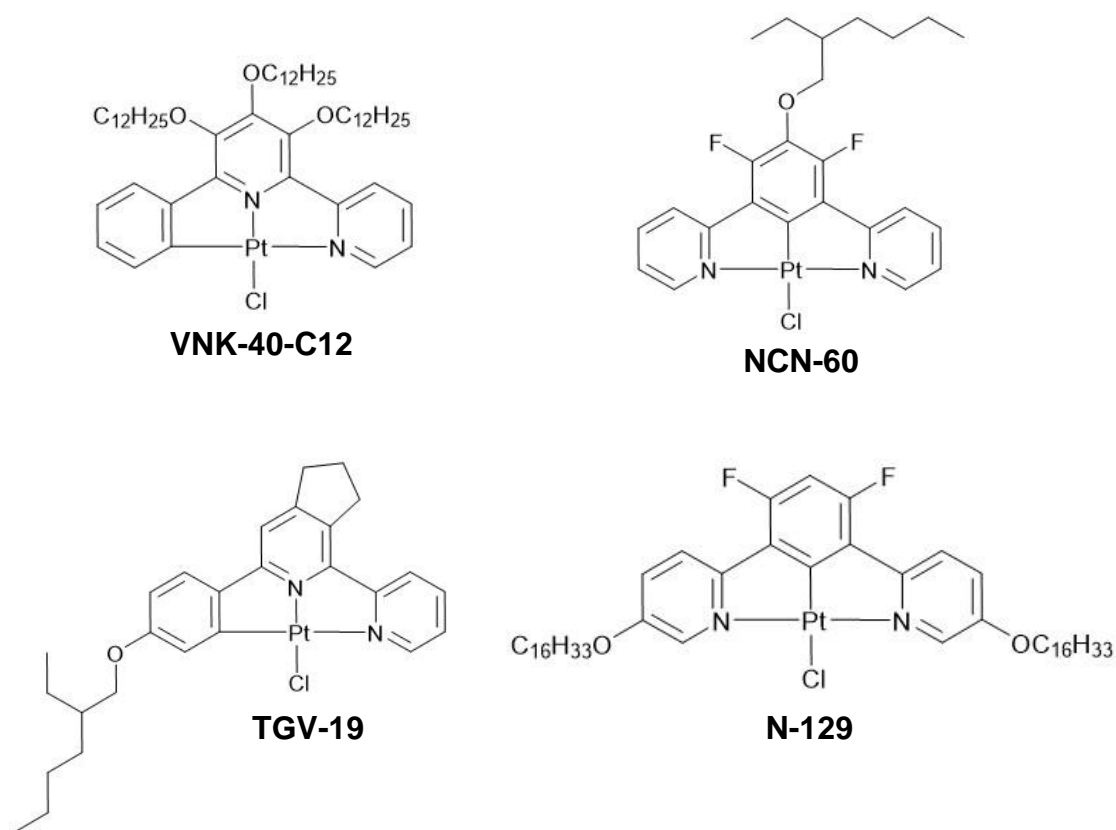


Figure 4: The four cyclometalated platinum(II) complexes used in this chapter.

Like **BPJ2**, these complexes all possess long alkyl moieties so that they can be incorporated into the CTAB-based micellar phase of MCM-41¹⁴ synthesis in order to achieve statistically homogeneous distribution throughout the material. Encapsulation in this way should benefit these systems in a number of ways. Firstly, as platinum is a precious metal, it is imperative that any dye made with it is durable enough to give the OLED a reasonable working lifetime. The silica scaffold should help to provide thermal, chemical and mechanical protection to these complexes.¹⁵ Secondly, it is thought that through insertion into the silica,

the aggregation via metallophilic interactions as shown in Figure 2 can be induced in the highly apolar region in the centre of the micellar template resulting in red-shifted emission. So, this will be performed at various dye-loadings (mol% compared to CTAB) to investigate whether this can be achieved without using excessive amounts of platinum. Additional benefits include increase of quantum yield via suppression of vibrational relaxation and containment of these potentially toxic complexes should a leak occur.

5.2.1 Micelle Formation and Morphology Changes

It is not always possible to synthesise an organic dye that is soluble in aqueous media, including those shown in Figure 4. This is due to the strong π -stacking between chromophores as a result of them typically comprising of extended conjugated and aromatic systems. Indeed, as shown in Chapter 3, acetonitrile (MeCN) was used as a co-solvent (approx. 1 % v/v) to dissolve the **BPJ2** dye molecule prior to its addition to the CTAB solution. This solvent was selected because it was miscible with water but still able to dissolve the **BPJ2**. The complexes shown in Figure 4 dissolve in tetrahydrofuran (THF) and acetonitrile (MeCN). Methanol (MeOH) and dimethylformamide (DMF) are also to be tested as these are miscible with water and as such could find use in future studies. However, as co-solvents can induce a change in the polarity of a medium, the structural integrity of the micellar template is at risk with their inclusion in the synthesis. As such, the first section of this chapter will investigate this with the intent of identifying an ideal co-solvent for the inclusion of the Pt(II) complexes into m-SiO₂. Further to this, these co-solvent studies will widen the scope of this research allowing the insertion of any number of guests within the field of photochemistry and beyond. Before the results are shown however, a brief introduction into the formation and morphology of micelles will be given.

First defined by J. W. McBain¹⁶ and expanded by G. S. Hartley¹⁷ in the early 20th century, micelles are aggregates of amphiphilic molecules known as surfactants. The structural requirements of such molecules are that they must have at least two portions that offer different intermolecular forces, most often possessing hydrophobic and hydrophilic moieties. Upon solvation in water, these surfactants aggregate in such a way as to have the hydrophobic groups pointing into the centre of the micelle and the hydrophilic groups pointing out toward the solvent in order to minimise potential energy forming a colloidal solution. This is a dynamic liquid crystal system or mesophase where individual surfactant molecules are exchanging between free and aggregated form.¹⁸ In the context of this thesis, two different surfactants need to be considered. First is hexadecyltrimethylammonium bromide

(cetyltrimethylammonium bromide, CTAB, Figure 5, left) which is the most common surfactant used for MCM-41 synthesis. The long alkyl chain is naturally hydrophobic while the ammonium bromide group solubilises this molecule in polar media due to its hydrophilic nature. The second example to be considered is a poly(ethylene glycol)-poly(propylene glycol)-poly(ethylene glycol) triblock co-polymer (PEO-PPO-PEO) commonly known as Pluronic P-123. The PPO portion of this non-ionic surfactant is hydrophobic and folds up inside the micelle to allow both hydrophilic PEO groups to point outwards.

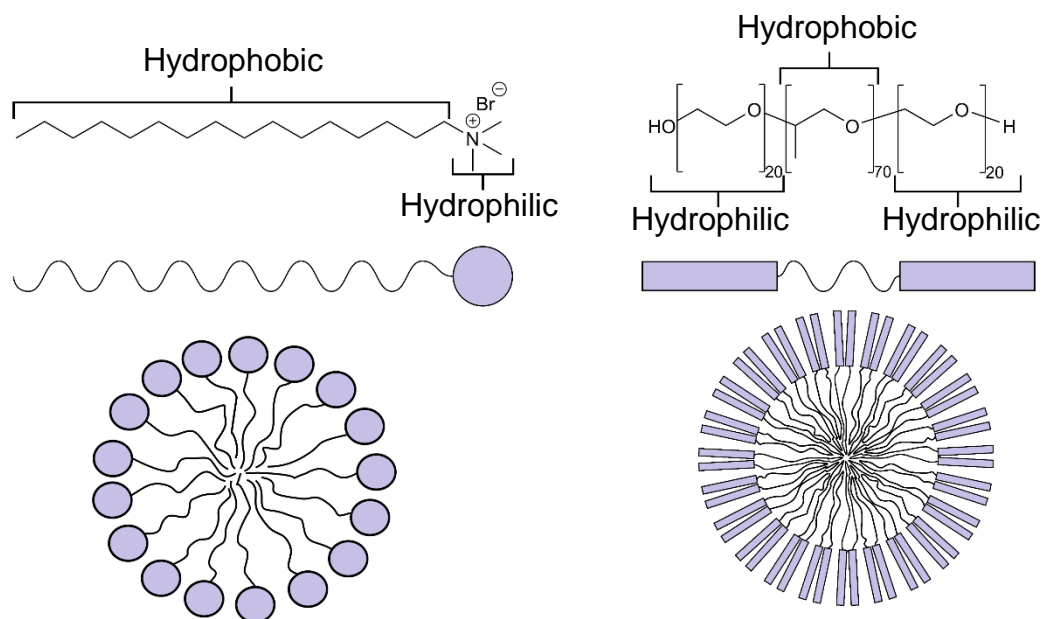


Figure 5: Chemical structures and spherical micelles schematics for CTAB and Pluronic-P123.

The morphology of these mesophases can be altered under certain stimuli,¹⁹⁻²¹ most commonly concentration of surfactant in the solution shown in Figure 6. Initially, at low concentrations, the surfactants occupy sites at the air-water interface with the hydrophilic head staying in solution and the tail pointing upwards as seen in Figure 6a). This works to minimise the potential energy by forming a hydrophobic environment above the solutions surface while still allowing the head groups to be solvated via hydrogen bonds with the water molecules. Once these sites become fully occupied, it is now possible for the surfactants to be entirely solubilised with an equilibrium is established between free molecules and those associated with the air-water interface.²²

Upon a further increase in concentration, the solution becomes saturated with monomeric surfactant units at which point spherical micelles begin to form. This is known as the first critical micelle concentration (cmc_1), typically specified as the point when the number of free

monomers is equal to the number of surfactants in micelles (for CTAB, $\text{cmc}_1 = 1 \text{ mM}$)²².

Here, solubilised head groups form an outer hydrophilic layer which encapsulates a core made from the tail groups associated via hydrophobic interactions. While small aggregates can occur, these micelles typically exhibit large numbers of surfactant monomers being typically made up of over 40 molecules.²³ These kinds of solutions have found many uses in research like micro-reactors and -emulsifiers as well as in everyday life in cleaning and the cosmetics industry.²⁴

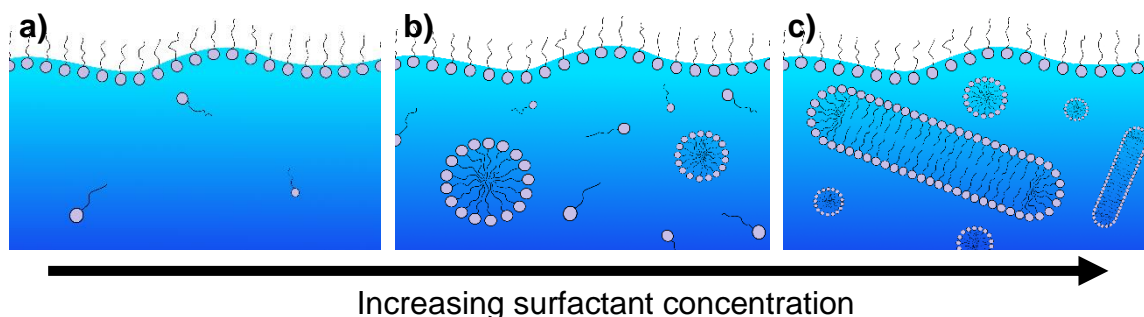


Figure 6: A diagram showing the effect of concentration on the self-assembly behaviour of CTAB where the concentration at **a)** $< \text{cmc}_1$, **b)** $\text{cmc}_1 < C < \text{cmc}_2$, and **c)** $> \text{cmc}_2$.

Eventually, the solution will be entirely comprised of these spheres which have a radius that is most energetically favourable due to the length of the hydrophobic portion. At this point, if spherical growth of these micelles were to take place as a result of increasing monomer concentration, a cavity would form in the centre which is highly unfavourable. As such, a change in morphology is induced to minimise the overall potential energy resulting in the sphere-to-rod transition which takes place above a second critical micelle concentration (cmc_2). At this point, instead of growing, the micelles split into two hemispheres down the middle and disks of surfactant monomers bridge the gap (see Figure 6c).²³

In fact, this is not a perfect depiction in that the radius of the hemispherical caps is larger than that of the cylindrical portion as seen in cryogenic transmission electron microscopy (cryo-TEM) studies of this morphology change²⁵ performed by Bates *et al.* Either way, “long” rod-like micelles exhibit well-defined hemisphere-cylinder-hemisphere regions. This deviation from the constant radius model does come into play when considering the relative stabilities of the different morphologies. Here, it is easier to relate the potential energy (strictly the chemical potential) of the surfactants molecules to the number of them in a particular aggregate, commonly referred to as the aggregation number, N . For reference therefore a fully solvated isolated monomer would have an aggregation number of 1 and, as

mentioned above, for spherical micelles $N > 40$. Also, as a surfactant molecule could be in several different microenvironments, particularly in a rod-like micelle (hemispherical cap, cylindrical portion etc.), potential values quoted in this kind of model are typically averages across the entire aggregate, commonly referred to as the packing energy.²³

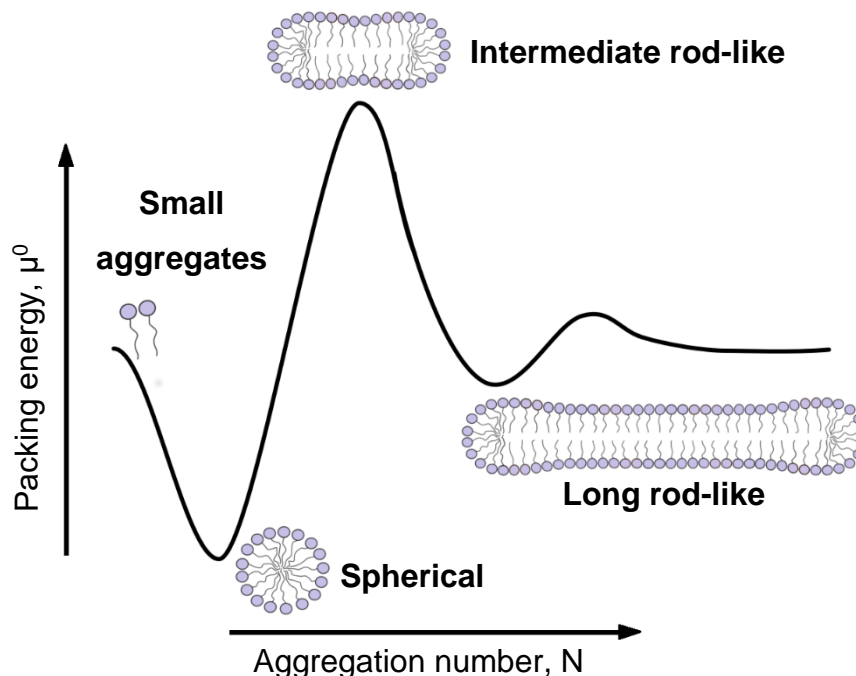


Figure 7: A plot showing the change in chemical potential as the number of surfactants in the aggregate increases with certain morphologies highlighted at points of particular interest.²³

Figure 7 plots how the packing energy changes as N increases showing a complex relationship between the two. Aggregates with a low N -value have a relatively high potential energy meaning that in solution, outside of the layer at the interface and micelles, the surfactant molecules tend to exist monomerically. The global minimum is then observed soon after, although its value can vary depending on the surfactant used. This trough is where spherical micelles exist with the aggregation number at the bottom referring to the most common aggregate observed above cmc_1 . The sphere-to-rod transition however sees a dramatic increase in the packing energy with intermediate rod-like micelles exhibiting the global maximum. This is due to the difference in radius between the hemispherical and cylindrical portions. Between these two, there is a transition region where the surfactants are contorted with particular strain put on the head group and methyl group at the end of the tail. Because these rods are relatively short, this transition region takes up all space between the two hemispheres meaning no surfactants are in a relatively stable cylindrical region.²³ This results in a very high packing energy and as such it is rare for these aggregates to occur in solution although they have been observed in the aforementioned cryo-TEM studies.²⁵

Increasing the aggregation number further sees a lowering of the packing energy as the morphology changes into the stable long rod-like micelles regime (relative to the intermediate rods). Here, as more monomers are added to the solution they add to the micelles by inserting extra disks into the cylindrical region. After a certain point, excluding slight local minima and maxima, micelles in this regime are of broadly similar packing energies regardless of aggregation number. However it is this longer cylindrical region that allows these micelles to be stable. There is now enough space between the hemispherical caps to allow the transition region to be longer resulting in a lower degree of strain between molecules in this region. This coupled with a higher proportion of the surfactants in the micelle being present in regions of low steric strain (hemisphere and cylinder regions) results in an overall lowering of the packing energy. Because of the much shallower trough in the packing energy, the concentration at which rod-like micelles become prominent (i.e. cmc_2) is much more difficult to determine and is typically quoted as an approximate figure (for CTAB, $cmc_2 \approx 3$ mM).²⁶

5.2.2 ¹H NMR Co-solvent Studies

As mentioned above, the addition of other chemicals into surfactant solutions can drastically affect how these morphology changes occur. As much of work described in this thesis is devoted to the incorporation of various dyes into the micellar template for m-SiO₂ synthesis, the use of organic co-solvents is common most notably with acetonitrile. However, it is possible that as research in this subject grows, a variety of co-solvents could be used for this incorporation, each of which could change the morphology of the template. By adding a non-aqueous solvent into a micellar solution, the environment surrounding the micelles may become more or less polar. This may make it easier for surfactant molecules to become wholly solvated thus shift the equilibrium between free and bound monomers. This could then result in a change in morphology or complete loss of self-assembly behaviour altogether rendering the whole process of dye distribution via micellar formation pointless. As such it is important to investigate how co-solvents affect the micellar template with no dye present in order to inform not only this thesis but future experiments as well.

It is possible to follow this morphology change with a variety of techniques such as dynamic light scattering (DLS), X-ray and neutron scattering, surface tension, conductivity and cryo-TEM to name but a few.²⁷ However, many of these techniques require equipment that is not standard in all research facilities. As such, NMR spectroscopy was used here to monitor the morphology of the surfactant solutions. Specifically, a Bruker 700 MHz NMR spectrometer was used for the following experiments but such pieces of equipment are not

uncommon. This technique can be used due to the contortion experienced by the monomers during micelle formation and the sphere-to-rod transition. By changing the morphology, the environment around a particular monomer changes drastically from highly stabilising spherical micelles to the destabilising strain seen in the transition regions of rod-like micelles.²⁸

As much of the work in this thesis revolves around the synthesis of MCM-41, CTAB was chosen as surfactant to use in these experiments. It is then important in these experiments to choose an appropriate diagnostic peak. Shown in Figure 8 are two environments; the methyl group at the end of the hexadecyl chain and the three methyl groups on the trimethyl ammonium group. These groups in particular will show the largest change in chemical shift as it is the head group and end of the tail that experience the greatest degree of steric strain throughout the morphology changes. Also of the two, the trimethyl ammonium environment is most likely to be more versatile as it is a rather unique environment (where dyes and solvents are concerned) and possesses a large number of protons making it a strong distinctive peak in most NMR spectra. This by no means diminishes the use of the environment at end of the tail group as it allows the use of two diagnostic handles rather than just one. However if these experiments were conducted with certain dyes used in this thesis such as **BPJ2**, which also has a long alkyl moiety, slight changes in chemical shift may be difficult to discern due to overlapping peaks.

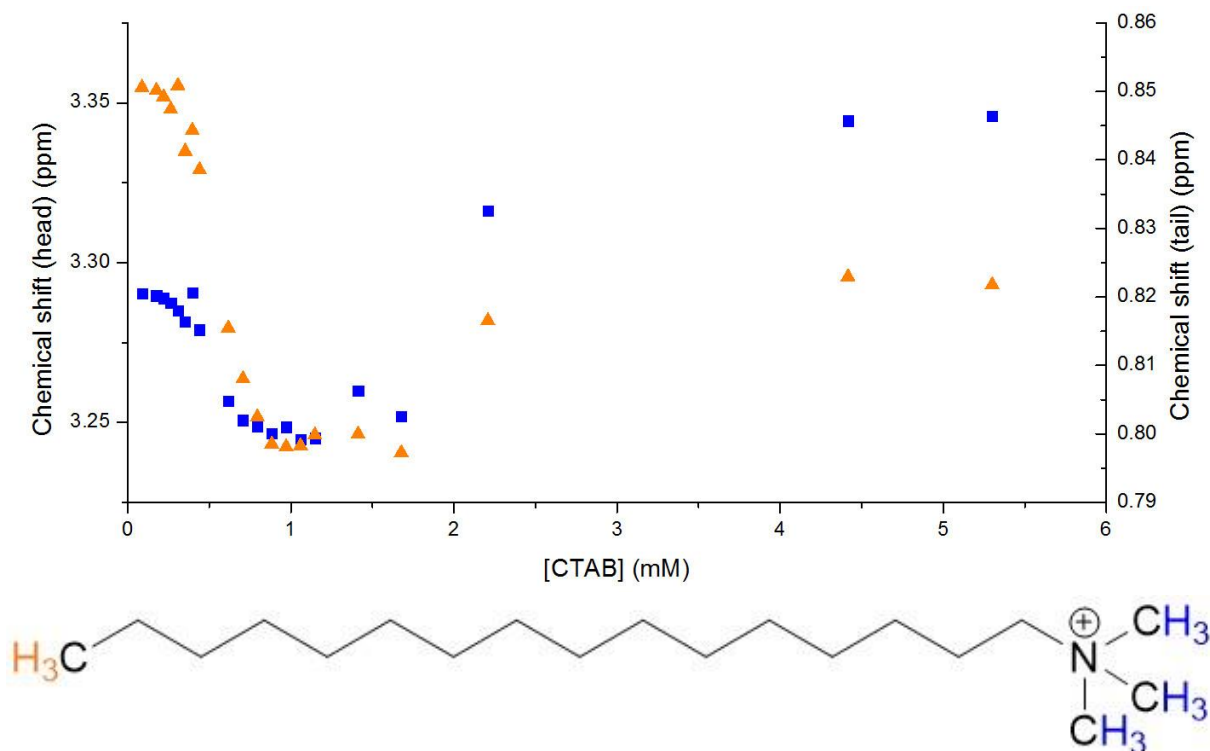


Figure 8: A plot of the change in chemical shift of diagnostic tail (orange) and head group (blue) protons in CTAB as concentration increases. All spectra were performed in D₂O.

Figure 8 also shows a plot of the chemical shift of the diagnostic environments over a wide range of concentrations which broadly follows the packing energy profile shown in Figure 3 with the exception of the peak in the intermediate rod-like region. At low concentrations, the chemical shifts for the head and tail groups are found at values expected for these groups isolated in solution (i.e. high dilution, standard NMR conditions). Above 0.2 mM, the chemical shifts begin to decrease drastically signalling a change in environment. As micelles are in dynamic equilibrium with free and bound monomers and NMR is a time averaged technique, these slight changes in chemical shifts seen here are indicative of the proportion of monomers in one environment over another. So when the decrease in chemical shift occurs, it is indicative of more monomers in the solution being associated into micelles until the trough at 1 mM which corresponds to cmc_1 .

From here, as concentration increases further so too does the average aggregation number. In the spectra, the chemical shifts begin to increase once more, again signalling a change in morphology. This is where the sphere-to-rod transition takes place for CTAB. It is worth noting here that instead of a uniform distribution of intermediate rod-like (single N value) micelles being formed, it is more likely that the solution still consists mainly of spherical micelles with the occasional long rod-like micelle (average of two N values). This is due to the peak in the packing energy in the intermediate region meaning that these rod-like micelles are inherently unstable. Therefore, once they are formed they must rapidly either grow into the long regime or shrink back to a sphere (increase or decrease in N respectively), analogous to a transition state in a chemical reaction. This also explains why no peak for this intermediate regime is observed in Figure 8. Unfortunately, this cannot be confirmed using this technique although analysis of the polydispersity using a technique such as DLS may suffice.²⁹

Somewhere between 2 and 3 mM the plot plateaus reflecting Figure 3 whereby surfactant concentration, and through which the aggregation number, has very little effect on the packing energy of the monomers. This corresponds to a lack of change in the environment as the rods become longer. It is worth noting that increasing the concentration may result in another morphology change, for example to a lamellar regime.³⁰ but this is outside of the scope of this project and as such will not be investigated. For the synthesis of MCM-41, the concentration of CTAB is 5.3 mM which is well beyond the threshold for the rod-like regime. Therefore, it is this concentration that will be used in the comparison between the effects of different co-solvents. As mentioned above, the effect of THF, MeCN, MeOH and DMF on the micellar

structure will be investigated as these co-solvents dissolve the Pt(II) complexes well and/or are miscible with water.

The results for this study are shown in Table 1 with two control solutions of 0.1 mM and 5.3 mM. These are used to illustrate the chemical shift values of the chosen diagnostic peaks in isolated monomers and rod-like micelles respectively. A number of conclusions can be drawn from these results. Firstly, the peak corresponding to the trimethyl ammonium group may not be as reliable as was theorised. This is most likely due to these protons being on the outer layer of the micelle and thus exposed to the surrounding solvent mixture. This means that these protons are in an inherently different environment to the control even before the steric interactions due to aggregate morphology are taken into account. As such, these head groups are not usable for this experiment. However, it is possible they could be used for reverse micellar systems where the surfactants are dissolved in an organic medium causing the hydrophilic head groups to be present in the centre of the aggregates with the hydrophobic tails pointing outwards.³¹ On the other hand, the peak associated with the methyl group at the end of the tail seems to be broadly unaffected by the solvent changes most likely due to their being shielded in the centre of the micelle. So, if the micellar structure is retained despite the presence of a co-solvent, the chemical shift will be similar to that of the 5.3 mM control

Solution	Concentration	δ(head) / ppm	δ(tail) / ppm
Control [CTAB]	0.1 mM	3.2903	0.8506
	5.3 mM	3.3456	0.8252
THF	1%	3.3138	0.8221
	5%	3.3321	0.8393
	10%	3.3336	0.8564
	15%	3.3031	0.8655
MeCN	5%	3.3260	0.8351
	10%	3.2932	0.8497
	20%	3.2366	0.8727
MeOH	5%	3.3385	0.8161
	10%	3.3440	0.8268
	20%	3.3588	0.8362
DMF	5%	3.3096	0.8194
	10%	3.3061	0.8188
	20%	3.2989	0.8222

Table 1: The chemical shift values for various 5.3 mM CTAB solutions in D₂O doped with deuterated co-solvents. Control solutions 0.1 and 5.3 mM are dissolved in D₂O alone.. All percentages are v/v values. **RED)** Chemical shift values corresponding to isolated monomers, **GREEN)** Values corresponding to rod-like micelles and **ORANGE)** Values in between.

solution. Conversely, if the co-solvent allows the monomers to become fully solubilised then it will fall to values close to those of the 0.1 mM control solution.

THF and MeCN both show disruption of the micellar phase even at low percentages meaning they are best avoided for future experiments. In conjunction to these results, when large proportions (>10% v/v) of either of these co-solvents are used in a silica synthesis, a fine suspension is formed which cannot be separated through filtration or centrifugation. In a standard synthesis, m-SiO₂ particles form as silica is polymerised in the interstitial space in the hexagonal array of the micellar template. Synthesised in this way, the particles are too large to be supported by the water under their own weight and precipitate out of solution. That this has not taken place when large amounts of THF or MeCN are present in conjunction with the NMR results, also suggests that the presence of these co-solvents causes solvation of the surfactant monomers resulting in amorphous silica. However, results seen in Table 1 do suggest that at low proportions (1% v/v), THF may leave the micellar phase intact. It is worth noting that crystalline MCM-41 can be synthesised in the presence of MeCN as long as it is kept to a minimum as proven in Chapter 3. However, this may go towards explaining the loss of porosity at higher dye-loadings for **BPJ2**/CTAB@ MCM-41 where, as a higher proportion of dye was used, a larger amount of MeCN was required. While it may be possible to use small amounts of these co-solvents, going forward it would be safer to use MeOH or DMF with only the former exhibiting any significant change in the chemical shift and even then only at higher proportions.

5.3 Platinum(II) Complexes in Silica

Like in Chapter 3, a variety of dye-loadings were used, namely 1, 10 and 25%. Again, dye-loading represents the mole percent of CTAB replaced with a dye so that the overall concentration of surfactant is unchanged throughout the samples. The 0% sample is made using the standard MCM-41 method with no dye added and is used as a control sample. The synthesis of MCM-41 was attempted using all four Pt(II) dyes via their incorporation during micelles formation. A low proportion (1% v/v) of acetonitrile was used for **N-129** at 1, 10 and 25% as well as **TGV-19** at 1 and 10% as this small amount has been shown to still result in crystalline silica. However, at 25% **TGV-19** as well as all proportions of **NCN-60** and **VNK-40** required too much MeCN to avoid disrupting micelle structure. These samples were shown to be highly soluble in THF but, given the results shown above, this method of inclusion was not deemed viable. Given this, and the fact that these dyes do not dissolve in MeOH or DMF, a new method for insertion into the micellar template was developed. Here, the dyes were

incorporated into the CTAB solution through vigorous stirring and infrequent treatments in an ultrasound bath over the course of 1-2 days. While this method is time consuming, it eliminates the chance of disruption of the micelles by the presence of co-solvents.

Photographs of these materials under ambient and 366 nm UV light are shown in Figure 8. While certain dyes show it better than others, it is clear to see that a red-shift is induced in emission of the materials as dye-loading increases. This effect seems to be particularly prominent in the **TGV-19** and **N-129** which seem to emit in the green at low dye-loading but exhibit deep red emission at 25%. Again, like in Chapter 3 these materials will be analysed both structurally to see how the introduction of the dyes has influenced the final silica structure as well as spectroscopically to investigate the effect of the increased dye-loading and rigid silica environment on the photophysical properties of the dyes.

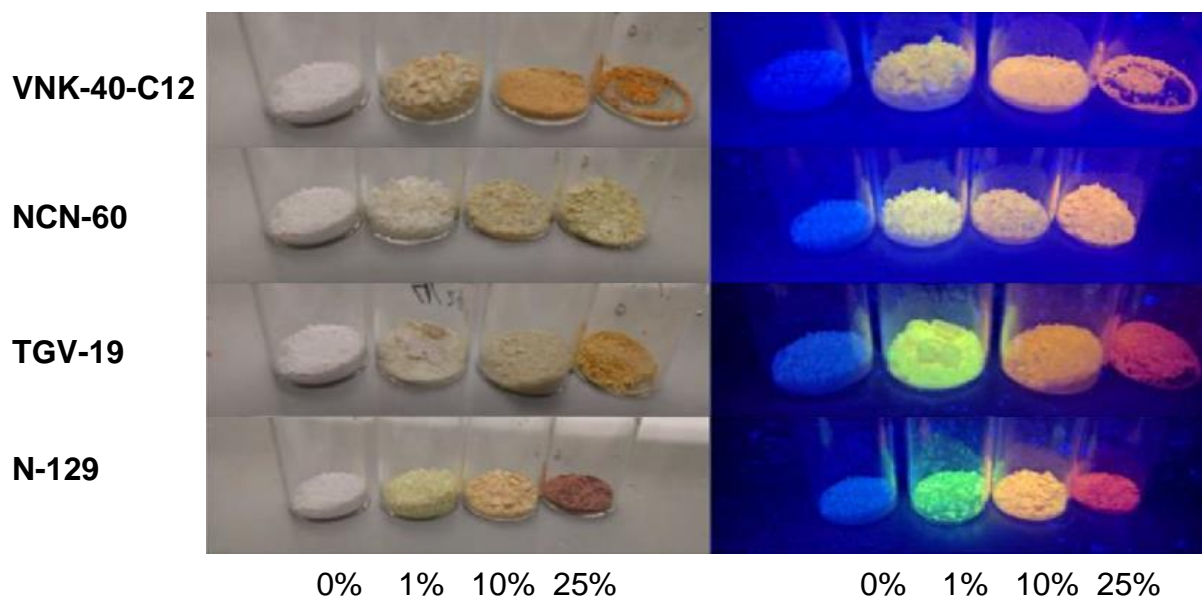


Figure 9: Photographs of the Pt(II)-complex doped silica under ambient and UV light.

Figure 10 shows the steady-state solution-phase UV/Vis and photoluminescence spectra of **NCN- 60** which best demonstrate the steady-state photophysical properties of these complexes (for the spectra of the other complexes, see Appendix). As is typical of dyes of this type, they exhibit high molar absorption coefficients ($40,000\text{-}65,000\text{ M}^{-1}\cdot\text{cm}^{-1}$) and large Stokes shifts as a result of the large degree of vibrational relaxation needed to reach T_1 . In this case however the emission band around 500 nm is particularly structured resulting from a high degree of vibronic coupling. As the ligand is very rigid, it is likely that this is due to the radiative decay from $T_1 \rightarrow S_0$ being mainly LC in character which is typical for $[\text{Pt}(\text{N}^{\wedge}\text{C}^{\wedge}\text{N})\text{Cl}]$

complexes. However, **N-129** which also has an N[^]C[^]N ligand shows a largely unstructured emission band suggesting MLCT character here. Complexes with C[^]N[^]N ligands like **VNK-40-C12** and **TGV-19** also exhibit a large degree of MLCT character in their emission resulting in the broad profile seen in their spectra.¹⁰

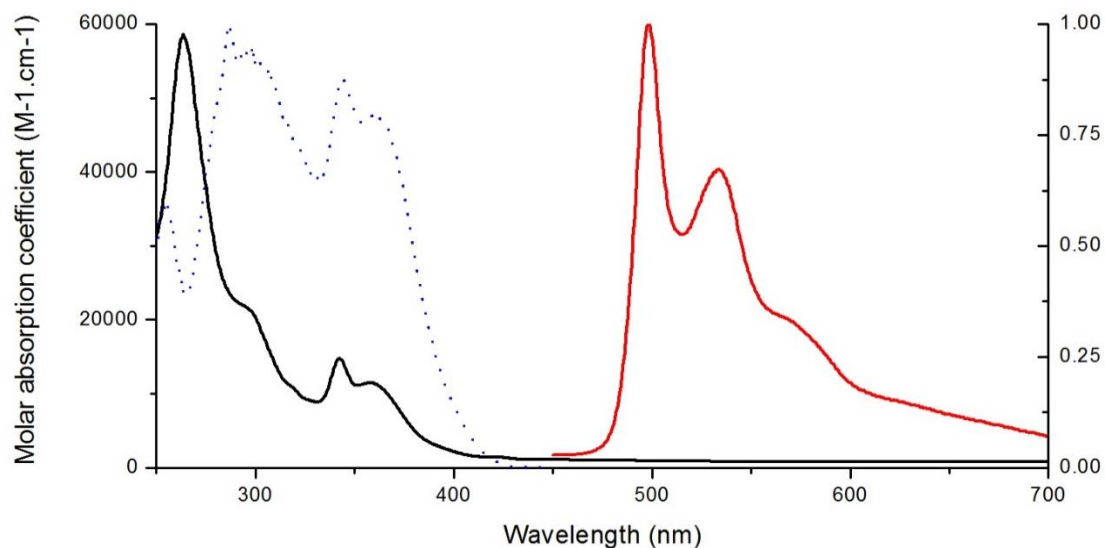


Figure 10: The UV/Vis absorption (black) and photoluminescence emission (red, $\lambda(\text{exc}) = 360 \text{ nm}$) and excitation (blue hashed, $\lambda(\text{em}) = 570 \text{ nm}$) spectra of **NCN-60** in DCM.

5.3.1 Structural and Morphological Analysis

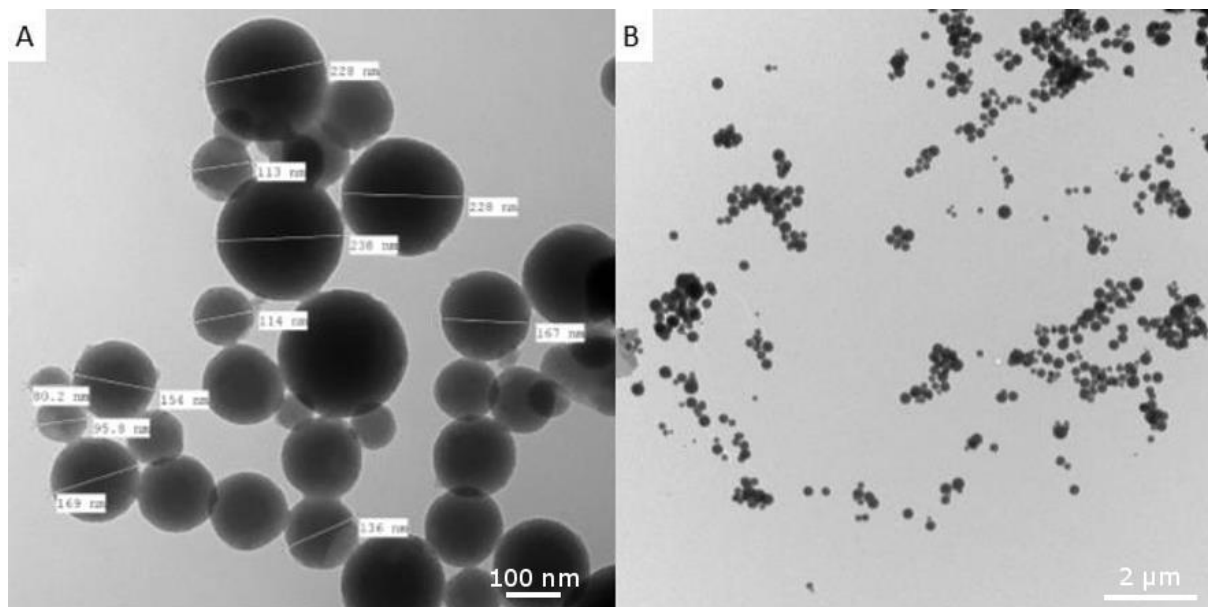


Figure 11: TEM images of MCM-41 with **N-129** at 25% dye-loading.

Transmission electron microscopy (TEM) was used to analyse the m-SiO₂ structure in this case with initial results shown in Figure 11. These images show zoomed-out micrographs of MCM-41 samples made with **N-129** at 25% dye-loading exhibiting similar structures to the silica samples made with all dyes at all proportions. Here, the samples consist of spherical micelles of m-SiO₂ which is typical of MCM-41 although it is also common to see the structure of the template to translate into hexagonal particles. Figure 12 shows images of the **N-129**/CTAB@MCM-41 samples at 1, 10 and 25% dye-loading as well as standard MCM-41 (0% dye-loading) as a control. Again, crystallinity can be observed in these samples similar to those where m-SiO₂ has been synthesised with the other Pt(II) dyes. Initially at 1%, the structure is relatively undisturbed, clearly exhibiting parallel channels. However, as dye-loading increases, the silica begins to become more disordered and radial pores similar to the effect of using **BPJ2** as seen in Chapter 3. This is most likely due to the amount of MeCN needed to dissolve the dyes in order to incorporate them into silica. Nevertheless, the particles still seem to show a large degree of porosity even up to 25% dye-loading.

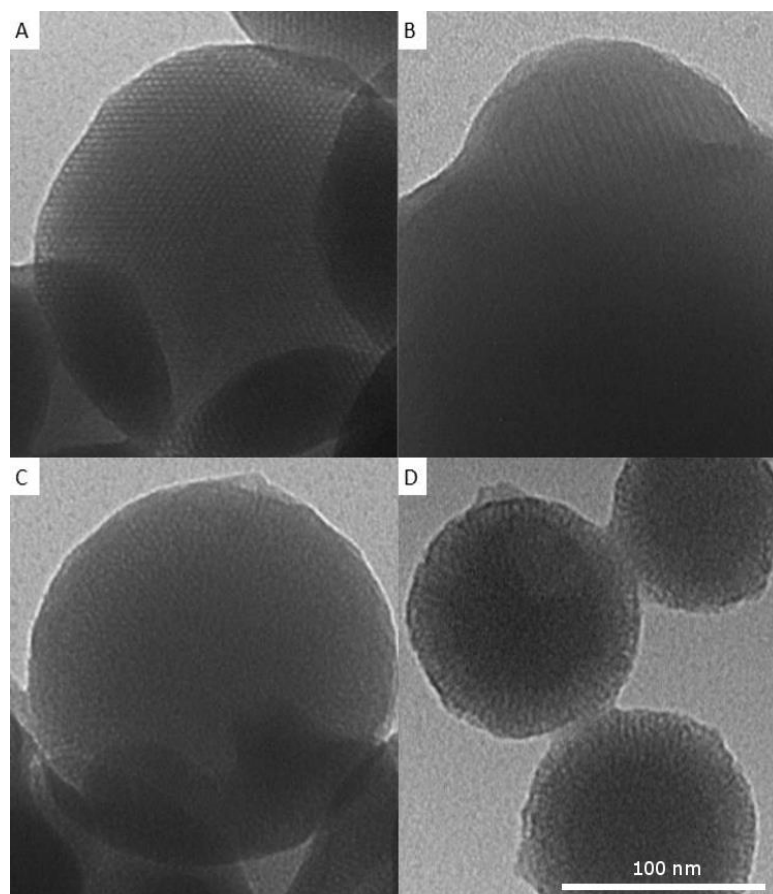
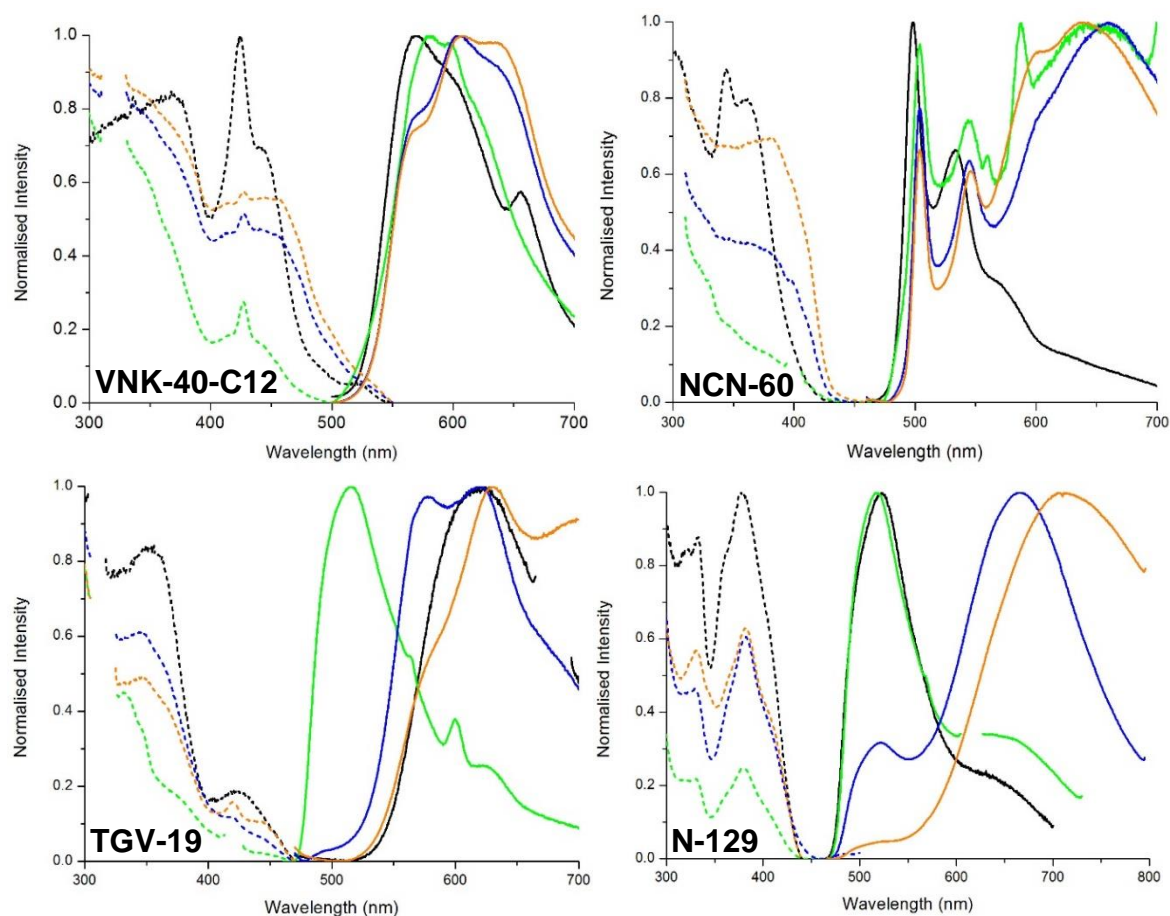


Figure 12: The TEM images of MCM-41 samples synthesised with **N-129** at dye-loadings of A) 0%, B) 1%, C) 10% and D) 25%.

5.4.2 Spectroscopic Analysis



Dye	$\lambda(\text{exc}) / \text{nm}$	$\lambda(\text{em}) / \text{nm}$
VNK-40-C12	390	570
NCN-60	390	600
TGV-19	400	630
N-129	410	520

Figure 13: The photoluminescence excitation (dashed lines) and emission (solid lines) spectra of the Pt(II) complexes in solution (black) and in silica at dye-loadings of 1 (green), 10 (blue) and 25% (orange). **Table 2:** The excitation (exc) and emission (em) wavelengths used for these spectra.

Figure 13 shows the excitation and emission spectra for the four Pt(II) complexes used in this study with most interest lying in the emissive peaks. While all spectra exhibit the same red-shift behaviour, **N-129** demonstrates this change the best of the four. At 1% dye-loading, it exhibits very similar bands to the solution phase spectrum with the predominant peak seen at around 520 nm resulting from the $T_1 \rightarrow S_0$ transition. As mentioned above, this band is broad and unstructured suggesting it has significant MLCT character as opposed to the analogous band for **NCN-60** shown in Figure 10. However, a slight rise in the intensity in the

red-region hints at what is to come as dye-loading increases. At 10%, the original band has depleted significantly giving way to a large broad band at around 700 nm. Moving further to the 25% sample, it shows that the red-shifted band is now predominant with only a small contribution from the original peak observed. This is caused by aggregation of the Pt(II) complexes as shown in Figure 2. The absorption and emission transitions become lower in energy as a result of the formation of aggregates. The peaks associated with this are also invariably broad across all complexes even in **NCN-60**. This is due to the new vibrational degree of freedom introduced when molecules associate into aggregates via the interaction between two dyes. As more molecules aggregate, the degree of red-shifting increases, as hence the peak in the 25% sample which is almost outside the detection range.

While the other complexes follow this trend, they each also exhibit behaviour specific to them. **NCN-60** for instance shows that a large proportion of the dye molecules are present as monomers even at 25% as shown by the sharp bands around 500 nm still clearly being visible above the broad aggregate band. Interestingly, **TGV-19** exhibits only the red-shifted band in solution suggesting lower solubility than **NCN-60** in the chosen solvent (MeCN) giving rise to only aggregates being present in solution. However, upon encapsulation in the silica scaffold, the emission is predominantly monomeric resulting from a large degree of statistical distribution. As dye-loading increases though, this monomeric peak all but disappears even at 10% with the 25% showing complete conversion to the aggregate form. **VNK-40-C12** behaves similarly but exhibits a much smaller red-shift suggesting a lower degree of aggregation when compared to the other three dyes. This is most likely due to the three C-12 chains located in close proximity to one another in the molecule. This introduces a large degree of steric hindrance which significantly limits aggregation. Nevertheless, a small red-shift is observed which at high dye-loadings still exhibits a shoulder corresponding to the monomeric emission.

Taking this further, the samples made with **N-129** and **TGV-19** underwent photoluminescence lifetime analysis with the results shown in Table 2. These two complexes in particular were chosen because of the pronounced red-shifting seen in the steady-state emission spectra of their corresponding silica samples. As expected, the complexes emit via phosphorescence i.e. a radiative $T_1 \rightarrow S_0$ transition which is formally spin-forbidden leading to lifetimes in the microsecond regime. Normally, a phosphorescent dye in solution typically has to be degassed (inert gas bubbled through, usually N_2 or Ar) in order to remove any oxygen dissolved in the solvent. This is because triplet-triplet annihilation can occur whereby depletion of the excited state takes place via reaction with another molecule in the triplet state.

As the ground state of oxygen is a triplet, this offers a particular challenge when working with phosphorescent molecules as they must be compartmentalised away from oxygen before they can be used effectively. If not, as well as the emission being quenched, the resulting singlet oxygen is highly reactive and can cause degradation of the dye over time.¹¹ The results gathered in Table 2 however were taken from suspensions that were not degassed, proving that the silica scaffold provides adequate protection even when oxygen is present in the surrounding medium.

Complex	Loading (%)	$\lambda(\text{em}) / \text{nm}$	$\tau / \mu\text{s}$
N-129	1	530 (M)	3.467
		650 (A)	2.558
	10	520 (M)	0.861
		700 (A)	1.233
	25	510 (M)	0.775
		720 (A)	0.674
TGV-19	1	530 (M)	3.018
	10	530 (M)	2.035
	25	530 (M)	2.094

Table 2: The weight-averaged photoluminescence lifetimes of MCM-41 synthesised with **N-129**- and **TGV-19**-loaded CTAB micelles at various percentages. All samples were excited with a 370 nm laser source. (M) and (A) correspond to the emission wavelength of monomers and aggregates respectively.

As to the effect of dye-loading on the lifetime, there is a marked observable change as the proportion of the dye in the micelles is increased. When probing the excited state of the monomer (approx. 530 nm), there is a more than 4-fold decrease in the excited state lifetime as the loading of **N-129** is increased. This decrease can be assigned to the formation of aggregate species once again with isolated monomers being rarer. As the aggregate species is red-shifted, any monomers will tend to transfer their energy to a nearby aggregate as opposed to emitting a photon resulting in non-radiative depletion of the excited state manifesting as a lowering of the lifetime. This effect is most pronounced when moving 1% to 10% with a further, albeit much smaller, decrease seen at 25%. This suggests that the majority of **N-129** molecules are aggregated even at 10% loading, supporting the conclusions made from the

steady-state spectra. The same effect is exhibited by the **TGV-19** loaded samples, although much less pronounced with only a 33% decrease when proportion is increased from 1% to 10%. This suggests that while aggregation does take place, it is a significantly weaker interaction. This is also supported by the steady-state spectra whereby the final red-shift in emission from 1% to 25% is much lower for **TGV-19** (3243 cm^{-1}) than **N-129** (4783 cm^{-1}).

5.4 Conclusions

The effects of two types of additives to the micellar template of MCM-41 were investigated in this chapter. Firstly, ^1H NMR studies were used to find to what extent the mesophase is disturbed through addition of a series of water-miscible co-solvents. Here, DMF and MeOH showed minimal interference even up to high percentages within the solution. THF and MeCN however exhibited almost complete collapse of the mesophase even at low percentages (5%). Using these findings, the incorporation of **N-129** and **TGV-19** (at low loadings) was performed using a small proportion of MeCN (1% v/v) as a co-solvent. No such system was deemed viable for 25% **TGV-19** or any loadings of **NCN-60** and **VNK-40-C12**. As such a new pure water method was developed involving vigorous stirring and intermittent sonication which, while time-consuming, successfully included the dyes into the micellar phase.

Secondly, a series of phosphorescent Pt(II) complexes with known aggregation behaviour were added to the micelles. This resulted in a red-shift in the emission upon increased dye-loadings with this being particularly pronounced for the complexes **TGV-19** and **N-129**. Interestingly, these complexes were highly emissive in the pores even when the samples were not purged of O_2 , demonstrating that the silica scaffold provides adequate protection from oxygen-induced quenching and degradation. These systems pave the way towards efficient OLED devices that only need one input dye for colour-tuning.

5.5 Experimental

Synthesis of MCM-41 mesoporous silica with a 100% CTAB micellar template:

Cetyltrimethylammonium bromide (350 mg, 1 mmol) was dissolved in H_2O (180 mL) using an ultrasound bath. Sodium hydroxide (2 M, 1.3 mL, 2.6 mmol) was then added causing the cloudy mixture to turn clear. This was heated to $80\text{ }^\circ\text{C}$ and tetraethylorthosilicate (1.8 mL, 8.2 mmol) was added. The mixture was then stirred under reflux at $80\text{ }^\circ\text{C}$ for 2 h after which it was filtered under vacuum. The filtrate was washed with H_2O until neutral and dried in an oven overnight. This resulted in a powdery white solid.

Synthesis of MCM with **N-129**-doped micelles using MeCN as co-solvent:

Cetyltrimethylammonium bromide and **N-129** were mixed in the following molar ratios to result in the desired dye loadings: 99:1 (CTAB: 0.26 mmol, **N-129**: 2.7 μmol), 90:10 (CTAB: 0.14 mmol, **N-129**: 16 μmol), 75:25 (CTAB: 80 μmol , **N-129**: 27 μmol). Generally, CTAB was dissolved in H_2O (50 ml) with the help of an ultrasonic bath. In parallel, **N-129** was dissolved in a minimum amount of MeCN (typically around 1 mL) and added dropwise to the CTAB resulting in a turbid yellow/orange mixture. Sodium hydroxide (2 M, 0.36 mL, 0.72 mmol) was then added turning the mixture red/purple. This was then heated to 80 °C at which point tetraethylorthosilicate (0.50 mL, 2.30 mmol) was added. The mixture was then heated at 80 °C under reflux for 2 h. The resulting pink precipitate was filtered and washed with H_2O . The filtrate was then dried in an oven overnight resulting in powders of varying colours: yellow (99:1, 90:10) and orange/brown (75:25).

Synthesis of MCM-41 with **TGV-19**-doped micelles using MeCN as co-solvent:

Cetyltrimethylammonium bromide and **TGV-19** were mixed in the following molar ratios to result in the desired dye loadings: 99:1 (CTAB: 0.26 mmol, **TGV-19**: 2.7 μmol), 90:10 (CTAB: 0.14 mmol, **TGV-19**: 16 μmol). Generally, CTAB was dissolved in H_2O (50 ml) with the help of an ultrasonic bath. In parallel, **N-129** was dissolved in a minimum amount of MeCN (typically around 1 mL) and added dropwise to the CTAB resulting in a turbid yellow/orange mixture. Sodium hydroxide (2 M, 0.36 mL, 0.72 mmol) was then added turning the mixture red/purple. This was then heated to 80 °C at which point tetraethylorthosilicate (0.50 mL, 2.30 mmol) was added. The mixture was then heated at 80 °C under reflux for 2 h. The resulting pink precipitate was filtered and washed with H_2O . The filtrate was then dried in an oven overnight resulting in pale yellow powders.

Synthesis of MCM-41 with 1% **NCN-60**-doped micelles using DMF as co-solvent:

Cetyltrimethylammonium bromide (96.2 mg, 0.264 mmol) was dissolved in H_2O (50 ml) with the help of an ultrasonic bath. In parallel, **N-129** was dissolved in a minimum amount of DMF (typically around 1 mL) and added dropwise to the CTAB resulting in a turbid yellow/orange mixture. Sodium hydroxide (2 M, 0.36 mL, 0.72 mmol) was then added turning the mixture red/purple. This was then heated to 80 °C at which point tetraethylorthosilicate (0.50 mL, 2.30 mmol) was added. The mixture was then heated at 80 °C under reflux for 2 h. The resulting pink precipitate was filtered and washed with H_2O . The filtrate was then dried in an oven overnight resulting in a pale yellow powder.

Synthesis of MCM-41 with 1% **VNK-40-C12**-doped micelles using DMF as co-solvent:

Cetyltrimethylammonium bromide (96.2 mg, 0.264 mmol) was dissolved in H_2O (50 ml) with the help of an ultrasonic bath. In parallel, **VNK-40-C12N-129** was dissolved in a minimum amount of DMF (typically around 1 mL) and added dropwise to the CTAB resulting in a turbid yellow/orange mixture. Sodium hydroxide (2 M, 0.36 mL, 0.72 mmol) was then added turning the mixture red/purple. This was then heated to 80 °C at which point tetraethylorthosilicate (0.50 mL, 2.30 mmol) was added. The mixture was then heated at 80 °C under reflux for 2 h. The resulting pink precipitate was filtered and washed with H_2O . The filtrate was then dried in an oven overnight resulting in a pale yellow powder.

Synthesis of MCM-41 with 25% **TGV-19**-doped micelles using no co-solvent:

TGV-19 (16.8 mg, 0.027 mmol) was added to water (10ml), where it did not dissolve. In parallel CTAB (29.1 mg, 0.080 mmol) was dissolved in water (10ml) with use of an ultrasound bath, forming a cloudy white solution. The **TGV19**/water mixture and CTAB solution were combined to form a cloudy yellow solution which started to dissolve the solid dye. Further ultrasound treatment followed by stirring overnight dissolved the remaining dye. 2M aqueous sodium hydroxide solution (0.139 ml, 0.218 mmol) was added to the CTAB/dye solution with stirring, the mixture was then heated with stirring under reflux to 80 °C where TEOS (0.195 ml, 0.877 mmol) was added, and left for 2 hours where a pale-yellow-orange precipitate had formed. The precipitate was removed by vacuum filtration, washed with water and dried overnight in a vacuum desiccator resulting in a pale-yellow powder.

Synthesis of MCM-41 with **NCN-60**-doped micelles using no co-solvent:

Cetyltrimethylammonium bromide and **NCN-60** were mixed in the following molar ratios to result in the desired dye loadings: 90:10 (CTAB: 96 µmol, **NCN-60**: 11 µmol), 75:25 (CTAB: 80 µmol, **NCN-60**: 27 µmol). Generally, **NCN-60** was added to water (10ml), where it did not dissolve. In parallel CTAB was dissolved in water (10ml) with use of an ultrasound bath, forming a cloudy white solution. The **NCN-60**/water mixture and CTAB solution were combined to form a cloudy yellow solution which started to dissolve the solid dye. Further ultrasound treatment followed by stirring overnight dissolved the remaining dye. 2M aqueous sodium hydroxide solution (0.139 ml, 0.218 mmol) was added to the CTAB/dye solution with stirring, the mixture was then heated with stirring under reflux to 80 °C where TEOS (0.195 ml, 0.877 mmol) was added, and left for 2 hours where a pale-yellow-orange precipitate had formed. The precipitate was removed by vacuum filtration, washed with water and dried overnight in a vacuum desiccator resulting in a pale-yellow powder.

Synthesis of MCM-41 with **VNK-40-C12**-doped micelles using no co-solvent:

Cetyltrimethylammonium bromide and **VNK-40-C12** were mixed in the following molar ratios to result in the desired dye loadings: 90:10 (CTAB: 96 µmol, **VNK-40-C12**: 11 µmol), 75:25 (CTAB: 80 µmol, **VNK-40-C12**: 27 µmol). Generally, **NCN-60** was added to water (10ml), where it did not dissolve. In parallel CTAB was dissolved in water (10ml) with use of an ultrasound bath, forming a cloudy white solution. The **VNK-40-C12**/water mixture and CTAB solution were combined to form a cloudy yellow solution which started to dissolve the solid dye. Further ultrasound treatment followed by stirring overnight dissolved the remaining dye. 2M aqueous sodium hydroxide solution (0.139 ml, 0.218 mmol) was added to the CTAB/dye solution with stirring, the mixture was then heated with stirring under reflux to 80 °C where TEOS (0.195 ml, 0.877 mmol) was added, and left for 2 hours where a pale-yellow-orange precipitate had formed. The precipitate was removed by vacuum filtration, washed with water and dried overnight in a vacuum desiccator resulting in a yellow/orange powder.

References

1. (a) A. Loudet, K. Burgess, *Chem. Rev.*, 2007, **107**, 4891-4932. (b) S. A. Baudron, *Dalton T.*, 2013, **42**, 7498-7509.
2. B. M. Estevão, F. Cucinotta, N. Hioka, M. Cossi, M. Argeri, G. Paul, L. Marchese and E. Gianotti, *Phys. Chem. Chem. Phys.*, 2015, **17**, 26804-26812.
3. L. Zhang, S. Qiao, Y. Jin, Z. Chen, H. Gu and G. Q. Lu, *Adv. Mater.*, 2008, **20**, 805-809.
4. F. Hoffmann and M. Froba, *Chem. Soc. Rev.*, 2011, **40**, 608-620.
5. J. Cho, J. H. Park, J. K. Kim and E. F. Schubert, *Laser Photonics Rev.*, 2017, **11**, 1-17.
6. E. Rossie, L. Murphy, P. L. Brothwood, A. Colombo, C. Dragonetti, D. Roberto, R. Ugo, M. Cocchi and J. A. G. Williams., *J. Mater. Chem.*, 2011, **21**, 15501-15510.
7. C. W. Tang, S. A. van Slyke, *Appl. Phys. Lett.*, 1987, **51**, 913-915.
8. J. A. G. Williams, A. J. Wilkinson and V. L. Whittle, *Dalton Trans.*, 2008, **0**, 2081-2099.
9. W. Sotoyama, T. Satoh, H. Sato, A. Matsuura and N. Sawatari, *J. Phys. Chem. A*, 2005, **109**, 9760-9766.
10. J. Kalinowski, V. Fattori, M. Cocchi and J. A. G. Williams, *Coord. Chem. Rev.*, 2011, **255**, 2401-2425.
11. V. N. Kozhevnikov, B. Donnio, B. Heinrich, J. A. G. Williams and D. W. Bruce, *J. Mater. Chem.*, 2015, **3**, 10177-10187.
12. F. Cucinotta, B. P. Jarman, C. Caplan, S. J. Cooper, H. J. Riggs, J. Martinelli, K. Djanashvili, E. La Mazza, F. Puntoriero, *ChemPhotoChem*, **2018**, **2**, 196-206.
13. A. F. Rausch, L. Murphy, J. A. G. Williams and H. Yersin, *Inorg. Chem.*, 2012, **51**, 312-319.
14. (a) C. Kresge, M. Leonowicz, W. Roth, J. Vartuli and J. Beck, *Nature*, 1992, **359**, 710-712. (b) J. S. Beck, J. C. Vartuli, W. J. Roth, M. E. Leonowicz, C. T. Kresge, K. D. Schmitt, C. T.-W. Chu, D. H. Olson, E. W. Sheppard, S. B. McCullen, J. B. Higgins and J. L. Schlenker, *J. Am. Chem. Soc.*, 1992, **114**, 10834-10843.
15. G. Calzaferri, S. Huber, H. Maas and C. Minkowski, *Angew. Chem. Int. Ed. Engl.*, 2003, **42**, 3732-3758.
16. J. W. McBain and C. S. Salmon, *J. Am. Chem. Soc.*, 1920, **42**, 426-460.
17. G. S. Hartley and D. F. Runnicles, *Proc. Royal Soc. A*, 1938, **168**, 420-440.
18. Y. Moroi, in *Micelles: Theoretical and Applied Aspects*, Plenum Press, New York City, New York, 1992, 1st edn., ch. 1, pp 1-5.
19. S. Ozeki and S. Ikeda, *Colloid Polym. Sci.*, 1984, **262**, 409-417.
20. T. Imae and S. Ikeda, *J. Phys. Chem.*, 1986, **90**, 5216-5223.
21. P. Parekh, R. Ganguly, V. K. Aswal and P. Bahadur, *Soft Matter*, 2012, **8**, 5864.
22. J. N. Israelachvili, D. J. Mitchell and B. W. Ninham, *J. Chem. Soc. Farad. T. 2*, 1975, **72**, 1525-1568.
23. S. May and A. Ben-Shaul, *J. Phys. Chem. B*, 2001, **105**, 630-640.
24. A. Evilevitch, V. Lobaskin, U. Olsson, P. Linse and P. Schurtenberger, *Langmuir*, 2001, **17**, 1043-1053.
25. Y-Y Won, A. K. Brannan, H. T. Davis and F. S. Bates, *J. Phys. Chem. B*, 2002, **106**, 3354-3364.
26. T. Imae, R. Kamiya and S. Ikeda, *J. Colloid Interf. Sci.*, 1985, **108**, 215-225.
27. Y. Moroi, in *Micelles: Theoretical and Applied Aspects*, Plenum Press, New York City, New York, 1992, 1st edn., ch. 4, pp 47-53.

28. (a) X.-Y. Lu, Y. Jiang, X.-H. Cui, S.-Z. Mao, M.-L. Liu and Y.-R. Du, *Acta Phys. - Chim. Sin.*, 2009, **25**, 1357-1361. (b) J.-Z. Zhang, L. Xie, S.-g. Chai and Q.-c. Zou, *Chinese J. Chem. Phys.*, 2014, **27**, 307-314.
29. H. Zhang, P. Dubin and J. Kaplan, *Langmuir*, 1991, **7**, 2103-2107.
30. K. A. Murthy and E. W. Kaler, *Colloid., Polym., Sci.*, 1989, **267**, 330-335.
31. L. Klicova, P. Sebej, P. Stacko, S. K. Filippov, A. Bogomolova, M. Padilla and P. Klan, *Langmuir*, 2012, **28**, 15185-15192.

Chapter 6. Synthesis and Optical Properties of a New Organometallosilica

6.1 Introduction

Moving away from incorporation of dyes into the micellar template in the synthesis of mesoporous silica, this chapter will cover preliminary experiments into the second step of the outline of this project shown in Chapter 1 i.e. the incorporation of metal complexes into the m-SiO₂. This has typically been achieved via diffusion of guests throughout the pores¹ which, as discussed previously, causes non-uniform distribution where molecules are preferentially found near the pore entrances.² Here, a co-condensation method will be used in order to synthesise a periodic mesoporous organometallosilica (PMOM), which for organic moieties such as bipyridine bridges has been proven to result in higher homogeneity throughout the silica framework. These can then act as a solid-state chelating ligand for iridium(III) centres introduced into the pores via diffusion. This was shown to be a promising heterogenous water oxidation catalyst with turnover frequencies an order of magnitude higher than standard Ir(III)-based materials.³

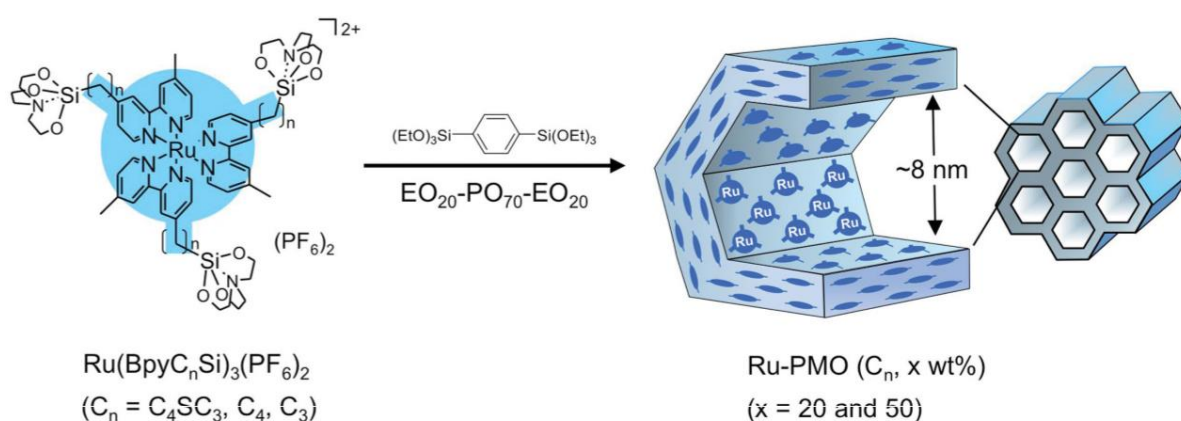


Figure 1: A figure showing the incorporation of a ruthenium complex into the walls of SBA-15 mesoporous silica reproduced with permission from a 2016 *Adv. Funct. Mater.* By Inagaki et al.⁴

In 2016, Inagaki et al. introduced a method that incorporated a ruthenium tris-bipyridine (bipy) complex functionalised with silicate precursor groups (in this case, silatranes) and in doing so synthesised the first PMOM. This was achieved by co-condensing the Ru(II) complex with 1,4-di(triethoxysilyl)benzene (BTEB) using the SBA-15 method (surfactant: Pluronic P123, pH = 0, hydrothermal conditions) as shown in Figure 1. While the order of the

pores was somewhat disturbed, the silica synthesised still showed porosity through powder XRD studies. This particular system was coupled with platinum nanoparticles as guests in the pores for use as a heterogeneous water oxidation photocatalyst. This system elegantly demonstrates the power of this kind of silicate chemistry to facilitate uniform distribution of metal complexes throughout a silica scaffold for light harvesting and conversion applications.⁴ However, this technology will struggle to progress industrially unless cheaper materials are used with both ruthenium and platinum are expensive and rare metals.⁵ To date, the largest bridge to be incorporated successfully into a PMO uses a Zn(II) phthalocyanine complex developed by Bein *et al.* This silica system exhibited stacking of the zinc complexes within the walls allowing electron transport and shifting the absorption bands into the near-IR. Impregnation of fullerene derivatives into the pores promoted photo-induced charge transfer facilitating photovoltaic behaviour.⁶

6.1.1 Zn(II) Complexes

This chapter will focus on zinc(II) complexes offering an alternative that is more economically viable at industrial scales. Zinc is often treated differently than other d-block elements. This is due to the d-orbitals being entirely filled resulting in a lack of transition behaviour meaning it effectively acts like a 2+ ion in the majority of its chemistry. It can form octahedral complexes but it commonly adopts a tetrahedral geometry typically with two bidentate ligands such as in zinc acetate ($\text{Zn}(\text{OAc})_2$).⁷ If photoactive ligands are used instead however, the zinc centre acts as a scaffold around which a bichromophoric antenna can be built. The effect of this on the chromophore is two-fold. Firstly, efficient light-absorbing ligands such as dipyrromethenes, which are unstable when free in solution, can be protected from degradation once coordinated to the metal.

Secondly, as zinc shows optical no transition behaviour, it is photochemically inert. By arranging chromophoric ligands around a metal centre of this nature, interactions between the two ligands can be observed, demonstrated in dipyrromethene complexes by Nishihara *et al.*⁶ Figure 2 shows how an inter-ligand charge transfer (ILCT, sometimes known as symmetry-breaking charge transfer, SBCT) takes place. Initially, one of the ligands is excited with a photon raising an electron into an excited state. From here, an electron is then transferred (**A** or **B**) resulting in a charge-separated species with a radical anion on one ligand and a radical cation on the other. As this process is favourable and the recombination of the charge-separated species non-radiative, these complexes tend to be non-emissive.⁸ It may be

possible however to use this final charged species to perform photocatalytic reactions as long as the ground state was reliably restored by an appropriate redox relay unit.

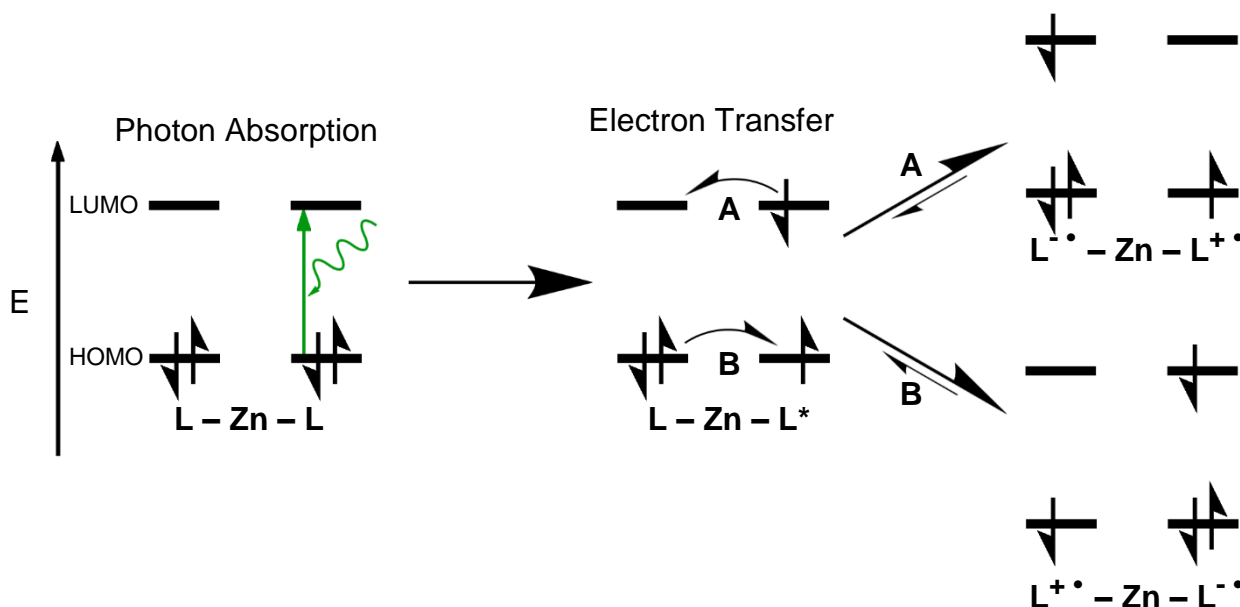


Figure 2: An electronic energy level diagram showing the photoinduced electron transfer in Zn(II) complexes. L = bidentate chromophoric ligand.⁸

6.1.2 Quinolate Ligands

Quinolinol (Hq, 8-hydroxyquinoline) and its derivatives are another class of organic ligands that have seen increased interest in the last 20 years as, in their deprotonated form, they act as bidentate cyclometalating ligands with many advantageous properties. Many variants of the ligand are commercially available like halogenated derivatives that offer a wide range of structural functionalisation through aromatic substitution reactions.⁹ As mentioned in the previous chapter, the first quinolate complex to attract attention was Al(q)₃ which found promising use when it exhibited electroluminescence making it the first OLED seen in the literature with many derivatives still being investigated for their optical properties.¹⁰ Zinc quinolate complexes also share this electroluminescent trait making it an interesting candidate for light-harvesting and optoelectronic materials.^{11, 12}

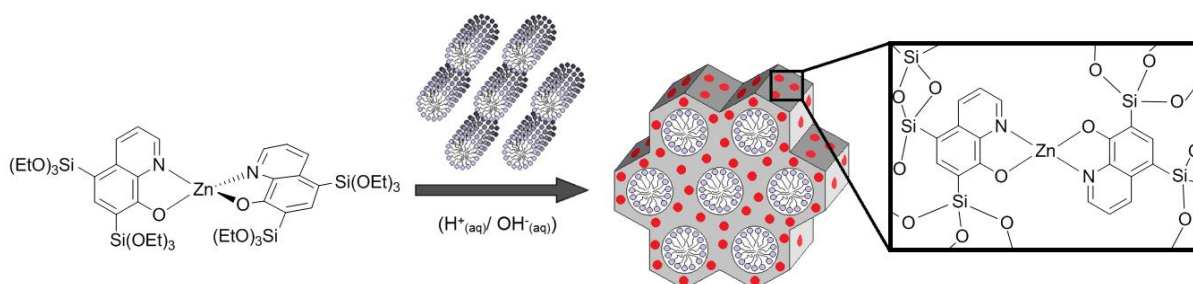


Figure 3: The synthesis of a periodic mesoporous organometallosilica (PMOM) using a zinc(II) quinolate complex.

To that end, this chapter presents work developing m-SiO₂ materials with zinc quinolate complexes incorporated within. This was performed using the periodic mesoporous organosilica method outlined in Figure 3. Here, an metallorganic precursor (in this case the zinc complex) is silylated through a transmetalation reaction then co-condensed with another silicate precursor to yield a PMOM. Preliminary experiments were also performed with this system and a fluorescent dye (Rhodamine B) in order to probe the possible energy transfer properties of such hybrid organic/inorganic materials.. This is with the aim that these PMOMs will be coupled with the dye-doped micelles of previous chapters for cheap and stable polychromophoric light-harvesting antennae based on m-SiO₂.

6.2 Synthesis and Photophysics of Zn(Br₂-q)₂ and Zn(Si₂-q)₂

The synthesis of the silicate precursor **Zn(Si₂-q)₂** is seen in Figure 4. It begins with a simple complexation reaction between 5,7-dibromo-8-hydroxyquinoline (**H(Br₂-q)**) and zinc acetate dihydrate to afford **Zn(Br₂-q)** in a high yield.⁹ The work-up of this reaction makes it particularly attractive as the resulting complex has low solubility in EtOH and precipitates as a yellow powder. This can then easily be filtered, washed with more EtOH and dried in air to give the product. The spectroscopic properties of this complex will be used to compare with the silica made from the eventual final product, **Zn(Si₂-q)₂**. This is because the silylated complex, like all silicate precursors, tend to hydrolyse and polycondense over time, even in the absence of a catalyst. However, the electronic effect of the bromide and silicate groups is minimal on the photophysical properties of the ligand making the two complexes comparable while using this analysis.¹³

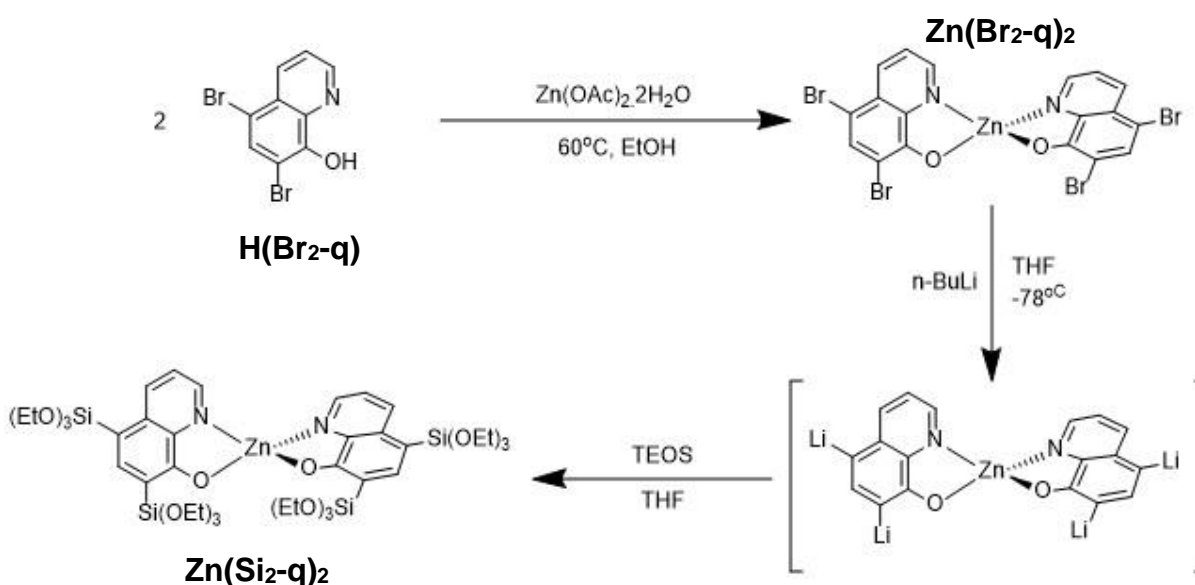
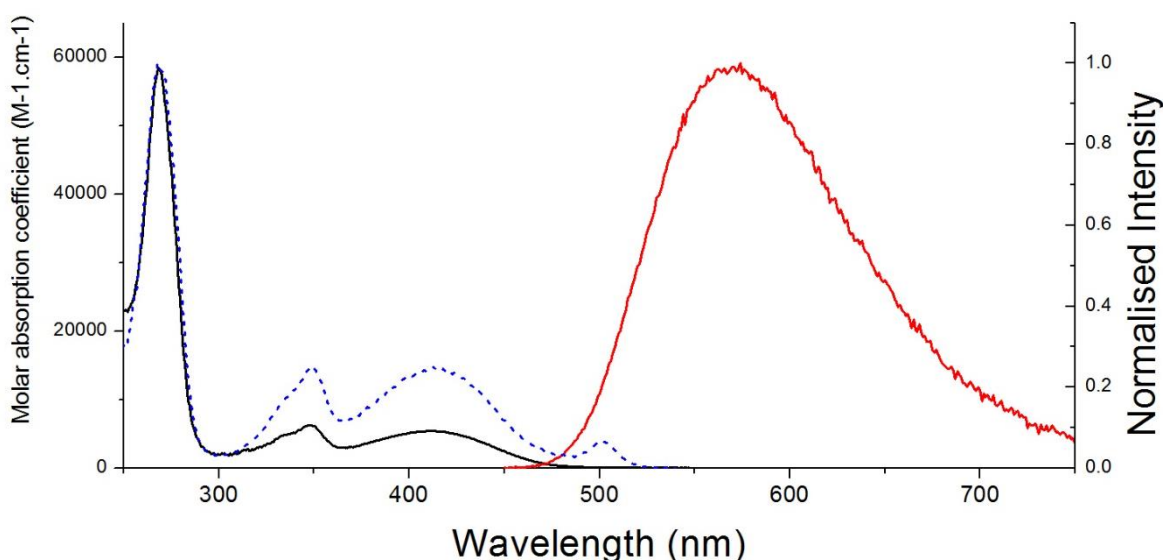


Figure 4: The synthesis of **Zn(Si₂-q)₂**.

Spectroscopic analysis of $\text{Zn}(\text{Br}_2\text{-q})_2$ was performed in a variety of solvents in order to gain insight into the photophysical behaviour with steady state absorption and photoluminescence spectra in THF shown in Figure 5. Comparing these to experiments performed by Armstrong *et al.*,⁹ this complex exhibits a very similar spectral profiles with the strongest absorption peak being found at 265 nm with molar absorption coefficient (ϵ) values ranging from 10,000-100,000 $\text{M}^{-1}\cdot\text{cm}^{-1}$ (with an exceptionally high value seen in ethanol). This is indicative of a ligand centred $\pi \rightarrow \pi^*$ transition which is typical for aromatic chromophores cemented by the fact that this transition is also in the spectrum of the free ligand,¹⁴ The small peaks at 345 and 405 nm which exhibit ϵ values around 4,000 $\text{M}^{-1}\cdot\text{cm}^{-1}$ however are not observed in the free ligand and so must be a result of the complexation of two of the ligands around a zinc centre possibly corresponding to the ILCT transitions mentioned above. Without further analysis such as computational methods this is difficult to ascertain, however these peaks do help to prove that complexation has taken place.^{9, 15}



Solvent	$\epsilon / \text{M}^{-1}\cdot\text{cm}^{-1}$ ($\lambda_{\text{max}} = 265 \text{ nm}$)	τ / ns	Φ_{F}	$k_{\text{R}} / 10^8 \text{ s}^{-1}$	$k_{\text{NR}} / 10^8 \text{ s}^{-1}$
DCM	33,754	4.4	-	-	-
EtOH	141,361	4.4	0.26	0.59	1.7
THF	58,503	5.3	0.26	0.49	1.4
DMF	32,826	4.9	0.73	1.5	0.54

Figure 5: The absorbance (black), excitation (blue dashed, $\lambda(\text{em}) = 560 \text{ nm}$) and emission (red, $\lambda(\text{exc}) = 270 \text{ nm}$) for $\text{Zn}(\text{Br}_2\text{-q})_2$ in THF (6.5 μM). **Table 2:** The photophysical data of $\text{Zn}(\text{Br}_2\text{-q})_2$ in various solvents.

A small degree of red-shifting is seen in the spectra taken in THF and DMF when compared with EtOH. THF and DMF are known to be coordinating solvents, displacing the axial aqua ligands upon solvation. It would seem therefore that the degree of this coordination is more important than solvent polarity on the transition energies seeing as EtOH is the most polar of the solvents tested. Taking this further, the red-shift is larger in DMF than in THF suggesting the strength of the coordination reaction is stronger in the former.¹⁶

The photoluminescence emission spectrum shows a band at 563 nm meaning this dye has a particularly large Stokes shift (Figure 5). This suggests a large geometric change in the molecule has taken place as it transitions from the Frank-Condon region of the excited state to the lowest vibrational state with the energy primarily lost as heat¹⁷ comparable to other work with complexes such as these. As there is only one emission peak, there must only be one emissive state but the excitation spectrum shows contribution from both the LC and CT states. According to Kasha's rule, the lowest energy state is most likely to be emissive i.e. the CT state absorbing at 405 nm. Also, the CT bands are of higher intensity (relative to the LC band) in the excitation spectrum than in the absorption one. This is because in an absorbance spectrum, only direct excitation via absorption of a photon contributes to the height of a band. However, due to the nature of photoluminescence excitation spectra (see Ch. 2, section 2.2.2), the intensity of the band is dependent on the activation of an emissive state by any means. In this case, the CT states are not only populated via direct absorption of a photon (like in an absorption spectrum) but also through the ILCT process shown in Figure 2. Here, the complex first directly absorbs a photon at 265 nm in an LC transition. This state then undergoes a symmetry break forming the emissive CT states. These two processes combined result in the CT bands being relatively higher in the excitation spectrum.⁹

The time-resolved spectroscopy of **Zn(Br₂-q)₂** gave excited state lifetimes of around 5 ns (Table 1) meaning that despite the large Stokes shift, this molecule decays via fluorescence i.e. a radiative $S_1 \rightarrow S_0$ transition with lifetimes in the different solvents being of comparable duration. Quantum yield calculations were not possible in DCM due to low solubility of the dye. However THF and EtOH gave similar Φ_F values of 0.26 with the rate constant of non-radiative processes (k_{NR}) outweighing the radiative rate (k_R) by around three-fold. DMF exhibits the largest quantum yield by far at 0.73 where fluorescence dominates over non-radiative decay processes. This could be due to the stronger coordination of DMF to the complex when compared to the other solvents as discussed above. In doing so, it could introduce more rigidity allowing less thermal deactivation of the excited state.¹⁶

The second step of the synthesis involves lithiation of $\text{Zn}(\text{Br}_2\text{-q})_2$ using *n*-butyllithium (*n*-BuLi) followed by reaction with TEOS in a one-pot reaction with the intention of forming the tetrasilylated product, $\text{Zn}(\text{Si}_2\text{-q})_2$.¹⁸ While various conditions were tested for this reaction (varying temperature, solvent etc.), only partial silylation was ever achieved. From the NMR spectrum of the crude product (see Appendix, Figure A17), typically only two positions were functionalised with a large amount of unreacted starting material still being present in the mixture even if excesses of *n*-BuLi and TEOS were used. One possibility for this is that the aqua ligands associated with the zinc acetate starting material stay in the complex even after complexation with $\text{Br}_2\text{-q}$. These could then have reacted with the *n*-BuLi instead of the bromo-groups resulting in a lower degree of substitution. Note that henceforth this mixture of silylated products will be given the moniker $\text{Zn}(\text{Si}_x\text{-q})_2$ for simplicity.

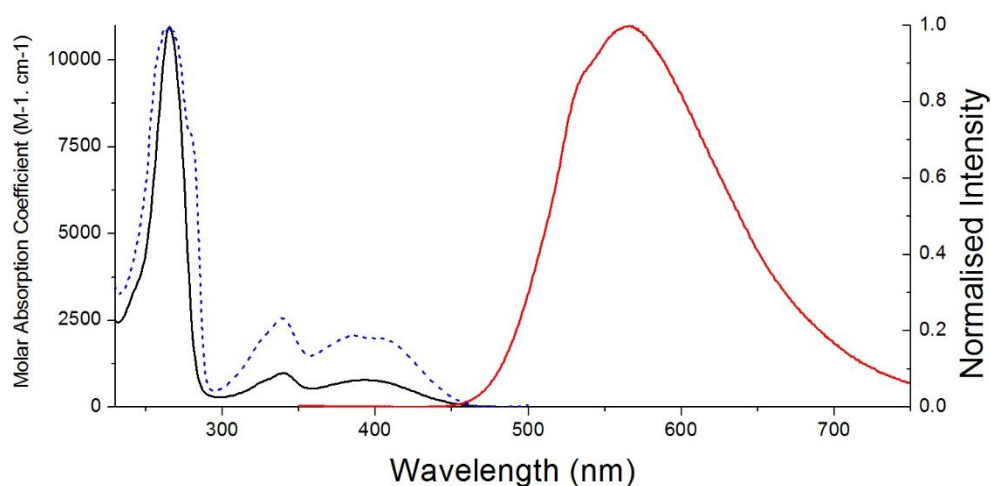


Figure 6: The absorption (black), excitation (blue hashed, $\lambda(\text{exc}) = 565$ nm) and emission (red, $\lambda(\text{exc}) = 265$ nm) spectra of $\text{Zn}(\text{Si}_x\text{-q})_2$.

Purification of these molecules was equally difficult. Recrystallisation was not possible as both the bromo- and triethoxysilyl-substituted complexes showed very similar solubilities in a variety of solvents. Column chromatography also proved a challenge as the silylated groups typically cause the complex to have a strong affinity for the silica used in this procedure. As such, even using highly polar eluent mixtures (e.g. 4:1 DCM:MeOH) does not yield useful separation of TLC spots. However, it is possible to use the silica formation reaction itself to purify the complex. Here, the silylated products will react together with the silicate precursor initially forming a highly-polar gel in which these products would sit. Any unreacted starting material would be extruded from this gel, staying in solution as the gel condenses into *m*- SiO_2 . The $\text{Zn}(\text{Si}_x\text{-q})_2$ -doped silica can then be washed with a variety of solvents.

Optical spectroscopic analysis was performed on $\text{Zn}(\text{Si}_x\text{-q})_2$ nonetheless as there was a concern that the harsh conditions of the silylation reaction, specifically the strongly basic environment provided by the presence of n-BuLi. Fortunately, as can be seen in Figure 6, the chromophore seems to be intact. This is shown by the presence of the bands corresponding to the CT transitions in the silylated sample. It is worth noting that certain shoulders (at approximately 280 and 530 nm in the excitation and emission spectra respectively) seem to be present in these spectra that were not present for $\text{Zn}(\text{Br}_2\text{-q})_2$. These are presumably due to the presence of both the silylated product as well as the bromo-substituted starting material in the sample used for the spectra. The low degree of silylation and difficulty of purification add to the reasons why $\text{Zn}(\text{Br}_2\text{-q})_2$ is used as a spectroscopic comparison to the final silica product instead of $\text{Zn}(\text{Si}_x\text{-q})_2$.

6.3 $\text{Zn}(\text{Si}_x\text{-q})_2$ -PMOM

The COK-12 method of silica synthesis of employed for these systems in order to minimise *in situ* degradation of the dye. Recalling the synthesis from Chapter 3, this involves dissolving polyethylene glycol-based surfactant Pluronic-P123 in a citric acid/trisodium citrate buffer after which sodium silicate is added and the mixture is stirred for 24 h at which time the resulting white precipitate is removed via filtration.¹⁹ Due to the lack of solubility of the $\text{Zn}(\text{Si}_x\text{-q})_2$ in water (as is common for quinolate complexes), DMSO was used as a co-solvent, being the only solvent that the complex dissolved in to any useful degree. As shown in the Chapter 5, the use of co-solvents should be kept to a minimum to avoid disruption of the micellar template. However, to facilitate the incorporation, a relatively large proportion of DMSO was had to be used (10% v/v). The complex was loaded at 1% w/w of sodium silicate where for simplicity the $\text{Zn}(\text{Si}_x\text{-q})_2$ was assumed to be pure. This typically resulted in gels being formed presumably as a result of the polarity of the liquid medium with the additional DMSO. These gels were then dried under mild heating at 50 °C in an oven forming yellow/green powders which were analysed structurally and spectroscopically.

6.3.1 Structural Analysis

Initially, it is usually useful to obtain diffractograms from X-ray techniques such as Powder XRD or SAXS. As mentioned before, the pores in COK-12 are wide enough (6-8 nm) that they cannot be analysed using Powder XRD as the main 2θ value lies below the measurement window of this technique meaning SAXS must be used. However, when this was performed for the $\text{Zn}(\text{Si}_x\text{-q})_2$ -PMOM samples (shown in Figure 7a)) no peaks were seen

above the baseline suggesting the silica was entirely amorphous. This is thought to be caused by the addition of DMSO as a co-solvent may interrupt the structure of the micelles by changing the polarity of the surrounding medium as discussed in Chapter 5. Upon further inspection with TEM however this was found to not be the case as shown by the micrographs in Figure 7b) and c). While the silica does present as highly distorted COK-12 with many nanoparticles being non-spherical in shape with disordered pores, a significant proportion do exhibit parallel channels (b) and a hexagonal arrangement of the pores (c). Indeed, Figure 7c) shows this best with the two top particles having highly disordered pores but the bottom two being almost exemplary COK-12 nanoparticles.

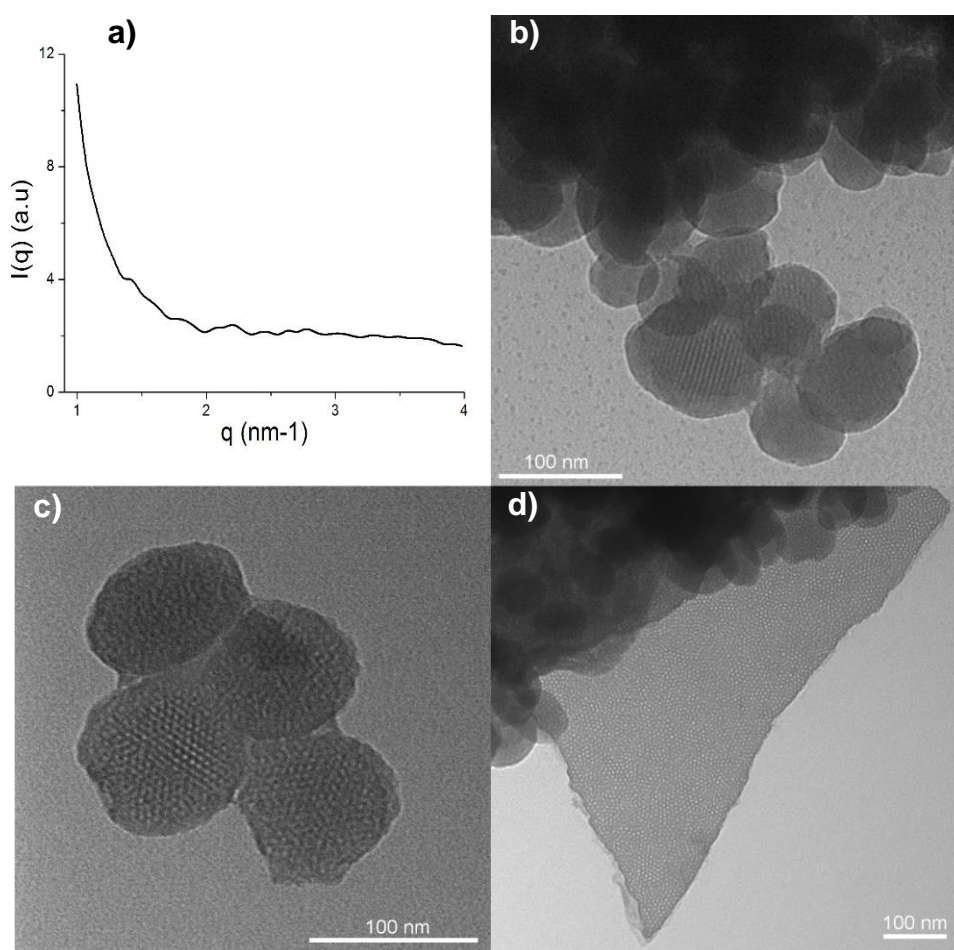


Figure 7: a) The SAXS profile for the 1% $\text{Zn}(\text{Si}_x\text{-q})_2$ -PMOM sample. b), c) and d) TEM images of different regions of this sample.

However, most intriguing is the region seen in Figure 7d) where a thin flat porous sheet of silica is shown. These pores, while uniform in terms on diameter (approx. 6 nm), are not ordered hexagonally throughout the sheet unlike typical COK-12. As it is the planes of the ordered pores that reflect X-rays for XRD and SAXS measurements,²⁰ these non-crystalline

sheets, as well as the amorphous particles may be the reason for the featureless scattering pattern seen in Figure 7a). This sheet-like morphology may have been caused by the presence of $\text{Zn}(\text{Si}_2\text{-q})_2$ as, while it was impure when it was added, only the bromo-substituted starting material was present in the crude product (as shown by NMR) which was removed via silica formation. It may be that these flat regions are where the zinc complex has incorporated into the silica.. It would be useful to perform an elemental analysis on this sample such as energy-dispersive X-ray spectroscopy (EDX) which would determine whether the zinc was confined to the flat regions or was spread uniformly throughout the sample.²¹

6.3.2 Spectroscopic Analysis

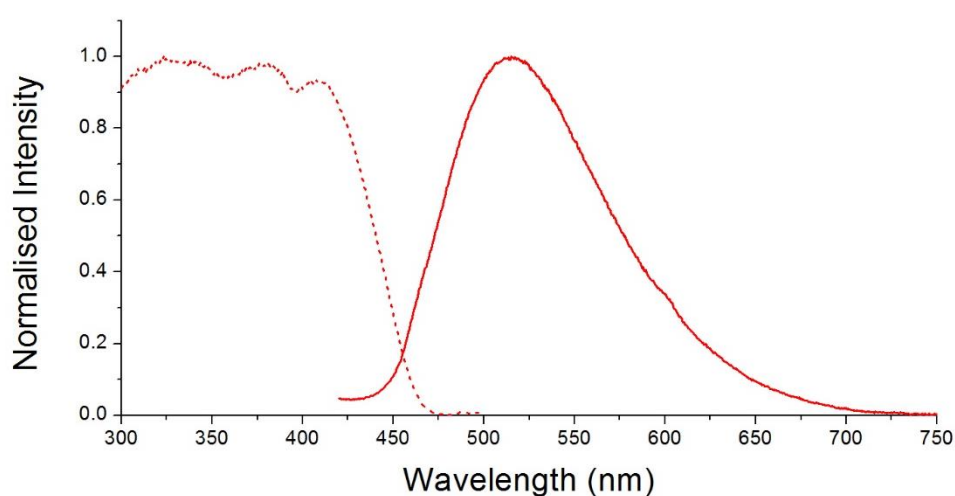


Figure 8: The excitation (hashed, $\lambda(\text{em}) = 530 \text{ nm}$) and emission (solid, $\lambda(\text{exc}) = 400 \text{ nm}$) spectra of the 1% $\text{Zn}(\text{Si}_x\text{-q})_2$ -PMOM taken as suspensions in water (make own).

The steady-state photoluminescence spectra of the 1% $\text{Zn}(\text{Si}_x\text{-q})_2$ -PMOM are shown in Figure 8 recorded as $1 \text{ mg}\cdot\text{mL}^{-1}$ suspensions in water. While the resolution of the peaks in excitation spectrum is lost as a result of m-SiO₂ encapsulation, most probably due to scattering, it is still clear to see the CT bands at around 380 and 410 nm. Assuming the latter is the emissive state and given that the emission peak maximum is found at 515 nm, this gives a Stokes Shift of $5,513 \text{ cm}^{-1}$. This sees a marked decrease when compared to the complex when free in solution where for $\text{Zn}(\text{Br}_2\text{-q})_2$ the Stokes shift is $6,929 \text{ cm}^{-1}$. This corresponds to a much lower geometrical change in the molecule as a result of excitation. Furthermore, this can be interpreted as evidence that incorporation of the complex into silica is successful, as molecular movement would be restricted by the rigid network.

Excited state lifetime analysis of the hybrid silica also suggests the encapsulation process was successful. Whereas, **Zn(Br₂-q)**₂ exhibited a monoexponential decay of the excited state with a lifetime of around 5 ns (depending on the solvent), the PMOM decays bi-exponentially with a weighted average lifetime of 1.43 ns. The deconvolution of the trace means a new species is formed as a result of silica formation. Looking back on Chapter 3,²² and by extension the work by Vu *et al.*,²³ this is most likely due to the formation of aggregates as a result of encapsulation opening up new non-radiative deactivation pathways whether via thermal relaxation within the solid matrix or energy transfer. Also, work into thin **Zn(q)**₂ films by Armstrong *et al.* reported a red-shifted emission as a result of deposition, which took place despite the increased rigidity introduced. This was attributed to excimers as the absorption spectrum remained unchanged. While it is a blue-shifted emission observed here, excited state aggregates could also be forming within the PMOM.⁹

6.3.3 Rhodamine B-Zn(Si_x-q)₂ Antenna

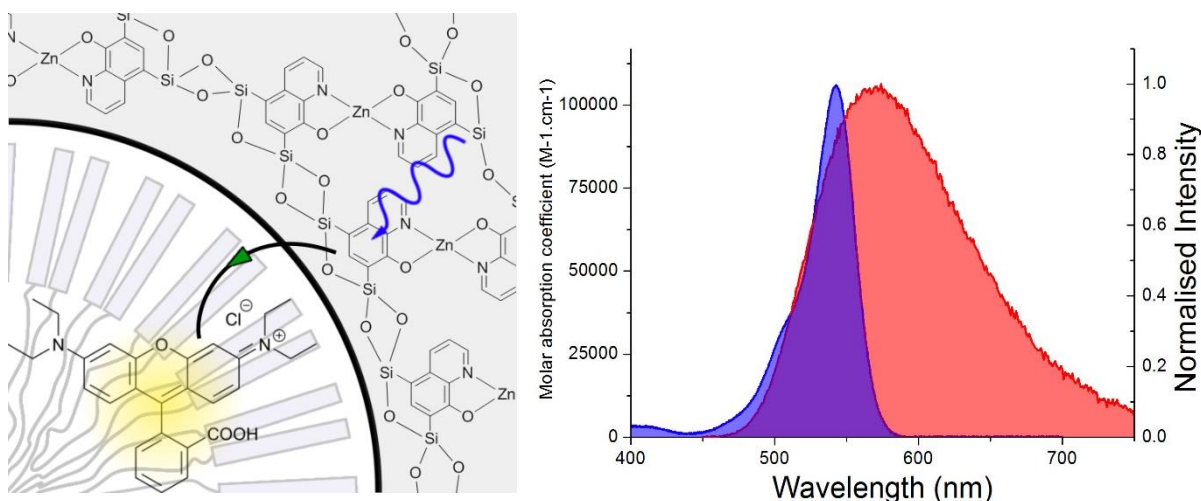


Figure 9: (left) A diagram showing energy transfer from the **Zn(Si_x-q)₂**-PMOM scaffold to a Rhodamine B guest molecule. (right) The spectral overlap (purple) between the emission spectrum of **Zn(Br₂-q)₂** in THF (red) and the absorption spectrum of Rhodamine B (blue).

As this project is working towards the synthesis of light-harvesting antennae with m-SiO₂, the energy transfer properties of these PMOMs were probed. This involved introducing a different dye in to the pores as a guest. With the absorption bands of the **Zn(Si_x-q)₂**-PMOM being shifted so far towards the blue, it was hypothesised that this would act as the donor in the FRET system with an appropriate guest acting as the acceptor. As such, a dye had to be chosen with absorption bands that overlapped with the emission bands of the **Zn(Si_x-q)₂**-PMOM, for instance **BPJ2** or **JM1**. As the photophysics of these dyes are still under

investigation however, it was decided that a well characterised dye would be better suited for these experiments. Among the wide variety of organic fluorescent molecules studied to date, rhodamine dyes have found many uses in photophysical research with their most common use as fluorescence quantum yield standard, most notably Rhodamine 6G.²⁴ They also have been applied in a variety of fields such as laser dyes,²⁵ fluorescence microscopy probes²⁶ and photodynamic therapy (PDT) agents²⁷ amongst many others. As one would expect, these dyes exhibit excellent photophysical properties with high ϵ and Φ_F values as well as being stable under a variety of conditions such as temperature and solvents.²⁴ Here, Rhodamine B (**RhB**) was chosen as its absorption spectrum overlaps well with the emission spectrum of the **Zn(Si_x-q)₂-PMOM** as shown in Figure 9. When the two are combined, the zinc complex in the silica walls will absorb blue light generating an exciton. This exciton will then be transferred via FRET to the **RhB** enhancing its emission.

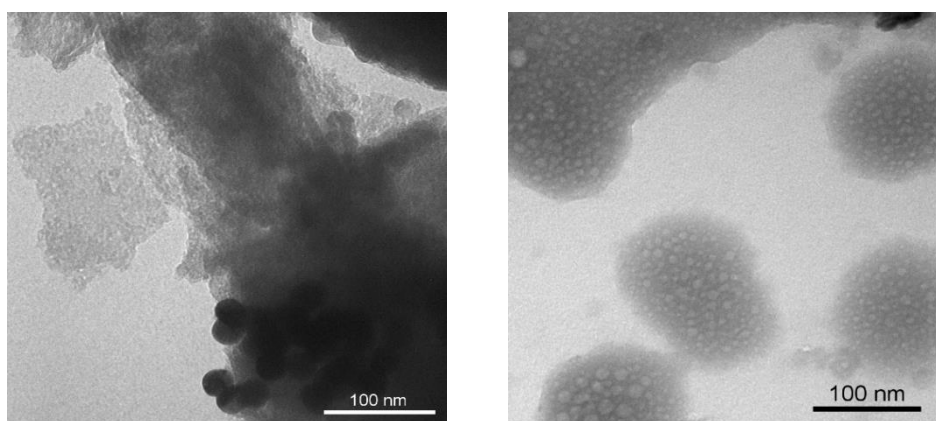


Figure 10: TEM images of 2% **RhB**-loaded COK-12.

In order to have a comparison with a reference system, COK-12 silica was first synthesised using only **RhB** at 2% dye-loading, whereby it was added alongside the Pluronic-P123 surfactant to insert it as a guest held in the pores. Thankfully, as **RhB** is soluble in water, no co-solvent was required. That being said, the addition of **RhB** shows distinct disturbance of the micellar structure as seen in the TEM images of the resulting silica (Figure 10). As seen in these micrographs, while spherical particles of silica are observed, there is a high proportion of amorphous regions throughout the sample suggesting an almost complete destruction of the template. Further analysis of the spherical regions shows highly porous particles but once again, the pores show no particular crystallinity with a wide range of diameters. However while both of these regions show no regular arrangement, they do appear to be highly porous allowing access to host-guest chemistry using these systems.

Spectroscopically, the **RhB**/Pluronic-P123@COK-12 exhibits very similar photoluminescence behaviour to **RhB** in solution (see Figure 11). The excitation and emission

peak maxima at 560 and 575 nm respectively show very little change with respect to **RhB** in solution (see Appendix, Figure A18) with the change being more pronounced in the shape of these bands. For instance, there is a higher degree of vibrational resolution exhibited, particularly in the excitation spectrum, suggesting the dyes are held in a static system like the pores of m-SiO₂. The bands also are slightly broader in the silica sample suggesting a slight variance in the environment in which the dye is held. This is explained by the lack of pore crystallinity exhibited by the sample as mentioned above. Different sized pores could cause slight shifts in the peak maxima and changes in vibrational dampening by providing more or less rigid environments and/or inducing aggregation behaviour. For both of these reasons, it is believed that the **RhB** is mostly held within the pores of this highly disturbed m-SiO₂.

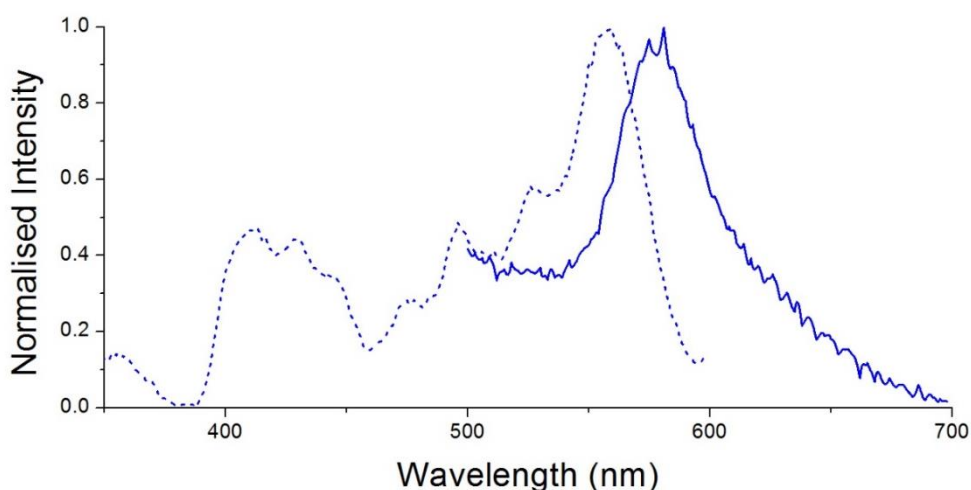


Figure 11: The photoluminescence excitation (hashed, $\lambda(\text{em}) = 530 \text{ nm}$) and emission (solid, $\lambda(\text{exc}) = 330 \text{ nm}$) spectra of 2% **RhB**/Pluronic-P123@COK-12 recorded in cyclohexane.

Next, a silica sample was synthesised with **RhB** added in tandem with the Pluronic-P123 surfactant as well as with **Zn(Si_x-q)₂** co-condensed with sodium silicate. This results in a uniformly dark pink sample suggesting successful incorporation of both dyes, as the overlaid absorption spectra of the two results in a systems that absorbs mostly in the blue and green regions of the visible spectrum. For consistency, the loadings of each dye was tested at 2% to be in line with the **RhB**/Pluronic-P123@COK-12 studies shown above. Note that the effect of increasing loading of **Zn(Si_x-q)₂** from 1% to 2% on the spectroscopic properties of the corresponding silica is minimal with excitation and emission bands and emission lifetimes being broadly unchanged. As expected, the structure of the resulting silica (named 2%,2% **RhB**/Pluronic-P123@**Zn(Si_x-q)₂**-PMOM) is highly disordered with a wide range of morphologies present with the two most common being those seen in Figure 12. First are sheet-like particles which exhibit a surprising degree of pore crystallinity, being very similar

to the structure of standard COK-12, albeit certainly less uniform. However, also observed are spherical particles similar to those seen in the samples where **RhB** is used alone in the silica synthesis. Again, these exhibit a large degree of disorder with respect to the pores suggesting a breakdown of the micellar structure as a result of the addition of the dyes.

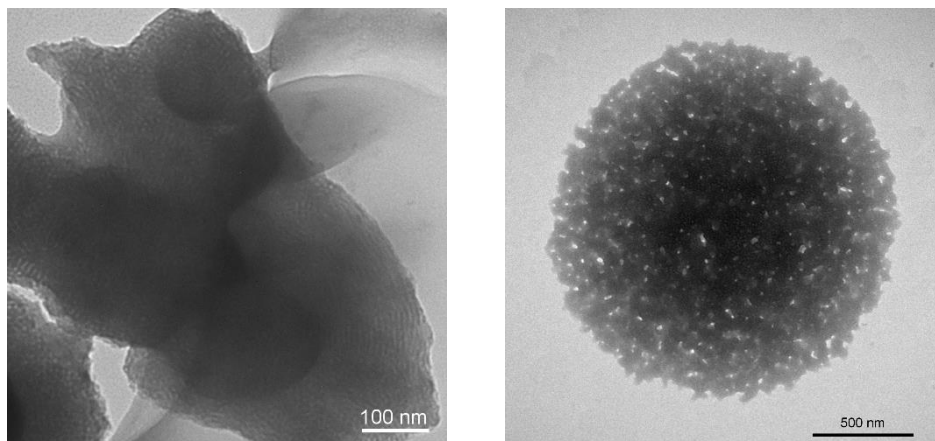


Figure 12: TEM images of the 2% $\text{Zn}(\text{Si}_x\text{-q})_2$ -PMOM synthesised with Pluronic-P123 micelles doped with 2% **RhB**.

Looking to the emission spectra shown in Figure 13, there is a marked difference when the $\text{Zn}(\text{Si}_x\text{-q})_2$ -PMOM is doped with **RhB**. Prior to this, there is a single low intensity emission band with a maximum at around 530 nm corresponding to the radiative decay of $\text{Zn}(\text{Si}_x\text{-q})_2$. Upon doping with **RhB**, a lowering of the intensity of this band was observed accompanied by the rise of a new strong vibronically coupled peak corresponding to the fluorescence of **RhB**. While not definitive proof, the quenching of the excited state on $\text{Zn}(\text{Si}_x\text{-q})_2$ suggests transfer of the exciton from the silica walls to **RhB** units held in the pores via FRET. However, it is difficult to prove this using steady-state spectra alone. As such, lifetime analysis was used to probe the excited state kinetics of this bichromophoric silica.

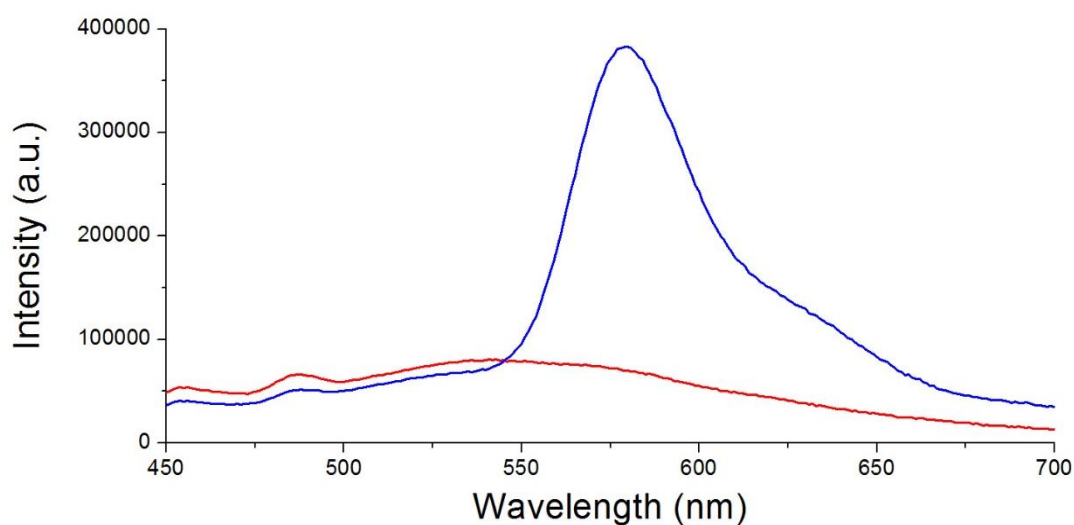


Figure 13: The photoluminescence emission spectra ($\lambda(\text{exc}) = 330 \text{ nm}$) of **RhB**-doped COK-12 (colour) and $\text{Zn}(\text{Si}_x\text{-q})_2$ -PMOM (colour).

The excited state of the **Zn(Si_x-q)₂**-PMOM, recorded at 471.8 nm, exhibits biexponential decay with a weighted average lifetime (τ_D) of 2.91 ns, typical for aromatic ligands such as quinolinates (for decay traces see Appendix, Figure A19). However, upon doping with **RhB**, the decay trace has average lifetime (τ_{DA}) of 1.26 ns, suggesting a new decay process is taking place. The short component of this biexponential is more prominent in this sample meaning fluorescence of the complex is no longer the preferred route of excited state deactivation. This behaviour is observed in a variety of PMO materials developed by Inagaki *et al.* whereby presence of a guest whether it be a rhenium complex or Pt nanoparticles depletes the lifetime of donors embedded in the silica walls like biphenyl groups or the Ru(bipy)₃ seen at the beginning of this chapter.^{3,4,28} This leads to the same conclusion here where FRET is taking place from **Zn(Si_x-q)₂** to **RhB**.²⁹ Using the lifetimes quoted above, it is possible to acquire an efficiency, E, and rate, k_{FRET} , of energy transfer via Equation 6.1 and 6.2, using Förster theory:

$$E = 1 - \frac{\tau_{DA}}{\tau_D} \quad (6.1)$$

$$k_{FRET} = \frac{1}{\tau_{DA}} - \frac{1}{\tau_D} \quad (6.2)$$

resulting in 57% and $4.56 \times 10^8 \text{ s}^{-1}$ respectively.²⁹ It is then possible to work out the donor-acceptor (r_{DA}) distance by using Equation 6.3:

$$k_{FRET} = \frac{1}{\tau_D} \left(\frac{R_0}{r_{DA}} \right)^6 \quad (6.3)$$

where R_0 is the Förster radius (the donor-acceptor distance at which $E = 50\%$), given by Equation 6.4:

$$R_0 = \sqrt[6]{\frac{9000 \ln 10 \cdot k^2 \cdot \Phi_D \cdot J_{DA}}{128 \pi^5 \cdot N_A \cdot n^4}} \quad (6.4)$$

where k^2 is the dipole-dipole orientation factor (assuming isotropic arrangement of both dyes this has a value of 2/3); Φ_D is the quantum yield of the donor in absence of the acceptor; J_{DA} is the integral overlap between the donor emission and acceptor excitation spectra with a value of $2.680 \times 10^{15} \text{ nm}^4 \cdot \text{M}^{-1} \cdot \text{cm}^{-1}$; N_A is Avagadro's constant, 6.02×10^{23} and n is the refractive index of the surrounding silica, 1.552. This results in an R_0 value of 4.4 nm from which the value for donor-acceptor distance is calculated as 4.2 nm using Equation 6.3. The pores of the **Zn(Si_x-q)₂**-PMOM have an approximate diameter of 6-7 nm assuming standard COK-12 structure so this donor-acceptor behaviour lends credence to the theory that at least some **RhB**

units are held within the pores. This is attributed to energy transfer from the walls causing activation of the guests located within the micellar template. Future work on this donor-acceptor system could look into optimisation of the dye insertion process into both the micelles and silica walls, with the aim of increasing the number of guest dyes such the zinc complex units inside the silica matrix and **RhB** held in the pores for instance by using the surfactant moieties presented in Chapters 3 and 4.²²

6.4 Conclusion

Through co-condensation of a silylated zinc-quinolate complex in a COK-12 process, a periodic mesoporous organometallosilica (PMOM) was synthesised. The silylation process showed only partial completion with much starting material left unreacted even after various changes in reaction conditions. The resulting silylated product was also difficult to purify by standard methods (i.e. column chromatography, recrystallisation etc.); however, the co-condensation process provides the expulsion of non-silylated products via polarity differences when the silicate gel is formed throughout the synthesis. While these PMOMs exhibited featureless SAXS profiles, TEM images show a highly porous silica nanoparticles that showed at least some crystallinity with respect to the pores. Surprisingly, however, thin silica sheets were also observed that showed non-periodic pores which could have contributed to the lack of peaks in the X-ray scattergram. This paves the way to using differing proportions of silicate precursors to alter the morphology of the resulting m-SiO₂.

Further to this the antenna properties of these materials were probed using the addition of rhodamine B guests inserted into the micellar template. While this did result in highly disordered silica, both steady-state and time-resolved photoluminescence spectroscopy suggested a distinct quenching of the **Zn(Si_x-q)₂** excited state. This was attributed to energy transfer from the **Zn(Si_x-q)₂** in the PMOM walls to the **RhB** guests held in the pores. Despite the non-crystalline m-SiO₂ formed, the calculated donor-acceptor distance of 4.4 nm provides evidence that the two dyes are held together in close proximity within the scaffold. Through careful consideration of spectral overlap, systems such as these could be synthesised with a variety of dyes in order to develop panchromatic light-harvesting antennae for use as solid-state photosensitiser, in photocatalysis and also in lighting devices.

6.5 Experimental

Synthesis of Zinc bis(5,7-dibromoquinolate), **Zn(Br₂-q)₂**:

Zn(OAc)₂·2H₂O (165 mg, 0.750 mmol) and 5,7-dibromo-8-hydroxyquinoline (450 mg, 1.5 mmol) were dissolved in ethanol (20 mL) resulting in a yellow solution. The mixture was heated under reflux at ~60°C for 5 h with stirring forming a yellow precipitate. The reaction mixture was allowed to cool to room temperature and the precipitate was then filtered under vacuum, washed with ethanol, and dried overnight in a vacuum desiccator to afford a yellow flaky solid (425 mg, 0.637 mmol, 85.0% yield). ¹H NMR (400MHz, d₆-DMSO): δ = 8.48 (d, J = 4.5 Hz, 2H, N-CHAr), 8.43 (d, J = 8.5 Hz, 2H, CHAr), 7.94 (s, 2H, Br-CHAr-Br), 7.70 (dd, J = 8.5, 4.5 Hz, 2H, CHAr).

Silylation of Zn(Br₂-q)₂ to form Zn(Si_x-q)₂:

Zn(Br₂-q)₂ (400 mg, 0.600 mmol) was partially dissolved in dry THF (100 mL) under N₂. n-BuLi (1.6 M in pentane, 1.50 mL, 2.40 mmol) was added dropwise to the mixture under N₂ at -78°C. Upon addition the reaction mixture turned from yellow to orange and from partially to fully dissolved. Meanwhile, in a separate flask, TEOS (1.60 mL, 7.20 mmol) was dissolved in dry THF (100 mL) under N₂ and was cooled to -78°C. 50 min after the addition of n-BuLi, the orange reaction mixture was transferred dropwise via a cannula to the flask containing the TEOS solution. After 1 h of stirring the orange reaction mixture was quenched with H₂O (10 mL) and was allowed to warm to room temperature. The THF was then removed under reduced pressure. The resulting orange solid was dissolved in diethyl ether (100 mL) and H₂O (100 mL). The yellow organic layer was washed with H₂O (2 x 60 mL), and the orange aqueous layer was washed with Et₂O (2 x 120 mL). The organic extracts were combined, dried with MgSO₄, filtered under vacuum, and the solvent was removed under reduced pressure to afford a yellow-orange solid which was dried under vacuum. The solid was purified by dissolving the soluble impurities in DCM and decanting of this liquid. The silica impurity that had formed in the reaction moved with this solution and the remaining yellow solid was partially purified product (49 mg, 0.049 mmol, 8.2%). ¹H NMR (400MHz, d₄-MeOD): δ = 8.77 (s, 2H, CHAr), 8.36 (d, J = 8.3 Hz, 2H, CHAr), 7.66 (d, J = 8.8 Hz, 2H, CHAr), 7.54 (dd, J = 8.2, 4.6 Hz, 2H, CHAr), 6.96 (d, J = 8.8 Hz, 2H, CHAr), 3.49 (q, J = 7.0 Hz, 15H, -OCH₂CH₃), 1.18 (t, J = 7.0 Hz, 23H, -OCH₂CH₃). Peaks corresponding to Zn(Br₂-q)₂ were still present in this mixture.

Synthesis of 1% Zn(Si_x-q)₂-PMOM:

Pluronic P123 (95 mg, 0.0163 mmol), citric acid monohydrate (91 mg, 0.472 mmol), and trisodium citrate dihydrate (86 mg, 0.293 mmol) were dissolved in H₂O (2.5 mL) with stirring. After 3.5 h, Zn(Si_x-q)₂ (11 mg, 0.011 mmol) in DMSO (650 μL) and sodium silicate solution (390 μL, 0.282 g·mL⁻¹) were added to the surfactant resulting in a cloudy, yellow-green reaction mixture. After 5 min of stirring, the stirrer bar was removed and the reaction mixture was covered and left to stand for 24 h. The green gel formed was filtered off under vacuum, washed with H₂O, and dried in air to afford a bright green granular solid (71 mg).

Synthesis of 2% Zn(Si_x-q)₂-PMOM:

Pluronic P123 (95 mg, 0.0163 mmol), citric acid monohydrate (91 mg, 0.472 mmol), and trisodium citrate dihydrate (86 mg, 0.293 mmol) were dissolved in H₂O (2.5 mL) with stirring. After 3.5 h, Zn(Si_x-q)₂ (22 mg, 0.011 mmol) in MeOH (380 μL) and sodium silicate solution (386 μL, 0.282 g·mL⁻¹) were added to the surfactant resulting in a cloudy, yellow-

green reaction mixture. After 5 min of stirring, the stirrer bar was removed and the reaction mixture was covered and left to stand for 24 h. The mixture was then left to dry in air for 48 h, producing a dark green gel. This was filtered under vacuum, washed with H₂O and dried in air to afford a grey-green flaky powder (83 mg).

Synthesis of 2% **RhB**/Pluronic-P123@COK-12:

Pluronic P123 (92 mg, 0.01538 mmol), citric acid monohydrate (91 mg, 0.472 mmol) and trisodium citrate dihydrate (86 mg, 0.293 mmol) were dissolved in H₂O (2.5 mL) with stirring. From a stock solution in H₂O, **RhB** (326 μL, 1 mM, 0.326 μmol) was also added, resulting in a bright pink mixture. After 24 hours, sodium silicate solution (393 μL) was added. After 30 min, a gel had formed, so the stirrer bar was removed, a stopper inserted in the flask and the mixture left to rest for 48 hours producing a bright pink gel. This was filtered under vacuum and washed with H₂O to afford a bright pink gel (77 mg).

Synthesis of 2%:2% **RhB**/Pluronic-P123@**Zn(Si_x-q)₂**-PMOM:

Pluronic P123 (92mg, 0.01538mmol), citric acid monohydrate (91mg, 0.472mmol) and trisodium citrate dihydrate (86mg, 0.293mmol) were dissolved in H₂O (2.5mL) with stirring. From a stock solution in H₂O, **RhB** (326 μL, 1 mM, 0.326 μmol) was also added, resulting in a bright pink mixture. After 24 hours, **Zn(Si_x-q)₂** (22 mg, 0.011 mmol) in MeOH (380 μL) and sodium silicate solution (386 μL, 0.282g mL⁻¹) were added. After 30 minutes a dark pink gel had formed, so the stirrer bar was removed, a stopper inserted in the flask and the mixture left to rest for 48 hours producing a bright pink gel. This was filtered under vacuum and washed with H₂O a dark pink solid (82mg, 0.0126mmol, 82%).

References

1. K. V. Rao, A. Jain and S. J. George, *J. Mater. Chem. C*, 2014, **2**, 3055-3064.
2. F. Hoffmann and M. Froba, *Chem. Soc. Rev.*, 2011, **40**, 608-620.
3. X. Liu, Y. Maegawa, Y. Goto, K. Hara and S. Inagaki, *Angew. Chem. Int. Ed*, 2016, **55**, 7943-7947.
4. H. Takeda, M. Ohashi, Y. Goto, T. Ohsuna, T. Tani and S. Inagaki, *Adv. Funct. Mater.*, 2016, **26**, 5068-5077.
5. London Metal Exchange, <https://www.lme.com/Metals/Ferrous> (accessed July 2018).
6. F. Aurus, Y. Li, F Löbermann, M. Dölinger, J. Schuster, L. M. Peter, D. Trauner and T. Bein, *Chem. Eur. J.*, 2014, **20**, 14971-14975.
7. A. Terenzi, A. Lauria, A. M. Almerico and G. Barone, *Dalton Trans.*, 2015, **44**, 3527-3535.
8. R. Sakamoto, T. Iwashima, M. Tsuchiya, R. Toyoda, R. Matsuoka, J. F. Kogel, S. Kusaka, K. Hoshiko, T. Yagi, T. Nagayama and H. Nishihara, *J. Mater Chem. A*, 2015, **3**, 15357-15371.
9. T. A. Hopkins, K. Meerholz, S. Shaheen, M. L. Anderson, A. Schmidt, B. Kippelen, A. B. Padias, H. K. Hall, N. Peyghambarian and N. R. Armstrong, *Chem. Mater.*, 1996, **8**, 344-351
10. (a) C. W. Tang and S. A. VanSlyke, *Appl. Phys. Lett.*, 1987, **51**, 913-915. (b) J.-A. Cheng and C. H. Chen, *J. Mater. Chem.*, 2005, **15**, 1179-1185.
11. A. Meyers, C. South and M. Weck, *Chem. Commun.*, 2014, 1176-1177.
12. (a) S. Pramanik, S. Bhandari and A. Chattopadhyay, *J. Mater. Chem. C*, 2017, **5**, 7291-7294. (b) S. Bhandari, S. Roy and A. Chattopadhyay, *RSC Adv.*, 2014, **4**, 24217-24221
13. A. Corma, U. Díaz, B. Ferrer, V. Fornés, M. S. Galletero and H. García, *Chem. Mater.*, 2004, **16**, 1170-1176.
14. N. Prabavathi, A. Nilufer and V. Krishnakumar, *Spectrochim. Acta A*, 2013, **114**, 449-474.
15. B. F. Minaev, G. V. Baryshnikov, A. A. Korop, V. A. Minaeva and M. G. Kaplunov, *Opt. & Spectrosc.*, 2012, **113**, 333-340.
16. R. Díaz-Torres and S. Alvarez, *Dalton Trans.*, 2011, **40**, 10742-10750.
17. J. Michl, M. Montalti, A. Credi, L. Prodi and M. T. Gandolfi, in *Handbook of Photochemistry*, CRC Press, Boca Raton, USA, 3rd edn., 2006, ch. 1, pp 19-21.
18. A. S. Manoso, C. Ahn, A. Soheili, C. J. Handy, R. Correia, W. M. Seganish and P. DeShong, *J. Org. Chem.*, 2004, **69**, 8305-8314.
19. (a) J. Jammaer, A. Aerts, J. D'Haen, J. W. Seo and J. A. Martens, *J. Mater. Chem.*, 2009, **19**, 8290-8293 (b) J. Jammaer, T. S. van Erp, A. Aerts, C. E. Kirschhock and J. A. Martens, *J. Am. Chem. Soc.*, 2011, **133**, 13737-13745.
20. F. Michaux, N. Baccile, M. Imperor-Clerc, L. Malfatti, N. Folliet, C. Gervais, S. Manet, F. Meneau, J. S. Pedersen and F. Babonneau, *Langmuir*, 2012, **28**, 17477-17493.
21. M. B. Ward, N. Hondow, A. P. Brown and R. Brydson, in *Nanocharacterisation*, ed. A. I. Kirkland and S. J. Haigh, Royal Society of Chemistry, Cambridge, UK, 2nd edn, 2015, ch. 4, pp 114-117.
22. F. Cucinotta, B. P. Jarman, C. Caplan, S. J. Cooper, H. J. Riggs, J. Martinelli, K. Djanashvili, E. La Mazza, F. Puntoriero, *ChemPhotoChem* **2018**, **2**, 196-206.

23. T. T. Vu, S. Badré, C. Dumas-Verdes, J-J Vachon, C. Julien, P. Audebert, E. Y. Senotrusova, E. Y. Schmidt, B. A. Trofimov, R. B. Pansu, G. Clavier and R. Méallet-Renault, *J. Phys. Chem. C*, **2009**, *113* (27), pp 11844–11855.
24. M. Beija, C. A. M. Afonso and J. M. G. Martinho, *Chem. Soc. Rev.*, 2009, **38**, 2410-2433
25. (a) K. H. Drexhage, *J. Res. Natl. Bur. Stand.*, 1976, **80A**, 421–428. (b) K. H. Drexhage, *Laser Focus*, 1973, **9**, 35–39.
26. (a) Z. G. Zhou, M. X. Yu, H. Yang, K. W. Huang, F. Y. Li, T. Yi and C. H. Huang, *Chem. Commun.*, 2008, 3387–3389. (b) W. Liu, M. Howarth, A. B. Greytak, Y. Zheng, D. G. Nocera, A. Y. Ting and M. G. Bawendi, *J. Am. Chem. Soc.*, 2008, **130**, 1274–1284.
27. K. S. Davies, M. K. Linder, M. W. Kryman and M. R. Detty, *Bioorg. Med. Chem.*, 2016, **24**, 3908-3917.
28. N. Mizoshita, Y. Goto, Y. Maegawa, T. Tani and S. Inagaki, *Chem. Mater.*, 2010, **22**, 2548-2554.
29. T. Förster, *Discuss. Faraday Soc.*, 1959, **27**, 7-17.

Chapter 7. Summary

7.1 Introduction

Presented in this thesis is research that explores the use of the host-guest chemistry of mesoporous silica (m-SiO₂) to develop new light-harvesting systems. Here, the micellar template and rigid matrix were used to better control the spatial arrangement of a series of dyes within the silica scaffold. Through this, the photophysical properties and energy transfer characteristics were probed and tuned, acting as preliminary experiments into m-SiO₂ based light-harvesting antennae. Chapter 1 presents a number of light-harvesting systems (both natural and artificial) that rely on the establishment of an energy cascade facilitated by strict spatial control of donor and acceptor units. While a number of host-guest materials have been used to achieve this (e.g. zeolites), this thesis has focussed on mesoporous silica which has found applications in a number of fields including supramolecular photochemistry.

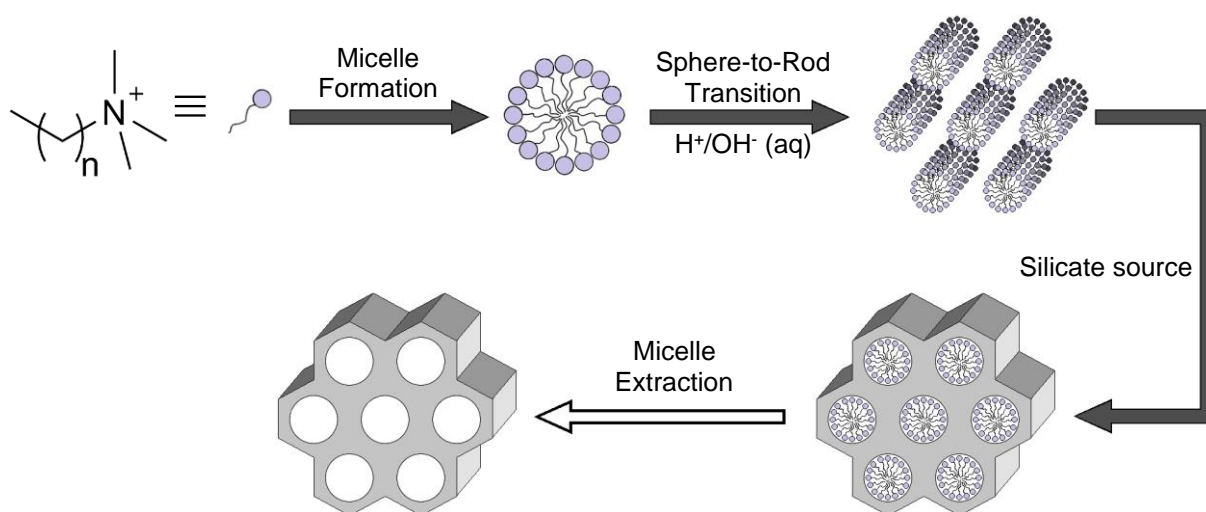


Figure S1: A scheme showing the steps involved in synthesis of mesoporous silica around micelles.

Depending on the synthesis used, the pore sizes of the mesoporous silica can be tuned making these systems highly versatile. For MCM-41, cetyltrimethylammonium bromide (CTAB) is used as the surfactant from which the micellar template is formed. Around these micelles, tetraethylorthosilicate (TEOS) is condensed in a basic medium producing mesoporous silica with pore diameters around 4 nm. Alternatively, a polyethylene-polypropylene (PEO-PPO) surfactant can be used instead of CTAB, like in the synthesis of SBA-15 and COK-12, with, respectively, an acidic or a neutral medium now used to form the

silica. This way, m-SiO₂ is formed with much larger pores of up to 30 nm in diameter. Since its introduction in the early 1990's, m-SiO₂ has been used in a variety of ways for light harvesting and conversion. This is because it can be functionalised with organic groups whether post-synthetically (grafting) or *in situ* (co-condensation or PMO). However, the micellar template is commonly removed after the silica is formed to make way for guests to be diffused through the pores. This thesis presents a number of experiments that show that the micelles can be used to introduce a more homogeneous distribution of guests throughout the matrix.

Chapter 2 presents the analytical techniques employed throughout this thesis as well as the theory underpinning them.

7.2 Mesoporous silica templated with dye-doped micelles

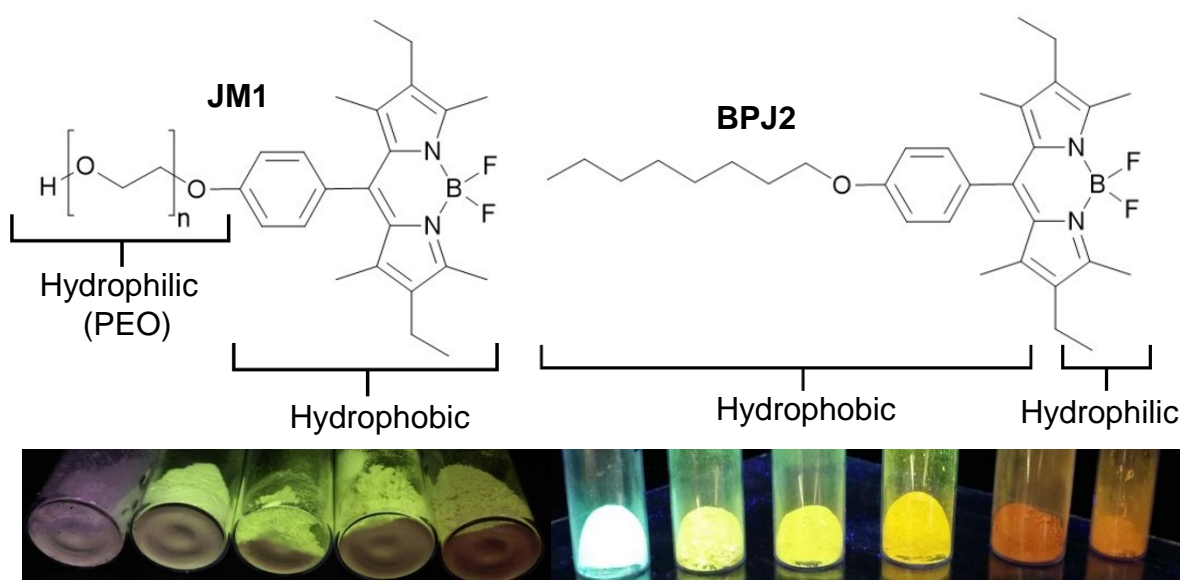


Figure S2: The structures of **JM1** (left) and **BPJ2** (right) with their hydrophilic and hydrophobic regions highlighted. On average, $n = 47$ PEG units. (bottom) The silica samples made with **JM1** and **BPJ2** (left and right respectively).

In Chapter 3, two BODIPY dyes, **JM1** and **BPJ2**, were synthesised with long chains mimicking the surfactants used in COK-12 and MCM-41 synthesis respectively. They were then dissolved in tandem with the micellar phase before being encapsulated in m-SiO₂ at various dye-loadings (1, 5, 7.5, 10, 20 and 50 mol% of the surfactant). Very little structural change was induced in the COK-12 samples as a result of **JM1** insertion with a slight pore shrinkage observed as dye-loading increased as seen by SAXS studies. While the steady state spectra of these materials showed no significant change, the excited state lifetime, run using

TCSPC measurements, exhibited a marked decrease induced by higher dye-loadings attributed to exciton traps and aggregation effects.

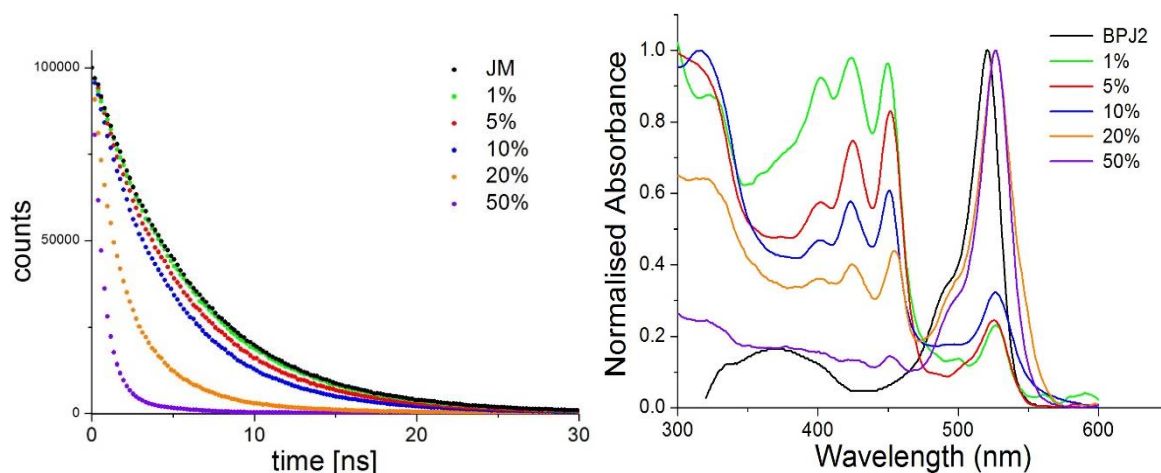


Figure S3: (left) The fluorescence decay traces of **JM1** in solution as well as the various **JM1/PluronicP-123@COK-12** samples. (right) The steady-state absorbance (as $0.3 \text{ mg}\cdot\text{mL}^{-1}$ suspensions in cyclohexane) of **BPJ2/CTAB@MCM-41** at a series of dye-loading.

The **BPJ2/CTAB@MCM-41** exhibited a number of unexpected behaviours. For instance, the crystallinity of the silica seems to decrease as dye-loading increases up to 10%. However, increasing the loading further sees the (100), (110) and (200) peaks resolve and sharpen with the TEM images of the 50% showing exemplary MCM-41 particles. This could be attributed to a number of factors including not allowing the micellar phase long enough to form properly or the use of MeCN as a co-solvent (required to dissolve **BPJ2**) causing the polarity of the medium to change resulting in a disrupted mesophase. Additionally, these samples exhibited a new blue-shifted species (**BS**) which formed at some point during the silica synthesis through H-aggregation or in silico reaction. Through photoluminescence excitation and transient absorption spectroscopy, FRET was shown to occur in a time scale of 20-80 ps (dye-loading dependent) from **BS** to **BPJ2** meaning these materials are bichromophoric antennae synthesised using only one input dye.

7.3 BODIPY-doped micelle and silica formation dynamics

Chapter 4 presents an in-depth series of experiments into the synthesis of MCM-41, where every step was investigated via photoluminescence emission spectroscopy using **BPJ2** as a fluorescent probe. These were initially performed in order to determine the nature and formation of **BS**, although a number of other interesting insights were gained. Through the spectra taken after addition of **BPJ2** to a CTAB solution, it was shown that the fluorescence intensity increased with time as shown in Figure S4. This acts as evidence for the distribution

of **BPJ2** throughout the template as a result of the dynamic nature of micelles. Initially, when **BPJ2** is added, it aggregates causing quenching of the excited state. However, over time the monomers within these aggregates dissociate from the micelles and re-insert elsewhere allowing radiative decay of the excited state. This process takes at least 24 h lending credence to the idea that the micellar template had not fully formed within 2 h as was previously thought. This could go towards explain the trend in m-SiO₂ crystallinity seen in the powder XRD patterns in Chapter 3.

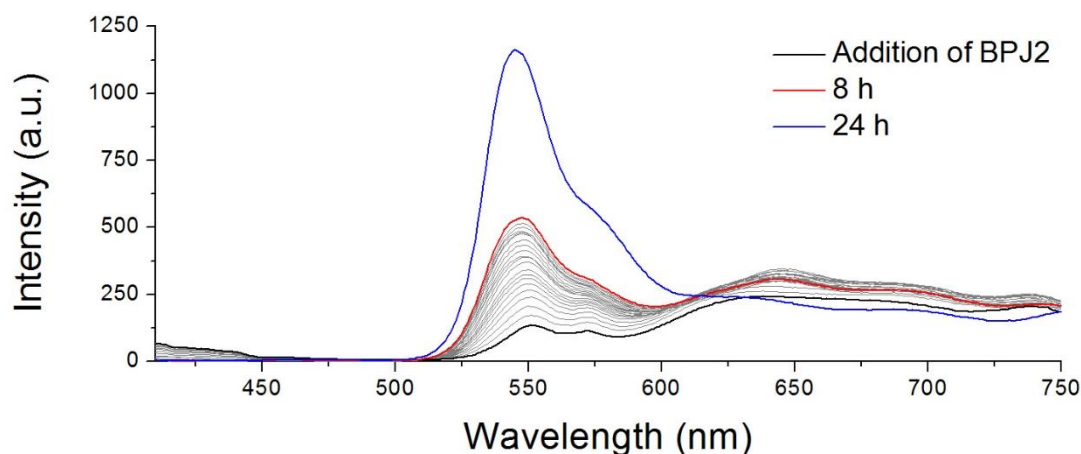


Figure S4: The first series of emission spectra of **BPJ2**-loaded CTAB micelles at 1% dye loading ($\lambda(\text{exc}) = 400 \text{ nm}$).

Eventually, it was found that upon heating of the final silica samples to dry them, the conversion of **BPJ2** to **BS** was induced. By running a kinetic study on this process, it was found that the formation of **BS** is a second order process (see Figure S5). Through this, rate laws could be derived depending on the hypothesis on the nature of **BS**, whether is through H-aggregation or in-silico reaction. These rate laws are as follows:

$$\text{rate} = k[\text{BPJ2}]^2 \quad (4.1)$$

for H-aggregation where k is the rate constant. Here, the elevated temperatures in the drying process allow the **BPJ2** molecules to re-orientate within the micellar template through which two nearby units can aggregate. This means that the rate is going to be dependent on the coming together of two monomers hence the second order process. The in-silico reaction rate law is:

$$\text{rate} = k[\text{BPJ2}][I] \quad (4.2)$$

where I is an impurity introduced at some point in the silica synthesis. By raising the temperature, **BPJ2** and I are taken above the activation energy required for the conversion to

BS. A number of candidates for I were considered including magnesium silicate (introduced as an impurity in commercially bought NaOH) or silanol groups formed through incomplete condensation of the silicate precursor. Further experiments will be required to determine both what **BS** is as well as the nature of its formation

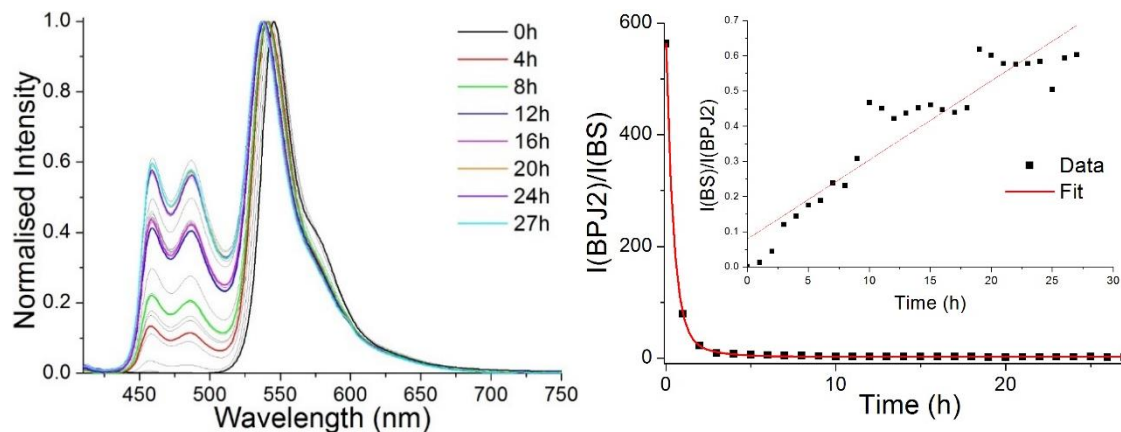


Figure S5: (left) The series of emission spectra ($\lambda(\text{exc}) = 400 \text{ nm}$) taken from the 1% **BPJ2/CTAB@MCM-41** samples removed periodically from the oven. (right) The plot and kinetic fitting of the **BPJ2/BS** intensity ratio against time. (inset) The plot of $I(\text{BS})/I(\text{BPJ2})$ ($1/\{I(\text{BPJ2})/I(\text{BS})\}$) against time.

7.4 Emission tuning with Pt(II) complexes in m-SiO₂ via aggregation

In Chapter 5, the incorporation of a different kind of dye to BODIPY into the micellar template of m-SiO₂ was introduced. The aim of this chapter was to widen the scope of the research presented in this thesis. The dyes chosen were four phosphorescent platinum(II) complexes known for their use in OLEDs, namely **VNK-40-C12**, **NCN-60**, **TGV-19** and **N-129**. These dyes also exhibit a marked red-shift upon film deposition brought on by aggregation. As such, these dyes were incorporated into the micellar phase of m-SiO₂ in order to induce this bathochromic shift without the need of excessive amounts of platinum as well as to improve their properties through encapsulation in a rigid and chemically inert scaffold. Being non-soluble in water however, a number of co-solvents miscible with water were tested using ¹H NMR studies to determine how much they affected the structure of the micellar template. From these experiments, it was found that while THF and MeCN can be used at small proportions (1% v/v), larger amounts easily resulted in the disruption of the micelles. However, MeOH and DMF were to not show much, if any, disruption and as such are put forward as ideal co-solvent for the inclusion of organic dyes into silica in future experiments.

With these findings in mind, the four Pt(II) dyes were incorporated into m-SiO₂ at a various dye-loadings (1, 10 and 25%). All four complexes exhibited an aggregation-induced red-shift upon increase in dye-loading (see Figure S6), although not to the same degree.

VNK-40-C12 in particular exhibited a very small bathochromic shift, most likely due it being functionalised with three C-12 chains which sterically hinder aggregation. The excited state lifetimes of the silica samples made with N-129 and TGV-19 were analysed using TCSPC measurements. They both showed significant decreases in the excited state of the monomer upon increased dye-loading further supporting the hypothesis that aggregation was taking place. Interestingly, these were performed in non-degassed samples meaning that the silica is shielding the dyes from triplet-triplet annihilation with O₂ molecules dissolved in the suspension.

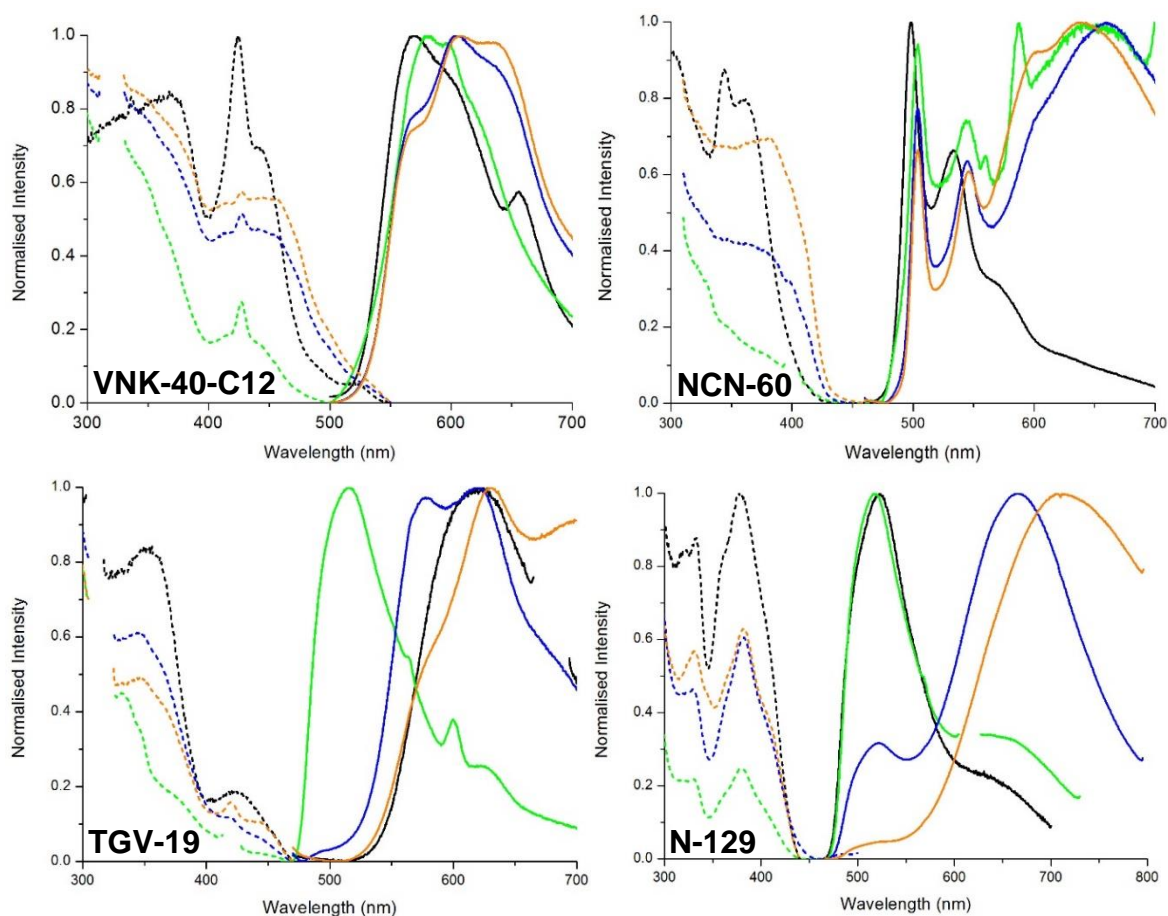


Figure S6: The photoluminescence excitation (dashed lines) and emission (solid lines) spectra of the Pt(II) complexes in solution (black) and in silica at dye-loadings of 1 (blue), 10 (yellow) and 25% (orange).

7.5 Synthesis and optical properties of a new organometallosilica

Chapter 6 saw a different method of incorporating organic (or in this case organometallic) groups into the mesoporous silica, namely co-condensation with bridges silicate precursors to make a PMO (or PMOM). Here, a zinc bis-quinolate complex was silylated and incorporated into COK-12, with TEM images of this material shown in Figure S7. While typical particles of COK-12 are present in this sample, a number of other morphologies are observed. Most common regions of amorphous silica that, while highly porous, show no

crystallinity with respect to the pores order. More intriguing however are the flat sheets of porous silica that, though not rare, certainly were not prevalent throughout the sample. While they exhibit pores of uniform size (approx. 6 nm), they are not ordered, hexagonally or otherwise. These different regions within the same sample contribute to a SAXS profile that shows no discernible peaks at all. Spectroscopically, these materials show the same photoluminescence peaks as the zinc complex in solution but with a marked decrease in Stokes shift which has been attributed to increased rigidity provided by the silica matrix.

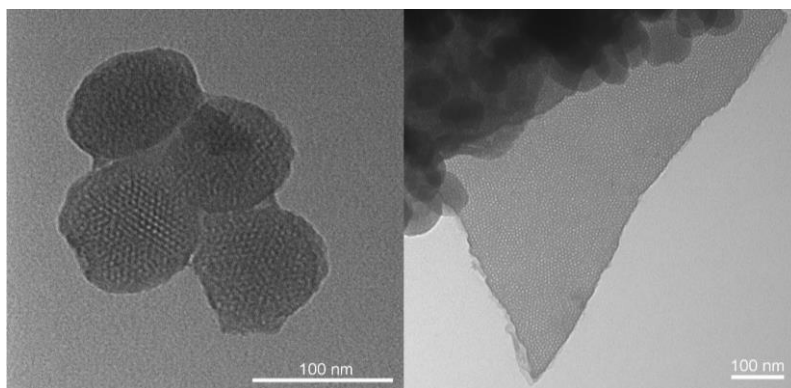


Figure S7: TEM images of different regions of the 1% $\text{Zn}(\text{Si}_x\text{-q})_2\text{-PMOM}$

Rhodamine B (**RhB**) was then incorporated into the micellar template of this $\text{Zn}(\text{Si}_x\text{-q})_2\text{-PMOM}$ in order to investigate whether energy transfer can occur between the two. Figure S8 shows the photoluminescence emission spectra of the $\text{Zn}(\text{Si}_x\text{-q})_2\text{-PMOM}$ synthesised with and without **RhB** doped micelles. A decrease in the fluorescence of $\text{Zn}(\text{Si}_x\text{-q})_2$ is observed concomitantly with the emission of **RhB** showing evidence of energy transfer from the former to the latter. TCSPC measurements and FRET theory were used to determine a donor-acceptor distance of 4.2 nm. This is plausible as the average pore diameter of COK-12 is 6-7 nm.

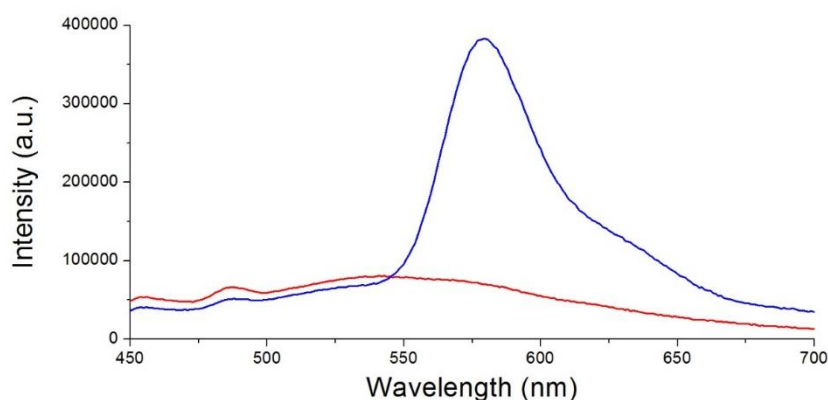


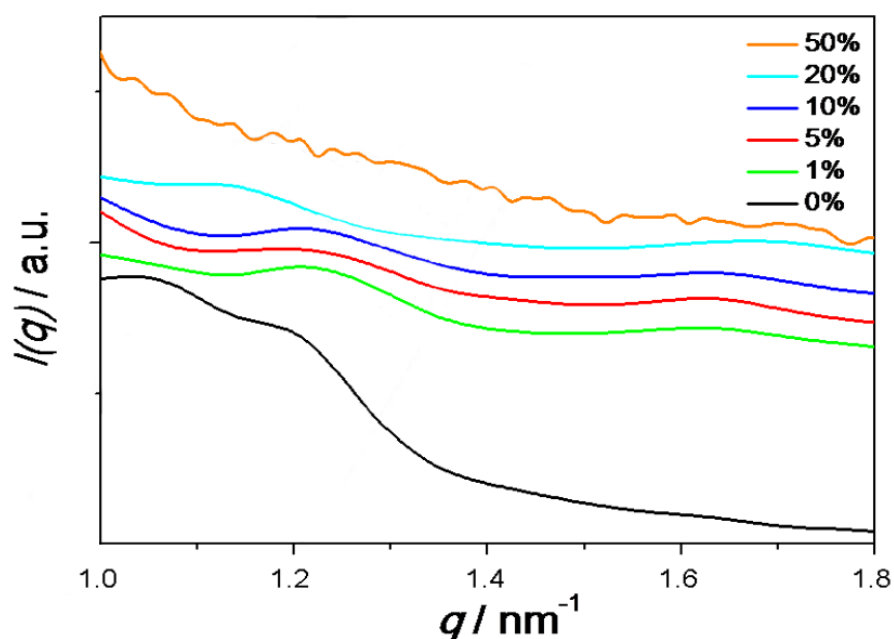
Figure S8: The photoluminescence emission spectra ($\lambda(\text{exc}) = 330 \text{ nm}$) of **RhB**-doped $\text{Zn}(\text{Si}_x\text{-q})_2\text{-PMOM}$ (blue) and $\text{Zn}(\text{Si}_x\text{-q})_2\text{-PMOM}$ (red).

To conclude, these findings are promising for the development of light-harvesting antennae based on mesoporous silica. Of the two BODIPYs presented in Chapter 3, **JM1** shows most promise for a number of reasons. Firstly, it is water-soluble meaning that no co-solvent is needed for its insertion into the micelles, meaning there is less danger of disrupting the template through a change in the polarity of the medium. Secondly, as it is used in the COK-12 synthesis, the conditions are particularly mild allowing co-condensation, as seen in Chapter 6, to be achieved even if the second guest is susceptible to degradation at elevated temperatures or away from neutral pH. However, if the formation of **BS** is more understood, a similar process could be induced with **JM1** allowing for this dye to be used to synthesis a bichromophoric system as seen in the **BPJ2/CTAB@MCM-41** samples in Chapter 3. As the **Zn(Si_x-q)₂-PMOM** emits in the green region, it could be used as a donor if BODIPYs are included in the micelles as acceptors, similar to how **RhB** is used in Chapter 6. This could also be applied to the Pt(II) complexes in Chapter 5 whereby energy transfer to these dyes would enhance their luminescence making a more efficient OLED device. Partial energy transfer in such a device could also result in a white light emitting device.

Appendix

Sample dye-loading(%)	$2\theta / ^\circ$	q / nm^{-1}	d / nm	Ratio	2D hexagonal reflection
0	0.8	0.57	11.00	1	(10)
	1.5	1.07	5.88	1.88	(11)
	1.7	1.21	5.19	2.12	(20)
1	0.9	0.64	9.80	1	(10)
	1.7	1.21	5.19	1.89	(11)/(20)
	2.3	1.64	3.83	2.56	(21)
5	0.9	0.64	9.80	1	(10)
	1.7	1.21	5.19	1.89	(11)/(20)
	2.3	1.64	3.83	2.56	(21)
10	0.9	0.64	9.80	1	(10)
	1.7	1.21	5.19	1.89	(11)/(20)
	2.3	1.64	3.83	2.56	(21)
20	0.9	0.64	9.80	1	(10)
	1.6	1.14	5.51	1.78	(11)/(20)
	2.4	1.70	3.68	2.65	(21)
50	0.9	0.67	9.39	1	(10)
	-	-	-	-	-
	-	-	-	-	-

Table A1: SAXS data for the JMI/Pluronic-P123@COK-12 samples.

Figure A1: SAXS profiles for the COK-12 silica hybrids in the q range 1-1.8 nm^{-1} .

Sample/dye-loading(%)	Decay Kinetics		
	τ_1 (ns)	τ_2 (ns)	τ_3 (ns)
JM1	6.05	-	-
1	5.81	-	-
5	5.33	-	-
10	5.25 (82%)	2.54 (18%)	-
20	3.75 (35%)	1.52 (65%)	-
50	3.13 (10%)	0.80 (60%)	0.20 (30%)

Table A2: The decay traces for **JM1** in solution and in COK-12 at various dye-loadings.

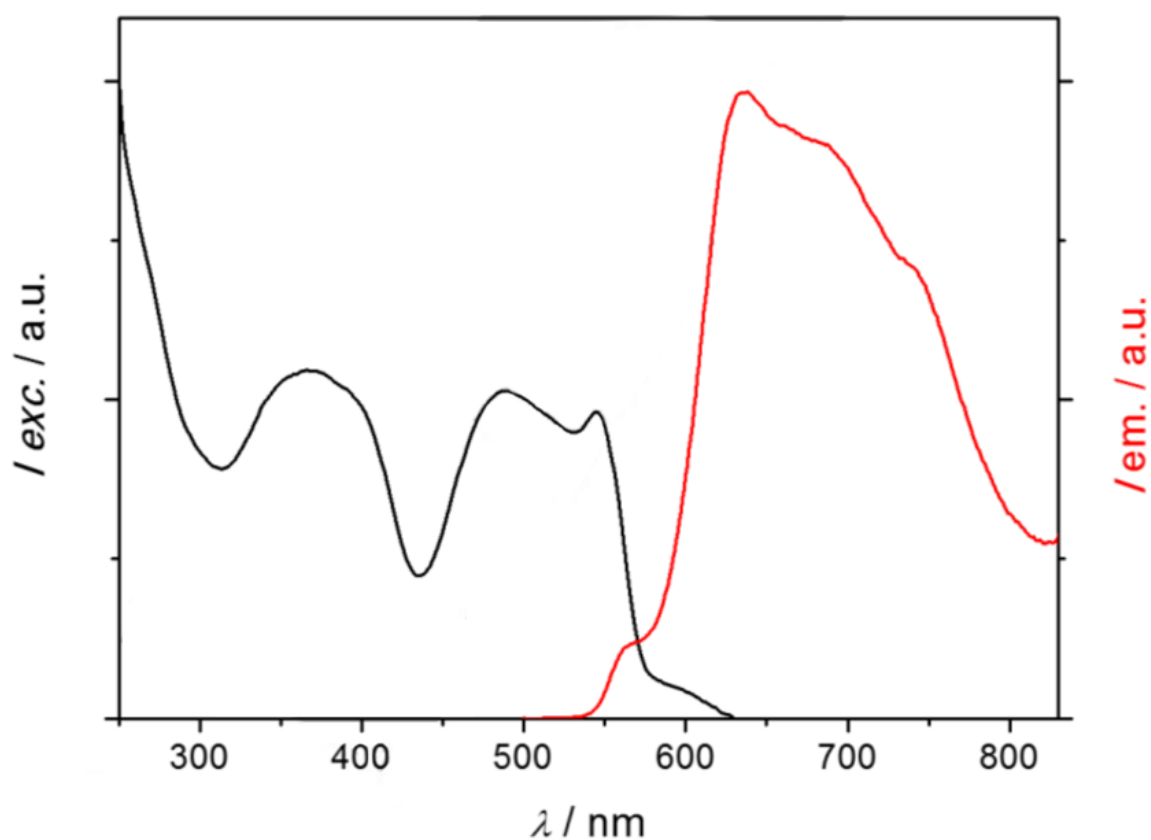


Figure A2: Photoluminescence excitation (black, $\lambda(\text{em}) = 700$ nm) and emission (red, $\lambda(\text{exc}) = 480$ nm) of a thin film of **JM1**.

Sample dye-loading(%)	$2\theta / ^\circ$	q / nm^{-1}	d / nm	Ratio	2D hexagonal reflection
0	2.2	1.56	4.01	1	(10)
	3.9	2.77	2.26	1.77	(11)
	4.5	3.20	1.96	2.05	(20)
1	2.2	1.56	4.01	1	(10)
	3.8	2.70	2.32	1.77	(11)
	4.4	3.13	2.00	2	(20)
5	2.1	1.49	4.20	1	(10)
	3.7	2.63	2.39	1.77	(11)
	4.3	3.06	2.05	2.05	(20)
10	2.1	1.49	4.2	1	(10)
	-	-	-	-	-
	-	-	-	-	-
20	2.1	1.49	4.2	1	(10)
	3.8	2.70	2.3	1.81	(11)
	4.2	2.99	2.1	2.1	(20)
	4.6	3.27	1.9	1.9	(20)
50	2.1	1.49	4.2	1	(10)
	3.6	2.56	2.5	1.68	(11)
	4.2	2.99	2.1	2	(20)

Table A3: SAXS data for the **BPJ2/CTAB@MCM-41** samples.

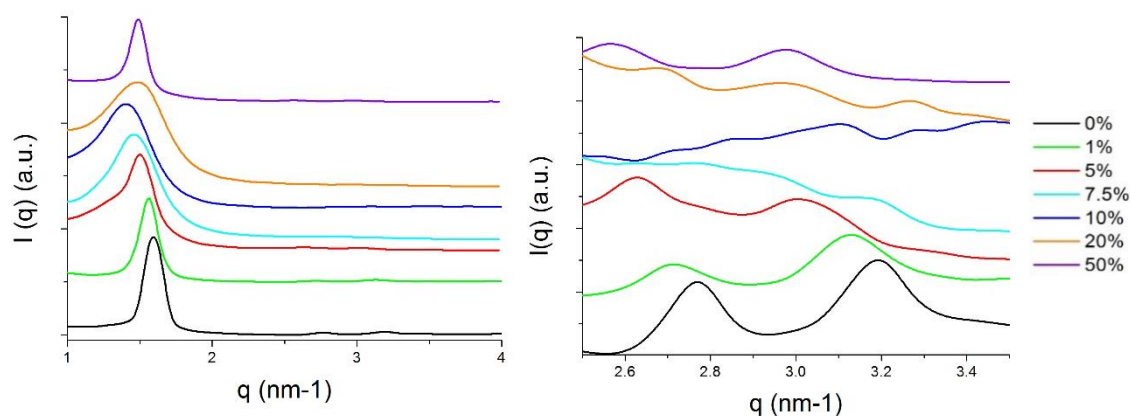


Figure A3: SAXS profiles of **BPJ2/CTAB@MCM-41** samples at various dye-loadings; full q range (left) and from 2.5 to 3.5 nm^{-1} .

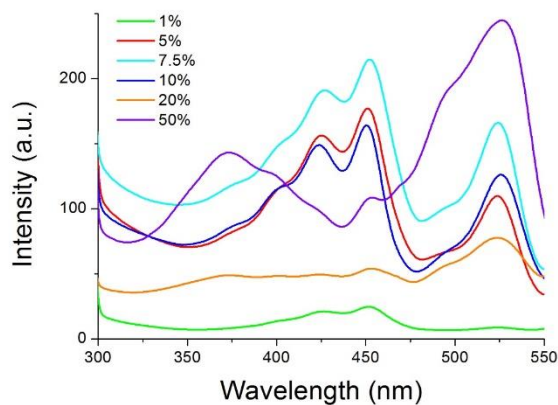


Figure A4: Fluorescence excitation spectra ($\lambda(\text{em}) = 580 \text{ nm}$) of the **BPJ2/CTAB@MCM-41** recorded from 0.3 mg/ml cyclohexane suspensions.

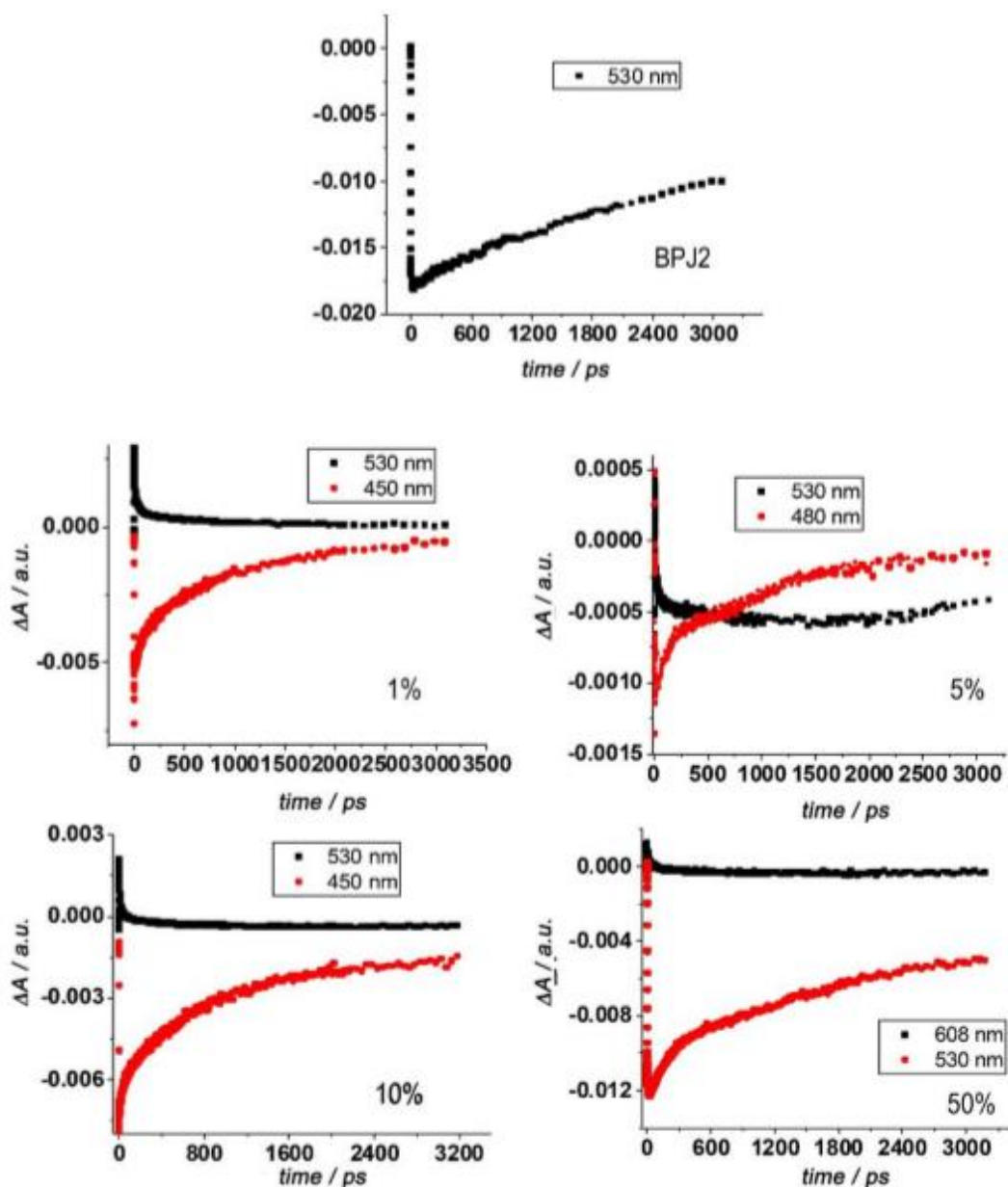
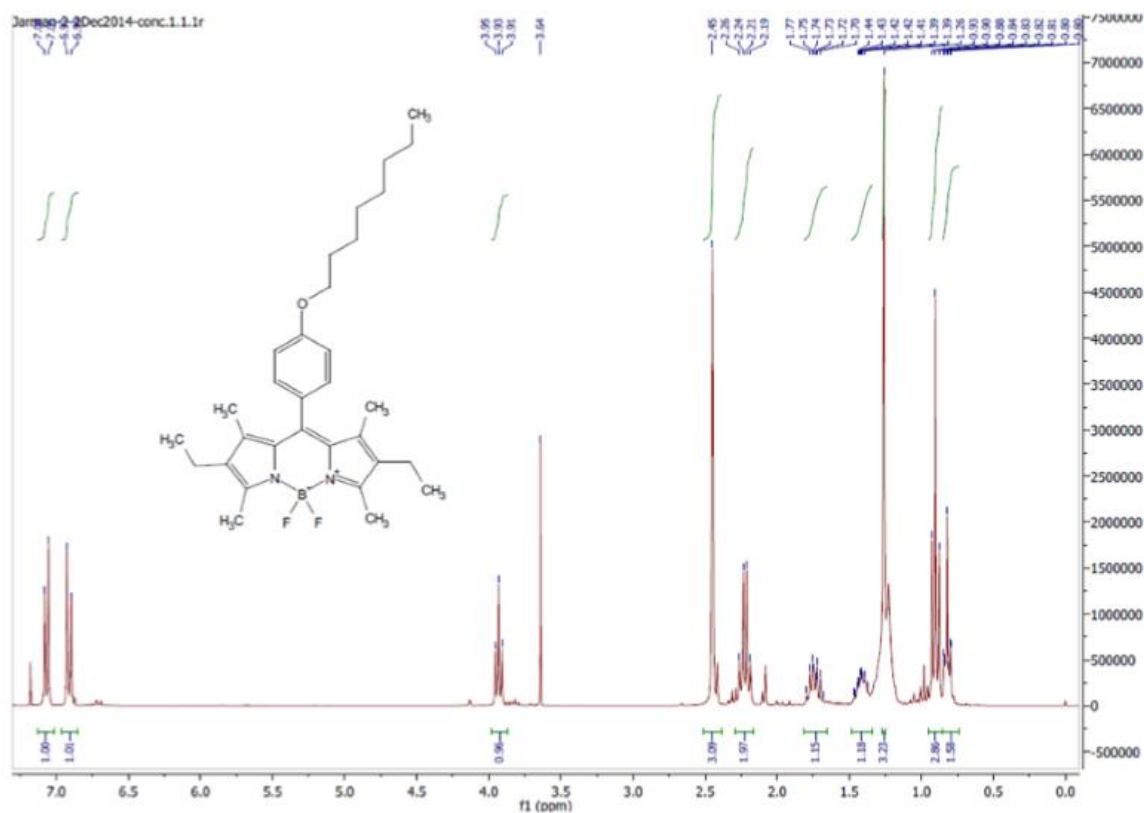
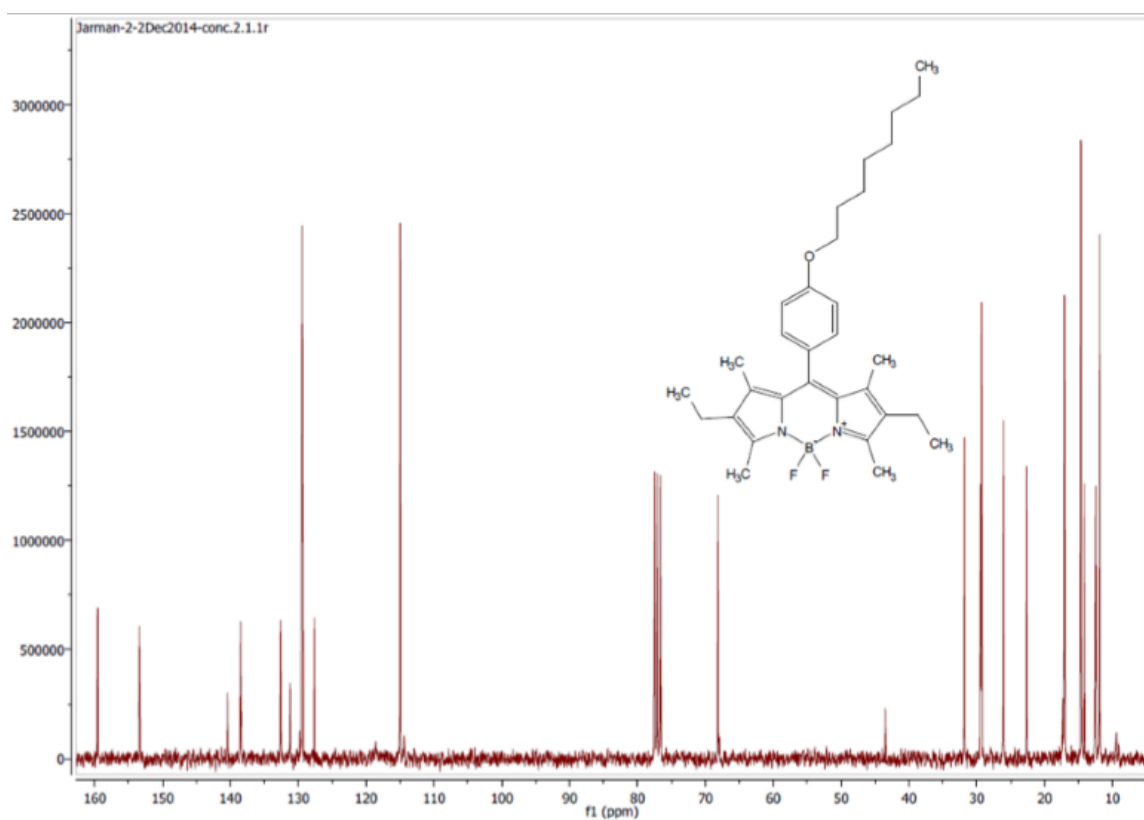


Figure A5: The kinetic traces from TAS experiments of BPJ2 in ethanol (top) and four representative **BPJ2/CTAB@MCM-41** samples (labelled) recorded in 0.3 mg mL^{-1} water suspensions.

Figure A6: The ^1H NMR spectrum of BPJ2.Figure A7: The ^{13}C NMR spectrum of BPJ2.

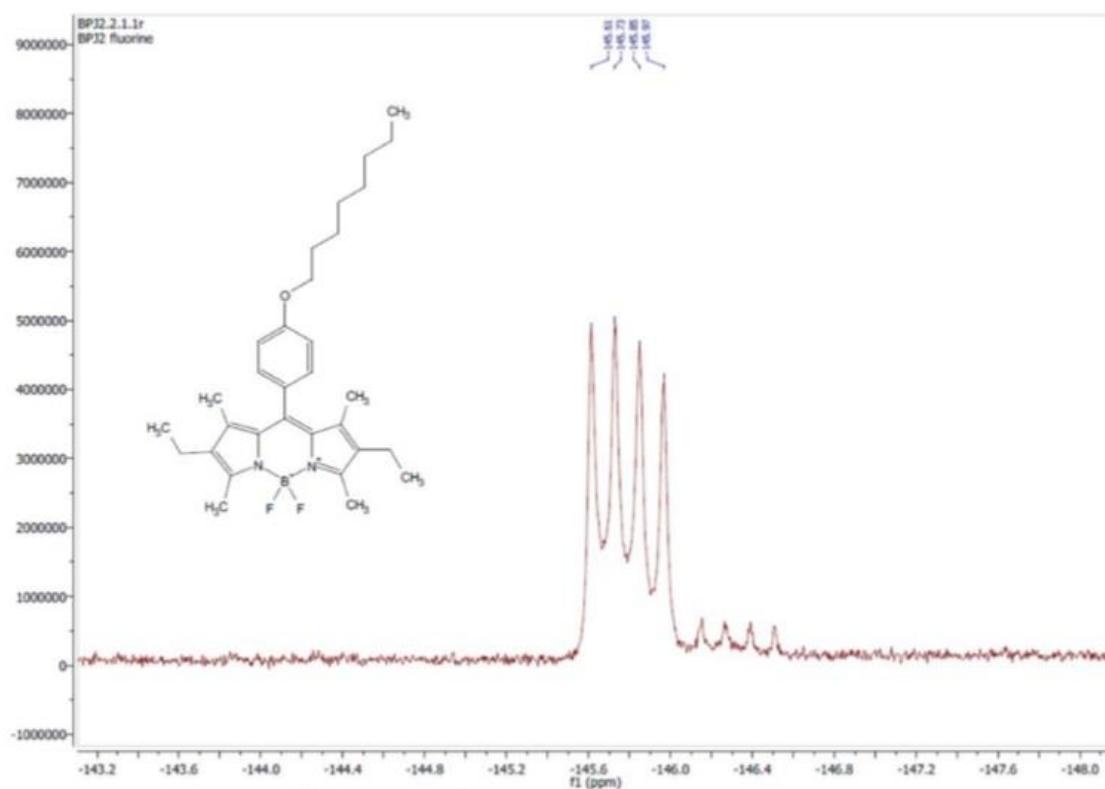


Figure A8: The ^{19}F NMR spectrum of BPJ2.

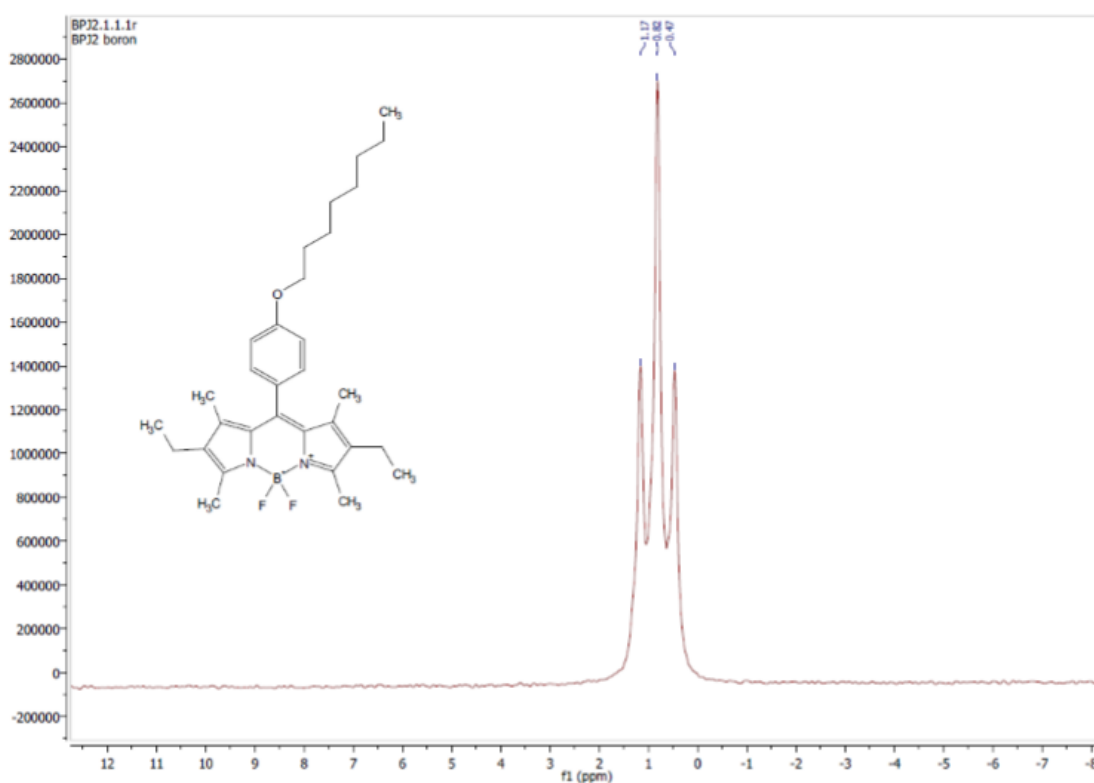


Figure A9: The ^{11}B NMR spectrum of BPJ2.

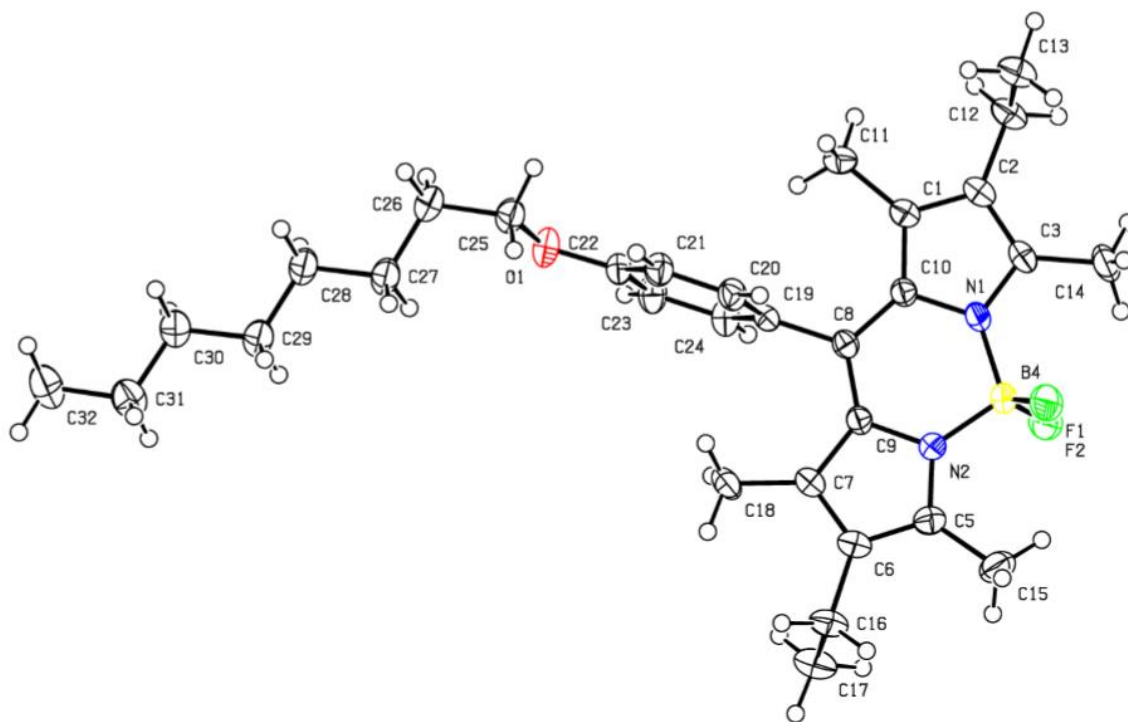


Figure A10: The crystal structure of BPJ2.

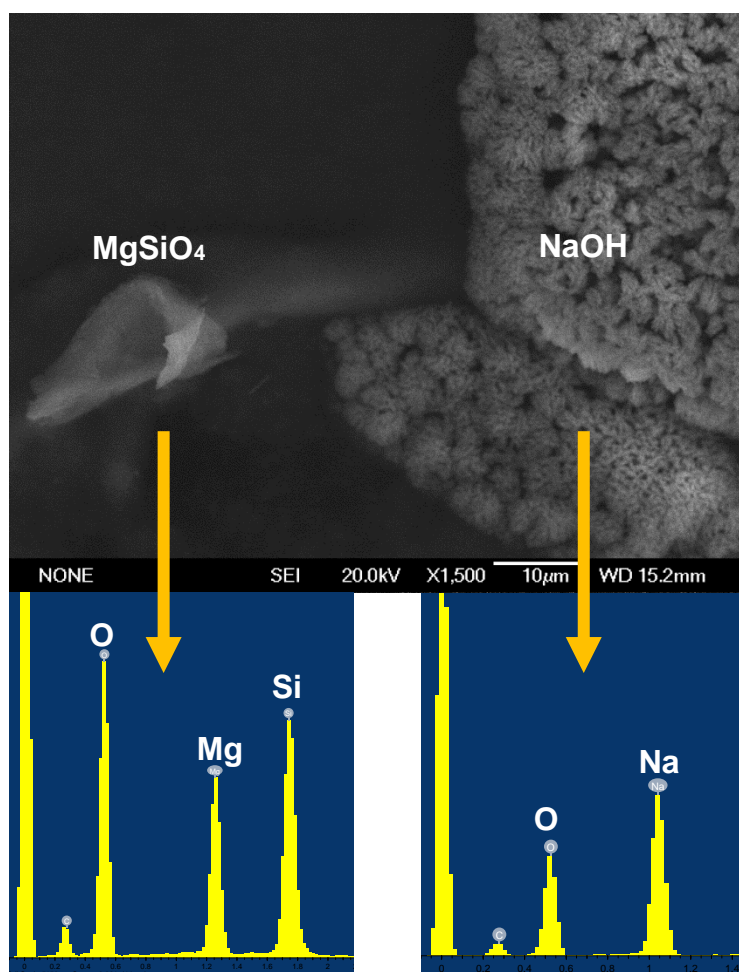


Figure A11: (top) SEM images of a sample of the commercial NaOH used by this group. (bottom) EDX spectra of the two crystals showing the presence of magnesium silicate in the NaOH sample.

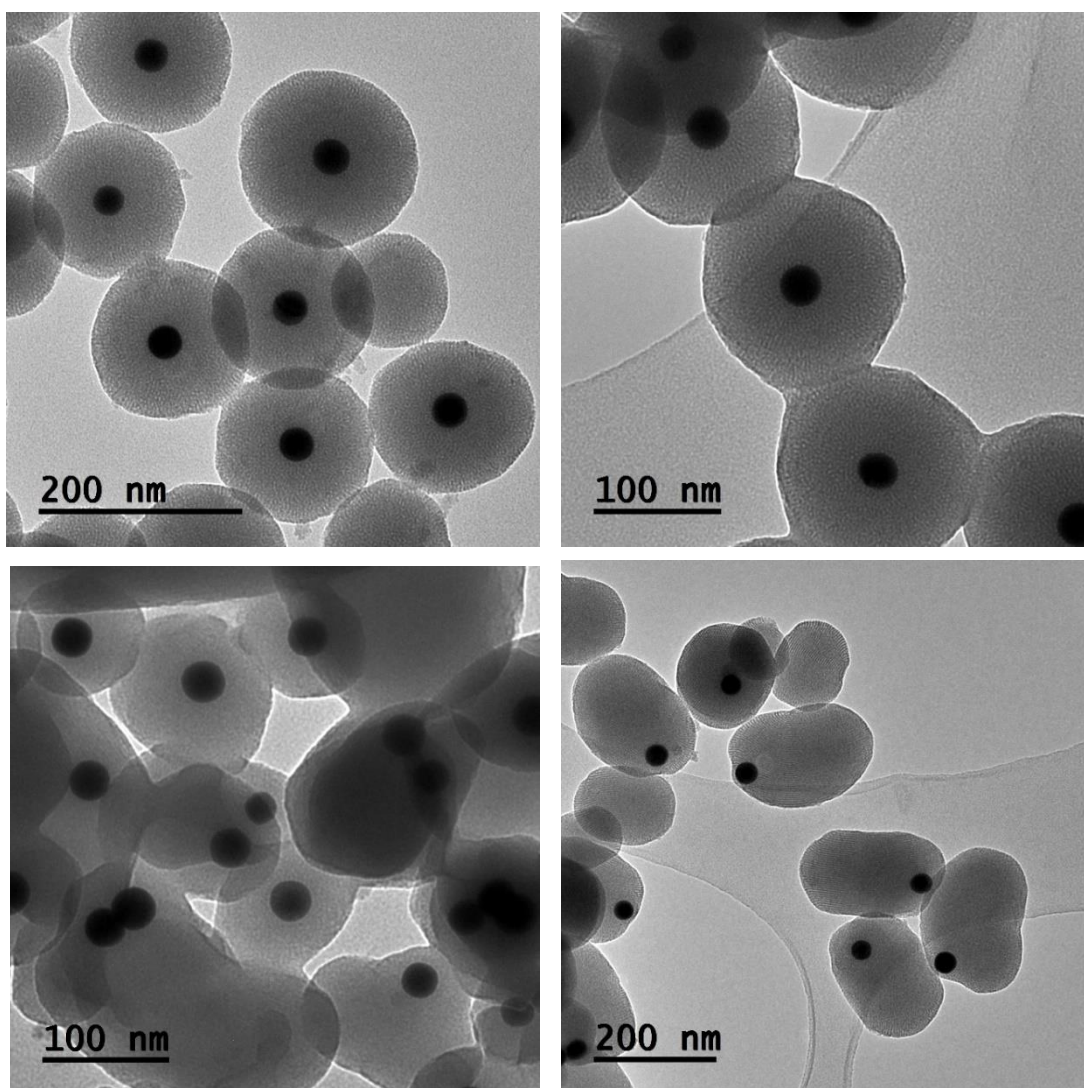


Figure A12: TEM images of gold nanoparticle doped MCM-41 synthesised with the addition (top left) 1 μL , (top right) 2 μL , (bottom left) 3 μL and (bottom right) 4 μL of sodium silicate solution. Note the migration of the nanoparticle to the edge of the silica as the amount of silicate increases.

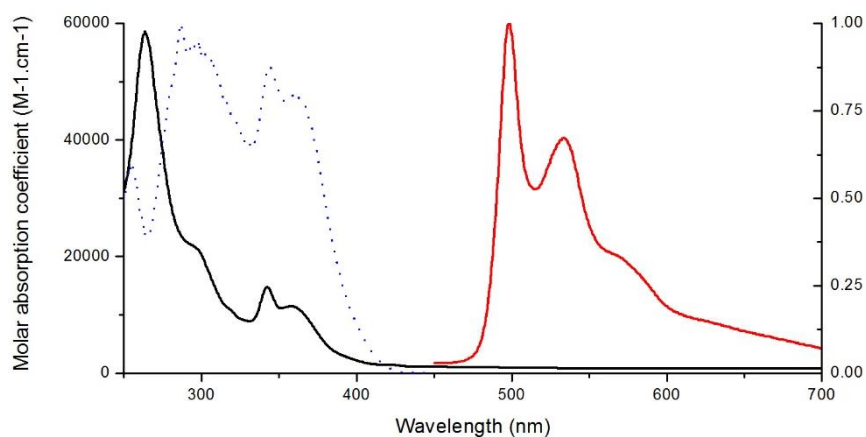


Figure A13: The UV/Vis absorption (black) and photoluminescence emission (red, $\lambda(\text{exc}) = 360$ nm) and excitation (blue hashed, $\lambda(\text{em}) = 570$ nm) spectra of **VNK-40-C12** in DCM.

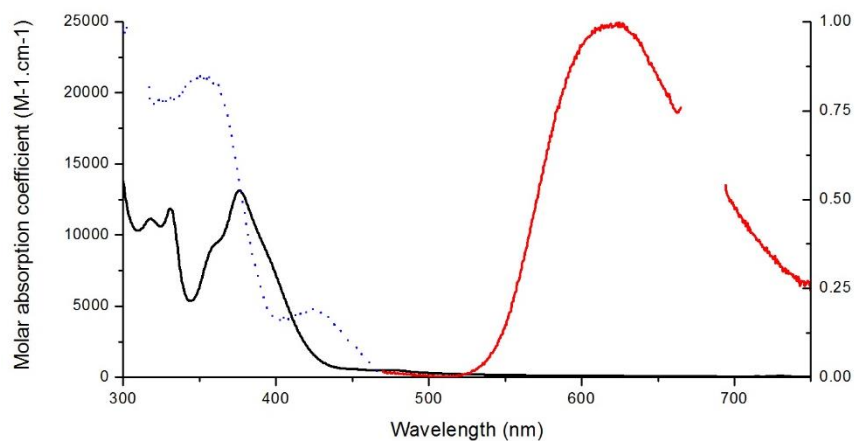


Figure A14: The UV/Vis absorption (black) and photoluminescence emission (red, $\lambda(\text{exc}) = 360$ nm) and excitation (blue hashed, $\lambda(\text{em}) = 570$ nm) spectra of **TGV-19** in DCM.

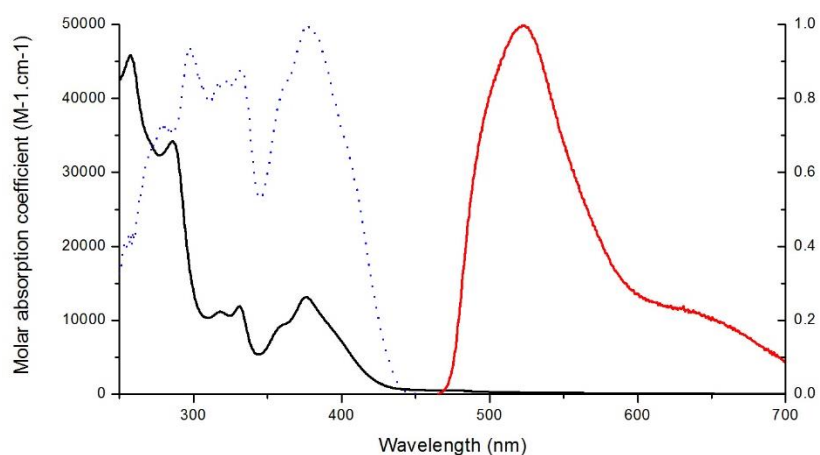
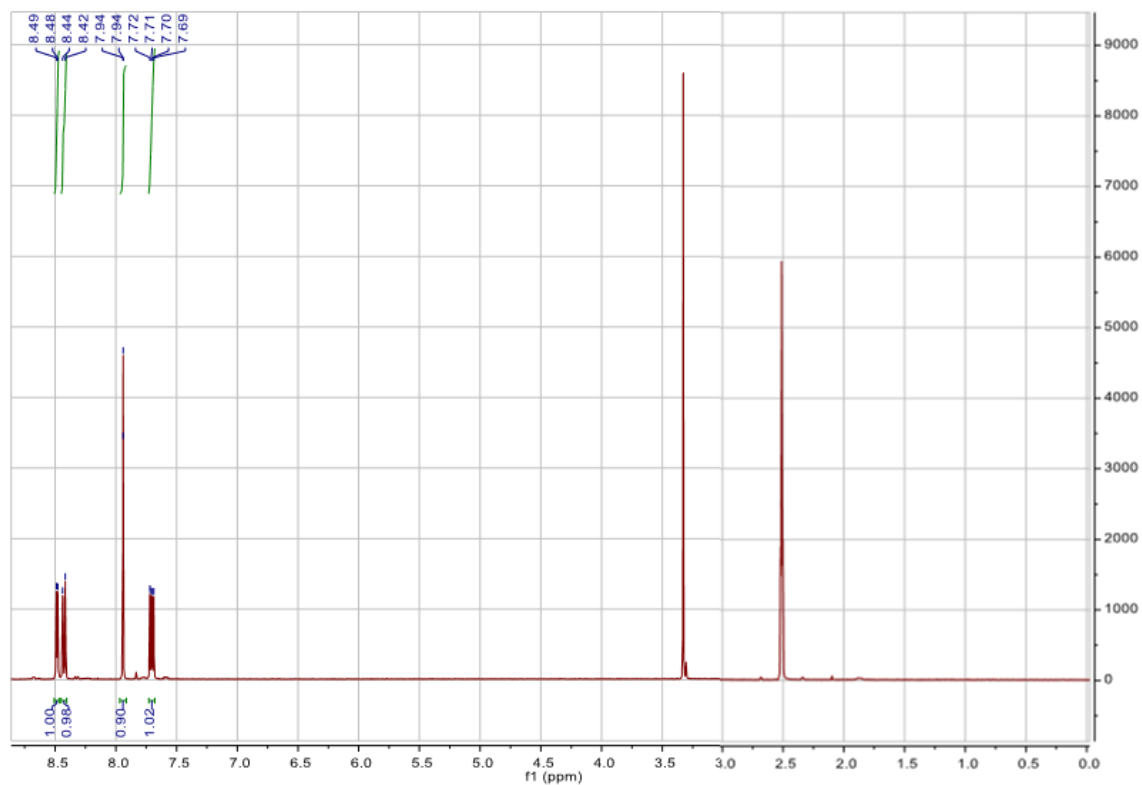
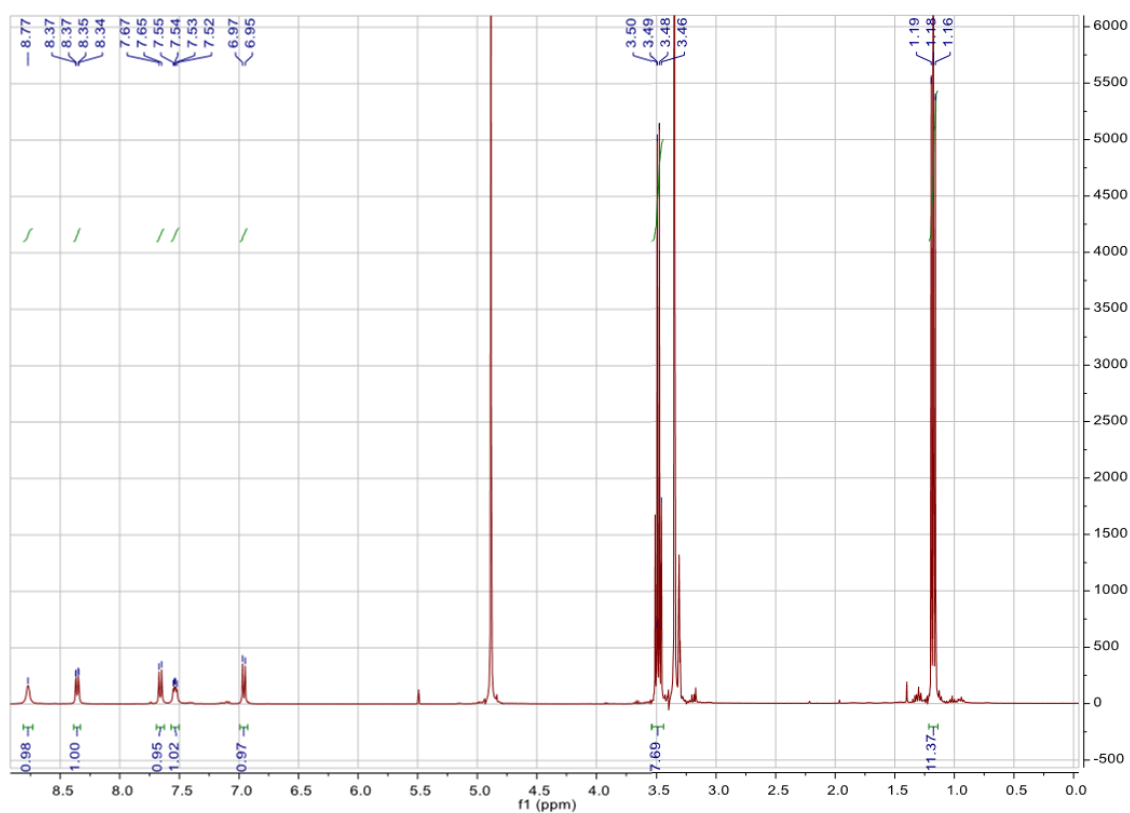


Figure A15: The UV/Vis absorption (black) and photoluminescence emission (red, $\lambda(\text{exc}) = 360$ nm) and excitation (blue hashed, $\lambda(\text{em}) = 570$ nm) spectra of **N-129** in DCM.

Figure A16: The ^1H NMR spectrum of $\text{Zn}(\text{Br}_2\text{-q})_2$.Figure A17: The ^1H NMR spectrum of $\text{Zn}(\text{Si}_x\text{-q})_2$.

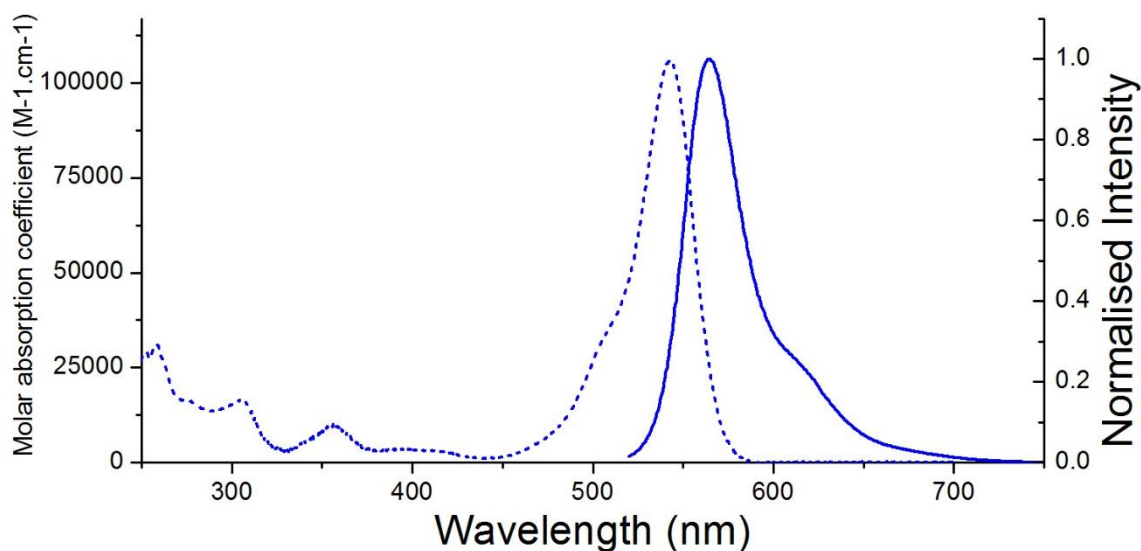


Figure A18: The UV/Vis absorption (hashed) and photoluminescence emission (solid, $\lambda(\text{exc}) = 500 \text{ nm}$) spectra of **RhB** in DCM. Data taken from http://www.photochemcad.com/compounds/N11_Rhodamine_B.htm (accessed July 2018)

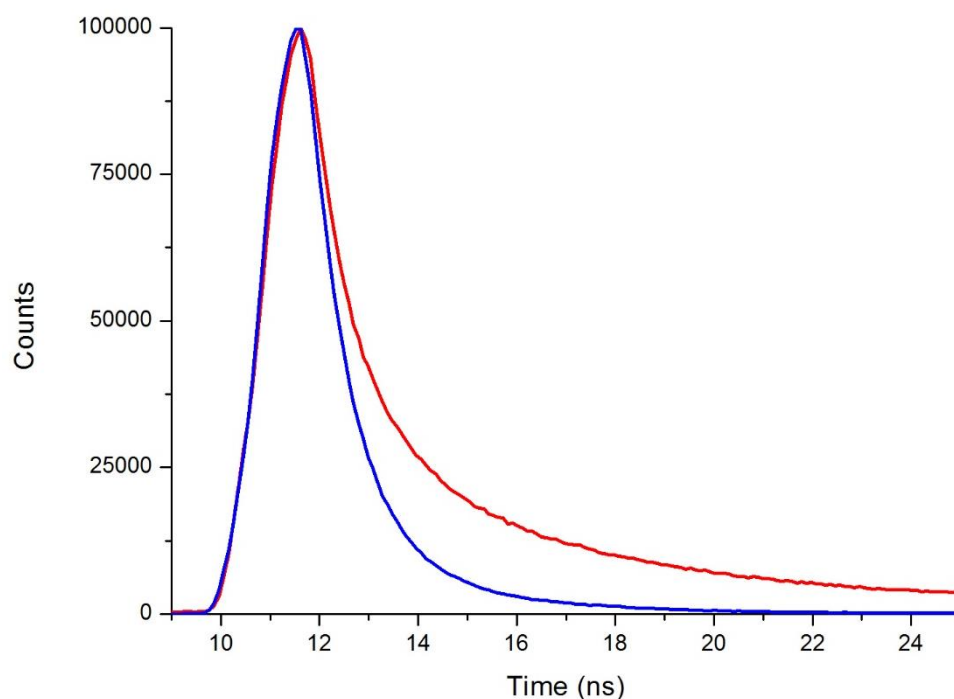


Figure A19: The excited state decay traces of the 2% $\text{Zn}(\text{Si}_x\text{-q})_2\text{-PMOM}$ (red) and the 2%/2% **RhB**/Pluronic-P123@ $\text{Zn}(\text{Si}_x\text{-q})_2\text{-PMOM}$ (blue) taken using the TCSPC method and 470.8 nm excitation pulse.

Publications

1. B. P. Jarman and F. Cucinotta, *Faraday Discuss.*, 2015, **185**, 471-479.
2. F. Cucinotta, B. P. Jarman, C. Caplan, S. J. Cooper, H. J. Riggs, J. Martinelli, K. Djanashvili, E. La Mazza and F. Puntoriero, *ChemPhotoChem*, 2018, **2**, 196-206.